

## CATALYSTS FOR THE HYDROGEN ECONOMY

ROBERT J. FARRAUTO

ENGELHARD CORPORATION,  
101 WOOD AVENUE, ISELIN, NJ 08830

Pollution emissions from mobile sources have been controlled for the last 30 years by monolithic catalysts in the exhaust system. The catalysts enhance the rate of conversion of unburned CO, HC and NO<sub>x</sub> to harmless products. Throughout the world emission standards are becoming ever more stringent, thus demanding more from the catalyst and engineering design of the power source. Furthermore, fossil fuel combustion generates large quantities of green house gases such as CO<sub>2</sub>. The widespread use of fuel efficient lean burn vehicles (diesel) is hindered by lack of an adequate technology for NO<sub>x</sub> reduction. Although progress has been made with NO<sub>x</sub>-storage systems, especially in Japan, the presence of sulfur and complicated regeneration requirements have hindered their application. As diesel engines gain in popularity due to their fuel efficiencies the problem of dry particulate removal from the exhaust must be managed. Although all of these problems are being addressed we must continue to be aware of the negative consequences of not having alternative technologies for energy and power generation.

The problem of limited energy supply, generation of primary pollutants and green house gases is raising the importance of a hydrogen economy and the need to investigate alternative means of power generation from reliable and ideally renewable- sources of fuel. The fuel cell is a critical technology for the future.

The fuel cell generates power by direct conversion of chemical energy, i.e. H<sub>2</sub> and O<sub>2</sub>, to electrical energy avoiding the traditional combustion processes that generate pollutants (Appleby 1999; St Pierre and Wilkinson 2001). Furthermore, the system power efficiency is no longer limited by the Carnot cycle in which chemicals must be first combusted to produce mechanical energy. Greater efficiency translates to energy conservation and lower emissions of CO<sub>2</sub> depending on the source of hydrogen necessary to operate the fuel cell. For this reason there has been tremendous research in attempting to develop fuel cells as an alternative to conventional combustion systems used for power generation. Ideally one can envision a system whereby natural sources of energy such as solar, wind, geothermal, hydroelectric, etc. can be used to extract hydrogen from water producing an essentially inexhaustible source of energy needed to operate a fuel cell. Natural gas is the logical fuel to convert to hydrogen during the transition to renewable sources.

There are four basic fuel cells systems, solid polymer electrolyte or the proton exchange membrane (PEM) with efficiency close to 40%, phosphoric acid (PAFC) at 45%, molten carbonate (MCFC) and solid oxide (SOFC) both between 60-70%. Each has its own particular application in diverse markets (Heck et al 2002). Alkaline fuel cells continue to be used for space applications but these require ultra clean pure hydrogen and oxygen and hence are not considered feasible for more earthly applications. Phosphoric acid fuel cells are operating throughout the world powering large buildings (> 250Kw) but are not considered cost effective for lower power applications.

The most highly visible fuel cell applications are for vehicles. Toyota and Honda have produced a few PEM powered fuel cell vehicles currently being demonstrated in the US and Japan but it

is now widely accepted that the market will not be realized until at the earliest 2010 mass production. Most automobile companies have abandoned the concept of generating hydrogen on-board from gasoline in favor of hydrogen storage. The later technology is critical for the implementation of fuel cell vehicles (Dagini 2002). The most feasible concept is to develop a hydrogen infrastructure where your local service station provides hydrogen generated from natural gas that is then stored on-board the vehicle as a liquid, gas or solid hydride.

An early market for PEM fuel cells will be residential or distributed power for homes. The concept is to reform natural gas or LPG in the home to provide H<sub>2</sub> for the anode of the PEM fuel cell. A common thread in all applications is the safe and compact generation of the H<sub>2</sub> by catalytic reforming of the liquid or gaseous fuel (Katikaneni and Song 2002).

Today's lecture will briefly describe the principles of the PEM fuel cell and the unit operations for the catalytic generation of hydrogen from fossil fuels.

### References:

- Appleby, A. "The electrochemical engine for vehicles" Scientific American 281 (1) 1999
- Dagini, R. "Tempest in a tiny tube" Chemical Engineering News, January 14, 25, 2002
- Heck, R., Farrauto, R. with Gulati, S. "Catalytic air pollution control: commercial technology" second edition, Wiley and Sons, NY. 2002
- Katikaneni, S. and Song, C. "Fuel processing for fuel cells" Catalysis Today 77 (1,2) 2002
- St. Pierre, J. and D. Wilkinson, "Fuel cells a new, efficient and cleaner power source" AIChE Journal 47, 1482 (2001)

# DESULFURIZATION BY ADSORPTION AND CATALYTIC STEAM REFORMING OF DIESEL FOR FUEL CELL APPLICATIONS

Shaker Haji, Joanna Ziemlewski, and Can Erkey

Department of Chemical Engineering  
Environmental Engineering Program  
University of Connecticut  
Storrs, CT 06269-3222

## Introduction

Hydrogen is the ideal fuel for PEM Fuel Cells in terms of system integration. The lack of an infrastructure for distribution of hydrogen necessitates the development of technologies for production of hydrogen from other sources such as methanol, gasoline and diesel. Liquid fuels can be converted to H<sub>2</sub> by a series of steps which include oxidation or steam reforming, high temperature shift conversion, low temperature shift conversion and preferential oxidation.<sup>1,2,3,4</sup>

An important consideration in reforming of hydrocarbon fuels is that they contain significant amounts of sulfur containing compounds such as thiophenes, benzothiophenes and dibenzothiophenes. Currently sulfur levels in diesel and gasoline are around 500 and 300 parts per million by weight (ppmw), respectively. The presence of such compounds at such concentrations has a detrimental effect on the performance of catalysts used in reforming, water gas shift reactors, and the fuel cell stacks. For example, the presence of 100 ppm thiophene in a simulated gasoline mixture caused the hydrogen content of the effluent from the fuel processing unit to drop from 60 to 40 % over a 25 hours reaction time.<sup>3</sup> It is generally agreed that hydrocarbon fuels need to be desulfurized to concentrations less than 0.1 ppm sulfur which necessitate incorporation of desulfurization technologies into the fuel processor.<sup>5</sup>

The use of diesel as a source of hydrogen for PEM fuel cells is advantageous since:

1. diesel has a much higher energy density than other fuels (42.5 MJ/kg, LHV for diesel vs. 20.0 MJ/kg LHV for methanol),
2. diesel fuel infrastructure is already in place.

However, reforming of diesel fuel is complicated and requires high temperatures.

In this article, we report our results on the use of carbon aerogels as an adsorbent for desulfurization of diesel. In addition, various precious metal commercial catalysts for steam reforming of diesel were tested and compared to a catalyst synthesized in house. Hexadecane was used as a model for diesel fuel while dibenzothiophene (DBT) was used as a model of sulfur compound. DBT is chosen for it is a refractory polyaromatic sulfur compound and is present in diesel in appreciable amount. The carbon aerogels were synthesized and characterized in our lab. Two different CAs with two different average pore diameters were studied. Both adsorption isotherms and approach to adsorption equilibrium curves are discussed here.

A laboratory scale reactor system was designed and constructed to investigate steam reforming of diesel for fuel cell applications. Using n-hexadecane as a surrogate diesel fuel, catalytic steam reforming was investigated at various conditions to maximize production of hydrogen.

## Experimental

**Carbon Aerogel.** The resorcinol-formaldehyde (RF) aerogels were synthesized by the reaction of resorcinol with formaldehyde in

aqueous solution in the presence of a catalyst. Two formulations were made using different catalyst amount and composition. After several days of curing the mixture, a monolith was formed and it was immersed in acetone overnight. Subsequently, acetone was extracted with liquid and supercritical carbon dioxide. Then the RF aerogels were converted to carbon aerogels by pyrolysis in an inert nitrogen atmosphere at 1085°C. The carbon aerogel was characterized using nitrogen adsorption.

**Sulfur Adsorption.** The carbon aerogel (CA) monoliths were crushed to pass through sieves with Tyler mesh number of 14 then vacuumed for 45 min at room temperature before it was used in the adsorption experiments. The adsorption data were obtained using batch technique. A series of vials containing 160 mg CA and 7.5 g of DBT solution in n-hexadecane solution along with a stirring bar were sealed and stirred at room temperature. Stirring was continued until equilibrium was reached for determination of adsorption isotherm curves or until a specified time to follow the kinetics of adsorption. Subsequently, the solution was filtered and analyzed by gas chromatography with FID detector.

**Reforming Catalysts.** Several commercially available catalysts were studied, including 0.5 wt.% Pt/Al<sub>2</sub>O<sub>3</sub>, 0.5 wt.% Rh/Al<sub>2</sub>O<sub>3</sub>, and 0.5 wt.% Pd/Al<sub>2</sub>O<sub>3</sub>. Additionally, 1 wt.% Pt/CeO<sub>2</sub>-ZrO<sub>2</sub> was synthesized via the sol-gel method using Zr(OC<sub>3</sub>H<sub>7</sub>)<sub>4</sub> and Ce(NO<sub>3</sub>)<sub>3</sub>·6H<sub>2</sub>O. Platinum was incorporated into the porous support using the supercritical deposition method. The catalysts were characterized by hydrogen chemisorption, BET and XRD.

**Steam Reforming.** The catalyst was inserted in a 1.27 cm OD tubular reactor within a tube furnace. Fuel and water were mixed and vaporized before the entrance and fed into the reactor. The steam-to-carbon ratio was set at one and conversion of the fuel was measured in the temperature range 500 – 1000 K. The steam-to-carbon ratio was then increased to two and again conversion was measured over the same temperature range. The product stream was analyzed with a gas chromatograph equipped with a thermal conductivity detector.

## Results and Discussion

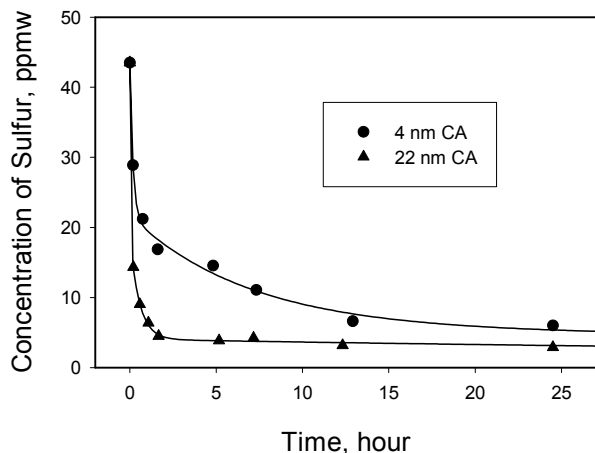
Carbon aerogels (CAs) were studied as adsorbents for the desulfurization of liquid hydrocarbon fuels for fuel cell applications. The properties of CA synthesized were found to depend on the resorcinol/catalyst and resorcinol/water mole ratios. This change in properties also affected the sulfur adsorption behavior and capacity as will be shown later. Table 1 summarizes the properties of the two different CAs obtained using the two different formulations.

Table 1. Properties of the prepared carbon aerogels.

Formulation	S <sub>tot</sub>	D		V <sub>tot</sub>	V <sub>mic</sub>	S <sub>mic</sub>	V <sub>mic</sub> /V <sub>tot</sub>
	(m <sup>2</sup> /g)	(nm)		(cm <sup>3</sup> /g)	(cm <sup>3</sup> /g)	(m <sup>2</sup> /g)	(%)
	BET	BET	BJH		t-plot		
F1	741	4.1	4.3	0.78	0.12	252	15.4
F2	670	21.1	22.2	3.63	0.12	233	3.3

S<sub>tot</sub>: BET total surface area. D: average pore diameter. V<sub>tot</sub>: total pore volume. V<sub>mic</sub>: micropore volume. S<sub>mic</sub>: micropore surface area.

First, an approach to equilibrium data was obtained to study the behavior of the sulfur-compound (DBT) adsorption onto CA. This was tested with a solution of 250 ppmw of DBT (43.5 ppmw S content) in n-HD. It took around 8 days for the adsorption process to reach to equilibrium. That could be explained by the presence of micropores in the CAs, which slows down the DBT adsorption process. The 4 nm CA adsorbed 93% of the sulfur initially present in the solution, while the 22 nm CA adsorbed 98.5% of it. Though the 4 nm CA has larger surface area, the 22 nm CA adsorbed more DBT than the earlier one. Figure 3 shows the first 24 hours of the adsorption process. The observation in the difference in the adsorption rate, with the two different CAs, may be attributed to the difference in the pore diameter.



**Figure 1.** The approach to equilibrium curves for the adsorption of DBT on CA.

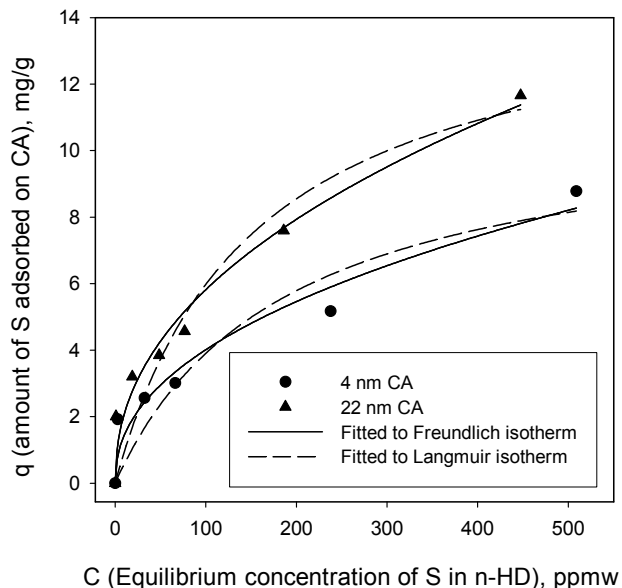


**Figure 2.** Adsorption isotherms for DBT at room temperature on CA. The experimental data is fitted to the equations of Freundlich and Langmuir isotherms.

Figure 2 illustrates the adsorption isotherms for DBT on the two different pore size CAs at room temperature and atmospheric pressure. As the initial concentration of sulfur in the solution increased, the amount of DBT adsorbed on CA increased. Up to the range of the initial sulfur concentration in these sets of experiments (4000 ppmw DBT = 696 ppmw S), the loading of DBT on CA is far from saturation. The trend of the adsorption isotherms shows that the 22 nm CA has higher sulfur adsorption capacity than the 4 nm CA. For a given sulfur concentration in the solution, the equilibrium adsorbed amount of DBT on the 22 nm CA is higher than that on the 4 nm CA. It was expected that the 4 nm CA would adsorb more amount of the sulfur compound (DBT) than the 22 nm CA, since the former has higher surface area. However, this was not the case. This demonstrates that changing the initial concentrations of the reactants and the catalyst not only changes the pore size, but also changes the chemical structure and the physical/chemical properties of the surface of the carbon aerogel. The adsorption isotherms for the adsorption of DBT on both carbon aerogels were fitted to both Freundlich and Langmuir isotherms, as shown in Figure 2. The Langmuir model corroborates what was mentioned earlier that the 22 nm CA has higher sulfur adsorption capacity than the 4 nm CA, giving an adsorption capacity different by 35%.

When DBT and NA are equally present in the solution (1.04 mM each), both carbon aerogels showed selectivity in adsorption for DBT. Both CAs have similar selectivity, 1.61 and 1.47 moles DBT adsorbed/moles NA adsorbed for 4 nm and 22 nm CA, respectively. However, the presence of NA in n-HD reduced the amount of DBT adsorbed onto both CA by around 6%. This means that if the diesel fuel contains high concentration of aromatic compounds that are similar in structure with sulfur compounds, then the capacity of the carbon aerogel will be reduced.

For steam reforming of diesel, the product stream included H<sub>2</sub>, CO, CO<sub>2</sub>, ethane, ethylene, and methane. Conversion of both the hexadecane and water increased with increasing temperature for each type of catalyst. The higher temperatures also resulted in little amounts of ethane and ethylene. However, the CO<sub>2</sub>:CO ratio decreased, due to reverse water gas shift at higher temperatures. Additionally, raising the steam-to-carbon ratio increased the CO<sub>2</sub>:CO ratio. The effluent gas compositions were close to the values calculated from equilibrium calculations using Gibbs Free Energy Minimization. Furthermore, it was found that CeO<sub>2</sub>-ZrO<sub>2</sub> as a support was more active than Al<sub>2</sub>O<sub>3</sub>.

**Acknowledgment.** This work was supported by the U.S. Army.

## References

1. Brown, L.F., *Int. J. Hydrogen Energy*, 2001, 26, 381-397.
2. Joensen, F., Rostrup-Nielsen, J. R., *J. Power Sources* 2002, 105(2), 195-201.
3. Moon, D.J., Sreekumar, K., Lee, S.D., Lee, B.G., Kim, H.S., *Appl.Catal. A: Gen.*, 2001, 215(1-2), 1-9.
4. Yanhui, W.; Diyong, W., *Int. J. Hydrogen Energy*, 2001, 26(8), 795-800.
5. Larminie, J., Dicks, A., *Fuel Cell Systems Explained*; John Wiley & Sons: England, 2002.

# ADSORPTIVE DESULFURIZATION OF JP-8 JET FUEL AND ITS LIGHT FRACTION OVER NICKEL-BASED ADSORBENTS FOR FUEL CELL APPLICATIONS

Xiaoliang Ma, Subramani Velu, Lu Sun, and Chunshan Song\*

Clean Fuels and Catalysis Program, The Energy Institute and Department of Energy and Geo-Environmental Engineering, Pennsylvania State University, University Park, PA 16802

\*E-mail: csong@psu.edu

Mehdi Namazian, and Siva Sethuraman

Altex Technologies Corporation, 650 Nuttman Road, Santa Clara, CA 95054

## Introduction

Fuel cell is one of the most promising and convenient energy conversion devices for generating electricity for mobile vehicles, portable power and stationary power plants. For the automotive fuel cells and micro-fuel cells, liquid hydrocarbon fuels are promising candidate fuels due to their higher energy density, availability, and safety (1). For the military fuel cell applications, jet fuel (JP-8) is a widely used logistic fuel. However, the sulfur level in JP-8 can be as high as 3000 ppm, as per the fuel spec, but in practice ranges from 400 to 1600 ppmw (2). The major sulfur compounds in JP-8 are alkyl sulfur compounds, especially 2,3-dimethylbenzo-thiophene (2,3-DMBT) and 2,3,7-trimethyl-benzothiophene (2,3,7-TMBT) (3,4). The sulfur compounds in the fuel, and the resulting H<sub>2</sub>S, produced during reforming process, are poisonous to the catalysts used in the reformer and the subsequent water-gas-shift system, and also to the electrode catalysts in fuel cell stack (1). Thus, the sulfur compounds in the liquid hydrocarbons have to be reduced to less than 0.1 ppmw for polymer electrolyte membrane fuel cell (PEMFC) and at least less than 30 ppmw for the solid oxide fuel cell (SOFC). The conventional hydrodesulfurization processes operate at high temperature (300-400 °C) and require high-pressure hydrogen (30-80 kg/cm<sup>2</sup>) and are not able to achieve such a low sulfur level economically (5). Consequently, the current hydrotreating technology is not suitable for meeting the need of ultra-clean liquid hydrocarbon fuels for the fuel cell applications.

Development of new deep desulfurization processes of the liquid hydrocarbon fuels has become one of the major challenges in developing the hydrocarbon processor for fuel cell applications. In our previous work, we proposed a process at Penn State University based on selective adsorption for removing sulfur (PSU-SARS) for on-board and on-site desulfurization (4-10). We have prepared, synthesized and tested many potential adsorbents, including metal complex, metal ions exchanged zeolites, carbon materials, reduced metals, metal halides, metal sulfides, and metal oxides with and without supports. In this paper, we report our current approaches in the adsorptive desulfurization of real jet fuels and fractionated fuels over nickel-based adsorbents.

## Experimental

The JP-8 jet fuel used in the present study was provided by US Air Force Wright Laboratory. From total sulfur analysis, the sulfur concentration in this jet fuel is 736 ppmw. A light fraction (light JP-8) of JP-8 with sulfur concentration of 380 ppmw was obtained from this JP-8 fuel by fractionation to cut off about 30 wt % of the fuel (heavy fraction). The adsorbents (Adsorbent-2 and Adsorbent-5) used in the present study are nickel-based materials. Adsorbent-2 has a surface area around 90 m<sup>2</sup>/g without any support, while Adsorbent-5 has a surface area around 150 m<sup>2</sup>/g with alumina support. The adsorption experiments were performed under ambient pressure in a

fixed-bed adsorption device, which was described in detail in one of our previous papers (8). The fuel was fed into the adsorption column through a LC pump and flowed down through the adsorption bed. Analysis of sulfur compounds in the JP-8 fuels and treated fuels was performed by using GC with a capillary column, XTI-5 (Restek) 30 m x 0.25 mm x 0.25 micrometer, and a pulsed flame photometric detector (PFPD). The method for identifying the sulfur compounds in the fuel was described in a previous paper (4). An Antek 9000 Series Sulfur Analyzer (detection limit 0.5 ppmw) was used for the determination of total sulfur in the fresh fuels and treated fuels.

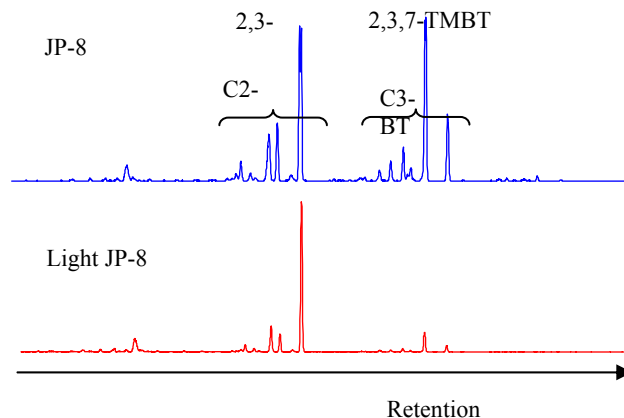


Figure 1. GC-PFPD chromatogram of JP-8 and light JP-8.

## Results and Discussion

The major sulfur compounds in the JP-8 and in the light fraction of JP-8 are the alkyl benzothiophenes with two to three carbon atoms in the alkyl group(s), as shown in Figure 1.

The breakthrough curves for adsorptive desulfurization of the light JP-8 over Adsorbent-2 at 27 °C and 200 °C are shown in Figure 2. It is clear that at the operating temperature of 27 °C, the sulfur concentration in the treated light JP-8 is less than 1 ppmw before the effluent amount increases to 8 g/g (gram of the treated light JP-8 per gram of the adsorbent), indicating that almost all sulfur in the JP-8 is removed by the selective adsorption. After 8 g/g of effluent amount, the sulfur concentration increases sharply with increasing elution fuel volume. At the operating temperature of 200 °C, the breakthrough curve is similar to that at 27 °C before 8 g/g of effluent amount, but after this point, the sulfur concentration increases slowly with further increasing elution volume, being only 60 ppmw at 56 g/g of effluent amount. This result implies that the increase in temperature results in better desulfurization performance of Adsorbent-2.

From comparison of adsorptive desulfurization of the two fuels over Adsorbent-2 at 200 °C, as shown in Figure 2, the breakthrough point for the whole JP-8 fuel at a sulfur level of 1 ppmw is 2 g/g, and then, the sulfur concentration in effluent increases much more quickly than that for the light JP-8. One of the reasons is that the total sulfur concentration in the initial JP-8 is about two times higher than that of the initial light JP-8.

Among the two adsorbents (Adsorbent-2 and Adsorbent-5) for desulfurization of the JP-8 at 200 °C, the breakthrough curve for Adsorbent-5 is below that for Adsorbent-2, indicating that Adsorbent-5 has better performance for adsorptive desulfurization than Adsorbent-2, probably because Adsorbent-5 has higher surface area than that of Adsorbent-2.

Figure 3 shows the adsorptive capacity as a function of outlet sulfur concentration. The adsorptive capacities were calculated by integration of the Figure 2 curves. From comparison between

Adsorbent-2 and Adsorbent-5 for adsorptive desulfurization of the JP-8 at 200 °C, the breakthrough capacity of the former at 30 ppmw sulfur level is 11.5 mg/g, while the latter is 5.0 mg/g, indicating again that Adsorbent-5 is significantly better than Adsorbent-2. The highest adsorptive capacity in the four cases shown in Figure 3 is 16 mg/g (milligram of sulfur per gram of adsorbent) at a breakthrough sulfur level of 30 ppmw for the light JP-8 over Adsorbent-2 at 200 °C, 4.8 h<sup>-1</sup> of LHSV. It is more than 3 times higher than that for the light JP-8 over Adsorbent-2 at 27 °C, 24 h<sup>-1</sup> of LHSV.

In comparison between the light JP-8 and the JP-8 over Adsorbent-2 at the same operating conditions, it is of interest to note that the breakthrough capacity for the light JP-8 is about 3 times higher than that for the JP-8. The results indicate that the adsorptive capacity is not only dependent on the adsorbent but also dependent on the operating conditions and the fuel composition.

Analysis of the effluent by GC-PFPD shows that the first breakthrough sulfur compounds in the adsorptive desulfurization of the JP-8 is 2,3,7-TMBT, indicating that the adsorbent has lower selectivity for 2,3,7-TMBT than for 2,3-DMBT. This result implies that at least a part of adsorption sites on the surface have only weak interaction with 2,3,7-TMBT, probably due to the steric hindrance of the methyl group at the 7-position of benzothiophene. As shown in Figure 1, the concentration of 2,3,7-TMBT in the JP-8 is much higher than that in the light JP-8. This is probably the main reason why the breakthrough capacity of the adsorbent for the whole JP-8 fuel is lower than that for the light JP-8. Another reason is that the heavy aromatics coexisting in the JP-8 might affect the adsorptive capacity of the adsorbent.

## Conclusions

The results presented here indicate that the nickel-based adsorbents show higher adsorptive capacity and selectivity for removing sulfur from real JP-8 fuels. The adsorptive capacity is not only dependent on the adsorbent but also dependent on the operating conditions and the fuel composition. The breakthrough capacity of Adsorbent-2 for desulfurization of the light JP-8 at 200 °C corresponding to 30 ppmw sulfur level is 16 mg/g. The alkyl group at the 7-position of benzothiophene appears to inhibit the approach of the alkyl benzothiophene to the adsorptive sites through the steric hindrance, resulting in the low adsorptive selectivity for such sulfur compounds.

**Acknowledgments.** This work was supported in part by US Department of Defense (DARPA Palm Power Program) and in part by US Department of Energy (National Energy Technology Laboratory). We are grateful to the DARPA Palm Power Program management team and DOE/NETL project management for helpful discussions, and for permission to publish this work.

## References

- (1) Song, C., *Catalysis Today*, 77 (1), 17-50 (2002).
- (2) Edwards, T., *Am. Chem. Soc. Div. Petrol. Chem. Prepr.*, 45, 436-439 (2000).
- (3) Ma, X., Sprague, M., Sun, L., and Song, C., *Prepr., Div. Pet. Chem., Am. Chem. Soc.*, 47, 48-49 (2002).
- (4) Ma, X., Sun, L., and Song, C., *Catal. Today*, 77, 107-116 (2002).
- (5) Song, C., Ma, X., *Appl. Catal. B*, 41, 207-238 (2003).
- (6) Velu, S., Ma, X., and Song, C., *Am. Chem. Soc. Div. Petrol. Chem. Prepr.*, 48, 58-59 (2003).
- (7) Velu, S., Watanabe, S., Ma, X., and Song, C., *Am. Chem. Soc. Div. Petrol. Chem. Prepr.*, 48, 56-57 (2003).
- (8) Ma, X., Sprague, M., Sun, L., and Song, C., *Am. Chem. Soc. Div. Fuel Chem. Prepr.*, 47, 452 (2002).
- (9) Velu, S., Ma, X., and Song, C., *Am. Chem. Soc. Div. Fuel Chem. Prepr.*, 47, 457 (2002).
- (10) Ma, X., Sun, L., Yin, Z. and Song, C., *Am. Chem. Soc. Div. Fuel Chem. Prepr.*, 46, 648-649 (2001).

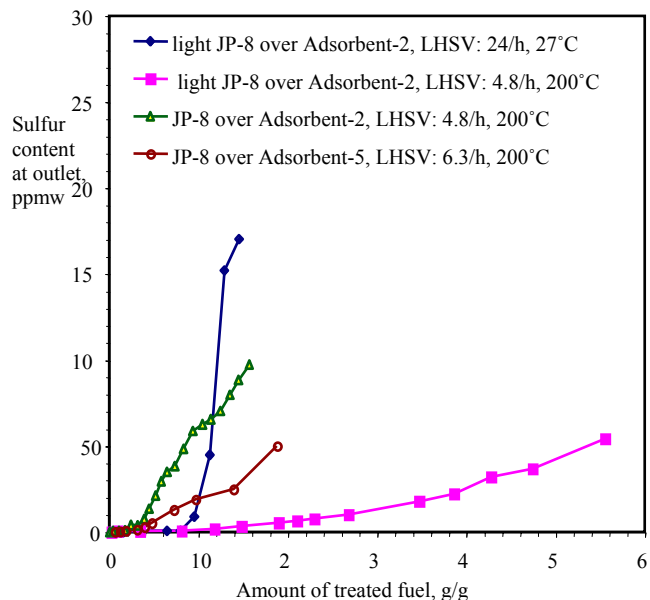


Figure 2 Breakthrough curves for adsorptive desulfurization.

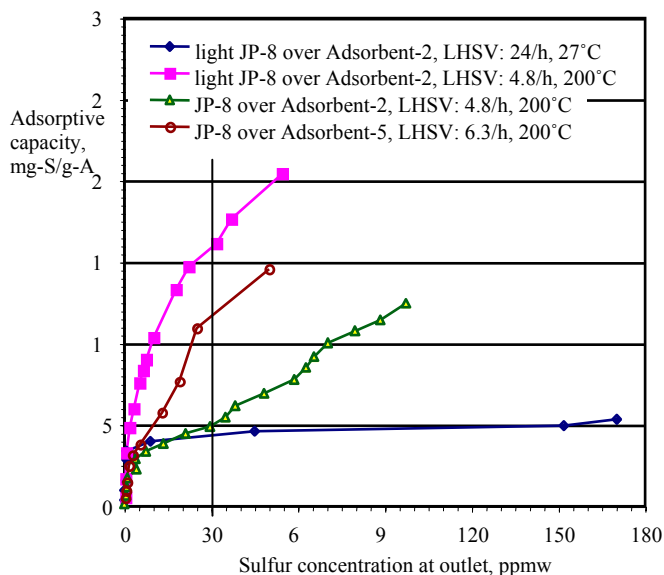


Figure 3 Adsorptive capacity as a function of sulfur concentration at outlet

# ADSORPTION/OXIDATION OF METHYL MERCAPTAN ON ACTIVATED CARBONS

Svetlana Bashkova<sup>2</sup>, Andrey Bagreev<sup>1</sup> and Teresa J. Bandosz<sup>1</sup>

<sup>1</sup>Department of Chemistry, the City College of New York and the

<sup>2</sup>Graduate School of the City University of New York, 138<sup>th</sup> street and Convent Ave, New York, NY 10031; e-mail: tbandosz@ccny.cuny.edu

## Introduction

The process of removal of mercaptans is of great scientific and practical importance.

Mercaptans (thiols) are highly reactive sulfur-containing species well known for their disagreeable odors. The most volatile of thiols is methyl mercaptan (CH<sub>3</sub>SH), which is one of the natural sources of sulfur emitted into the atmosphere. It is a colorless gas with a smell like rotten cabbage. Methyl mercaptan has very low odor threshold (one part in 5 x 10<sup>10</sup> parts of air) [1] and therefore is added at low concentrations to natural gas to detect the leak if it develops. Occupational exposure limit for CH<sub>3</sub>SH is 0.5 ppm or 0.9 mg/m<sup>3</sup>. At a higher concentrations methyl mercaptan becomes very toxic and may cause harmful health effects.

Taking into account the chemical and physical features of methyl mercaptan molecule [2], it can be adsorbed at room temperature and presence of air on the activated carbon surface in small pores via dispersive interactions. On the surface of the carbons methyl mercaptan is converted to dimethyl disulfide (DMDS) the adsorption of which at room temperature is much stronger than that of methyl mercaptan (MM) [2].

An objective of this paper is to describe the adsorption/oxidation of methyl mercaptan from wet air streams on commercial activated carbons, to identify the reaction products and to study the influence of the carbon surface and structural parameters on the removal/oxidation of methyl mercaptan.

## Experimental

**Materials.** Adsorption of methyl mercaptan was performed on four samples of activated carbons of various origins. Among the carbons studied were BAX-1500 (wood based -Westvaco), S208 (coconut shell - Waterlink Barnabey and Sutcliffe), BPL (bituminous coal - Calgon) and PCB (coconut shell-Calgon).

The as received materials were studied as adsorbents for methyl mercaptan in the dynamic tests described below. After this test and purging with air the samples are considered as exhausted and they are designated with an additional letter "E".

**Methods.** To evaluate the capacity of carbon adsorbents for CH<sub>3</sub>SH removal under wet conditions dynamic tests were carried out at room temperature. Adsorbent samples were ground and packed into a glass column (length 370 mm, internal diameter 9 mm, bed volume 6 cm<sup>3</sup>) and prehumidified with moist air (relative humidity 80 % at 25 °C) for one hour. The amount of water adsorbed was then estimated from the increase in the sample weight. Moist air containing 0.3 % (3,000 ppm) CH<sub>3</sub>SH in nitrogen was then be passed through the column of adsorbent at 0.5 L/min. The breakthrough of CH<sub>3</sub>SH was monitored using a MicroMax monitoring system (Lumidor) with an electrochemical sensor. The adsorption capacities of each sorbent in terms of mg of CH<sub>3</sub>SH per g of carbon can be calculated by integration of the area above the breakthrough curve and from the CH<sub>3</sub>SH concentration in the inlet gas, flow rate, breakthrough time, and mass of sorbent. The amount of weakly

adsorbed CH<sub>3</sub>SH was evaluated by purging the adsorbent column with air immediately after the breakthrough experiment.

Nitrogen adsorption isotherms were measured using an ASAP 2010 analyzer (Micromeritics, Norcross, GA, USA) at 77K. Before the experiment the samples were degassed at 393K to constant pressure of 10<sup>-5</sup> torr. The isotherms were used to calculate the specific surface area, S<sub>N2</sub>; micropore volume, V<sub>mic</sub> and total pore volume, V<sub>t</sub>. All the parameters were determined using Density Functional Theory (DFT) [3,4,12].

To evaluate the surface pH a 0.4 g sample of dry adsorbent was added to 20 mL of deionized water and the suspension stirred overnight to reach equilibrium. The pH of the suspension was measured using an Accumet Basic pH meter (Fisher Scientific, Springfield, NJ, USA).

Thermal analysis was carried out using TA Instruments Thermal Analyzer (New Castle, DE, USA). The heating rate was 10 deg/min in a nitrogen atmosphere at 100 mL/min flow rate.

To get information about the oxidation products GC/MS study was done using Shimadzu Gas Chromatograph/Mass Spectrometer model QP 5050. In this case the separation was done on Shimadzu XTI -5 column (bonded 5 % phenyl) 30 m long, 0.25 mm internal diameter. Temperature programming was set to ensure the complete separation of the reaction products. The samples for analysis were received by extraction with methanol and some heating.

The surface chemistry was evaluated using the Boehm titration method [5]. In this approach one gram of carbon sample was placed in 50 ml of the following 0.05 N solutions: sodium hydroxide, sodium carbonate, sodium bicarbonate and hydrochloric acid. The vials were sealed and shaken for 24 h and then 10 ml of each filtrate was pipetted and the excess of base or acid was titrated with HCl or NaOH.

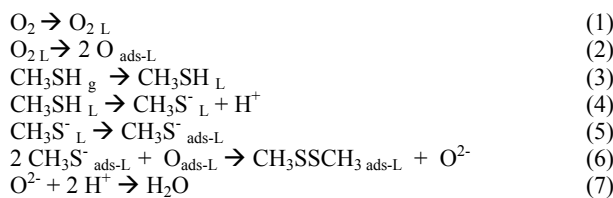
## Results and Discussion

From the breakthrough tests, methyl mercaptan breakthrough curves are obtained and collected in **Figure 1**. The results show the highest breakthrough capacity for the BPL carbon, the capacity of S208 carbon is a little smaller after that goes PCB and the smallest capacity is obtained for the BAX. According to the **Table 1**, all the carbons have approximately the same pH around 7, so the differences in their performance must lie in their structural and surface parameters.

The adsorption of MM on the carbon surface can be physical or chemical. For instance, for the BAX carbon, the amount of MM desorbed during air purging is relatively high (more than 10 %). For the other three carbons only traces of methyl mercaptan are desorbed suggesting strong adsorption of the CH<sub>3</sub>SH and/or oxidation products.

In order to link the behavior of carbons as methyl mercaptan adsorbents to specific features of materials, the chemical analysis of the surface was done using Boehm titration [5]. The results are presented in **Table 2**. The total amount of groups can be linked to the adsorption capacities of the carbons studied (**Table 1**) for the three of our samples. Despite the highest amount of total groups for the BAX carbon, its amount of basic groups and pH (**Table 1**) may be too small for the efficient removal of CH<sub>3</sub>SH.

To explain the dependence of the capacity on the surface pH the possible mechanism of adsorption/oxidation process is taken into consideration. It is supposed that adsorbed MM reacts with oxygen and than it is stored in the pore system in the form of DMDS [6-8].



where subscripts g, ads, and ads-L correspond to the species in gas, adsorbed, and liquid phases, respectively;  $\text{O}_{\text{ads}}$  is dissociatively adsorbed oxygen.

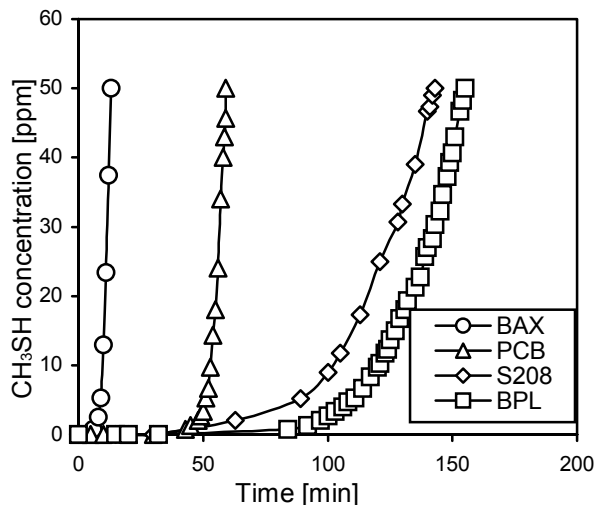


Figure 1.  $\text{CH}_3\text{SH}$  breakthrough curves.

**Table 1. pH of the surface, amount of water preadsorbed, breakthrough time and  $\text{CH}_3\text{SH}$  breakthrough capacities for the materials studied.**

Sample	pH	pHE	Amount of water [mg/g]	Brthr.time [min]	$\text{CH}_3\text{SH}$ capacity [mg/g]	$\text{CH}_3\text{SH}$ desorbed [mg/g]
BAX	7.20	6.78	163.4	13	28.2	0.48
BPL	7.41	3.82	89.9	155	216.8	0.03
S208	7.47	5.94	92.6	143	162.2	0.04
PCB	7.57	5.34	78.2	59	68.2	0.11

**Table 2. Results of Boehm titration [mmol/g].**

Sample	Carboxylic groups	Lactonic groups	Phenolic groups	Basic groups	Acidic groups	Total groups
BPL	0.00	0.05	0.45	0.40	0.50	0.90
S208	0.00	0.05	0.31	0.40	0.36	0.81
BAX	0.20	0.21	0.49	0.35	0.90	1.25
PCB	0.00	0.00	0.25	0.45	0.25	0.70

By solving a set of equations, describing the steps of MM dissociation and adsorption/oxidation [8], it was found that the pH where the transition in capacity may occur is about 7.5. It suggests that for all carbons with the average surface pH greater than 7.5 concentration of  $\text{CH}_3\text{S}^-$  in the adsorbed state will be equal to  $\text{CH}_3\text{SH}$  in a gas phase (100% dissociation + adsorption), which is required for effective  $\text{CH}_3\text{SH}$  removal. It is about 2.7 pH unit less than for simple dissociation in water. These results support the significance of the activated carbon surface and its effect on physicochemical processes taking place in the pore system.

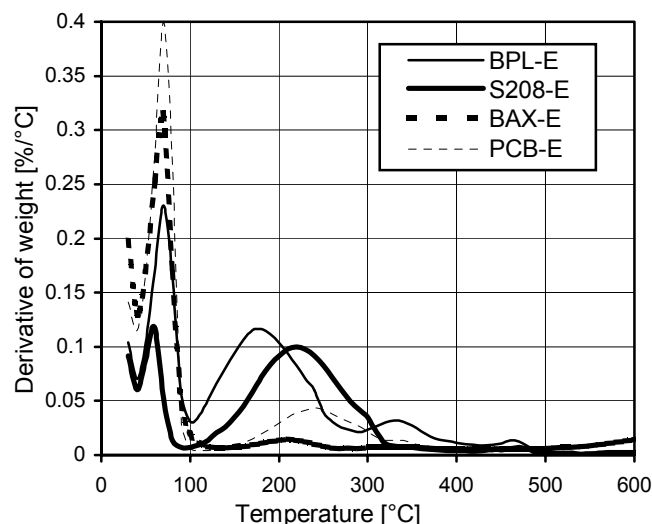


Figure 2. DTG curves in nitrogen for exhausted samples.

To study the reaction products, the GC/MS analysis was carried out [7]. Received chromatograms indicated two peaks for most of the samples: DMDS as a first peak and methyl methane thiosulfonate (MMTS) as a second peak. Intensity of the first peak is 10-50 times bigger than that of the second peak indicating formation of DMDS as a main reaction product.

Another way to investigate surface reaction products is to perform thermal analysis (TA) [6-11]. The curves received for our carbons from differential thermogravimetric analysis (DTG) are presented in Figure 2. DTG gives the weight derivative as a function of temperature. For all of the curves there are two major peaks present. First, centered at about 80 °C represents desorption of water [6-7] and second, centered between 100 °C and 300 °C (depending on the sample) is assigned to desorption of DMDS. Methyl mercaptan physically adsorbed is very unstable, boiling temperature of  $\text{CH}_3\text{SH}$  is 4.4 – 7.5 °C [1]. From Figure 2 it is seen that for BPL and BAX samples DTG curves are shifted to the lower temperatures of desorption suggesting weaker adsorption of DMDS than in the case of S208 and PCB carbons which may be caused by the differences in the structural parameters between these samples. For most of the samples there is a shoulder centered at about 300 °C, which may correspond to MMTS. This shoulder is more pronounced for BPL and S208 carbons and indeed there is more MMTS detected using GC-MS for these two samples. The formation of MMTS as one of the reaction products may partially explain the decrease in pH for our carbons (Table 1). Another reason for a pH decrease can be the formation of sulfonic acid adsorbed strongly adsorbed inside the carbon pores from where it cannot be easily extracted. Sulfonic acid

may also react with the carbon surface to form some derivatives strongly bonded to the carbon matrix.

From the analysis of the structural parameters [6,7], BAX and BPL are the most heterogeneous ones with the wide range of pores mostly in the mesoporous region. S208 and PCB, on the other hand, are very homogeneous with all the pores smaller than 20 Å. This may explain the weaker adsorption forces for dimethyl disulfide on BPL and BAX demonstrated by a shift of the second DTG peak to a lower temperature of desorption. Another reason for the low capacity of the BAX carbon is, even though it structurally resembles BPL, it has a small volume of the pores smaller than 10 Å [7], which should be active in the process of CH<sub>3</sub>SH adsorption/oxidation.

#### Acknowledgment

This work was supported by the donors of the Petroleum Research Fund, administered by the ACS (Grant # ACS-PRF#35449-AC5).

#### References

1. Karchmer, J.H. Wiley, New York, 1970, 1, 466.
2. Tanada, S.; Boki, K.; Matsumoto, K. *Chem. Pharm. Bull.* 1978, 26, 1527.
3. Lastoskie, C.M., Gubbins, K.E.; Quirke, N. *J. Phys. Chem.* 1993, 97, 4786.
4. Olivier, J.P. *J. Porous Materials*, 1995, 2, 9.
5. Boehm, H.P. *Carbon* 1994, 32, 759.
6. Bashkova, S.; Bagreev, A.; Bandosz, T.J. *Environ. Sci. Technol.*, 2002, 36, 2777.
7. Bashkova, S.; Bagreev, A.; Bandosz, T.J. *Ind.Eng.Chem..Res.*, 2002, 41, 4346.
8. Bagreev, A.; Bashkova, S.; Bandosz, T.J. *Langmuir*, 2002, 18, 8553.
9. Adib, F.; Bagreev, A.; Bandosz, T.J. *Environ. Sci. Technol.* 2000, 34, 686.
10. Adib, F.; Bagreev, A.; Bandosz, T.J. *J. Coll. Interface Sci.* 1999, 214, 407.
11. Adib, F.; Bagreev, A.; Bandosz, T.J. *J. Coll. Interface Sci.* 1999, 216, 360.
12. Gregg, S.J.; Sing, K.S.W. Academic press, New York, 1982.

# MECHANISTIC INVESTIGATIONS ON THE ADSORPTION OF ORGANIC SULFUR COMPOUNDS OVER SOLID ADSORBENTS IN THE ADSORPTIVE DESULFURIZATION OF TRANSPORTATION FUELS

S.Velu, Xiaoliang Ma and Chunshan Song\*

Clean Fuels and Catalysis Program, The Energy Institute, and  
Department of Energy and Geo-Environmental Engineering,  
The Pennsylvania State University,  
209 Academic Projects Building, University Park, PA 16802  
E-mail: csong@psu.edu

## Introduction

The deep removal of organic sulfur compounds from gasoline, diesel and jet fuel to produce ultra-clean transportation fuels, particularly for fuel cell applications, is becoming a paramount issue in recent years because the sulfur content in the fuel needs to be reduced to < 1 ppmw. Adsorptive desulfurization is a promising approach to produce fuel cell grade gasoline and diesel at relatively low temperature and low pressure without using hydrogen gas, and advantageous compared to the conventional hydrodesulfurization method that uses high temperature and high hydrogen pressure.<sup>1</sup>

Adsorptive desulfurization is based on the ability of a solid adsorbent to selectively adsorb organic sulfur compounds from liquid transportation fuels. Since these fuels consist of various thiophenic sulfur compounds together with considerable amount of aromatics and olefins, the selective removal of sulfur compounds is challenging. A new concept developed at Penn State University known as selective adsorption for removing sulfur (PSU-SARS) is being explored in our laboratory with a variety of adsorbents based on various materials such as zeolites, metal compounds, and mixed metal oxides.<sup>1-3</sup>

In order to develop a selective adsorbent for removing sulfur compounds, it is necessary to understand the nature of interaction between sulfur compounds and adsorbents. Thiophene has two pairs of electrons on S atom. One pair of electrons is in the six-electron  $\pi$  system and the other lies in the plane of the ring. Consequently, thiophene can act as either an n-type donor by donating the lone pair of electrons of the sulfur atom to the metal (direct S—M bond) or as a  $\pi$ -type donor by utilizing the delocalized electrons of the aromatic ring to form a  $\pi$ -complex with the metal or metal ion. At least eight different coordination geometries of thiophene are known in organometallic complexes and they include direct S—M bond,  $\pi$ -complex formation and geometries involving both direct S—M bond and  $\pi$ -complexes.<sup>1,4</sup> This indicates that thiophenic sulfur compounds can be removed from the transportation fuels either by the formation of direct S—M bonds or by  $\pi$ -complexation. However, in the later, aromatics and olefins in the fuel may compete and this would decrease the selectivity for the adsorption of sulfur compounds.

The objective of the present study is to investigate if the direct S—M interaction or  $\pi$ -complex formation is involved in the adsorption of thiophenic sulfur compounds on the given adsorbent. And also to understand which type of interaction (direct S—M interaction or  $\pi$ -complex formation) is favorable for the selective adsorption of only sulfur compounds without adsorbing aromatics and olefins present in the fuel. For this purpose, a model fuel containing thiophene (aromatic sulfur compound), tetrahydrothiophene (non-aromatic sulfur compound), benzene (non-sulfur aromatic) and 1,5-hexadiene (non-sulfur olefin) as shown in Scheme-1 has been prepared and used as a feed. Adsorbents based on zeolites, mixed metal oxides, supported metal compounds, etc have been tested. Since Ag-exchanged zeolite is known to form  $\pi$ -

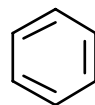
complexes with aromatics and olefins,<sup>5</sup> it is considered as representative for adsorption of sulfur by  $\pi$ -complexation. The observed results are corroborated with electron density on S atom and C—C bond order of the sulfur compounds, aromatic and olefin derived from computer simulation. Understanding the mechanism of sulfur adsorption in this study will be very useful to develop selective adsorbents for removing sulfur from transportation fuels for refinery and fuel cell applications.



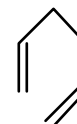
Thiophene



Tetrahydrothiophene



Benzene



1,5-hexadiene

**Scheme 1. Adsorbates added to n-decane solvent in the preparation of a model fuel**

## Experimental

Zeolites containing various metal ions were prepared either by ion exchange or impregnation of NH<sub>4</sub>Y-zeolite with a SiO<sub>2</sub>/Al<sub>2</sub>O<sub>3</sub> molar ratio = 5 as described earlier.<sup>3</sup> Mixed metal oxide and supported metal adsorbents were prepared by co-precipitation and impregnation, respectively. The model fuel containing thiophene, tetrahydrothiophene as sulfur compounds, each 270 ppmw on the sulfur basis, in n-decane was prepared. About 270 ppmw of benzene and 270 ppmw of 1,5-hexadiene were also added to the fuel. The adsorptive desulfurization was performed using a flow apparatus as described elsewhere.<sup>1-3</sup> Analysis of treated fuel was performed using an Antek 9000 Series Sulfur Analyzer as well as a GC equipped with a flame ionization detector. Computer-aided molecular orbital calculations were performed using CAChe and MOPAC as described earlier.<sup>6</sup>

## Results and Discussion

Figure 1 shows the breakthrough curves for the adsorptive desulfurization of the model fuel used in the present study over Ag-exchanged Y-zeolite. As can be seen, all the compounds, namely thiophene, tetrahydrothiophene, benzene and 1,5-hexadiene are completely adsorbed. The breakthrough points for the adsorption of benzene, thiophene and 1,5-hexadiene are about 22, 28, and 50 g, respectively. Tetrahydrothiophene was not detected in the treated fuel even after 50 g of fuel treatment. These results indicate that Ag-exchanged Y-zeolite forms  $\pi$ -complexes with benzene, 1,5-hexadiene and thiophene and that the  $\pi$ -complexation with 1,5-hexadiene being stronger than that with benzene and thiophene. The absence of tetrahydrothiophene in the treated fuel indicates that Ag-exchanged zeolite also makes direct S—M bond and this is even more stronger compared to the  $\pi$ -complexation with 1,5-hexadiene or thiophene. Since thiophene has a pair of electrons in the plane of the ring, it could form a direct S—M bond and  $\pi$ -complexation simultaneously.<sup>1,2</sup> In such case, the adsorption of thiophene could be much more stronger than that of tetrahydrothiophene because of the simultaneous involvement of both types of bonding interactions. However, the observed results indicate that thiophene involves mainly  $\pi$ -complexation using delocalized electrons of the aromatic ring rather

than a direct S—M bond with Ag-exchanged zeolite. This is because the electron density on S atom of the thiophene is only 5.696 compared 6.042 in tetrahydrothiophene as calculated from computer simulation, implying that the S—M bond between the adsorption site and thiophene is much weaker than that between the adsorption site and tetrahydrothiophene.

The initial concentration of benzene was around 270 ppmw. However, its concentration in the outlet reached up to 700 ppmw after reaching the saturation value. This indicates that benzene initially adsorbed is desorbed during the course of the adsorption under the present experimental conditions. Similar result has also been observed in the adsorption of thiophene and this further substantiates that probably only  $\pi$ -type interaction exists between thiophene and Ag-exchanged zeolite.

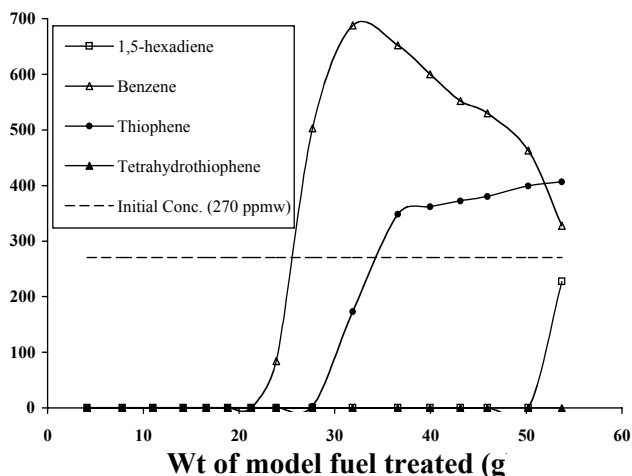


**Figure 1.** Breakthrough curves for the adsorption of thiophene, tetrahydrothiophene, benzene and 1,5-hexadiene in n-decane over Ag-exchanged Y-zeolite at 80°C. Wt of adsorbent: 3.5 g; LHSV = 12 h<sup>-1</sup>. The outlet conc. of thiophene and tetrahydrothiophene are on the sulfur basis.

The adsorption of aromatics and olefins along with sulfur compounds by  $\pi$ -complexation would deteriorate the quality of transportation fuels. The competitive adsorption of aromatics and olefins with sulfur compounds would also decrease the selectivity and adsorption capacity. In fact, it has been found from our earlier experiments that the presence of about 10 wt % of toluene in a model gasoline fuel decreases the adsorption capacity of Ag-exchanged zeolite by about 20 times.<sup>7</sup> Similarly, the presence of olefin decreases the capacity by about 6 times.

Figure 2 shows the breakthrough curves for the adsorptive desulfurization of the model fuel over a Ni-based supported metal adsorbent. Unlike that observed over Ag-exchanged Y-zeolites, only sulfur compounds (thiophene and tetrahydrothiophene) are removed over this adsorbent. The outlet concentrations of benzene and 1,5-hexadiene are very close to that present in the feed, indicating that they are not adsorbed at all. These results suggest that sulfur compounds are adsorbed by the direct S—M bond formation rather than by  $\pi$ -complexation over the Ni-based supported metal adsorbent. It is also interesting to note that the breakthrough curve of thiophene coincides with that of the tetrahydrothiophene and this indicates that these two compounds interact with the adsorbent to the same extent although there is a considerable difference in the electron density on S atom between these two sulfur compounds.

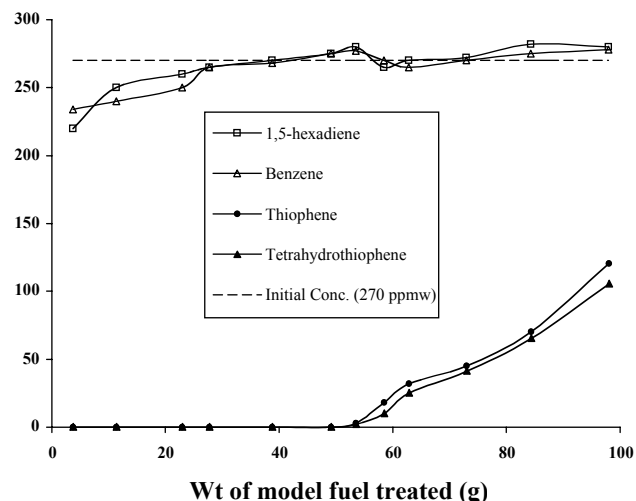


**Figure 2.** Breakthrough curves for the adsorption of thiophene, tetrahydrothiophene, benzene and 1,5-hexadiene in n-decane over Ni-based supported metal adsorbent at 80°C. Wt of adsorbent: 4.5 g; LHSV = 12 h<sup>-1</sup>. The outlet conc. of thiophene and tetrahydrothiophene are on the sulfur basis.

Various other adsorbents such as mixed oxides derived from hydrotalcite-like anionic clays, transition metals supported on mesoporous materials, etc have also been tested in the present study. Based on the results obtained, better adsorbents selective for removing only sulfur compounds have been selected for the adsorptive desulfurization of real gasoline, diesel and jet fuel.

## Conclusions

Depending on the nature of adsorbent used, thiophenic sulfur compounds form either  $\pi$ -complexes using delocalized electrons of the aromatic ring or a direct S—M bond using the lone pair of electrons of the sulfur atom present in the plane of the ring. While thiophene is removed by  $\pi$ -complexation over adsorbents such as Ag-exchanged zeolites, it is removed by the direct S—M interaction over Ni-based supported metal adsorbent.

Sulfur removal by  $\pi$ -complexation is less selective due to the competitive adsorption of aromatics and olefins present in the transportation fuels. On the other hand, sulfur compounds can be selectively removed by the direct S—M interaction.

**Acknowledgements.** This work was supported in part by the US department of Energy and in part by the US department of Defense.

## References

- (1) Song, C.; Ma, X. *Applied Catalysis B: Environmental*, **2003**, 41, 207.
- (2) (a) Ma, X.; Sun, L.; Song, C. *Catal.Today*, **2002**, 77, 107; (b) Song, C. *Catal.Today*, **2002**, 77, 17.
- (3) Velu, S.; Ma, X.; Song, C. *Submitted for publication*.
- (4) Reynolds, M.A.; Guzei, A.; Angelici, R.J. *J.Am.Chem.Soc.* **2002**, 124, 1689.
- (5) Takahashi, A.; Yang, R.T.; Munson, C.L.; Chinn, D. *Langmuir*, **2001**, 17, 8405.
- (6) Song, C.; Ma, X.; Schmitz, A.D.; Schobert, H.H. *Appl.Catal. A*, **1999**, 182, 175.
- (7) Velu, S.; Watanabe, S. Ma, X.; Song, C. *Preprints-Am.Chem.Soc., Division of Petroleum Chemistry*, **2003**, 48, 56.

# NEW CERIA-BASED SELECTIVE ADSORBENTS FOR REMOVING SULFUR FROM GASOLINE FOR FUEL CELL APPLICATIONS

Shingo Watanabe, S. Velu, Xiaoliang Ma and Chunshan Song\*

Clean Fuels and Catalysis Program, The Energy Institute and  
Department of Energy and Geo-Environmental Engineering  
The Pennsylvania State University  
209 Academic Project Building, University Park, PA 16802  
\*E-mail: csong@psu.edu

## Introduction

In order to improve the air quality, the federal governments in various countries have announced new regulations to reduce the sulfur contents in transportation fuels. The U.S. Environmental Protection Agency (EPA), for example, has recently announced a new regulation that mandates refineries to reduce the sulfur content in gasoline to below 30 ppmw from the current average of 300 ppmw and in diesel to below 15 ppmw from the current level of 500 ppmw by 2006. The interest in the desulfurization of transportation fuels is further motivated by the development of fuel cells to power automobiles, because fuel cell powered vehicles do not emit noxious gases such as SO<sub>x</sub>, NO<sub>x</sub>, CO, etc. However, for fuel cell applications, the sulfur content in the transportation fuels need to be further reduced to <1 ppm.

Catalytic hydrodesulfurization (HDS) is the conventional method that is being employed by the refineries to produce clean transportation fuels.<sup>1</sup> Although HDS process can remove sulfur compounds from gasoline close to 30 ppmw, it is highly inconvenient and very expensive process to produce fuel cell grade gasoline. Several alternative methods such as adsorption, alkylation, oxidation, extraction, etc. have been developed in recent years. Among them adsorption is considered to be more promising because adsorption can be accomplished at low temperature and pressure. Since gasoline contains significant amount of olefins and aromatics, the adsorbent should be selective to remove only organic sulfur compounds without co-adsorbing the olefins and aromatics.

A new concept is being developed in our laboratory at Penn State University known as "Selective adsorption for removing sulfur (PSU-SARS)" for the selective removal of organic sulfur compounds from gasoline, diesel and jet fuel. Several new adsorbents based on zeolites, mixed oxides, supported metal compounds, activated carbons, etc. are being developed and some of them exhibit excellent adsorption capacity for the desulfurization of gasoline and jet fuels.<sup>2-4</sup>

Owing to its high oxygen storage capacity, redox properties and good metal-support interactions, CeO<sub>2</sub> has been known as an excellent support for base and noble metals in variety of catalytic process, including auto exhaust three-way catalyst.<sup>5</sup> It also enhances the reducibility of base and noble metals supported on it. CeO<sub>2</sub>-based adsorbents have also been developed in recent years for the removal of H<sub>2</sub>S and SO<sub>x</sub> from flue gas, natural gas and coal-derived gas.<sup>6</sup> CeO<sub>2</sub> has been evaluated as a high temperature regenerable desulfurization sorbent, which yields elemental sulfur upon regeneration. Our recent work on the desulfurization of jet fuel indicated that Ce loaded zeolites exhibit fairly good adsorption properties.<sup>7</sup>

Taking into account the interesting properties of the CeO<sub>2</sub>, the present study aimed at developing CeO<sub>2</sub>-based regenerable adsorbents for the removal of thiophenic sulfur compounds present in the gasoline. Various metal-loaded high-surface-area CeO<sub>2</sub> mixed oxides synthesized by coprecipitation and impregnation methods have been used as adsorbents for the desulfurization of a model gasoline containing 265 ppmw of sulfur in the form of thiophene in a

batch reactor at ambient temperature and pressure. The best adsorbents screened have been used to test in the dynamic adsorption study for the desulfurization of model and real gasoline.

## Experimental

All the adsorbents were prepared using metal nitrates (Aldrich Chem. Co.) by urea gelation/co-precipitation method.<sup>6</sup> 10 atomic % metal containing CeO<sub>2</sub> adsorbents had metal/Ce=1/9 mole ratio. 20 at.% and 40at.% correspond to metal/Ce=2/8 and 4/6 mole ratio, respectively. Precipitates were dried at 110°C over night, and calcined at 450°C for 6 hrs in air employing a temperature ramp of 2°C/min. Model gasoline feed containing thiophene (sulfur concentration 265ppmw) in isooctane was used for studying the sulfur removal capacity.

The adsorptive desulfurization was performed using 25mL bottle (I.D.=2.4cm) with cap as a batch reactor and a flow apparatus. In the batch reaction 0.1 g of adsorbent was stirred well with 5 g of fuels under ambient temperature and pressure for 10 min. For flow system desulfurization the adsorbents were packed in a stainless steel column with an internal diameter of 4.6 mm and length of 75 mm. The adsorbent bed volume was about 1.25 cc. The model gasoline was fed into the column using HPLC pump. The feed flow rate was 0.05 cc/min. Antek 9000 Series Sulfur Analyzer (detection limit 0.5 ppm) determined the total sulfur concentration of the treated. The breakthrough volume and capacity were calculated from the breakthrough curves considering the sulfur content at the breakthrough point was below 1 wppm.

## Result and Discussion

The study on sulfur removal capacity and the amount of sulfur removed are shown in Figure 1 and Table 1, respectively. Doping metal into ceria improved the adsorption capacity for removing thiophene. The adsorption capacity of CeO<sub>2</sub> is only about 2 mg/g of adsorbent and the capacity increases up to about 9 mg/g when 10 atomic % Y, La, Zn, Ni, Sr and Ag doped on to CeO<sub>2</sub>. Y-CeO<sub>2</sub> and La-CeO<sub>2</sub> show sulfur adsorption capacity almost 4.5 times larger compared to the capacity of CeO<sub>2</sub> alone.

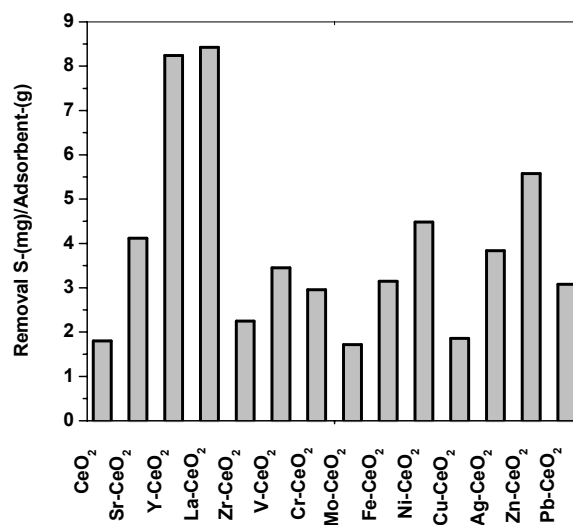


Figure 1. Adsorptive desulfurization of CeO<sub>2</sub>-based adsorbents

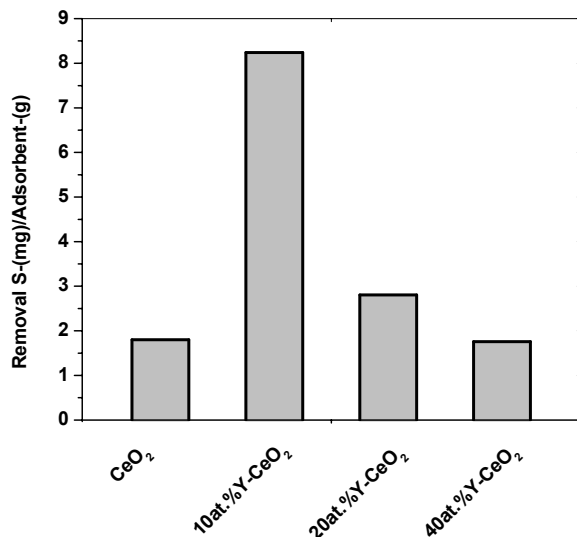


Figure 2. Comparison of various mole ratio of Y doped CeO<sub>2</sub> of adsorptive desulfurization

The 10at.% of Y-CeO<sub>2</sub> has been compared with different concentration of Y-CeO<sub>2</sub>. As can be seen from figure 2, the 10at.% Y doped CeO<sub>2</sub> adsorbent has higher sulfur removal capacity than 20 and 40 at.% Y-CeO<sub>2</sub> adsorbents. Therefore, 10 atomic % of Y is the optimum amount for doping with CeO<sub>2</sub> for the adsorptive desulfurization of gasoline of the present study.

Table 1. Amount of Sulfur Adsorbed by CeO<sub>2</sub> based Adsorbents, Initial Fuel/Adsorbent=50,wt

Adsorbents	Amount of Sulfur Adsorbed (%)
CeO <sub>2</sub>	12.6
Sr/CeO <sub>2</sub>	30.1
Y/CeO <sub>2</sub>	60.3
La/CeO <sub>2</sub>	58.5
Zr/CeO <sub>2</sub>	15.6
V/CeO <sub>2</sub>	22.1
Cr/CeO <sub>2</sub>	20.4
Mo/CeO <sub>2</sub>	11.9
Fe/CeO <sub>2</sub>	20.9
Ni/CeO <sub>2</sub>	31.8
Cu/CeO <sub>2</sub>	13.6
Ag/CeO <sub>2</sub>	27.4
Zn/CeO <sub>2</sub>	40.1
Pb/CeO <sub>2</sub>	22.4

Ag doped CeO<sub>2</sub> adsorbents were modified by additional 10 atomic % metals. Additional metals offer significant improvement on sulfur adsorption performance as seen in figure 3. A 10 at.% Ag-CeO<sub>2</sub> exhibit higher capacity compared to 20 at.% Ag-CeO<sub>2</sub>. Increasing Ag concentration showed similar trend on Y-CeO<sub>2</sub> adsorbents results. Addition of Cu dramatically decreases the capacity compare to the addition of other metals under the present experimental conditions.

Further modifications of adsorbents are currently underway in order to increase the sulfur adsorption capacity. Since the adsorbents, in the present study have been used without any

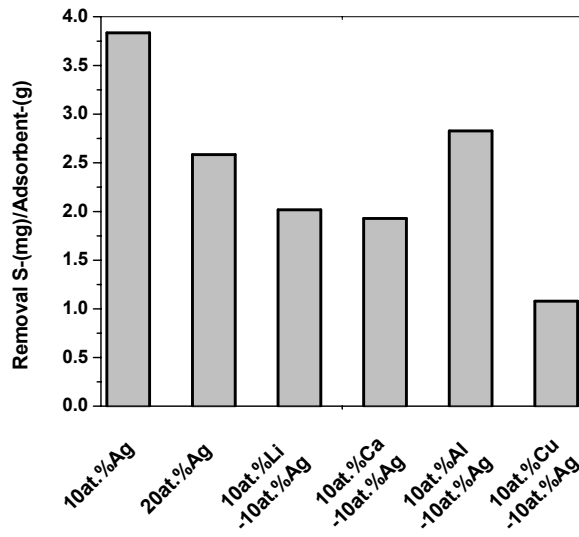


Figure 3. Comparison of modified Ag-CeO<sub>2</sub> of adsorptive desulfurization

reduction treatment, these adsorbents will be able to regenerate easily for the subsequent desulfurization.

### Summary

A new series of high-surface-area CeO<sub>2</sub>-based mixed oxides have been tested as adsorbents in the desulfurization of a model gasoline containing 265 ppmw of sulfur at ambient temperature. The results indicated that a 10 at.% of Y and La doped into CeO<sub>2</sub> exhibit higher desulfurization capacity of about 9 mg of sulfur per g of adsorbent at room temperature just in 10 min stirring. Effect of Y loading on the adsorption performance indicated that the 10 at % loading is the optimum for the adsorptive desulfurization of thiophenic sulfur compounds under the present study.

The study on selectivity between thiophenic sulfur compounds, olefins and aromatics over these CeO<sub>2</sub>-based mixed oxide adsorbents under the batch as well as dynamic adsorption is currently underway and the detailed results will be reported.

**Acknowledgments.** This work was supported in part by the US department of Energy and in part by the US department of Defense.

### References

- (1) C. Song and X. Ma, Applied Catalysis B Environmental, **2003**, 41(1-2) 207-238; C. Song, Catalysis Today, **2002**, 77, 17-49.
- (2) X. Ma, L. Sun, Z. Yin and C. Song, Preprint Paper – American Chemical Society, Division Fuel Chemistry, **2001**, 46(2), 648-649.
- (3) X. Ma, M. Sprague, L. Sun and C. Song, Preprint Paper – American Chemical Society, Division Fuel Chemistry **2002**, 47(2), 452-453.
- (4) S. Velu, S. Watanabe, X. Ma, L. Sun and C. Song, Preprint Paper – American Chemical Society, Division Petroleum Chemistry **2003**, 48(2), 56-57.
- (5) A.B. Hungria, A. Iglesias-Juez, Martinez-Arias, A.; M. Fernandez-Garcia.; J.A. Anderson; J.C. Conesa; J. Soria, Journal of Catalysis, **2002**, 206, 281.
- (6) M. Kobayashi.; M. Flytzani-Stephanopoulos, Industrial and Engineering Chemistry Research, **2002**, 41, 3115.
- (7) S. Velu, X. Ma and C. Song, Preprint Paper – American Chemical Society, Division Fuel Chemistry **2002**, 47(2), 447-448.



$$\text{FPS efficiency} = \frac{(\text{H}_2\text{ consumed @ stack} * \text{LHV}_{\text{H}_2})}{(\text{Fuel\_into\_fuel\_processor} * \text{LHV}_{\text{fuel}})}$$

This enables comparison of the IH fuel supply system with the direct hydrogen fuel supply system (where utilization is ~99% and air-bleed losses are zero). The one caveat here is that the parasitic losses due to the ATR (and burner) compressor is not included in the FPS efficiency but is treated as a fuel cell system loss. The IH fuel processor overall efficiency was found to be in the range 67-64 % for 10-100% power (Note: this included 85 % utilization efficiency and 97 % air bleed efficiency).

The dynamic response of the fuel processor is influenced by a number of factors. One is the steam generation rate, which is in turn related to the anode exhaust energy content (the primary source of heat for the steam generator). Under transient conditions, during up-transients, there is not much energy available in the anode stream. On the other hand, during down transients, there is excess energy available in the anode stream. The other factors are associated with the control scheme adopted to manage fuel/air/steam flows.

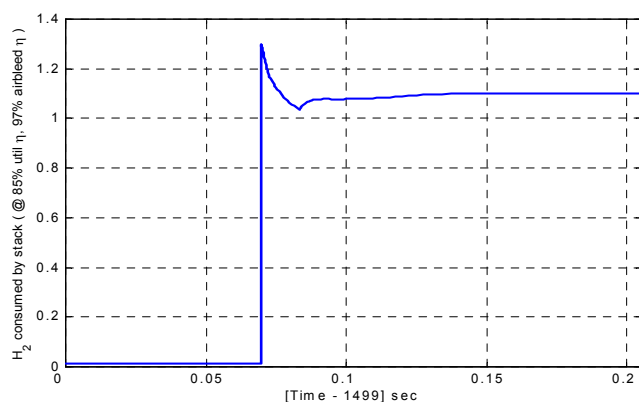


**Figure 2:** Transient response of the FPS unit from idle to 100% power; quick response a consequence of internal volumes and assumptions related to fast air & steam supply.

The control scheme slaves the fuel and air-flow rates to the steam generation rates while trying to maintain proper O/C levels in the ATR. Additionally the optimized HTS and LTS units are sensitive to any departures from the design inlet flow temperatures. During our preliminary investigations, we found that under transient conditions there were phase lags in the supply of steam during ramp-up and ramp-downs caused by interactions with the stack subsystem. As a consequence, it was difficult to limit CO at levels below 1% at the PROX entry if we did not have water injection AND steam storage (buffer) prior to the HTS & LTS. Once the water injection and steam storage (<2 liters volume) systems were introduced prior to the shift units, we were able to demonstrate the transient performance seen in Figure 2

Dynamic operation also has an impact on the overall efficiency over the drive cycle. Since the vehicle velocity profile over different drive-cycles can be quite different, the efficiency also depends on the drive-cycle considered for the analysis. Table 1 shows the impact of drive cycles on the fuel processor efficiency, with the corresponding vehicle efficiency (based on  $[\text{work done by vehicle against drag/friction forces}]/[\text{fuel energy supplied}]$ ). The main impact on the fuel processor efficiency is due to the varying degrees of stack H<sub>2</sub> utilization under dynamic conditions.

**Table 1: Efficiency variation with drive cycle, comparison of the FUDS, HIWAY and US06 drive cycles**

	IH FUDS	IH HIWAY	IH US06
FP overall eff (%)	56	66	65
• FP efficiency	82	82	81
• H <sub>2</sub> airbleed eff	97	97	97
• H <sub>2</sub> utilization eff	70	83	82
Vehicle Efficiency (%)	20	27	25

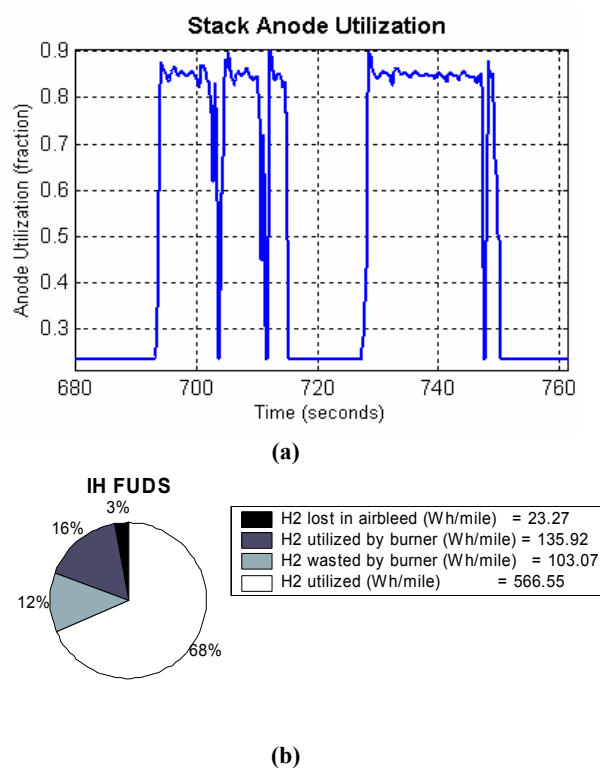


**Figure 3:** (a) Stack Anode Hydrogen utilization - snapshot over the FUDS cycle. (b) Hydrogen utilization and losses in Wh/mile – total Hydrogen production – 829 Wh/mile

Figure 3a shows a snapshot of the hydrogen utilization in the stack over the FUDS drive cycle – a cycle characterized not so much by high average power but more by the number of up-down transients encountered. As mentioned before, despite a fairly fast fuel processor, the nature of the interaction between the fuel-processor and the fuel cell stack, can cause variations in the H<sub>2</sub> utilization, thus impacting overall efficiency. The low utilizations occur during turn-downs; this results in high energy availability at the burner, not all which can be used for generating steam (since the steam is available at a point when the FP is also ramping down). Figure 3b shows the breakdown of where the hydrogen produced ends up and highlights the fact that 12% of the hydrogen produced effectively ends up being flared. This indicates that in order to improve the efficiency of the process, alternative approaches (hybridization, hydrogen buffering,

different control approaches, recycle loop) may need to be investigated. However, the authors believe that these approaches have their own set of problems and will have to be carefully analyzed taking both system dynamics and interactions into account.

In summary, on-board fuel processor design & controls present formidable challenges and our dynamic models have helped highlight some of them. Additionally, we have presented some of the issues that can come up when integrating the fuel processor with the rest of the fuel cell system. Alternative approaches both in the design and control space need to be explored further.

**Acknowledgment.** This work was supported by Fuel Cell Vehicle Modeling consortium at ITS, University of California at Davis [<http://fcv.ucdavis.edu>].

#### References

1. Chan, S.H. and Wang, H.M., International Journal of Hydrogen Energy, **2000**, v. 25, pp. 441-449,
2. Podolski, Walter F. and Young, G. Kim, Ind. Eng. Chem., Process Des. Develop. , **1974** v.13, No. 4, pp. 415-421
3. Amadeo, N.E. and Laborde, M.A., International Journal of Hydrogen Energy, **1995**, v. 20, no. 12, pp. 949-956
4. Kahlich, M.J., Gasteiger, H.A., Behm, R.J., Journal of Catalysis, **1997** v. 171, pp. 93-105,

## EFFECT OF WATER ON PERFORMANCE AND SIZING OF FUEL-PROCESSING REACTORS

Marco J. Castald, Rene LaPierre, Maxim Lyubovski, William Pfefferle and Subir Roychoudhury

Precision Combustion, Inc., 410 Sackett Point, North Haven, CT 06473

### Introduction

Current fuel processor design analyses, that comprise autothermal reformers (ATR), water-gas-shift (WGS) and preferential oxidation (PROX) reactors, either focus on individual reactor performance or on overall system integration and efficiency. This has led to a significant level of understanding of the requirements for a fuel processor system. For individual reactors, the analyses have indicated that fast start-up, transient response, size and weight are very important. On the other hand, the overall system analyses have highlighted the importance of heat management and the necessity to recycle as much water as possible, while maintaining its demand to a minimum. To date, connection has mainly been made on the effect of water on ATR performance and its impact on overall fuel processor design. However, a connection between the effect of water on CO clean-up reactors, i.e the WGS and PROX, and, in turn, the effect on overall system efficiency, has been lacking. While it is recognized that water will directly impact the WGS reactor, as water is a reactant in that system, the full extent has not been explored. Recent kinetic data coupled with a reactor design model sheds light on the impact water has on WGS reactor sizing and performance, where its impact on the overall system efficiency can be quantified. Moreover, water is generally considered an inert in the PROX reactor, yet recent experimentation on those reactors indicate that water has a significant impact on the multiplicity of steady-state operation and can impact the performance in terms of a synergistic effect with oxygen.

To identify the issues that need to be considered when designing a fuel processor system for optimized efficiency a preliminary process flow diagram (PFD) has been generated. The PFD was then simulated in ASPEN to calculate the amount of heat removal or addition that would be needed to ensure efficient operation of the system. The feed rate of the fuel, water and air led to a steam-to-carbon (S/C) ratio of 2.0 and an oxygen-to-carbon (O/C) ratio of 1.0. The intent of the simulation was to determine the critical issues that need to be investigated when designing a fuel processor system. To that extent, only major components were incorporated and the ancillary components such as blowers, pumps and vaporizers were not included because they are considered secondary in terms of system design for maximum efficiency. It is recognized that those components add some complexity but for a first cut analysis they are considered less important.

### Results and Discussion

The results of the simulation of the preliminary PFD identified some issues that should be a focus for proper design and layout of all the components of the fuel processor. One main issue that was revealed during the simulation was the possible integration of various streams into components that would not have been expected from an overall system analysis. For example, analyses have been done to determine the effect of water input and recycle on overall efficiency without much regard given to the impact on reactor performance. A viable solution often proposed is the use of a condensing heat exchanger where the water recovered could be recycled into the ATR and lessen the demand of the water feed rate.

### Water gas shift reactor analysis.

Tests were done to generate input data for ASPEN and to explore the impact of water on reactor performance. Those tests varied the steam to carbon (H<sub>2</sub>O/C) ratio entering an autothermal reactor (ATR) from 1.5 to 2.0, while keeping O/C ratio constant at 0.9. The WGS reactor was initially investigated in order to determine needed space velocities in the WGSR to achieve 90% or higher of equilibrium CO conversion. The experiments were done to evaluate the effectiveness of the LTS reactor at high space velocities with different water concentrations. The test results show that a higher water concentration in the ATR stage allows smaller WGS stages. In general, a slight increase in water addition to the ATR inlet results in a significant decrease in WGS reactor size and consequently pressure drop. In fact, if the water supplied to the ATR is at a steam to carbon ratio of 2.0, PCI's water gas shift reactor can reduce the CO, in a single stage, to below 1%, which is where a PROX reactor could be used. Experiments and calculations indicate that for every 1% increase in H<sub>2</sub>O to the ATR, there is almost a 10% decrease in water-gas shift reactor size when using conditions approximately similar to those tested.

From the experiments and modeling, it is clear that ATR H<sub>2</sub>O/C ratio greater than 1.5 would allow efficient WGS reactor design. To determine the optimal steam content entering the ATR, a system level calculation must be done to couple the effects of additional steam on fuel processor efficiency in light of a single stage WGS. The calculation must include parameters such as pressure drop, reactor size and weight, heat exchanger size and weight and dynamic interaction between the various components comprising the fuel processor.

### Preferential oxidation reactor analysis:

To complete the effect of water on the CO clean-up train reactors, investigation into PROX performance was done for various water concentrations. Those tests resulted in two significant findings that impact the design of PROX reactors and consequently system design. Dual steady state nature of the Reactor was the first finding from those tests. Generally a reactor in which a single, exothermic reaction is occurring will operate in one of two stable steady states. Additionally an unstable steady state solution to the mass and energy balance will be present. However, when multiple reactions are occurring in a reactor, there is the possibility of more than three possible steady state solutions. This arises from the fact that each reaction has a unique mole balance curve that superimposes upon each other. The energy balance line can then intersect each mole balance curve more than once adding up to four or more stable steady state conditions where the mole and energy balances are satisfied[1]. This phenomena is seen with the PROX reactor being developed, particularly at dry feed concentrations. Selective oxidation of CO in hydrogen over different catalysts has been extensively examined. In general, different precious metal catalysts have been found to be highly selective for the PROX reaction.

A general understanding of these systems is that at temperatures before the onset of the CO lightoff the surface is covered with adsorbed CO. As the temperature is increased the fraction of the surface covered with CO decreases, and this opens up sites for oxygen adsorption and subsequent reaction. Above a certain temperature the fraction of CO occupying the surface decreases even further and hydrogen chemisorbs and reacts on the surface in competition with CO, reducing the selectivity towards CO oxidation. Therefore, a common feature of all these systems is that there exists a window of operation in temperature between the lightoff curves for CO and H<sub>2</sub>, the object being to operate at a catalyst temperature sufficient for high activity of CO oxidation (for reduced size of catalytic reactor), but below that for significant consumption of the

hydrogen. This results in different temperature windows and optimum catalyst temperatures, which need to be identified for different catalyst formulations.

We observed the dual steady state behavior of the reactor only at dry feed conditions. However, when the water content is above 15% in the feed, the reactor consistently gives high CO conversion with nearly 45% selectivity. In addition, oxygen is detected in the product stream at varying levels, depending on the conditions tested. In comparison to monolith or pellet beds, we suspect that short contact time substrates should allow PROX reactors to operate at significantly lower water concentrations before the onset of the hydrogen oxidation reaction, i.e. the high temperature steady state. Initial analysis indicates that heat removal at the catalyst surface is a very important parameter in avoiding dual steady state operation because heat generated from the CO oxidation reaction is quickly transferred into the gas phase, thus moderating the surface temperature.

Table 1 displays representative results from experiments that show the dual steady state nature of the selective CO oxidation reactor. The first row provides the results of the reactor operating in the preferred steady state. The CO conversion was 22% with oxygen conversion at 30%, which results in a selectivity of slightly above 40% with a commensurate temperature rise. The second row shows for the exact same inlet compositions and temperature, the reactor was operating in another, high temperature, and undesired steady state. The data indicate that this state was one in which high hydrogen consumption occurred. The evidence for that was seen in the complete conversion of oxygen, without a change in CO conversion and the higher surface temperature as compared to the previous state. Since hydrogen was considered the fuel in this case, this state must be avoided to ensure the efficiency of the reactor system remains high.

**Table 1: Results of dual steady state behavior of the PROX reactor.**

----- Inlet Concentrations -----					--Reactor Temperature--		---Conversion---	
O <sub>2</sub>	H <sub>2</sub>	CO	CO <sub>2</sub>	H <sub>2</sub> O	Inlet	Surface	O <sub>2</sub>	CO
1.69	43.46	1.41	18.08	7.30	91.8	160.1	30.12	22.15
1.68	44.40	1.41	18.10	7.30	90.0	253.5	101.34	23.01

Additional experiments have been conducted that varied it from 0.7 to 3.0 holding all other feed conditions constant. Dual steady state operation was observed for the entire range tested providing more evidence that the water amount in the feed composition is probably the dominant factor. This type of experiment was repeated for a different CO feed concentration and nearly the same behavior was recorded. This dual steady state nature persists for a wide range of lambda, which points to the fact that dual steady state is more influenced by feed composition and more specifically by water amount. Since water has high heat capacity this may temper the heat rise and delay the onset of H<sub>2</sub> oxidation reaction.

The second significant result from the PROX testing with various water concentrations was evidence of a water-oxygen synergy within the Reactor. Table 2 comprises representative conditions and results from repeat experiments that indicated a water oxygen synergistic reaction occurring. The objective of the three experiments were to determine the contribution of oxygen and water separately toward oxidation of CO and consumption of hydrogen. The first row of the table provides the conditions and results of a baseline experiment, where the system was operating at its targeted steady state position. Here the conversion is as expected, greater than 90% with 50% selectivity. The temperature rise from the inlet to the outlet is consistent with the amount of reaction. The surface temperature rise also tracks with the gas phase temperature rise; recall this reactor substrate operates close to the gas phase due to

high transport properties. The second row has the results of the condition where the water is not included in the influent. The third row shows the results of an experiment where the water influent was resumed and the oxygen was turned off. Each time a reactant was turned off, nitrogen was adjusted to compensate for that loss to maintain a constant GHSV. Inspection of the CO conversion shows that the sum of the CO conversions from the individual reactants does not add up to the conversion when they are both present. In fact, the water alone shows nearly zero reaction which is expected because that condition represents a water gas shift reaction of which the kinetics are very slow at that temperature. It is clear, however, that it is not only the oxygen that is converting the CO since its conversion is only 26% as compared to a 92% conversion when water is present. It is evident that water somehow initiates or promotes the CO oxidation reaction.

**Table 2: Evidence for a water-oxygen synergy within the PROX reactor.**

----- Inlet Concentrations -----					--Reactor Temperature--			---Conversion---		
O <sub>2</sub>	H <sub>2</sub>	CO	CO <sub>2</sub>	H <sub>2</sub> O	Inlet	Surface	Outlet	O <sub>2</sub>	CO	lambda
0.65	31.79	0.55	13.90	32.88	101.2	194.3	192.2	73.33	92.36	2.36
0.65	31.74	0.55	13.91	--	109.6	136.0	135.5	6.15	26.23	2.36
--	31.86	0.55	13.91	32.88	110.4	112.4	109.9	--	-0.50	--

Other researchers have observed similar water enhanced reactions. For example there was a study that showed a hydrogen water synergy[2] and a carbon dioxide water synergy[3]. Both studies indicated that water addition increased the amount of CO oxidation more than expected or predicted. The current experiments, shown in the table, add another piece of evidence to the water assisted or water enhance CO oxidation observations. These results point toward water acting as a catalyst or promoter for the selective CO oxidation on alumina supported platinum based catalysts. It is known that water has a high heat capacity, thus its temperature controlling, or heat absorbing, capability is recognized as one way to control reactions that liberate heat. In the case of the selective oxidation of CO this is very important, as discussed above, so as not to activate or light-off the hydrogen oxidation reaction. Yet water plays a significant role as a promoter in this reaction sequence.

One possible explanation for why water promotes this type of reaction is that water is conjectured to absorb and become activated by the stabilized alumina support while the CO is preferentially absorbed and activated by the catalyst metal. The CO can now be oxidized by the activated water or incoming oxygen. That leaves behind a hydrogen molecule from the water and an oxygen radical. The oxygen radical probably reacts with gas phase hydrogen more readily than gas phase CO purely because of the abundance of hydrogen. However, the hydrogen molecule left behind from the water may desorb or become displaced by another incoming CO molecule and enter the gas phase. This may help explain why we see a water oxygen synergy and a high selectivity toward CO oxidation when the hydrogen concentration is nearly 60 times greater.

**Acknowledgement.** The authors are appreciative of the experimental support from Brian Nentwick and also acknowledge the National Science Foundation's support in conducting a significant portion of this research. Opinions, findings, and conclusions or recommendations are those of the authors and do not necessarily reflect the views of the National Science Foundation.

#### References

- (1) Fogler H.S. In *Elements of Chemical Reaction Engineering*; Second Ed.; Prentice Hall: Englewood Cliffs, N.J., 1990; pp. 383-485.
- (2) Kahlich, M.J., Gasteiger, H.A., Behm, R.J., *J. New Mat. Electrochem. Systems.* **1997**, 171, 93.
- (3) Avgouropoulos, G., Ioannides, T., Matralis, H.K., Bastista, J., Hocevar, S., *Catal. Today*, 2002, 75, 157.

# Hydrocarbon Fuel Composition Effects on Fuel Cell Reformer Performance and Light-off

Rod Borup, Michael A. Inbody, José I. Tafuya, Will J. Vigil and Dennis Guidry

Los Alamos National Laboratory  
MST-11, MS J579  
P.O. Box 1663  
Los Alamos, NM 87545

## Introduction

Fuel cells have high efficiency for conversion of fuel to electricity. However, most types of fuel cells do not have high power density and efficiency operating directly from the hydrocarbon fuels currently widely available for transportation applications (gasoline and diesel), thus require fuel reforming. The choice of fuel for fuel cells is likely to be different for differing fuel cell applications, and debates exist about what the future fuels for fuel cell transportation applications will be. Potential on-board vehicle applications for fuel cells include both prime mobility power and auxiliary power production, and the fuel requirements will vary depending upon the power production application.

The start-up of fuel processors for transportation applications is one challenging area requiring development for commercialization. The light-off of the fuel processor is examined with different fuel components to examine the fuel composition effect during start-up. Chemical equilibrium favoring carbon formation may be impossible to avoid during a fuel rich start-up of a fuel processor.

Hydrogen production from the catalytic oxidation and steam reforming (ATR) of liquid hydrocarbon fuels is examined to determine fuel composition effects on the partial oxidation and reforming aspects of the fuels. Fuel processing performance of individual fuel components is compared with the fuel processing performance of blended fuel components and the reformulated gasoline to examine synergistic or detrimental effects the fuel components have in a real fuel blend.

## Experimental

To examine the effect of the fuel on hydrogen production devices, various fuel components and real fuels have been tested in fuel auto-thermal reformers (ATR) and fuel reforming systems. Fuel reforming has been conducted by catalytic partial oxidation and reforming using air as oxidant. Typical ATR catalysts which are noble metal based (such as platinum and rhodium) have been employed in this work. The catalysts are supported onto a high surface area substrate, either a monolith honeycomb, or a reticulated foam. For gasoline reforming, the gasoline, or gasoline component is vaporized, then mixed in vapor phase with steam. The fuel/water mixture is then mixed with air, preheated and introduced to the reforming catalyst. Carbon formation during light-off was measured by monitoring carbon via *in situ* laser absorption and scattering measurements. The oxidation catalyst is preheated to a temperature of about 250 – 300 °C so that fuel light-off occurs when the fuel/air mixture is introduced.

The analysis of the fuel effect on the product composition stream is conducted by various analytical techniques, specifically laser scattering and laser fluorescence, gas chromatography, FTIR (Fourier transform infrared), NDIR (non-dispersive infrared), paramagnetic oxygen and GC/MS (gas chromatography/mass spectrometry).

Various fuel compositions and components have been measured in these reactor systems. Main components include aliphatic (straight-chained and branched chained), aromatic, naphthenic, olefinic. Hydrotreated naphtha, reformulated gasoline, kerosene, de-odorized kerosene, low sulfur diesel, diesel fuel and bio-diesels are some of the fuels which have been used. Additives examined include anti-oxidant No. 29 (2,6-Di-Tert-Butyl-4-methylphenol), anti-oxidant No. 22 (N, N'-Di-Sec-Butyl-P-Phenylenediamine) and DMA-548.

## Results and Discussion

The start-up of the fuel processor for transportation applications is a key challenge for commercialization. Some of the challenges in starting the fuel processor system include: the speed of start-up to limit on-board energy storage, start-up without stored water onboard the vehicle, limiting the energy consumed during the start-up, and limiting the fuel processor durability by the formation of carbon. These start-up challenges can be affected by the fuel composition used for the reformer. Hydrocarbon components and fuel blends were measured for their propensity for light-off. The light-off of a reformer, especially under rich conditions and without use of steam, makes it difficult to avoid regimes in which carbon formation is not favored by chemical equilibrium.

The reformer light-off was measured by introducing fuel/air/steam mixture to the reformer at a O/C = 0.9, S/C = 1.0, then ramping the temperature of the catalyst bed in the reformer. The outlet composition was measured in real time by a mass spectrometer to observed when oxygen consumption started, and hydrogen, carbon monoxide and carbon dioxide were generated. An example light-off for iso-octane with 20% pentane is shown in figure 1.

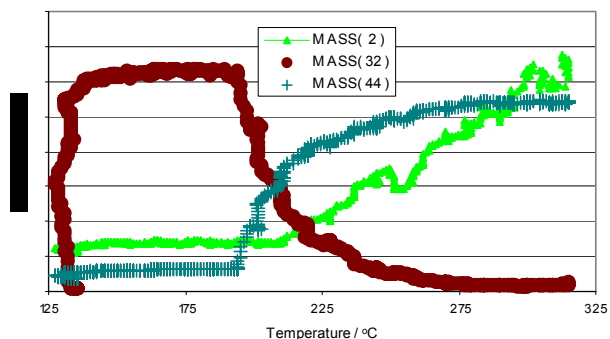


**Figure 1.** Reformer light-off with iso-octane and 20% pentane at O/C = 0.9 and S/C = 1.0.

Monitoring the light-off temperature of the reformer as a function of fuel helps determine the relative fuel effect on the reformer start-up. Iso-octane is typically used as a gasoline fuel simulant, and is thus used in all measurements for comparison purposes. Figure 2 shows the light-off of various straight-chained hydrocarbons, from n-pentane to n-decane, iso-octane and mixtures of iso-octane and pentane and hexane at 80% iso-octane. As the carbon length of the straight chained molecules is increased, the light-off temperature of the reformer increases. However, the light-off temperature of all of the straight-chained hydrocarbons are lower than the light-off temperature of iso-octane. As iso-octane is mixed with the straight-chained hydrocarbons, the light-off temperature is reduced.

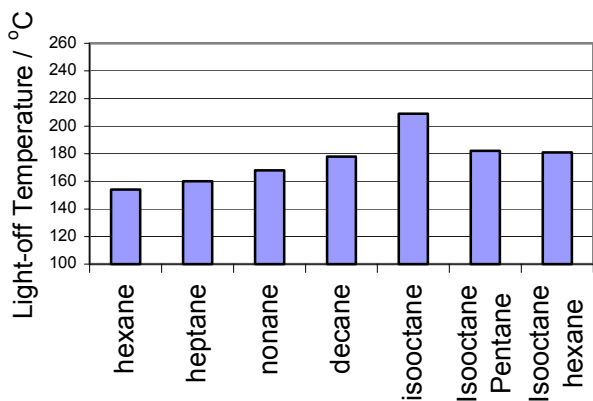


**Figure 2.** Reformer light-off with various aliphatic hydrocarbons (n-hexane, n-heptane, n-nonane, n-decane, iso-octane, iso-octane + 20 % n-pentane and iso-octane + 20 % n-hexane).

A ubiquitous impurity in hydrocarbon fuels tends to be sulfur, in various compounds, and has been shown to be detrimental to the reforming of hydrocarbons.<sup>1</sup> To examine the effect of sulfur and sulfur compounds on the light-off of reformers, thiophene and dibenzothiophene were added to iso-octane at levels of 100 ppm and 1000 ppm. These results are shown in figure 3. The sulfur at levels of 100 ppm for both thiophene and dibenzothiophene are not detrimental to the light-off of the reformer, in fact decrease the light-off temperature of the catalyst by 10 to 15 °C. However, when the compounds are added at a concentration of 1000 ppm, favorable effect disappears with thiophene, and dibenzothiophene increases the light-off temperature by over 30 °C.

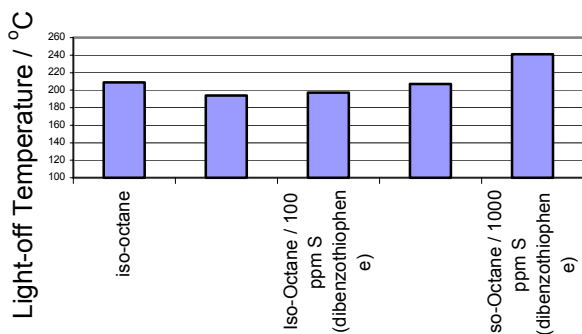


**Figure 3.** Reformer light-off with iso-octane and iso-octane with 100 ppm thiophene, 100 ppm dibenzothiophene, 1000 ppm thiophene and 1000 ppm dibenzothiophene (ppm by weight of S).

The current fuel infrastructure for transportation applications consists mainly of gasoline and diesel fuel. These fuels have many constituents, including generally relatively high content of aromatic components (~ 20 %). Aromatic components have been shown to slow the reforming kinetics and to increase carbon formation.<sup>2</sup> Figure 4 shows the light-off measurements of iso-octane, and iso-octane mixed with various aromatic compounds found in gasoline (xylene) and diesel fuel (anthracene, naphthalene). In addition, reformulated gasoline (RFG), kerosene, low sulfur diesel fuel and a commercial diesel fuel were measured for their light-off.

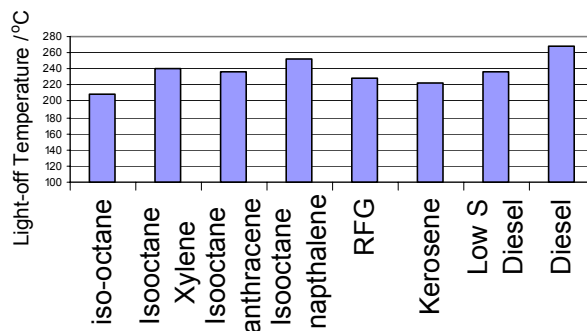


**Figure 4.** Reformer light-off with various aromatic hydrocarbons and fuels (iso-octane, iso-octane + 20 % xylene, iso-octane + 5 % anthracene, iso-octane + 5 % naphthalene, RFG – reformulated gasoline, kerosene, Low sulfur diesel fuel, and commercial diesel fuel).

The addition of aromatic compounds all increased the light-off temperature of iso-octane. The fuel blends all showed higher light-off temperatures than did iso-octane.

The steady-state relative rates for catalytic partial oxidation for different fuels has also been measured for various operating conditions after reformer light-off has occurred. Figure 5 shows relative reaction rate for various fuel components, mixtures and a Phillips Petroleum Hydrotreated Naptha stream at a S/C of 1.0. The relative reaction rates vary as the O/C ratio varies due to temperature changes. At lower O/C ratios, the adiabatic temperature rise is lower, thus the overall reaction rate is lower. The reaction rate for all components is higher at higher O/C, and subsequently, higher temperatures. The oxidation rates for O/C's of 0.7 and 0.8 are fastest for iso-octane. The addition of aromatics such as xylene slows the oxidation rate and conversion. Real fuel composition mixtures such as the Phillips Naptha and reformulated gasoline show a faster oxidation rate than that of iso-octane/xylene mixtures even though the relative aromatic concentration is approximately the same. At high O/C ratios (O/C = 1.0), the real fuel mixtures show an equal or faster oxidation rate compared with pure iso-octane. The resulting decrease in the oxidation rate due to the presences of aromatic hydrocarbons indicates that the fuel composition will have an affect on the required size (and cost due to catalyst loading) of the fuel processor. If it is possible to make a non-aromatic containing fuel available, the fuel processing size and cost would be positively affected.

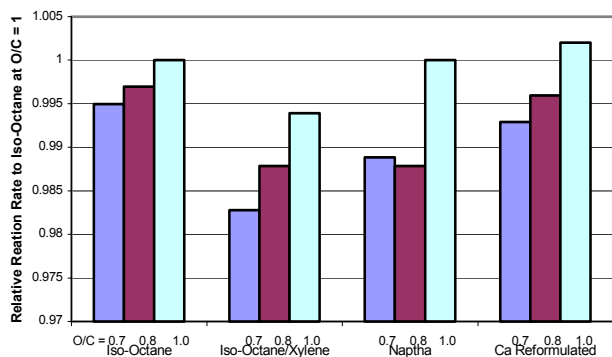


**Figure 5.** Relative oxidation rates of iso-octane, iso-octane/20% xylene, naptha and reformulated gasoline.

### Conclusions

Fuel composition is important to reforming of fuel for transportation fuel cell systems. The fuel composition can affect the reformer light-off and start-up, the oxidation and reforming kinetics. Aliphatic hydrocarbons tend to have favorable light-off and reforming characteristics compared with aromatic components.

### Acknowledgment

This work was supported by the Department of Energy Hydrogen, Fuel Cells and Infrastructure Technologies Program.

### References

- (1) Paul Berlowitz et al. 2003 Spring AIChE Meeting, New Orleans, March 30 – April 3.
- (2) Borup et al. Fuel Composition Effects on Fuel Processor Dynamics, Office of Advanced Automotive Technologies Transportation Fuel Cell Power Systems FY 2000 Accomplishments Report.

# CeO<sub>2</sub>-Al<sub>2</sub>O<sub>3</sub>-SUPPORTED NOBLE METAL CATALYSTS FOR STEAM REFORMING OF HYDROCARBONS FOR FUEL CELLS

Jian Zheng, James Jon Strohm, Chunshan Song\*

Clean Fuels and Catalysis Program, The Energy Institute, and  
Department of Energy & Geo-Environmental Engineering,  
Pennsylvania State University, 209 Academic Projects Building,  
University Park, PA 16802

\*Email: csong@psu.edu; Tel: 814-863-4466; Fax: 814-865-3248

## Introduction

Recently, increasing attention has been paid on exploring compact fuel processors for fuel cell applications around the world<sup>1,2</sup>. We are exploring a fuel-cell fuel processor using logistic fuel (such as JP-8 jet fuel) for portable fuel cell application. As mentioned in our recent papers<sup>3,4</sup>, our approach to solving the potential problem of carbon formation during reforming of higher hydrocarbon fuels is to conduct catalytic fuel reformation in two stages, with a pre-reformer (oxygen-assisted if necessary) to break-down most C<sub>8</sub>-C<sub>13</sub> hydrocarbons to C<sub>1</sub> to C<sub>2</sub> molecules plus CO and H<sub>2</sub>, followed by steam reforming (possibly also oxygen-assisted) in main reformer to produce reformats (H<sub>2</sub>, CO, CO<sub>2</sub>).

Most industrial steam reforming of light hydrocarbons (C<sub>1</sub>-C<sub>4</sub>) uses a supported Ni catalyst. While the studies on steam reforming using noble-metal catalysts are limited, there are evidences indicating that these materials can be more active and more resistant to carbon formation than conventional Ni catalysts<sup>3-10</sup>. However, the metal activity over various supported materials for steam reforming under different conditions results in some contradictory trends in the literature. The specific activities of metals supported on alumina or magnesia have generally been found to be<sup>5</sup>: Rh ~ Ru > Ni ~ Pd ~ Pt > Re > Co. Turnover numbers have also been reported for steam reforming of methane and ethane on noble metals relative to Ni. For silica-supported catalysts used for methane steam reforming, the relative activities are<sup>6</sup>: Rh (1.6) > Ru (1.4) > Ni (1) > Pd (0.6) > Pt (0.5), whereas for alumina-supported systems with ethane<sup>7,8</sup>: Rh (13) > Ru (9.5) > Pd (1.0) ~ Ni (1.0) > Pt (0.9). For the steam reforming of propane/propene mixtures, the order of activity is<sup>9</sup>: Rh ~ Ir > Pt > Co > Ru > Ni ~ Re. While the order of activity per metal site (on the base 100 for Rh) for the toluene steam reforming is<sup>10</sup>: Rh (100) > Pd (29) > Pt (19) > Ni (17) > Ir (13). It seems that rhodium has been generally found to be the most active metal, whereas no common agreement and knowledge has been achieved on the activity of iridium as catalyst for steam reforming of hydrocarbons.

With the need for on-board reforming for fuel cell applications, there has been renewed interest in developing more active catalysts that can operate under more demanding conditions at lower steam-to-carbon ratios for reforming of hydrocarbons. Instead of using Al<sub>2</sub>O<sub>3</sub> as support, some new materials, such as those having unique features for stabilizing noble metal dispersion and for improving the oxygen storage (e.g., CeO<sub>2</sub>, ZrO<sub>2</sub>, etc.), have been examined<sup>11-14</sup>. Catalytic properties of CeO<sub>2</sub> and CeO<sub>2</sub>-containing materials have been studied extensively<sup>13</sup>. Noble metal based catalysts (Pt, Pd and Rh) deposited on various support such as Al<sub>2</sub>O<sub>3</sub>, CeO<sub>2</sub> and ZrO<sub>2</sub>, have been tested in various reforming processes, and they provide good catalytic activity in methane, propane or n-butane steam reforming reactions<sup>11, 14</sup>. The presence of CeO<sub>2</sub> as a promoter has also been found to confer high catalytic activity to the alumina-supported Pd catalyst for methane steam reforming<sup>11</sup>. Furthermore, the catalytic activity and the synergetic effect for the Pd/CeO<sub>2</sub>/Al<sub>2</sub>O<sub>3</sub> catalysts are strongly dependent on the crystallinity, dispersion and stoichiometry of the

CeO<sub>2</sub> promoter deposited. Highly crystalline CeO<sub>2</sub> increases the catalytic activity of a Pd-supported catalyst when used in methane steam reforming<sup>11</sup>.

In the present work, various noble metals have been supported on CeO<sub>2</sub> modified Al<sub>2</sub>O<sub>3</sub> for the steam reforming of jet fuel via a two-step process (i.e. pre-reforming under low temperature and main reforming at high temperature). Ce has been found to improve both the activity and coke-resistance of Rh and Ir supported Al<sub>2</sub>O<sub>3</sub> catalysts.

## Experimental

CeO<sub>2</sub>-Al<sub>2</sub>O<sub>3</sub> (containing 20wt% CeO<sub>2</sub>) support was prepared by wet impregnation of  $\gamma$ -Al<sub>2</sub>O<sub>3</sub> (UOP LaRoche VGL-15) with Ce(NO<sub>3</sub>)<sub>3</sub>·6H<sub>2</sub>O (Aldrich) followed by calcinations at 800°C in air for 3 hours.

RhCl<sub>2</sub> (Aldrich) has been supported on both  $\gamma$ -Al<sub>2</sub>O<sub>3</sub> and CeO<sub>2</sub>•Al<sub>2</sub>O<sub>3</sub> by wet impregnation, with nominal metal content of 2wt%. In both cases, the obtained RhCl<sub>2</sub> supported material was soaked into NH<sub>4</sub>OH solution for several hours, followed by filtration and calcinations to remove NH<sub>3</sub>, Cl<sup>-</sup>, and other impurities.

Various noble metals (such as Pt, Pd, Ru, Rh, Ir) have also been supported on Al<sub>2</sub>O<sub>3</sub> and CeO<sub>2</sub>-Al<sub>2</sub>O<sub>3</sub> by wet impregnation, with nominal metal content fixed at 1 wt% for main reforming.

**Jet fuel formulation.** A readily available NORPAR-13 (consisting mainly normal paraffin, with average carbon number of 13) has been chosen as an important type of jet fuel. Since there is no much sulfur in NORPAR-13 (the sulfur content of NORPAR-13 is 4ppmw as analyzed by us using Antek 9000ES total sulfur analyzer), it can actually be regarded as a near sulfur-free clean jet fuel that can be utilized in large amount and directly for steam reforming in fuel processor for fuel cell application.

**Simulated gas mixture.** As described previously<sup>4</sup>, SGM-2 (47.5% CH<sub>4</sub>, 35.5% H<sub>2</sub>, 7.0% CO<sub>2</sub>, 9.0% C<sub>2</sub>H<sub>6</sub>, and 1.0% C<sub>3</sub>H<sub>8</sub>) has been chosen as an extreme example for the reformats from incomplete pre-reforming, since there is a significant concentration of higher hydrocarbons (C<sub>2</sub>H<sub>6</sub> and C<sub>3</sub>H<sub>8</sub>).

**Reaction conditions.** A given amount of catalyst sample (1g for pre-reforming, 0.1 g for main reforming) was loaded in the middle of the stainless steel reactor tube (Inconel 800H alloy, with 0.54" O.D. X 0.375" I.D. and 24" long), with the remaining tube filled with  $\alpha$ -Al<sub>2</sub>O<sub>3</sub> beads.

For pre-reforming, NORPAR-13 jet fuel was introduced with one of the two HPLC pumps through the pre-heater into the reactor with a volumetric flow rate of 1.38 ml/hr. The water flow is kept at 4.02 ml/hr with a steam to carbon ratio of 3:1. The fuel flow is to simulate the real conditions defined by the calculations for a 20 watts solid-oxide fuel cell

For main reforming, CH<sub>4</sub> feed flow rate in the SGM-2 was chosen to be 13.7 ml/min, which also simulates the energy requirement for a 20 watts solid-oxide fuel cell.

Before starting the reforming, water was introduced for 30 minutes before pumping/flowing the reactant oil/gases. Catalyst screening is then performed in a laboratory continuous-down-flow tubular reactor (as described in our previous papers<sup>3,4</sup>) at atmospheric pressure in the temperature range of 514°C (for pre-reforming) and 600-800°C (for main reforming), respectively.

During the pre-reforming reaction, the liquid products are collected every several hours by a liquid condenser with volume measured for the calculation of total conversion. For the main reforming, the gas products after condensing of remaining steam are analyzed on-line by a multi-gas analyzer GC-TCD for the calculation of conversion and product distributions.

## Results and Discussion

**Figure 1** shows a 10-hour pre-reforming run of the NORPAR-13 (4ppm S) at 514°C using the modified 2%Rh/CeO<sub>2</sub>•Al<sub>2</sub>O<sub>3</sub> catalyst.

It can be found that the conversion is always near 100%. In the products, hydrogen is near 55%, the content of CO is only 5%, while the CO<sub>2</sub> and CH<sub>4</sub> are the dominant carbon-containing products with similar contents (both around 20%). There is almost no higher hydrocarbon such as ethane in the product gases.

In order to understand the effect of Ce on the Rh/CeO<sub>2</sub>•Al<sub>2</sub>O<sub>3</sub> catalyst for pre-reforming of jet fuels, we also prepared a comparative 2%Rh/Al<sub>2</sub>O<sub>3</sub> followed by same NH<sub>3</sub>-H<sub>2</sub>O treatment.

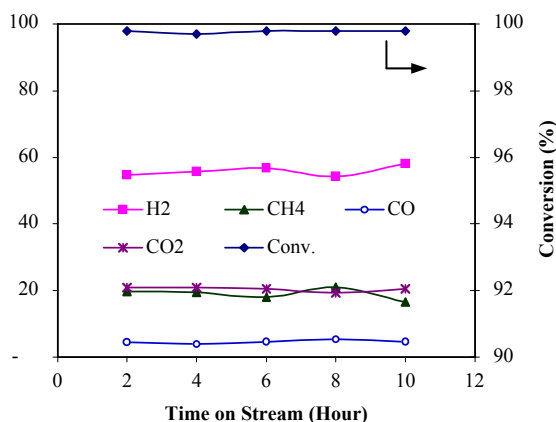


**Figure 1.** Pre-reforming of NORPAR-13 over modified 2%Rh/CeO<sub>2</sub>•Al<sub>2</sub>O<sub>3</sub> catalyst at 514°C, S/C=3, atm.

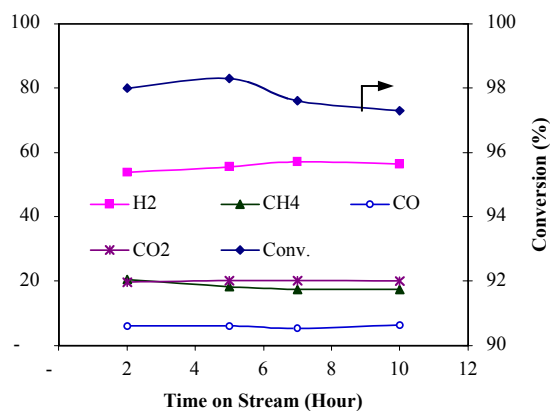


**Figure 2.** Pre-reforming of NORPAR-13 at 514°C over modified 2%Rh/Al<sub>2</sub>O<sub>3</sub> catalyst (S/C=3, atm).

**Figure 2** shows another 10-hour pre-reforming run of the NORPAR-13 (4ppm S) at 514°C using the modified 2%Rh/Al<sub>2</sub>O<sub>3</sub> catalyst under exactly same reaction conditions as in **Figure 1**.

It can be seen that with the absence of Ce, the modified 2%Rh/Al<sub>2</sub>O<sub>3</sub> catalyst shows lower activity: the conversion is around 97%-98% and there is a trend of deactivation with time on stream, which indicates that Ce in the modified Rh/CeO<sub>2</sub>•Al<sub>2</sub>O<sub>3</sub> catalyst is important for the improved catalytic activity. The composition of the gas products is similar to previous 10-hour run, with hydrogen around 56%, CO at 6%, CO<sub>2</sub> around 20%, and methane around 18%, which are close to the equilibrium pre-reformate composition<sup>15</sup>.

**Figure 3** shows the TPO-IR results of used catalysts Rh/CeO<sub>2</sub>•Al<sub>2</sub>O<sub>3</sub> (a) and Rh/Al<sub>2</sub>O<sub>3</sub> (b), after 10-hour pre-reforming of NORPAR-13 at 514°C. Peaks at 200-400°C can be attributed to either the desorption of CO<sub>2</sub> or the oxidation of highly amorphous carbon while any peak at 400°C-600°C is the oxidation of carbon filament on the used catalysts<sup>16, 17</sup>.

It can be seen that there is an obvious high temperature peak at 400-600°C in the case of Rh/Al<sub>2</sub>O<sub>3</sub>, indicating that the presence of Ce is important to prevent carbon formation during pre-reforming of jet fuel.

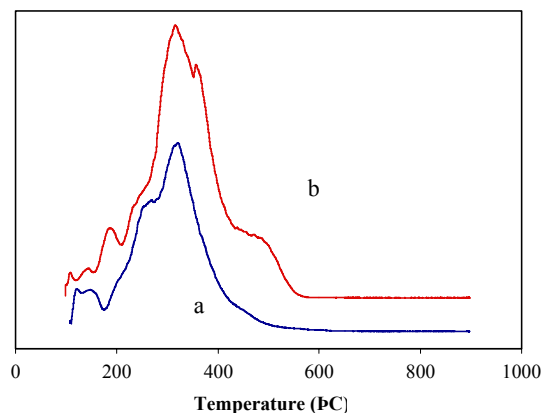


**Figure 3.** TPO-IR of used catalysts 2%Rh/CeO<sub>2</sub>•Al<sub>2</sub>O<sub>3</sub> (a) and 2%Rh/Al<sub>2</sub>O<sub>3</sub> (b), after 10-hour pre-reforming of NORPAR-13 at 514°C, S/C=3, atm.

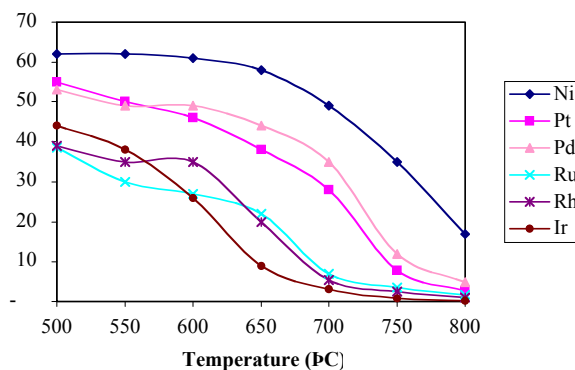
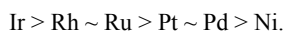


**Figure 4.** Steam reforming of SGM-2 on 1wt% noble metal supported on CeO<sub>2</sub>•Al<sub>2</sub>O<sub>3</sub> (GHSV=21500h<sup>-1</sup>, S/C=1.5, atm)

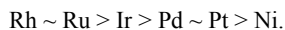
As studied previously<sup>4</sup>, we found that different metal shows different activity for steam reforming of methane at high temperature (800°C). The understanding of this metal activity trend is important that can serve as a guide for the selection of good catalyst composition for steam reforming of hydrocarbons. We have carried more systematic studies on the activity trend for different transition metal supported on same CeO<sub>2</sub>•Al<sub>2</sub>O<sub>3</sub> for the steam reforming of SGM-2 (contains not only methane, but also ethane and propane) under various reaction temperatures.

**Figure 4** shows the steam reforming of SGM-2 at 500°C-800°C of 1wt% metals on the same CeO<sub>2</sub>•Al<sub>2</sub>O<sub>3</sub> support. The y-axis of **Figure 4** is the CH<sub>4</sub> content in the product gases. The lower of this value means the less un-reacted CH<sub>4</sub> (thus the higher conversion of

CH<sub>4</sub>). It can be seen that at higher temperature (e.g. 800°C), Ir is the most active among all the metals, which show following trend:



However, at lower temperature (e.g. 500°C), Ir loses its superiority to Rh and Ru, showing the following trend:



This actually indicates that in the case of pre-reforming (usually working at around 500°C), the most active metal could be Rh rather than Ir, which has already been verified by our previous pre-reforming work<sup>3</sup>.

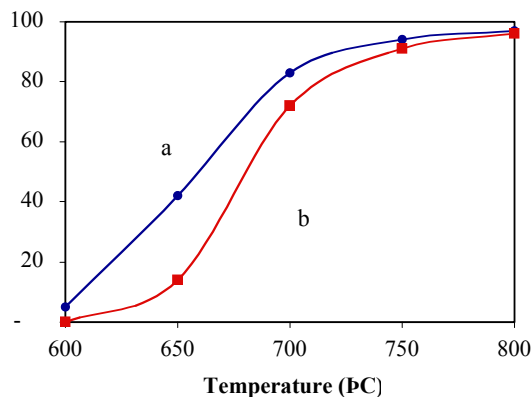


**Figure 5.** Steam reforming of SGM-2 on 1wt% Ir supported on CeO<sub>2</sub>-Al<sub>2</sub>O<sub>3</sub> (a) and Al<sub>2</sub>O<sub>3</sub> (b) (GHSV=21500h<sup>-1</sup>, S/C=1.5, atm)

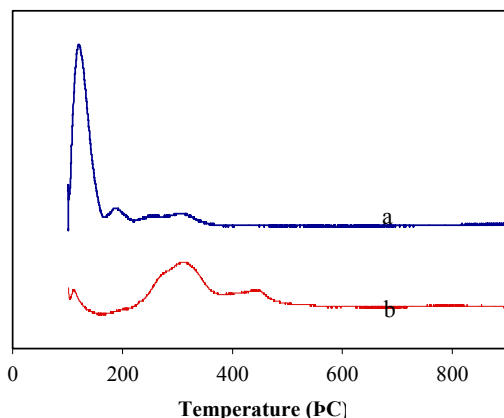


**Figure 6.** TPO-IR of used catalysts 1%Ir/CeO<sub>2</sub>·Al<sub>2</sub>O<sub>3</sub> (a) and 1%Ir/Al<sub>2</sub>O<sub>3</sub> (b), after 10-hour main reforming of SGM-2 at 800°C, S/C=1.5, atm.

**Figure 5** shows the steam reforming results of SGM-2 over Ir supported on CeO<sub>2</sub>-Al<sub>2</sub>O<sub>3</sub> and Al<sub>2</sub>O<sub>3</sub> under same steam/carbon ratio with changing temperature. It is clear that in the presence of Ce, the Ir/CeO<sub>2</sub>-Al<sub>2</sub>O<sub>3</sub> catalyst is more reactive, especially at lower temperature, than the Ir supported on Al<sub>2</sub>O<sub>3</sub> alone. This indicates that Ce helps promote the steam reforming of hydrocarbons.

**Figure 6** shows the TPO-IR results of used catalysts Ir/CeO<sub>2</sub>·Al<sub>2</sub>O<sub>3</sub> (a) and Ir/Al<sub>2</sub>O<sub>3</sub> (b), after 10-hour main reforming of

SGM-2 at 800°C. Peaks at 200-400°C can be attributed to either the desorption of CO<sub>2</sub> or the oxidation of highly amorphous carbon, while any peak at 400°C-600°C is the oxidation of carbon filament on the used catalysts<sup>16,17</sup>.

It can be seen that, similar to the results shown in **Figure 3**, there is an obvious high temperature peak at 400-600°C in the case of un-promoted Ir/Al<sub>2</sub>O<sub>3</sub>, indicating that the presence of Ce is important to prevent carbon formation during steam reforming of lower hydrocarbons at 800°C due to enhanced oxidative property.

## Conclusions

Various metals (Rh, Ru, Ir, Pt, Pd, Ni) supported on CeO<sub>2</sub> promoted Al<sub>2</sub>O<sub>3</sub> have been studied for steam reforming of liquid hydrocarbons (such as jet fuel). At higher temperature (such as 800°C), Ir/CeO<sub>2</sub>-Al<sub>2</sub>O<sub>3</sub> catalyst shows the highest activity for steam reforming of lower hydrocarbons among all the CeO<sub>2</sub>-Al<sub>2</sub>O<sub>3</sub> supported noble metal catalysts. However, at lower temperature as in the case of pre-reforming (at around 500°C), Ir loses its superiority to Rh and Ru. Ce helps promote the steam reforming of hydrocarbons by improving both the activity and coke-resistance of Rh and Ir supported catalysts.

**Acknowledgement.** We are grateful to the DoD/DARPA Palm Power Program management for supporting this work under sub-contract to Altex Technologies Inc. We also wish to thank Dr. Mehdi Namazian of Altex for helpful discussions on fuel reforming, and UOP for providing LaRoche  $\gamma$ -Al<sub>2</sub>O<sub>3</sub> samples. Thanks also go to Dr. Jian-Ping Shen, Dr. Altin Orhan, Mr. Ronald Copenhagen and Ms. Lu Sun of PSU for their assistance.

## References

- (1) Song, C. *Catalysis Today*, **2002**, 77, 17-49.
- (2) Trimm, D.L.; Onsan, Z.I. *Catal. Rev.*, **2001**, 43 (1,2), 31-84; Larminie, J.; Dicks, A. In *Fuel cell Systems Explained*; John Wiley: New York, **2000**, pp.308.
- (3) Zheng, J.; Shen, J.P.; Song, C.; Pan, W.; Strohm, J.J. *Prepr. Pap. - Am. Chem. Soc., Div. Fuel. Chem.*, **2003**, 48 (1), 374.
- (4) Zheng, J.; Song, C. *Prepr. Pap. - Am. Chem. Soc., Div. Fuel. Chem.*, **2003**, 48 (1), 378.
- (5) Kikuchi, E.; Tanaka, E.; Yamazaki, Y.; Morita, Y. *Bull. Japan Petrol. Inst.*, **1974**, 16, 95.
- (6) Rostrup Nielsen, J.R. In *Catalysis Science and Technology*; Andersen, J.R.; Boudart, M., Ed.; Springer-Verlag, New York, **1984**; Vol. 4, pp.34.
- (7) Grenoble, D.C. *J. Catal.* **1973**, 51, 203.
- (8) Gandhi, H.S.; Piken, A.G.; Stepien, H.K.; Shelef, M.; Delosh, R.G.; Heyde, M.E. *SAE Techn. Pap. Ser. No. 770166*, in SAE Automotive Engineering Congress, Detroit, **1977**.
- (9) Duprez, D.; Pereira, P.; Grand, M.; Maurel, R. *J. Catal.*, **1982**, 75, 151.
- (10) Igarashi, A.; Ohtaka, T.; Motoki, S. *Catal. Lett.*, **1991**, 13, 189-194.
- (11) Craciun, R.; Daniell, W.; Knozinger, H. *Appl. Catal. A: Gen.*, **2002**, in press.
- (12) Hofstad, K.H.; Rokstad, O.A.; Holman, A. *Catal. Lett.*, **1996**, 36, 25.
- (13) Barbier, J.Jr.; Duprez, D. *Appl. Catal. B: Environ.* **1993**, 4, 105.
- (14) Kikuchi, E.; Nemoro, Y.; Kajiwara, M.; Uemiya, S.; Kojima, T. *Catal. Today*, **2000**, 56, 75.
- (15) Wei, P.; Song, C. Unpublished data.
- (16) Zheng, J.; Song, C.; Pan, W.; Sun, Lu; Armor, J.; Nataraj, S.; Wilhelm, F. *Prepr. Pap. - Am. Chem. Soc., Div. Fuel. Chem.*, **2003**, 48 (2), to be accepted.
- (17) Strohm, J.J.; Zheng, J.; Song, C. *Prepr. Pap. - Am. Chem. Soc., Div. Fuel. Chem.*, **2003**, 48 (2), to be accepted.

# AN INNOVATIVE EFFICIENT COMBINED CYCLE FOSSIL AND BIOMASS FUEL POWER GENERATION AND HYDROGEN PRODUCTION PLANT WITH ZERO CO<sub>2</sub> EMISSION

*Meyer Steinberg, Consultant*

Energy Resources Division  
Brookhaven National Laboratory  
Upton, NY 11973-5000

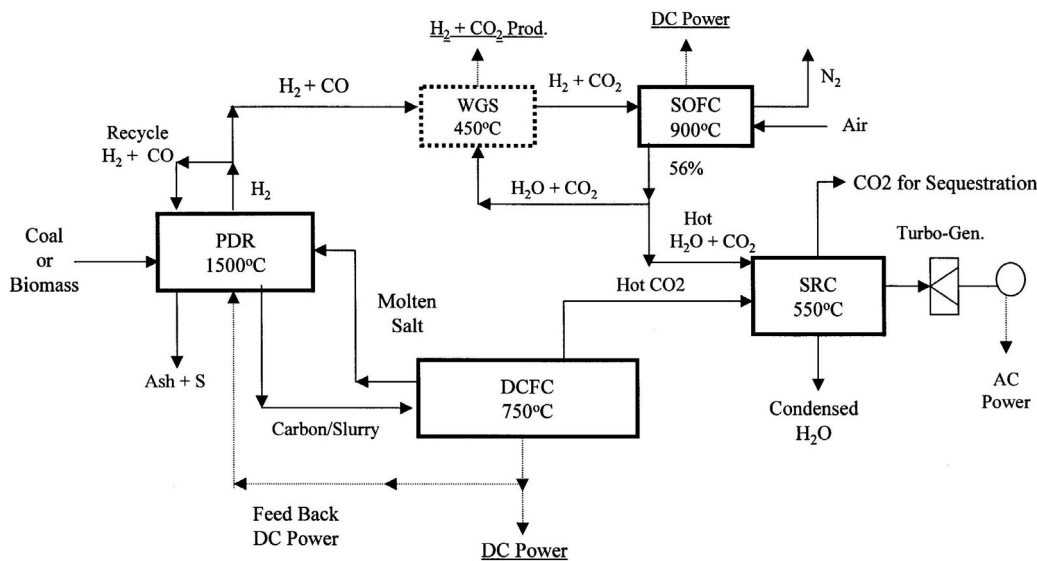
## Introduction

An advanced combined cycle for fossil and biomass fuel power generation and hydrogen production is described. An electric arc hydrogen plasma black reactor (HPBR)<sup>(1)</sup> decomposes the carbonaceous fuel (natural gas, oil, coal and biomass) to elemental carbon and hydrogen. When coal and biomass feedstocks are used, the contained oxygen converts to carbon monoxide. Any ash and sulfur present are separated and removed. The elemental carbon is fed to a molten carbonate direct carbon fuel cell (DCFC)<sup>(2)</sup> to produce electrical power, part of, which is fed back to the HPBR to power the hydrogen plasma. The hydrogen is used in a solid oxide fuel (SOFC) cell for power generation. The remaining high temperature energy in the gases from the fuel cells are used in a back-end steam rankine cycle (SRC) for generating additional power. The CO formed is converted to hydrogen using a water gas shift reactor (WGS). The plasma reactor is 60% process efficient, the direct carbon fuel cell is up to 90% thermal efficient, the solid oxide fuel cell is 56% efficient and the steam reaction cycle is 38% efficient. Depending on the feedstock, the combined cycles have efficiencies ranging from over 70% to exceeding 80% based on the higher heating value of the feedstock and are thus twice as high as conventional steam plants which are 38% efficient. The CO<sub>2</sub> emissions are proportionately reduced. Since the CO<sub>2</sub> from the direct carbon fuel cell and the water gas shift is highly concentrated, the CO<sub>2</sub> can be sequestered to reduce emission to zero with much less energy loss than occurs in conventional plants. Alternatively, these combined cycle plants can produce hydrogen for the freedomCAR program in combination with electrical power production at total thermal efficiencies much greater than obtained with fossil fuel reforming and gasification plants producing hydrogen alone.

Figure 1 presents a flow diagram of the combined cycle plant based on coal and biomass feedstock and indicates the functions of each of the units and the stoichiometric reactions taking place. A thermodynamic evaluation of the combined cycle system is given in Table 1. The mass balance, the energy distribution and the thermal efficiency of the entire system are given for a range of fossil and biomass fuels and includes the corresponding CO<sub>2</sub> emissions. The conclusion of this study is that for a wide variety of fossil fuels and biomass (wood), this combined cycle system results in efficiencies for electrical power production that are more than twice as high as conventional steam plants. The CO<sub>2</sub> emissions are thus cut in half. When the system is configured to produce hydrogen in addition to electrical power, the SOFC is eliminated and only the direct carbon fuel cell (DCFC) generates power, in which case, the total thermal efficiency can exceed 90%. This shows how integrated the hydrogen plasma black reactor (HPBR) functions with the direct carbon fuel cell (DCFC) in a combined system. The HPBR supplies the carbon fuel for the DCFC, which in turn supplies the power to the HPBR.

## References

1. Sequin, L., The Karbomont Production Plant, Montreal, Canada, Private Presentation, 2002.
2. Cooper, J. F., Turning Carbon Directly into Electricity, Science and Technology Review, Lawrence Livermore National Laboratory, CA, 2001, 4-12.



**HPBR - Hydrogen Plasma Black Reactor**  
 Lignite Coal  $\text{CH}_{0.77}\text{O}_{0.24} = 0.76\text{C} + 0.24\text{CO} + 0.385\text{H}_2$   
 Kentucky Bit. Coal  $\text{CH}_{0.81}\text{O}_{0.08} = 0.92\text{C} + 0.08\text{CO} + 0.40\text{H}_2$   
 Biomass:  $\text{CH}_{1.38}\text{O}_{0.59} = 0.41\text{C} + 0.59\text{CO} + 0.69\text{H}_2$   
**WGS - Water Gas Shift**  
 Lignite  $0.24\text{CO} + 0.24\text{H}_2\text{O} = 0.24\text{CO}_2 + 0.24\text{H}_2$   
 Bituminous  $0.08\text{CO} + 0.08\text{H}_2\text{O} = 0.08\text{CO}_2 + 0.08\text{H}_2$   
 Biomass:  $0.59\text{CO} + 0.59\text{H}_2\text{O} = 0.59\text{CO}_2 + 0.59\text{H}_2$   
**SOFC - Solid Oxide Fuel Cell**  
 $\text{H}_2 + 1/2\text{O}_2 = \text{H}_2\text{O}$  (High Transport)  
**DCFC - Direct Carbon Fuel Cell**  
 $\text{C} + \text{O}_2 + \text{CO}_2$  ( $\text{CO}_3^-$  Ion Transport)  
**SRC - Steam Boiler Rankine Cycle**

**Figure 1. Coal or Biomass Fueled Combined Cycle Plasma Composition (PDR) with Direct Carbon Fuel Cell (DCFC), Hydrogen Solid Oxide Fuel Cell (SOFC) Backend Steam Rankine Cycle (SRC) Power Generation**

**Table 1**  
**Electrical Power Production in the HPBR/DCFC/SOFC/SRC Combined Power Cycle Plant**  
**Thermal Efficiency Evaluation and CO<sub>2</sub> Emission**  
**Basis: -1 gmol of Fuel**

Fuel Feedstock	Natural Gas	Crude Oil	N. Dakota Lignite Coal	Kentucky Bituminous Coal	Biomass Wood
Molar Composition (MAF)	CH <sub>4</sub>	CH <sub>1.7</sub>	CH <sub>0.77</sub> O <sub>0.24</sub>	CH <sub>0.81</sub> O <sub>0.08</sub>	CH <sub>1.38</sub> O <sub>0.59</sub>
Plasma Decomp. Products					
Mole/Mole Fuel					
C	1.0	1.0	0.76	0.92	0.41
CO	-	-	0.24	0.08	0.59
H <sub>2</sub>	2.0	0.85	0.39	0.41	0.69
Ash, S, N (wt%)	-	~1.0	9.8	12.6	1.1
Enthalpy of Decomposition Kcal/gmol	18.0	+3.0	+3.6	+4.8	+12.7
<b>Electrical Energy Generation All Energy Values in Kcal/gmol fuel</b>					
Unit	Eff. %				
DCFC	90	84.6	84.6	64.3	77.8
SOFC	56	76.2	32.4	23.8	18.7
SRC	38	26.3	13.3	9.8	8.8
HPBR	60 - Consumed	-30.0	-5.0	-6.0	-8.0
Net Electricity Generation, Kcal(e)	157.1	125.3	91.9	97.3	78.4
HHV of Fuel, Kcal(t)	212.0	149.0	110.3	119.0	112.8
Heat Exch. for Preheat* Kcal(t)	14.8	16.2	7.7	6.5	18.9
<b>Thermal Efficiency - %</b>	<b>74.1</b>	<b>84.1</b>	<b>83.3</b>	<b>81.8</b>	<b>69.5</b>
CO <sub>2</sub> Emission, Lbs/Kwh(e)	0.531	0.610	0.955	0.833	(0.986)**
CO <sub>2</sub> Reduction from conventional 38% SRC cycle - %	48.7	56.5	54.4	53.6	100.0

HPBR = Hydrogen Plasma Black Reactor  
 DCFC = Direct Carbon Fuel Cell  
 SOFC = Solid Oxide Fuel Cell  
 SRC = Steam Rankine Cycle

\* This is the amount of heat unconverted from high temperature gas and can be used to preheat the incoming feed to reactor temperature by heat exchange.  
 \*\*For biomass this is the amount of CO<sub>2</sub> emitted from power cycle, however, because of the photosynthesis of biomass there is a zero net emission of CO<sub>2</sub>.

## Prediction of Deactivation Rates and Mechanisms of Reforming Catalysts

Aaron L. Wagner, R. Scott Osborne, Jon P. Wagner

1600 W. Hill St., Louisville, KY 40210

### Introduction

As fuel cells near commercialization for industrial and residential applications, failure of the fuel processing system becomes less and less tolerable. Fuel cell system manufacturers must deliver reliable performance of both the stack and reformer for several years without significant change-out of components. One key to guaranteeing lifetime performance of the fuel processor is an accurate prediction of the deactivation of the catalytic components of the processor.

The conversion of hydrocarbons to high quality hydrogen as a feed for PEM fuel cells typically utilizes a series of reactions. These reactions include desulfurization of the hydrocarbon followed by reforming to syngas and then the CO cleanup reactions of water-gas shift and partial oxidation or partial methanation. The competing methods for converting hydrocarbons to a hydrogen rich syngas include steam reforming (SR), catalytic partial oxidation (CPOX) and autothermal reforming (ATR). Steam reforming has a high efficiency but heat transfer and mass transfer present non-trivial challenges and can significantly limit catalyst performance. CPOX generates excess heat and therefore does not require external heat input but produces a reformat with lower hydrogen content and typically exhibits higher operating temperatures. Many fuel processor developers favor ATR due to the balance of efficiency to produce hydrogen and the self-sustaining nature of the reaction at moderate temperatures.

### Steam Reforming Catalysts

Traditional tubular nickel steam reforming catalysts have a typical lifetime of 3 to 5 years when employed for large-scale hydrogen production (1,000,000scf/day). Primary steam reforming catalysts contain 10-20% Ni supported on  $\alpha$ - $\text{Al}_2\text{O}_3$ , calcium aluminate, or Magnesium aluminate. Typically, natural gas steam reformers are operated with exit temperatures from 800°C to 870°C (but tube wall temperatures can range from 700°C up to a maximum hot spot of 920°C) at S:C ratios from 2.5 to 4.0 and at a GHSV on the order of 2,000/hr.

Catalyst failure is due to either coke formation, the presence of fouling agents such as sulfur, chlorine, or iron, or can be the result of physical breakdown due to thermal cycling and/or poor initial physical integrity. Deactivation manifests itself by an increase in tube wall temperature or an increase in pressure drop.

**Determination of Coke Resistance.** Since standard reforming catalysts require several months to form carbonaceous deposits under standard operating conditions, a test was designed to accelerate the coke formation reaction. Coke is usually formed when the rate of carbon deposit caused by cracking is greater than the rate of oxidation or hydrogenation. This coke grows in needle like formations underneath the active nickel sites on the catalyst.

The accelerated test consists of performing steam reforming of *n*-hexane on 300cc of 12 x 16 mesh sized catalyst particulates. The test is conducted at ~3,000/hr at an initial S:C of 6. After 24hrs on stream, the S:C ratio is lowered. The test is run until an increase in  $\Delta P$  is observed between the inlet and outlet of the reactor. The increase in pressure is a result of carbon formation on the catalyst and will occur quite rapidly when conditions are conducive to coke formation. This test is useful for determining relative coking resistance between catalysts. Data from this test is used in

conjunction with field data to predict operating lifetimes. As an example, in **Figure 1** an experiment was carried out at a S:C ratio of 3. A Ni/ $\alpha$ - $\text{Al}_2\text{O}_3$  catalyst shows immediate pressure increase whereas a Ni/-Ca aluminate promoted with potassium can operate for hundreds of hours. Decreasing the S:C ratio to 1.6 was necessary to facilitate coking of the catalyst and thereby an increase in pressure.

The acidity of a steam reforming catalyst is proportional to its propensity to form coke. By utilizing a more basic support such as calcium aluminate and by promoting with the basic K, the coking resistance of tubular steam reforming catalysts has been greatly increased. The laboratory results have been confirmed by field operation.

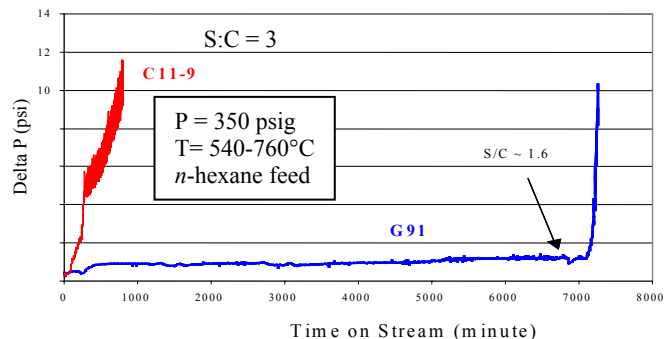


**Figure 1.** Change in pressure across commercial Ni /  $\alpha\text{Al}_2\text{O}_3$  (C11-9) and Ni/Calcium Aluminate + K (G91) catalysts as a function of time on stream.

**The Effect of Sulfur.** Nickel catalysts are susceptible to poisoning by sulfur by the formation of nickel sulfide on the surface of the catalyst. Sulfur by itself will not cause a catastrophic failure of the reformer, but will decrease activity of the catalyst to the point that methane conversion is no longer at acceptable levels. Due to the drop in steam reforming activity, tube wall temperatures can increase to non-optimal levels. In addition, the suppression of the reforming reaction can increase the propensity to form carbon leading to pressure drop build-up.

Sulfur poisoning can also cause coke formation necessitating more frequent coke removal steps such as steaming.

**Hydrothermal Effects on the Catalyst.** As Ni/-Alumina type catalysts operate at high temperatures and in the presence of steam, nickel aluminate spinel may form on the catalyst. This inactive phase is evidenced by either discoloration of the catalyst from dark gray to light green or can be seen by XRD. Nickel spinel can be difficult to reduce resulting in decreased catalyst performance. The spinel can also add to the loss of physical integrity of the catalyst increasing the attrition of the catalyst as evidenced by increased  $\Delta P$  across the bed.

A test was designed to show differences between catalysts in the presence of steam at elevated temperatures. Initial methane conversion activity was measured on a series of catalysts. The catalysts were then exposed to 100% steam for 16hrs at 870°C. Activity measurements are repeated after this treatment. Deactivation of catalysts following the steam treatment was easily explained by Ni spinel formation as detected and quantified by XRD.

### Autothermal Reforming Catalysts

There are several differences between Autothermal reforming catalysts and traditional steam reforming catalysts. As a rule, ATR

catalyst must possess higher activity, stability in both oxidizing and reducing atmospheres and be supported on high geometric surface area substrates with minimal pressure drop. Sulfur tolerance and coking resistance are as essential to ATR catalysts as they are to steam reforming catalysts but since ATR catalysts are typically precious metal based, sulfur tolerance is even more crucial.

**Stable substrates.** The most effective ATR catalysts contain Rh supported on a stabilized alumina washcoat. The catalyst is typically washcoated on either a high cell density cordierite or metal monolith or reticulated ceramic or metal foam structures. A main constituent of cordierite is silica that has a propensity to migrate under high steam conditions at elevated temperatures. The migration of silica could be disastrous to down stream catalysts and should be avoided at all costs. In order to examine whether silica migrates from cordierite making the support unsuitable for ATR applications, monoliths coated with ATR catalysts were operated under ATR conditions for several thousand hours.<sup>1</sup> SEM images were made and EDAX elemental mapping conducted across the channels of the monolith (Figure 2). Silica was present in the areas where the cordierite substrate was found but no evidence of silica was found in the catalytic layers. Based upon this evidence, cordierite appears to be acceptable for ATR applications and is usually the substrate of choice based on the wide availability and reasonable cost.

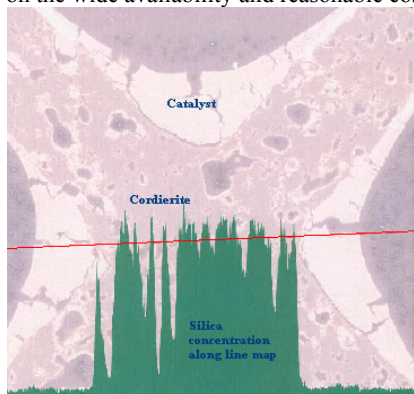


**Figure 2.** EDAX line map of silica concentration from Rh ATR catalyst to cordierite support.

**The ATR testing apparatus.** Autothermal reforming experiments are performed in a triple heated zone reactor with a separate pre-reactor vaporization vessel. Monolithic catalysts are wrapped in ceramic gauze and placed into the bottom zone of the furnace with the upper two zones used for mixing. After condensing excess water from the reactor outlet, gas flow-rates are measured with an American Meter Company<sup>®</sup> wet test meter and gas composition is determined by a Varian<sup>®</sup> CP2003 micro gas chromatograph with separations carried out in both molecular sieve and PPQ columns. Test unit gas and temperature control is handled by a Camile<sup>®</sup> PC based control system.

**Designing an accelerated aging test.** Typically, ATR reactors will operate at a gas hourly space velocity of  $\geq 100,000$ /hr at a S:C ratios from 2 to 3 and O:C ratios from 0.7 to 1.0. The goal is to design a test that will elucidate differences between catalysts that would not manifest themselves until thousands of hours on stream are achieved. To accelerate deactivation, it was found that operation at elevated O:C ratios or decreased S:C ratios was necessary. It is possible to show differences between relatively stable catalysts under these conditions. Increasing pressure or steam does not have the same effect as it does for Ni steam reforming catalyst. Increased S:C has the effect of increasing the maximum operating temperature for

the catalyst thereby increasing the rate of surface area loss due to sintering. Increased O:C appears to effect the nature of the active Rh sites more than the stabilized alumina support. Figure 3 is an example of various reactions conditions on the deactivation rate of a Rh/ stabilized alumina catalyst.

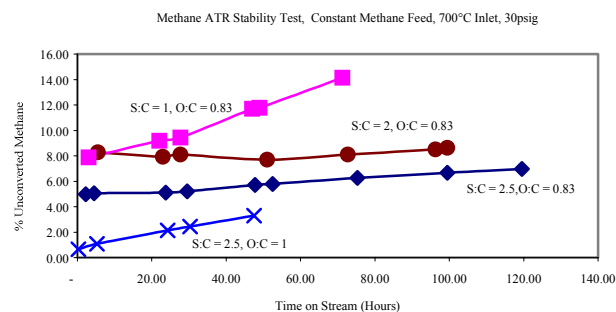


**Figure 3.** Unconverted methane as a function of time on stream for various reaction conditions.

**Deactivation mechanisms.** There are three main deactivation mechanisms that are assumed to be involved for Rh-Alumina based ATR catalysts. The first is sulfur poisoning. Due to the complexities in testing for sulfur tolerance, this issue will be addressed in future papers. The second deactivation mechanism is the loss of surface area by the support and the resulting decrease in Rh dispersion. Simple BET surface area measurements can offer evidence of this mechanism but the traditional air calcinations may not be adequate to sinter stabilized alumina supports. The presence of steam and reducing atmospheres is often necessary to reveal differences in surface area stability but may still not account for catalyst deactivation. In particular, catalysts that were tested for several hundred hours that showed ATR deactivation did not show significant decreases in surface area. As a result, the observations of Wong and McCabe<sup>2</sup> appear to be the most relevant to catalyst deactivation. They found that oxidation of Rh / alumina catalysts caused most of the Rh to diffuse into the bulk and resulted in a large decrease in CO oxidation activity. As a result, modifications to both the alumina as well as the addition of promoters and stabilizers to the Rh increase the stability of ATR catalysts.

## Conclusions

Traditional steam reforming catalysts deactivate due to poisoning by sulfur, formation of Ni spinel and coke formation on the catalyst. Several tests have been designed to simulate these poisoning events in an effort to accelerate the deactivation of these catalysts. These accelerated deactivation tests have proven useful in the improvement of Ni steam reforming catalysts. For ATR and CPOX catalysts, surface area stability and the anchoring of precious metals such as Rh is of utmost importance for the stability of catalysts. Tests have been designed to accelerate these deactivation mechanisms in an effort to both compare catalyst formulations as well as to predict activity over 40,000 hour lifetimes.

**Acknowledgement.** We would like to acknowledge the contributions of Paul Steppe, Steve Spivey, Don Tackett, Wolfgang Gabriel, Dr. Yeping Cai and Dr. Jason Zhao to this work.

## References

- (1) Flytzani-Stephanopoulos, M.; Voecks, G.E. *Conversion of Hydrocarbons for Fuel-Cell Applications*. **1981**, JPL Publication 82-37, DOE/ET-11326, p. 77.
- (2) Wong, C. and McCabe, R.W. *J of Catal* **1989**, 119, pp. 47-64.

## Sulfur Resistance of Rh/CeO<sub>2</sub>-Al<sub>2</sub>O<sub>3</sub> Catalysts During Steam Reforming of Jet Fuels at Low Temperature

Jian Zheng, James Jon Strohm, Chunshan Song\*, Xiaoliang Ma, Lu Sun

Clean Fuels and Catalysis Program, The Energy Institute, and Department of Energy & Geo-Environmental Engineering, Pennsylvania State University, 209 Academic Projects Building, University Park, PA 16802

\*Email: csong@psu.edu; Tel: 814-863-4466; Fax: 814-865-3248

### Introduction

Fuel cell has been identified as a potential device for portable power supply because it is convenient, quiet and energy efficient. The choice of liquid fuels such as jet fuel and diesel fuel as logistic fuels is an important consideration for portable fuel cells, because they are widely available and have lower volume and higher energy density. The challenges and opportunities on fuel processing for fuel cell applications have been discussed in a recent review<sup>1</sup>.

One of the main problems in developing fuel pre-processor for micro-fuel cell application using liquid hydrocarbon fuels such as JP-8 jet fuel is how to eliminate the carbon formation from higher hydrocarbons during reforming. Our approach<sup>2, 3</sup> to solving this problem is to conduct catalytic fuel reformation in two stages with a pre-reformer (at temperature around 450-550°C) to break-down most C<sub>8</sub>-C<sub>13</sub> hydrocarbons to C<sub>1</sub> to C<sub>2</sub> molecules plus CO and H<sub>2</sub>, followed by steam reforming (at temperature of around 800°C) in main reformer to produce final reformates (H<sub>2</sub>, CO, CO<sub>2</sub>). A 2wt% Rh supported CeO<sub>2</sub>-promoted  $\gamma$ -Al<sub>2</sub>O<sub>3</sub> catalyst with thorough removal of impurity Cl has been found to exhibit stabilized excellent activity for the steam reforming of various sulfur-clean model jet fuels at 514°C<sup>2</sup>.

Most of the original liquid hydrocarbon fuels contain certain amount of sulfur (ranging from several wppm to over a thousand wppm), which is a severe poison for steam reforming catalysts because sulfur compounds are strongly chemisorbed on metal surface<sup>4, 5</sup>. The development of sulfur-resistant reforming catalysts for fuel processor is therefore another important yet challenging task.

In order to improve the sulfur-resistance of metal supported catalysts, one must have a fundamental understanding of how sulfur interacts with the metal surfaces. Tremendous work has been done in the literature on studies of sulfur chemisorption on metal surfaces<sup>4-10</sup>. Ni or noble metal supported catalysts for both steam reforming at low temperature (such as pre-reforming at around 500°C)<sup>11-15</sup> and oxygen-assisted reforming at high temperature (such as autothermal reforming and partial oxidation at around 800°C)<sup>16-23</sup> have been reported to show certain levels of sulfur-resistance.

The adsorption equilibrium of sulfur compounds (typically H<sub>2</sub>S) depends on mainly temperature besides factors such as the composition of gas phase (such as P<sub>H<sub>2</sub>S</sub>/P<sub>H<sub>2</sub></sub> and P<sub>H<sub>2</sub>O</sub>/P<sub>H<sub>2</sub></sub> etc)<sup>4</sup>. In general, the sulfur adsorption on metal such as Ni decreases with increasing temperature (between 500°C-850°C)<sup>4</sup>. As a consequence, higher sulfur-resistance has been reported for autothermal reforming at high temperature than that for low temperature reforming.

The present paper reports on our preliminary work on the sulfur-poisoning of noble metal supported CeO<sub>2</sub>-Al<sub>2</sub>O<sub>3</sub> catalysts for the steam reforming of sulfur-containing model jet fuel (NORPAR-13) at both low and high temperature. A bimetallic Rh-Ni/CeO<sub>2</sub>-Al<sub>2</sub>O<sub>3</sub> catalyst has been found to show excellent sulfur-resistance even at low temperature.

### Experimental

CeO<sub>2</sub>-Al<sub>2</sub>O<sub>3</sub> (containing 20wt% CeO<sub>2</sub>) support was prepared by wet impregnation of  $\gamma$ -Al<sub>2</sub>O<sub>3</sub> (UOP LaRoche VGL-15) with Ce(NO<sub>3</sub>)<sub>3</sub>·6H<sub>2</sub>O (Aldrich) followed by calcinations at 800°C in air for 3 hours.

RhCl<sub>2</sub> (Aldrich) has been supported on both  $\gamma$ -Al<sub>2</sub>O<sub>3</sub> and CeO<sub>2</sub>·Al<sub>2</sub>O<sub>3</sub> by wet impregnation, with nominal metal content of 2wt%. In both cases, the obtained RhCl<sub>2</sub> supported material was soaked into NH<sub>4</sub>OH solution for several hours, followed by filtration and calcinations to remove NH<sub>3</sub>, Cl<sup>-</sup>, and other impurities.

**Jet fuel formulation.** A readily available NORPAR-13 (consisting mainly normal paraffin, with average carbon number of 13) has been chosen as an important type of jet fuel. Since there is no much sulfur in NORPAR-13 (the sulfur content of NORPAR-13 is 4 wppm as analyzed by us using Antek 9000ES total sulfur analyzer), it can actually be regarded as a near sulfur-free clean jet fuel that can be utilized in large amount and directly for steam reforming in fuel processor for fuel cell application.

**Reaction system.** A catalyst (1.0 gram with particle size of 18-35 mesh) is placed into the middle of stainless steel reactor tube (Inconel 800H alloy, with 0.54" O.D. X 0.375" I.D. and 24" long), with the remaining tube filled with  $\gamma$ -Al<sub>2</sub>O<sub>3</sub> beads. Before introducing the fuel, the catalyst is heated up to a certain temperature (500°C) under the hydrogen flow of 20 ml/min, which is controlled by the mass flow controller system, and kept at this temperature for several hours. Then the carrier gas is switched to nitrogen. At the same time, the pre-heater is turned up to certain temperature high enough for vaporizing of the fuel (C<sub>13</sub>H<sub>28</sub>, b.p. 234°C) and water before entering the reactor.

To start the test, water was first introduced for 30 minutes before opening the fuel flow to ensure that there is always steam accompanying fuel flow in the reactor lines. The fuel is then introduced with one of the two HPLC pumps through the pre-heater into the reactor with a volumetric flow rate of 1.38 ml/hr. The water flow is kept at 4.02 ml/hr with a steam to carbon ratio of 3:1.

During the reaction, the liquid products are collected every hour by a liquid condenser with volume measured for the calculation of total conversion; the gas products are analyzed on-line by a multi-gas analyzer GC-TCD for the calculation of product distributions.

### Results and Discussion

In general, higher temperature will result in higher conversion of the fuels, since the steam reforming alone is endothermic. However, there is also a risk for carbon formation. In order to prevent carbon formation, the pre-reforming temperature should be around 500°C<sup>2, 24</sup>.

Previously, we have screened various noble metal supported catalysts for pre-reforming of different model jet fuels, such as dodecane (model jet fuel MJF-1), 20wt% trimethylbenzene containing dodecane (MJF-2), and 10wt% 1,3,5-trimethylbenzene, 5wt% ethylbenzene and 5wt% butylbenzene containing dodecane (MJF-3). A modified noble metal catalyst, 2wt% Rh supported on CeO<sub>2</sub>·Al<sub>2</sub>O<sub>3</sub> followed by soaking in NH<sub>4</sub>OH, has been found to exhibit satisfactory catalytic activity and stability for pre-reforming of these model jet fuels at 514°C for up to 240 hours (accumulated 10 days)<sup>2</sup>. The same catalyst has also been utilized for pre-reforming of NORPAR-13 (containing 4ppm impurity sulfur) and shows good performances<sup>25</sup>.

It is important to know the sulfur resistance of such noble metal supported catalyst for a long-term pre-reforming with certain sulfur content level. We thus added 3-methylbenzo-

thiophen in pure NORPAR-13 to form NORPAR-S1 (15ppm total sulfur) and NORPAR-S2 (33ppm total sulfur).

**Figure 1** shows a 34-hour pre-reforming run of the NORPAR-S2 (33ppm S) at initially 514°C using the same modified catalyst. From **Figure 1** it can be seen that within 11 hours on stream the conversion of NORPAR-S2 (33ppm S) on the modified 2%Rh/CeO<sub>2</sub>•Al<sub>2</sub>O<sub>3</sub> catalyst is very high and close to that of pure NORPAR-13 (4ppm S)<sup>25</sup>. But the activity decreases gradually during 11-22 hours on stream, and dramatically down to only 72% within another 3 hours on stream. Meanwhile, the CH<sub>4</sub> selectivity keeps decreasing throughout the entire experiment.

By increasing the reaction temperature slightly (from 514°C to 535°C), the activity is recovered to some extent, but with further time on stream, it deactivates again. This indicates that sulfur poisoning of the current 2%Rh/CeO<sub>2</sub>•Al<sub>2</sub>O<sub>3</sub> catalyst is very severe even in the presence of 33ppm S.

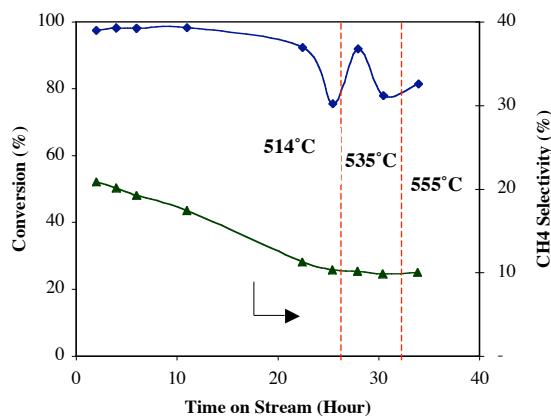


**Figure 1.** Pre-reforming of NORPAR-S2 (33ppm total sulfur) over modified catalyst (2% Rh/CeO<sub>2</sub>•Al<sub>2</sub>O<sub>3</sub>, NH<sub>4</sub>OH treated)

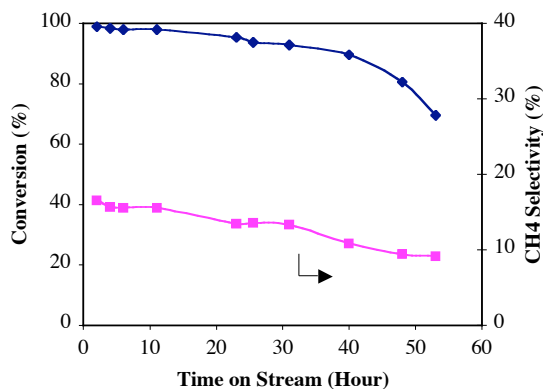


**Figure 2.** Pre-reforming of NORPAR-S1 (15ppm total sulfur) over modified catalyst (2% Rh/CeO<sub>2</sub>•Al<sub>2</sub>O<sub>3</sub>, NH<sub>4</sub>OH treated)

There seems certain critical point in terms of accumulated sulfur to Rh ratio which causes the dramatic poisoning and deactivation of active Rh sites: at around 20th hour on stream, the S/Rh ratio is estimated to be 0.10 as assuming all the sulfur is bond to Rh metal. So the sulfur-poisoning results from **Figure 1**

indicate that when S/Rh ratio reaches around 0.10, the Rh clusters will no longer be as good catalytic active sites for pre-reforming of jet fuel as previously without sulfur poisoning.

In order to verify this, we carry out another long-term pre-reforming run using NORPAR-13 containing lower sulfur level. **Figure 2** shows a 53-hour pre-reforming run of the NORPAR-S1 (15ppm S) at 514°C using the same modified 2%Rh/CeO<sub>2</sub>•Al<sub>2</sub>O<sub>3</sub> catalyst.

From **Figure 2** it can be seen that similarly within 11 hours on stream the conversion of NORPAR-S1 (15ppm S) on the modified 2%Rh/CeO<sub>2</sub>•Al<sub>2</sub>O<sub>3</sub> catalyst is very high and close to that of pure NORPAR-13 (4ppm S)<sup>25</sup>. The activity decreases gradually during 11th-40th hours on stream, with conversion at 23rd hour still around 95.5%. But then it decreased dramatically down to only 70% within another 13 hours on stream (from 40th hour to 53rd hour). There is also certain break-through point at around 40th hour on stream, at which the deactivation rate is suddenly increasing. By calculation, the S/Rh ratio at around 40th hour on stream in this pre-reforming run is also around 0.10. Therefore, it seems true that when S/Rh ratio reaches around 0.10, the Rh clusters will no longer be as good catalytic active sites for pre-reforming of jet fuel as previously without sulfur poisoning. According to Rostrup-Nielsen's pioneering study, sulfur poisoning of a steam reforming catalyst takes place as a shell poisoning due to pore diffusion restrictions and the sulfur coverage in the shell is typically 80-90% at conventional pre-reforming conditions<sup>14</sup>. Our results indicate that most of the shell Rh have been covered by sulfur at S/Rh break-through ratio of 0.1.

**Figure 3** shows the TPO-IR results of the used 2% Rh/CeO<sub>2</sub>•Al<sub>2</sub>O<sub>3</sub> after pre-reforming of pure NORPAR-13, NORPAR-S1 and NORPAR-S2 at the conditions described above for same time-on-stream (10 hours). There are a few peaks shown in the TPO-IR temperature ranges of <400°C, which can be attributed to desorption of CO<sub>2</sub> and combustion of highly amorphous carbon previously adsorbed on the used catalysts<sup>24</sup>. There is almost no peak appearing in the range of 400°C-600°C that is attributed to filament carbon, indicating no significant carbon formation on these catalysts. Furthermore, there is no much difference among the three samples within the error range, showing that the slight increase of sulfur content does not promote carbon formation problem.

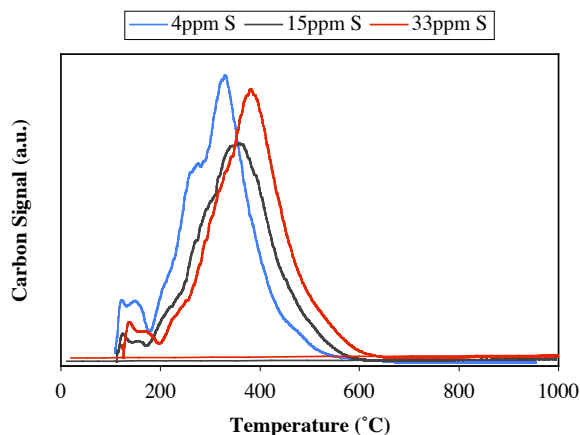


**Figure 3.** TPO-IR results of used 2% Rh/CeO<sub>2</sub>•Al<sub>2</sub>O<sub>3</sub> catalyst after pre-reforming of NORPAR-13, NORPAR-S1 and NORPAR-S2 at 514°C for 10 hours.

By on-line analyzing the product gas mixtures, we do not find H<sub>2</sub>S gas (<1 ppm); meanwhile there is only around 1ppm total sulfur in the remaining liquid products. So it is clear that almost all the sulfur goes to the catalyst and the mechanism for S-poisoning during pre-reforming seems to be purely sulfur bonding on the metal sites.

One way to solve this sulfur-poisoning problem is to carry out oxidative steam reforming at higher temperature (such as 800°C). **Figure 4** shows a 22-hour oxidative reforming test of the NORPAR-S2 jet fuel (with total sulfur of 33ppm) at 800°C using the same 2% Rh/CeO<sub>2</sub>•Al<sub>2</sub>O<sub>3</sub> catalyst that has already undergone the previous 34-hour pre-reforming at 514-555°C (as seen in **Figure 1**).

The conversion is always 100% throughout the entire experiment, which shows that the sulfur poisoning of the Rh metal supported catalyst (in the presence of 33ppm S) is no longer a severe problem itself during oxidative steam reforming at higher temperature. The composition of the products is as follows: H<sub>2</sub> around 63%, CO at 23% and CO<sub>2</sub> around 14%, with no CH<sub>4</sub> remaining.

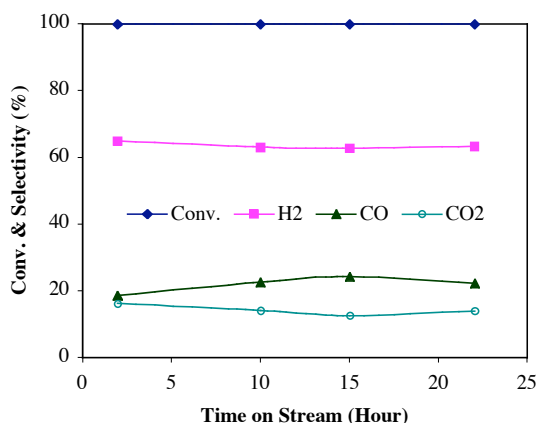


**Figure 4.** Oxidative Steam reforming of NORPAR-S2 (33ppm total sulfur) on modified 2%Rh/CeO<sub>2</sub>•Al<sub>2</sub>O<sub>3</sub> catalyst (S/C=3, O/C=0.8, 800°C, atm).

However, as measuring on-line the H<sub>2</sub>S content from the gas products, we do observe around 3ppm H<sub>2</sub>S, together with large amount of H<sub>2</sub> and CH<sub>4</sub> etc. This indicates that the one-step oxidative reforming of jet fuel, although shows no sign of deactivation by sulfur poisoning, still causes potential problem for the following integrated processes for utilization of fuel cell system, which also shows high sensitivity to sulfur poisoning.

Another disadvantage of the one-step oxidative reforming at high temperature is the much severe carbon formation problem, as seen in the TPO-IR of used catalyst and □-Al<sub>2</sub>O<sub>3</sub> beads around the catalysts in **Figure 5**.

In **Figure 5**, the peak in the range of 400°C-600°C appears slightly in the case of used catalyst but very significantly on Al<sub>2</sub>O<sub>3</sub> beads (noting the different y-axis). Therefore, it is challenging to have good control of reforming system due to the coke formation in not only the catalyst but also the inert material (such as Al<sub>2</sub>O<sub>3</sub> beads in the current case).

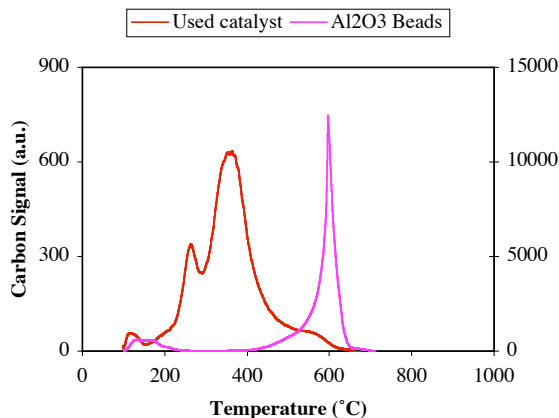


**Figure 5.** TPO-IR results of used 2%Rh/CeO<sub>2</sub>•Al<sub>2</sub>O<sub>3</sub> catalyst after oxidative steam reforming of NORPAR-S2 (containing 33ppm sulfur) at 800°C for 22 hours.

In order to solve the sulfur-poisoning problem of the 2%Rh/CeO<sub>2</sub>•Al<sub>2</sub>O<sub>3</sub> catalyst during pre-reforming, the modify of the catalyst is necessary, such as introducing second metal component that can easily bond with sulfur atom so that the Rh active sites can be protected. Based on this, we prepared a bimetallic Rh-Ni/CeO<sub>2</sub>•Al<sub>2</sub>O<sub>3</sub> catalyst and tested it for pre-reforming of NORPAR-S2 (33ppm sulfur). **Figure 6** shows a 72-hour pre-reforming of the NORPAR-S2 jet fuel using the promoted Rh-Ni/CeO<sub>2</sub>•Al<sub>2</sub>O<sub>3</sub> catalyst under exactly same conditions as in **Figure 1**.

The conversion is almost 100% throughout the entire experiment, only drops to around 98% at the end of the 72-hour run, showing that the promoted bimetallic Rh-Ni/CeO<sub>2</sub>•Al<sub>2</sub>O<sub>3</sub> catalyst has good sulfur resistance during pre-reforming of jet fuels. The composition of the products as follows is constant throughout the test: H<sub>2</sub> around 58.5%, CH<sub>4</sub> at 19.6%, CO<sub>2</sub> around 21.8%, and less than 1% CO. There is no H<sub>2</sub>S (within the detection limit) in the product gas. The excellent sulfur-resistant catalyst therefore provides much more flexibility for fuel cell application.

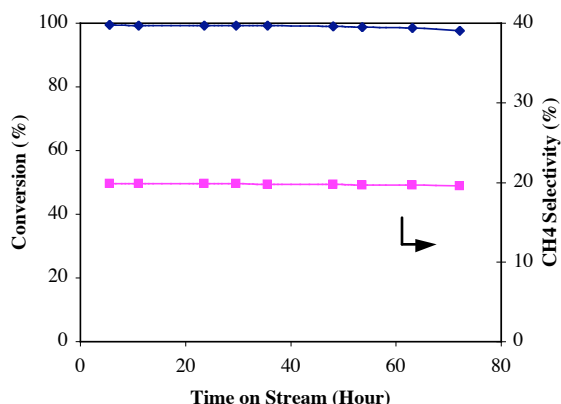


**Figure 6.** Pre-reforming of NORPAR-S2 (33ppm total sulfur) over promoted Rh-Ni/CeO<sub>2</sub>•Al<sub>2</sub>O<sub>3</sub> catalyst at 514°C, atm.

## Conclusions

An active pre-reforming catalyst, the monometallic 2%Rh/CeO<sub>2</sub>•Al<sub>2</sub>O<sub>3</sub>, deactivates by sulfur poisoning during the pre-reforming of sulfur-containing jet fuels. Sulfur tends to bond with Rh metal so strongly that almost no remaining sulfur can be detected in the products, both in the liquids and the gases. A breakthrough point for faster deactivation rate is found at S/Rh coverage around 0.10. An oxidative steam reforming of the sulfur-containing jet fuels over the same monometallic catalyst avoids the sulfur poisoning problem but causes severe carbon formation on even inert Al<sub>2</sub>O<sub>3</sub> beads. A promoted bimetallic Rh-Ni/CeO<sub>2</sub>•Al<sub>2</sub>O<sub>3</sub> catalyst proves to be sulfur-tolerant and shows excellent activity for the pre-reforming of jet fuel containing 33 ppm sulfur.

**Acknowledgement.** We are grateful to the DoD/DARPA Palm Power Program management for supporting this work under sub-contract to Altex Technologies Inc. We also wish to thank Dr. Mehdi Namazian of Altex for helpful discussions on fuel reforming, and UOP for providing LaRoche □-Al<sub>2</sub>O<sub>3</sub> samples. Thanks also go to Mr. Ronald Copenhagen of PSU for help in setting up the reactor system.

## References

- (1) Song, C. *Catal. Today*, **2002**, *77*, 17-49.
- (2) Zheng, J.; Shen, J.P.; Song, C.; Pan, W.; Strohm, J.J. *Prepr. Pap. - Am. Chem. Soc., Div. Fuel Chem.*, **2003**, *48 (1)*, 374-377.
- (3) Zheng, J.; Song, C. *Prepr. Pap. - Am. Chem. Soc., Div. Fuel Chem.*, **2003**, *48 (1)*, 378-381.
- (4) Rostrup-Nielsen, J.R. in *Catalysis, Science and Technology*, Anderson, J.R.; Boudart, M., Eds, **1984**, *Vol. 5*, 1-117.
- (5) Bartholomew, C.H.; Agrawal, P.K. *Adv. Catal.*, **1982**, *31*, 135-242.
- (6) Foord, J.S.; Reynolds, A.E. *Surf. Sci.*, **1985**, *152/153*, 426-433.
- (7) Foord, J.S.; Reynolds, A.E. *Surf. Sci.*, **1985**, *164*, 640-648.
- (8) Rodriguiz, J.A.; Chaturvedi, S.; Jirsak, T. *Chem. Phys. Lett.*, **1998**, *296*, 421-428.
- (9) Rodriguez, J.A.; Hrbek, J. *Acc. Chem. Res.*, **1999**, *32*, 719-728.
- (10) Zolfaghari, A.; Villiard, F.; Chayer, M.; Jerkiewicz, G. *J. Alloys Comp.*, **1997**, *253/254*, 481-487.
- (11) Duprez, D.; Mendez, M.; Little, J. *Appl. Catal.*, **1986**, *27*, 145-160.
- (12) Delahay, G.; Duprez, D. *Appl. Catal.*, **1989**, *53*, 95-105.
- (13) Christiansen, L.J.; Andersen, S.L. *Chem. Eng. Sci.*, **1980**, *35*, 314-321.
- (14) Christensen, T.S. *Appl. Catal. A: Gen.*, **1996**, *138*, 285-309.
- (15) Rostrup-Nielsen, J.R.; Christensen, T.S.; Dybkjaer, I. *Stud. Surf. Sci. Catal.*, **1998**, *113*, 81-95.
- (16) Moon, D.J.; Scekumar, K.; Lee, S.D.; Lee, B.G.; Kim, H.S. *Appl. Catal. A: Gen.*, **2001**, *215*, 1-9.
- (17) Ming, Q.; Healey, T.; Allen, L.; Irving, P. *Catal. Today*, **2002**, *77*, 51-64.
- (18) Kramarz, K.; Bloom, I.D.; Kumar, R.; Ahmed, S.; Wilkenhoener, R.; Krumpelt, M. *US Pat., No. 6,303,098*, **2001**.
- (19) Kopasz, J.P.; Miller, L.E.; Ahmed, S.; Devlin, P.; Pacheco, M. *SAE Technical Paper Series*, **2002**, 2002-01-1885.
- (20) Palm, C.; Cremer, P.; Peters, R.; Stolten, D. *J. Power Sources*, **2002**, *106*, 231-237.
- (21) O'Connor, R.P.; Klein, E.J.; Schmidt, L.D. *Catal. Lett.*, **2000**, *70*, 99-107.
- (22) Kruppenacher, J.J.; West, K.N.; Schmidt, L.D. *J. Catal.*, in press.
- (23) Cable, T.L.; Brakas, A.B.; Ruhl, R.C.; Milliken, C.E. *US Pat., No. 6,238,816*, **2001**.
- (24) Strohm, J.J.; Zheng, J.; Song, C. *Prepr. Pap. - Am. Chem. Soc., Div. Fuel Chem.*, **2003**, *48 (2)*, to be accepted.
- (25) Zheng, J.; Strohm, J.J.; Song, C. *Prepr. Pap. - Am. Chem. Soc., Div. Fuel Chem.*, **2003**, *48 (2)*, to be accepted.

# Novel CeO<sub>2</sub> supported Ni-Rh bimetallic catalysts for reforming of bio-ethanol to produce hydrogen for fuel cells

Junichiro Kugai, S. Velu, Chunshan Song\*

Clean Fuels and Catalysis Program, The Energy Institute, and  
Department of Energy and Geo-Environmental Engineering  
The Pennsylvania State University  
209 Academic Projects Building, University Park, PA 16802.  
\*E-mail: csong@psu.edu

## Introduction

Recently, there is a growing interest worldwide in the development of fuel cells for automobiles and stationary power plants because they have the potential to offer unique opportunities for significant reduction in energy use and emissions of environmental pollutants. Polymer electrolyte membrane fuel cell (PEMFC), which operates at low temperature, is considered as promising candidate for automobile applications. However, the PEMFC uses pure H<sub>2</sub> or H<sub>2</sub>-rich gas as a fuel and this needs to be produced on-board a vehicle from a suitable liquid hydrocarbon fuels. Owing to the high energy density and ready availability, methanol and gasoline are considered as preferred fuels, and methods for the catalytic reforming of these fuels to H<sub>2</sub>-rich gas has been reported.<sup>1-4</sup> On the other hand, bio-ethanol, which is a mixture of water and ethanol, produced from fermentation of biomass, is a renewable raw material and could be used as an alternative primary fuel for the on-board production of H<sub>2</sub> for fuel cells. Some of the advantages of using bio-ethanol to produce H<sub>2</sub> for fuel cell applications are; (i) Bio-ethanol is a renewable raw material and can be cheaply obtained from sugarcane, corn or cellulose feedstock such as wood chips. (ii) The process is CO<sub>2</sub> neutral as the CO<sub>2</sub> produced in the reforming reaction can be consumed for the biomass growth. The system therefore offers a closed carbon loop. (iii) Unlike methanol, the bio-ethanol is non-toxic, and (iv) Unlike gasoline, the bio-ethanol is sulfur-free, and this avoids the risk of sulfur poisoning on the reforming and fuel cell electrode catalysts.

Unlike methanol reforming, the catalytic methodology for ethanol reforming is not well developed, and more efficient and highly active catalysts are needed. Steam reforming of ethanol has been reported to occur relatively at high temperature, around 700°C. In lower temperature, the reaction produces a wide range of liquid and gaseous products, including H<sub>2</sub>, CO, CO<sub>2</sub>, CH<sub>4</sub>, CH<sub>3</sub>CHO, CH<sub>3</sub>COOH, C<sub>2</sub>H<sub>5</sub>OC<sub>2</sub>H<sub>5</sub>, ethylene depending on the nature of metal and support.<sup>5-7</sup> Oxidative steam reforming of ethanol has also been reported to be more efficient for the low temperature reforming of ethanol for H<sub>2</sub> production.<sup>8</sup>

The objective of the present study was to develop a novel highly efficient catalyst system for the on-board reforming of bio-ethanol to produce fuel cell grade H<sub>2</sub> gas at relatively lower temperature. A detailed literature review reveals that C—C bond cleavage is an important step in the reforming of ethanol to produce H<sub>2</sub> and carbon oxides<sup>5-8</sup>. Both Ni and Rh are known to favor the C—C bond rupture effectively.<sup>9</sup> In addition, since Ni has hydrogenation ability, it is expected to combine chemisorbed hydrogen to form H<sub>2</sub> gas. Thus, a series of Ni-Rh bimetallic catalysts with different Ni/Rh atomic ratios have been synthesized. The nature of support also plays an important role in the ethanol reforming. Acidic and basic supports are known to favor dehydrogenation / dehydration and condensation reactions. Hence, in the present study, redox supports such as CeO<sub>2</sub>, ZrO<sub>2</sub> and CeO<sub>2</sub>-ZrO<sub>2</sub> mixed oxides having high surface area, above 100 m<sup>2</sup> g<sup>-1</sup> have been chosen. The effect of combination of Rh and Ni, and the nature of support on the catalytic performance in the

steam reforming and oxidative steam reforming of ethanol are studied over these catalysts for the first time.

## Experimental

In order to optimize the Ni/Rh atomic ratio for the better catalytic performance in the ethanol reforming, commercially available high surface area CeO<sub>2</sub> (BET surface area = 148 m<sup>2</sup> g<sup>-1</sup>) obtained from Rhodia Co. Three catalysts, 10wt%Ni/CeO<sub>2</sub>, 2wt%Rh/CeO<sub>2</sub>, and 2wt%Rh-10wt%Ni/CeO<sub>2</sub> were prepared by the incipient wetness impregnation method. The catalysts were calcined at 450°C for 3 h in air, palletized, crushed and sieved to 18-35 mesh. About 0.5g of catalyst was loaded in the reactor. Steam reforming of ethanol was performed in a fixed bed stainless-steel down-flow reactor. A premixed ethanol-water mixture with a water/ethanol molar ratio of 4 was fed into the reactor through a vaporizer and the mixed with Ar carrier gas. Prior to the catalytic reaction, the catalysts were reduced in-situ in a H<sub>2</sub> flow (10% H<sub>2</sub> in Ar). Effluent of the reaction was analyzed using an on-line GC equipped with a sampling loop injector, 30 feet Haysep DB packed column, and a TCD detector.

## Results and Discussion

Steam reforming of ethanol has been performed at 335 and 395°C over Rh-Ni/CeO<sub>2</sub> catalysts synthesized in the present study. Fig. 1 compares the conversion of ethanol in the steam reforming over these catalysts at 335 and 395°C. It can be seen that at 335°C, the Rh-Ni/CeO<sub>2</sub> catalyst exhibited slightly higher activity than Rh/CeO<sub>2</sub> catalyst. The Ni/CeO<sub>2</sub> catalyst is much less active compared to other two catalysts. On the other hand, all catalysts exhibited almost complete conversion, close to 100 %, at 395°C. These results indicate that Rh is more active than Ni in the low temperature range though Ni becomes as active as Rh in the high temperature range. The high activity of Rh can be attributed to the ease of C—C bond cleavage of ethanol on Rh metal surface<sup>9</sup>. The support CeO<sub>2</sub> exhibits very poor performance under the present experimental conditions, indicating that the metals supported on the CeO<sub>2</sub> display active sites for the ethanol reforming.

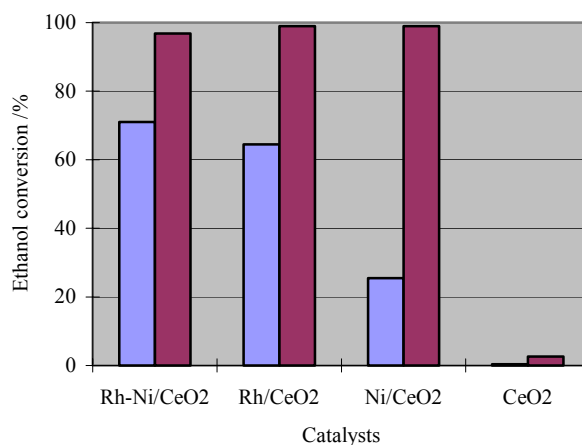


**Figure 1** Comparison of ethanol conversion at 335 and 395°C over CeO<sub>2</sub>-based Bimetallic catalysts. Left bar; 335°C and right bar; 395°C

H<sub>2</sub>, CO, CO<sub>2</sub>, CH<sub>4</sub>, and acetaldehyde are the major products obtained in the steam reforming of ethanol in the present study. The selectivities of H<sub>2</sub> and carbon containing products at 335°C and 395°C are shown in the Table 1. Hydrogen selectivity was indicated

by molar ratio of produced hydrogen in all the products. Carbon selectivity was indicated by molar ratio of carbon included in each carbon-containing products to carbon included in all carbon-containing products. From the table, it can be seen that H<sub>2</sub>, CO, CO<sub>2</sub>, CH<sub>4</sub> are main products and acetaldehyde is only produced at 335 °C, which is insufficient temperature for complete C—C bond cleavage. Acetaldehyde can be considered to be an intermediate in the steam reforming of ethanol.<sup>5-8</sup> Higher selectivity of H<sub>2</sub> has been observed Rh/CeO<sub>2</sub> catalyst despite the highest ethanol conversion obtained over Rh-Ni/CeO<sub>2</sub>.

**Table 1 Product selectivity of ethanol reforming at 335 and 395 °C unit: %**

Catalyst Temp.	H <sub>2</sub>	CO	CO <sub>2</sub>	CH <sub>4</sub>	acetaldehyde	acetone	
Rh-Ni	335	33.4	21.8	34.6	30.4	13.3	0
	395	34.5	8.6	55.0	33.5	2.9	0
Rh	335	35.4	46.9	14.6	30.8	7.7	0
	395	38.8	8.2	62.3	29.5	0	0
Ni	335	29.1	14.0	40.8	6.1	23.5	10.8
	395	29.7	4.9	56.0	39.0	0	0

At 335 °C, the selectivity for CO<sub>2</sub> decreases in the order, Ni/CeO<sub>2</sub> > Rh-Ni/CeO<sub>2</sub> > Rh/CeO<sub>2</sub>. When taking the ratio of CO<sub>2</sub> selectivity to CO selectivity into account, it is clear that the presence of Ni causes the reaction of CO to CO<sub>2</sub>. At 395 °C, CO<sub>2</sub> selectivity over all three catalysts increases and becomes closer to each other. This means under the present experimental conditions, water-gas shift reaction also takes place over these catalysts. It should be that Ni has higher water-gas shift reactivity than Rh at 335 °C, but Rh also exhibits as high water-gas shift reactivity as Ni at 395 °C. Diagne et al.<sup>10</sup> reported that Rh/CeO<sub>2</sub>-ZrO<sub>2</sub> catalyst has much higher CO<sub>2</sub>/CO ratio than Rh/CeO<sub>2</sub> and Rh/ZrO<sub>2</sub> in the selectivity of ethanol steam reforming reaction. Therefore it is anticipated that using CeO<sub>2</sub>-ZrO<sub>2</sub> support with Rh and Ni metals leads to further increase in CO<sub>2</sub>/CO ratio.

Suppressing methane production is one of the interests of this work. Ni was added to promote the combination of atomic hydrogen species on the metal surface into molecular hydrogen. But Ni functioned as a promoter for water-gas shift reaction and hydrogenation of surface CH<sub>x</sub> species rather than a promoter for dehydrogenation of surface hydrogen. It is reported that ethanol is dehydrogenated to adsorbed acetaldehyde species, then further dehydrogenated to H<sub>2</sub>, CO, and CH<sub>x</sub>(x=2,3) on Ni surface<sup>11</sup>. Therefore CH<sub>x</sub> species is considered to be hydrogenated easily to produce methane in the presence of molecular or adsorbed hydrogen and more methane is produced on Ni surface. On Rh surface, on the other hand, ethanol is dehydrogenated into oxametallacycle species, which is readily decomposed to H<sub>2</sub>, CO, CH<sub>x</sub>(x≤2) and suppress the production of methane<sup>12</sup>. Some amount of ethanol is converted via acetaldehyde intermediate according to the fact that acetaldehyde was observed on Rh/CeO<sub>2</sub> catalyst in low temperature in our work. This might be a cause of a lot of methane production even on Rh-containing catalysts.

## Conclusions

The steam reforming of ethanol on Rh-Ni/CeO<sub>2</sub> bimetallic catalyst exhibited high ethanol conversion and CO<sub>2</sub> selectivity. It is concluded that Ni has higher water-gas shift activity than Rh. However its hydrogen selectivity was slightly lower than Rh/CeO<sub>2</sub> catalyst.

## Acknowledgement

This work was supported by Nippon Shokubai Co., Ltd. and by the Pennsylvania State University.

## References

- (1) Song, C. *Catal.Today*, **2002**, 77, 17.
- (2) Velu, S.; Suzuki, K.; Okazaki, M.; Kapoor, M.P.; Osakai, T.; Ohashi, F. *J.Catal.* **2000**, 194, 373.
- (3) Ming, Q.M.; Healey, T.; Allen, L.; Irving, P. *Catal.Today*, **2002**, 77, 51.
- (4) Moon, D.J.; Sreekumar, K.; Lee, S.D.; Lee, B.G.; Kim, H.S. *Appl.Catal. A General*, **2001**, 215, 1.
- (5) Marino, F.; Boveri, M.; Baronetti, G.; Laborde, M. *Int. J. Hydrogen Energy*, **2001**, 26, 665.
- (6) Breen, J. P., Burch, R., Coleman, H. M., *Appl. Catal. B Environmental*, **2002**, 39, 65.
- (7) Fierro, V.; Akdim, O.; Mirodatos, C.; *Green Chemistry*, **2003**, 5, 20.
- (8) Velu, S., Satoh, N., Gopinath, C. S., Suzuki, K., *Catal. Lett.*, **2002**, 82, 145.
- (9) Sheng, P.-Y.; Yee, A.; Bowmaker, G.A.; Idriss, H. *J.Catal.* **2002**, 208, 393.
- (10) Diagne, C., Idriss, H., Kiennemann, A., *Catal. Commun.*, **2002**, 3, 565.
- (11) Takezawa, N., Iwasa, N., *Catal. Today*, **1997**, 36, 45.
- (12) Brown, N. F., Barteau, M. A., *Langmuir*, **1992**, 8, 862.

## GOLD BASED CORE-SHELL NANOPARTICLES AS FUEL CELL CATALYSTS

Mathew M. Maye, Jin Luo, Sandy Chen, Wai-Ben Chan,  
H. Richard Nasland, Chuan-Jian Zhong\*

Department of Chemistry, State University of New York at  
Binghamton, Binghamton, NY 13902. \* cjzhong@binghamton.edu

The ability to control the size of gold materials in the range of a few nanometers is important for the exploration of the unique catalytic properties of gold [1,2]. This presentation describes an investigation of the preparation of gold and gold alloy nanoparticles as electrocatalysts in several reactions including methanol oxidation, carbon monoxide oxidation and oxygen reduction. The goal is to explore the potential use of such nanoparticles as fuel cell catalysts. Core-shell type gold nanoparticles of 1-10 nm core size with organic monolayer encapsulation are studied for the preparation of catalysts towards the electroreduction of oxygen and the electrooxidation of carbon monoxide and methanol. The low catalytic activity, poisoning or instability of many existing platinum based metal catalysts are some of the current challenges to the development of fuel cell catalyst technology. It is thus important to develop a fundamental understanding of the correlation between the size, shape, and interparticle spatial properties and the catalytic activities.

We choose to explore monolayer-capped nanoparticles because highly monodispersed nanoparticles with 2-5 nm core sizes ( $\pm 0.3$ - $0.7$  nm) can be easily prepared by a combination of two-phase synthesis and thermal processing protocols [3,4]. We have studied the assembly of these core-shell nanoparticles on high surface area carbon materials to evaluate their catalytic properties. The catalytic activities of the nanostructured catalysts have been studied in both acidic and alkaline electrolytes. Different alloy compositions of gold with other transition metals were varied using synthetic and processing protocols. The loading of catalysts on metal oxides (e.g.,  $\text{TiO}_2$ ) and carbon supporting materials has been systematically investigated. The catalytic activation and fuel cell performance have also been evaluated.

Both electrochemical and thermal approaches have been used to activate the catalysts. For the electrochemically-activated gold nanoparticles assembled on glassy carbon electrodes, which involved the application of a polarization potential to  $\sim +800$  mV, an anodic wave was observed for the oxidation of methanol in alkaline electrolytes, which closely matched the potential for Au oxide formation (Figure 1) (5,6). This observation, along with the anodic current exhibiting a linear increase with methanol concentration, whereas the cathodic wave decreased with methanol concentration, is again supportive of an electrocatalytic mediation mechanism. In electrochemical quartz crystal nanobalance measurements, a mass wave was detected corresponding to this current wave, implying an initial product release followed by formation of surface oxygenated species. The surface of the activated nanocrystals was examined using x-ray photoelectron spectroscopy (XPS) (7), which indicated the effective removal of the capping agents and the formation of surface oxides on gold nanocrystals. In comparison with the electrochemically-activated catalysts, similar results have been observed for thermally activated gold catalysts. XPS analysis of the catalysts has revealed a complete removal of the shell components

and the formation of oxides less than the electrochemical activation (8). Interestingly, the catalytic activity upon activation was also found to be dependant on the nature of the molecular-wire agent used to assemble the nanoparticle catalysts. We are systematically investigating several parameters that can be controlled (i.e., alloy composition, size, calcination, loading, etc.), and develop an in-depth delineation of these parameters with the catalytic activities. The results should provide important insights for the exploration of gold nanoparticles in practical fuel cell catalysis.

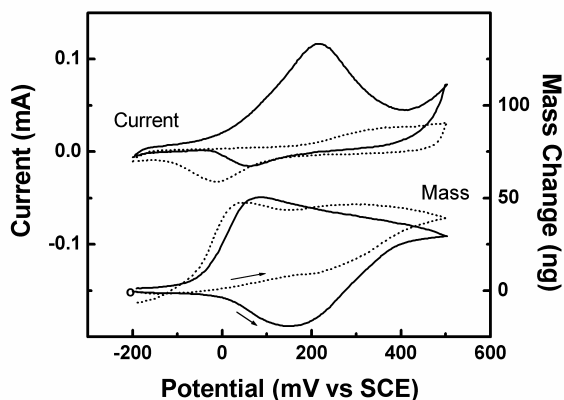


**Figure 1.** Current and mass responses for the electrocatalytic oxidation of methanol at activated NDT-linked  $\text{Au}_{2\text{-nm}}$  on GC electrode in 0.5 M KOH with 3.0 M methanol (solid line) and without (dotted line). (Electrode geometric area:  $0.2 \text{ cm}^2$ ; scan rate:  $50 \text{ mV/s}$ ).

Recently, we have been investigating the catalytic properties of these nanomaterials in several fuel cell reactions. Latest results from electrochemical measurements of catalytic activities, along with XPS, XRD, HRTEM, and FTIR characterizations of structures and morphologies, have revealed that gold-based alloy nanoparticles (1-5 nm) are electrocatalytically active towards MeOH oxidation, CO oxidation, and  $\text{O}_2$  reduction. Using carbon black and  $\text{TiO}_2$  as supporting materials, these nanoparticles have shown high catalytic activity in both acidic and alkaline electrolytes under room temperature. Implications of the results to further refinement of the catalyst preparation in terms of composition and size will be discussed.

### References:

- (1) Haruta, M. *Catal. Today*, **1997**, *36*, 153.
- (2) Valden, M.; Lai, X.; Goodman, D. W. *Science*, **1998**, *281*, 1647.
- (3) Brust, M.; Walker, M.; Bethell, D.; Schiffrin, D. J.; Whyman, R. *J. Chem. Soc., Chem. Comm.* **1994**, 801.
- (4) (a) Maye, M. M.; Zheng, W. X.; Leibowitz, F. L.; Ly, N. K.; Zhong, C. *J. Langmuir*, **2000**, *16*, 490 (b) Maye, M. M.; Zhong, C. *J. Mater. Chem.*, **2000**, *10*, 1895.
- (5) Lou, Y.; Maye, M. M.; Han, L.; Luo, J.; Zhong, C. *J. Chem. Commun.*, **2001**, 473.
- (6) Luo, J.; Maye, M. M.; Lou, Y.; Han, L.; Hepel, M.; Zhong, C. *J. Catal. Today*, **2002**, *77*, 127.
- (7) Maye, M. M.; Luo, J.; Lin, Y.; Engelhard, M. H.; Hepel, M.; Zhong, C. *J. Langmuir*, **2003**, *19*, 125.

## Hydrodesulfurization Studies on SBA-15 Supported CoMo, NiMo Catalysts

G. Murali Dhar\*, Manoj Kumar, K S Rawat, G Muthukumaran, & L D Sharma

Indian Institute of Petroleum, Dehradun – 248005

B. David Raju and K S Rama Rao

Indian Institute of Chemical Technology, Hyderabad – 500 007

### ABSTRACT

Development of fuel cells is receiving increasing attention due to their high efficiency and environmental benefits. There are five types of fuel cells that attracted attention, among which proton exchange membrane fuel cell (PEMFC) is promising prospects. hydrocarbon fuels such as gasoline and diesel and useful fuels for fuel cells provided the sulfur level in fuels is brought down to few ppm. ultradeep desulfurization to bring sulfur to such a low level is a challenging task. Calculations reveal that to bring down sulfur from present level to 500 ppm to 0.1 ppm, seven times more active catalysts are needed. In quest highly active of novel catalysts for this purpose use of novel supports is a very important approach. In this communication hydrodesulfurization studies on SBA-15 supported Mo, CoMo, NiMo catalysts will be discussed with help of TPR, oxygen chemisorption etc characterization studies. The catalysts showed out standing activities for thiophene HDS. A comparison will also be made with HMS mesoporous material supported analogues of the same catalysts of comparable composition and evaluated under identical conditions.

# OPPORTUNITIES AND CHALLENGES FOR FUEL CELLS IN INDIA

*T.S.R. Prasada Rao<sup>1</sup> and Uday T. Turaga<sup>2</sup>*

<sup>1</sup>Sarasijam Technologies, New Delhi 110024, India

<sup>2</sup>Fuel Science Program, Department of Energy and Geo-Environmental Engineering, The Pennsylvania State University, University Park, PA 16802, U.S.A.

## Introduction

Recent U.S. initiatives such as Freedom CAR exemplify a growing commitment to energy conversion using fuel cells because of their efficiency and environmental advantages. The growing feasibility of fuel cells has important implications particularly for developing countries like India. Fuel cells could make available an opportunity to provide clean energy to India's population of one billion and reduce its energy supply-demand gap. Such opportunities, however, are tempered by enormous technical and economic challenges. Technical challenges include identification and development of suitable fuel cell technologies for applications often unique to the developing world. Some of the available fuels might call for modified reforming technologies to produce hydrogen. Economic challenges include the need for more stringent environmental regulations, incentives for cleaner forms of energy, infrastructure development, and a less risk-averse business climate.

## Increased Capacity and Productivity of Energy Conversion and Utilization

The consulting firm, McKinsey and Co., Inc., in a recent study said that India needs economic growth of 10% every year to avoid societal conflict and satisfy the needs and aspirations of a population that is already at one billion and growing. Providing energy required to fuel such economic growth is not a trivial issue of simply producing more petroleum, natural gas, and electricity. Because of constrained resources and new environmental drivers, e.g., the Kyoto Protocol to which India is a signatory, a significant increase in the productivity of energy conversion and utilization is required.

Fuel cells, in principle, could provide that jump in both environmental and economic productivity. For example, from an environmental productivity perspective, it is estimated that a 200 kW fuel cell-based power plant will generate 60% less carbon dioxide than a coal or natural gas fired power plant. Although fuel cells for transportation are an area of intense research in the developed world and have relevance for public transportation in developing countries like India, e.g., buses and railways, this paper will highlight the role of fuel cells for power generation which will most likely be the first commercial application of fuel cells in India.

## Fuel Cells for Power Generation

In 2000, the total electricity generation capacity in India was almost 100,000 MW, the bulk of which came from coal-fired power plants (see Table 1 for a distribution of power generation by fuel-type). On a per capita basis, electricity sold to consumers in India was a paltry 0.3 MWh as compared to 11 MWh in the U.S. Obviously, with development, per capita electricity consumption in India is bound to increase in the future. Although generation capacity has been growing at 5% annually, growth needs to be 15% to meet the target economic growth rate of 10%.

More substantially, there needs to be a drastic improvement in the efficiency or productivity of both electricity generation and transmission and distribution (T&D). Currently, India's productivity

levels are abysmally low at 34 and 4% of those in the U.S. for the generation and T&D of electricity, respectively. While policy reforms will certainly improve these productivity levels substantially, they cannot be expected to account entirely for the growth required in electricity generation.

Fuel cells for power generation have the most near-term potential in three Indian markets. The first of these is the premium power market i.e., segments willing to pay a premium for power supply that is adequate and, more importantly, reliable. Because of shortage (exceeding 11% in 1997) and uncertainty of power supply, several segments of this market, e.g., hotels, hospitals, information technology companies, and certain manufacturing plants, have invested in some form of captive power generation. These segments that already have some form of captive power generation will evolve into niche markets for fuel cells. The Tata Energy Research Institute recently studied this niche markets and found that the key issues are cost and the availability of fuels for either direct use in fuel cells or reforming to produce hydrogen. Some results from this study are presented in Table 2. While some segments of this markets will support capital costs of \$3,000-4,000/kW, extensive penetration will occur only when the costs come down to \$500-1,000/kW.

The second market could comprise remote and rural areas where electricity supply is currently unavailable and difficult because of infrastructure problems. These areas would typically use locally available opportunity fuels such as biomass. It is expected that significant governmental incentives and support would create and sustain this niche market.

The final market comprises large stationary-power generation using fuel cells particularly if technologies using molten carbonate and solid-oxide fuel cells become cost-effective and commercially available. A significant problem with the Indian power industry is T&D losses of the order of 20-25% of total electricity generated, as compared to less than 2% in the U.S. Although effective policy reforms should reduce this number considerably, any continuation of this situation could result in the development of a strong distributed fuel cell-based power generation market.

It is expected that the distributed power generation market will see players besides typical power producers. These new entrants could include fuel supply and transport companies seeking growth through the fuel cell-based power generation. These markets will, however, become real only if the cost of fuel cell-based power decreases from current estimates of \$3,000-5,000/kW to \$800-1,000/kW or less.

## Fuel Processing Issues

The availability of fuels for either direct use or reforming to produce hydrogen will be a critical issue. Hydrogen, natural gas, methanol, gasoline, and diesel are all typical fuels or hydrogen sources for fuel cells. Of these, gasoline and diesel are currently produced in surplus of demand in India. However, consumption rates for both are going to increase substantially in the near future. Further, sulfur specifications for these fuels are much higher than tolerated by reforming catalysts or the fuel cells. The remaining fuels, hydrogen, natural gas, and methanol, are all in short supply. The utilization of these fuels in fuel cells could also be limited because of safety and infrastructure considerations. For example, widespread use of compressed natural gas for public transportation was recently not found viable because of the absence of a pipeline-based distribution network.

Two other fuels, dimethyl ether (DME) and renewable biomass, could become important in the long-term for hydrogen production. Key success factors for a DME scheme are access to cost advantaged gas, proximity to market, and the presence of credible business and technology partners. DME is distinct from liquefied natural gas (LNG) because (1) DME requires cheaper receiving facilities and (2) a competitively priced fuel on a much smaller scale can be delivered.

In the late 1990s, one of this paper's authors conceptualized and spearheaded the DME Project Consortium which included British Petroleum, Indian Oil Corporation (India's largest publicly-owned oil company), Gas Authority of India (India's largest natural gas company), and the Indian Institute of Petroleum (India's premier downstream petroleum research and development organization). The project was initially established to promote DME as a clean alternative to diesel fuel. Rapid changes in market economics, however, changed the project's focus into positioning DME as a fuel for power generation. Briefly, the plan was to produce DME directly from methanol using Haldor Topsoe's proprietary technology (licensed to BP). DME from such a plant, ideally located in the Middle East, would be shipped to India via tanker and sold to power generators to produce clean electricity. Economic feasibility studies had suggested a viable rate of return for such a project. Although the project has been shelved, it remains an interesting and viable proposal.

Sixty percent of India's labor is employed in agriculture which is the cornerstone of the country's economy. Agriculture-derived biomass is a renewable feedstock that is underutilized for generating energy. Recently, several initiatives have been taken to exploit the use of agricultural biomass for power generation. There is strong governmental support for these initiatives and technologies utilizing renewable feedstocks for hydrogen production, e.g., hydrogen production using carbohydrates, should be advantageous for the fuel cells market.

### Conclusions

Several economic and environmental drivers are motivating developing countries like India to evaluate fuel cells. The development of new fuel cell technology that is cost-effective, suited to local needs, and employs region-specific and opportunity fuels should be commercially successful. This paper has highlighted the Indian situation with respect to the need for fuel cells, the power generation needs, and identified specific fuel supply strategies to meet any growth in fuel cells.

**Acknowledgements.** The authors are grateful to Uma Parameswaran, Anju Sharma, Manoj Kumar, and Vibhuti Shekhar Mishra of Sci Tech Patent Art Limited, Hyderabad for useful inputs.

**Table 1. Electricity generation in India (1998) and the U.S. (1999) by fuel type.**

Fuel	Percent of electricity generated in India	Percent of electricity generated in U.S.
Coal	71	58
Natural gas	8	9
Oil	1	3
Nuclear	2	20
Hydro	18	10
Total	100	100

**Table 2. A summary of issues concerning representative niche markets for stationary power generation using fuel cells in India.**

Market	Power needs (MW)	Potential fuel cell (FC) types <sup>1</sup>	Potential FC-based electricity	Comments <sup>2</sup>
Hotels	0.5-5.0	PAFC, MCFC, SOFC	Multiple 0.2-0.25 MW units	Natural gas must be available
Chlor-alkali industry	5-45	MCFC, SOFC	Multiple 0.2-0.25 MW units	Hydrogen readily available; balance of plant requires heat
Pulp and paper industry	2-50	MCFC, SOFC	Multiple 0.2-0.25 MW units	Natural gas must be available; balance of plant requires heat
Dairy industry	<5	PEMFC, AFC, PAFC	One or two 10-50 kW units	Biogas reforming technologies for hydrogen will be an advantage
Telecom and IT	<5	PEMFC, AFC, PAFC	One or two 10-50 kW units	Natural gas must be available

<sup>1</sup>PAFC, Phosphoric acid fuel cell; MCFC, Molten carbonate fuel cell; SOFC, Solid oxide fuel cell; PEMFC, Polymer electrolyte membrane fuel cell; AFC, Alkaline fuel cell.

<sup>2</sup>It is trivial to state that cost is an issue common to all markets.

# REFORMING CATALYSTS FOR ON-BOARD FUEL PROCESSING

Theodore Krause, Magali Ferrandon, and Cécile Rossignol

Chemical Engineering Division  
Argonne National Laboratory  
9700 South Cass Ave.  
Argonne, IL 60439

## Introduction

Fuel cell development has seen remarkable progress in the past decade because of an increasing need to improve energy efficiency as well as to address concerns about the environmental consequences of using fossil fuels for the propulsion of vehicles.<sup>1</sup> The lack of an infrastructure for producing and distributing H<sub>2</sub> has led to a research effort to develop on-board fuel processing technology for reforming hydrocarbon fuels to generate H<sub>2</sub>.<sup>2</sup> The primary focus is on reforming gasoline, because a production and distribution infrastructure for gasoline already exists to supply internal combustion engines.<sup>3</sup>

The choice of the reaction process for on-board reforming depends on the operating characteristics (e.g., varying power demand, rapid startup, frequent shutdowns) for transportation applications. Steam reforming results in the highest concentration of H<sub>2</sub> but has heat transfer limitations. Autothermal reforming and partial oxidation may be self-sustaining but result in lower H<sub>2</sub> concentrations due to the N<sub>2</sub> dilution because air, and not pure oxygen, is used. Because steam reforming is heat and mass transfer limited, it does not respond rapidly to changes in the power demand (i.e., "load following"), which would be experienced frequently during a normal driving cycle. When power demand decreases rapidly, the catalyst can overheat, causing sintering, which in turn results in a loss of activity. Autothermal reforming can overcome the load following limitations of steam reforming since the heat required for the endothermic reactions is generated within the catalyst bed, a property that allows for more rapid response to changing power demands and faster startup.<sup>4</sup> The lower operating temperature of catalytic autothermal reforming has several advantages, including less complicated reactor design, wider choice of materials of construction, and lower fuel requirements during startup over the higher operating temperature of partial oxidation or the endothermic steam reforming processes for transportation applications.<sup>5</sup>

To meet the performance targets established by the Department of Energy for on-board fuel processing for transportation applications (i.e., process the feed at a gas hourly space velocity (GHSV) of 200,000 h<sup>-1</sup> with a fuel conversion of >99.9% and a H<sub>2</sub> selectivity of >80% and have a lifetime of 5,000 h) new reforming catalysts will have to be developed that exhibit higher activity and better thermal and mechanical stability than commercial Ni-based steam reforming catalysts.

## Experimental

Three different formulations of the ANL catalyst,<sup>6</sup> Rh, Pt or Rh-Pt dispersed on a gadolinium-doped ceria substrate and coated onto 600 cpi cordierite monoliths, were evaluated for autothermal reforming of a sulfur-free (<450 ppb S) gasoline and a low sulfur (30 ppm S) gasoline, both purchased from Chevron Phillips Chemical Company. These catalysts were tested in a microreactor system consisting of a 0.50-in. diameter stainless steel reactor tube contained in a temperature-programmable furnace. The fuel feed rate was 0.18 mL/min and the air and water feed rates were set so that O<sub>2</sub>:C ratio ranged from 0.45–0.50 and H<sub>2</sub>O:C ratio ranged from 1.6–1.8. The length of the monolith samples was varied so that the gas-hourly space velocity, based on the feed composition, ranged

from 27,000–110,000 h<sup>-1</sup>. A blank-tube experiment was conducted to determine the extent of gas-phase thermal cracking. For these experiments, the furnace was maintained at a constant temperature over the range of 500–800°C and the temperatures at the top and the bottom of the monolith were measured using Omega K-type thermocouples. Samples of the product gas were analyzed for H<sub>2</sub>, CO, CO<sub>2</sub>, and C<sub>1</sub>–C<sub>8</sub> hydrocarbons using either a Hewlett-Packard 5890 Series II gas chromatograph or a Wasson gas chromatograph-mass spectrometer.

## Results and Discussion

The Rh-containing catalysts (Rh and the bimetallic Rh-Pt) were more active than the Pt catalysts, both producing a fuel gas containing >55% H<sub>2</sub> on a N<sub>2</sub>-free, dry basis from the sulfur-free gasoline at a furnace temperature of 700°C, as shown in **Figure 1**. For the two Rh-containing catalysts, the carbon selectivity to CO<sub>x</sub> exceeded 90% and fuel gas contained 3–3.5% hydrocarbon by volume, with CH<sub>4</sub> being the primary hydrocarbon product. The Pt catalyst was less active, producing a fuel gas containing 33% H<sub>2</sub> on a N<sub>2</sub>-free, dry basis. For the Pt catalyst, the carbon selectivity to CO<sub>x</sub> was ~50% and the fuel gas contained 19% hydrocarbon by volume, consisting mainly of aromatics, such as benzene and toluene, and C<sub>2</sub>–C<sub>6</sub> olefins. A blank-tube experiment showed that the gasoline can undergo gas-phase reactions, including oxidation reactions involving O<sub>2</sub> to produce CO and CO<sub>2</sub>, and thermal cracking to yield a wide range of hydrocarbons, including benzene, toluene, and C<sub>2</sub>–C<sub>6</sub> olefins, and some H<sub>2</sub>. The fact that the Rh-containing catalysts performed better is not surprising, since studies have shown that Rh is more active than Pt for steam reforming.<sup>7</sup>

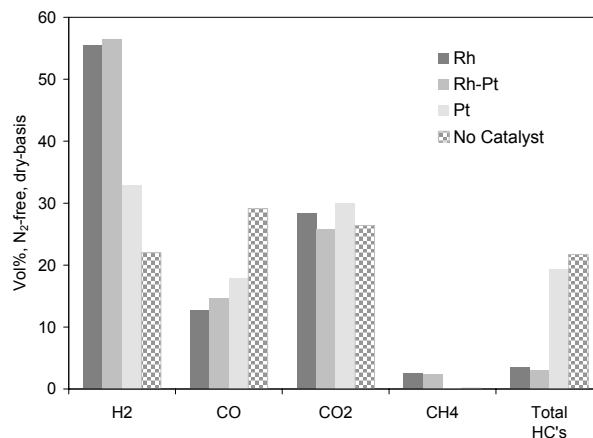


**Figure 1.** Primary product yield for Rh, Rh-Pt, and Pt catalysts for reforming sulfur-free gasoline at a GHSV of 27,000 h<sup>-1</sup>. The O<sub>2</sub>:C ratio was 0.5 and H<sub>2</sub>O:C ratio was 1.8. Furnace temperature is 700°C.

The effect of the gas-hourly space velocity (based on the feed rate) on product yield for the Rh-catalyst was investigated as shown in **Figure 2**. The H<sub>2</sub> concentration in the fuel gas decreased very slightly from 55% to 54% as the GHSV was increased from 27,000 to 110,000 h<sup>-1</sup>. Although the H<sub>2</sub> concentration was relatively independent of GHSV, the CO concentration increased from 12.7 to 17.0% and the CO<sub>2</sub> concentration decreased from 28.4 to 23.6% as the GHSV was increased from 27,000 to 110,000 h<sup>-1</sup>. The increase in the CO concentration with increasing GHSV is significant because it can increase the size of the water-gas shift reactor in the fuel processor.

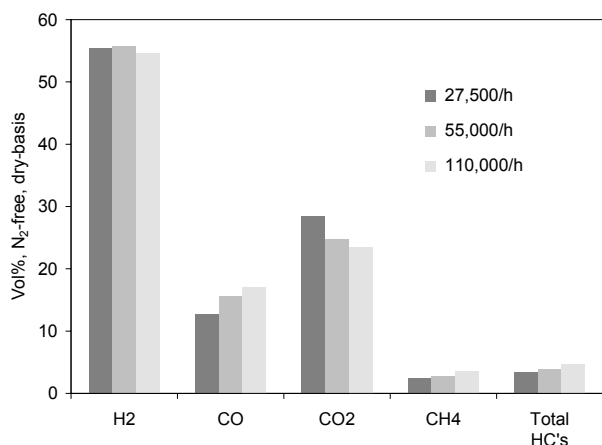


**Figure 2.** Primary product yield for Rh catalyst for reforming sulfur-free gasoline for GHSV from 27,000-110,000 h<sup>-1</sup>. The O<sub>2</sub>:C ratio was 0.5 and H<sub>2</sub>O:C ratio was 1.8. Furnace temperature was 700°C.

Hydrocarbon breakthrough is a concern because it reduces the fuel efficiency and, depending on the nature of the hydrocarbon, may poison other catalysts in the fuel processor. **Figure 3** shows the yield of C<sub>2</sub>-C<sub>6</sub> hydrocarbons, benzene, toluene, and xylenes, for the Rh catalyst at three different furnace temperatures. As expected, the hydrocarbon yield decreases as the furnace temperature is increased. Generally, the low carbon number (C<sub>2</sub>-C<sub>3</sub>) hydrocarbons are produced by the cracking of higher carbon number hydrocarbons present in gasoline. In addition to being present in gasoline, benzene and toluene can be produced by a number of reactions during reforming, including demethylation of toluene and xylenes, dehydrogenation of cyclohexane and cyclohexane derivatives,<sup>8</sup> and cyclic rearrangement of paraffinic molecules larger than C<sub>6</sub>,<sup>9</sup> that are present in the gasoline. Aromatics are problematic because they tend to adsorb more strongly on the active metal sites and are more difficult to reduce than aliphatic hydrocarbons.<sup>8</sup>

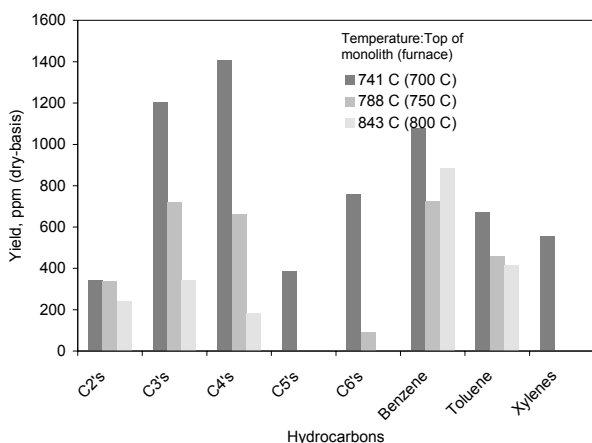


**Figure 3.** Selected hydrocarbon yields for Rh catalyst from reforming sulfur-free gasoline at three different furnace temperatures. GHSV, 27,000 h<sup>-1</sup>; O<sub>2</sub>:C ratio, 0.5; and H<sub>2</sub>O:C ratio, 1.8.

A long-term test using both the no-sulfur and low sulfur gasolines was conducted to investigate the stability and sulfur tolerance of the Rh catalyst. As shown in **Figure 4**, the H<sub>2</sub> concentration decreased slightly from 59% to 56% in the fuel gas produced from the no sulfur gasoline during the first 48 h. When the

fuel was switched to the low sulfur gasoline, the H<sub>2</sub> concentration decreased from 54% to 49% and the CH<sub>4</sub> concentration increased from 2.7% to 5%.

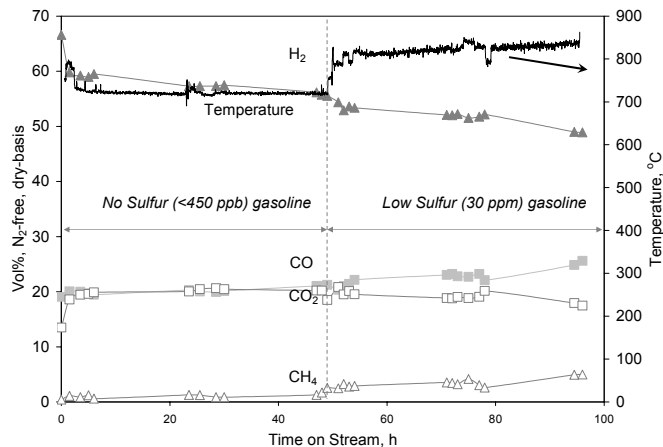


**Figure 4.** Primary product yields for Rh catalyst from reforming sulfur-free gasoline and a low sulfur gasoline. GHSV, 57,000 h<sup>-1</sup>; O<sub>2</sub>:C ratio, 0.45; and H<sub>2</sub>O:C ratio, 1.6.

## Conclusions

Rh, Pt, and Pt-Rh supported on a gadolinium-doped ceria substrate were evaluated for their ability to autothermally reform a no-sulfur gasoline. The Rh-containing catalysts produced a fuel gas with >55% H<sub>2</sub> (N<sub>2</sub>-free, dry-basis) at a furnace temperature of 700°C and a GHSV of 27,000 h<sup>-1</sup>. The H<sub>2</sub> concentration in the fuel gas produced by the Rh catalyst was constant at 54–55% as the GHSV was increased from 27,000 to 110,000 h<sup>-1</sup>; however, the CO concentration increased as the GHSV was increased. Long-term testing of the Rh catalyst with both no sulfur and low sulfur gasolines showed that the catalyst loses activity due to deactivation and sulfur poisoning, but complete loss of reforming activity was not observed.

**Acknowledgement.** This work was supported by the Office of Hydrogen, Fuel Cells, and Infrastructure Technologies, U.S. Department of Energy, Office of Energy Efficiency and Renewable Energy, under Contract W-31-109-ENG-38.

## References

- (1) Carrette, L.; Friedrich, K. A.; Stimming, U. *Fuel Cells*, **2001**, *1(1)*, 5.
- (2) Ranabm, V. *Chem. Ind.*, **1997**, 771.
- (3) Arthur D. Little, Inc., Multifuel Reformers for Fuel Cells Used in Transportation - Assessment of Hydrogen Storage Technologies, U.S. Department of Energy, DOE/CE/50343-1, **1994**.
- (4) Kumar, R.; Ahmed, S.; Krumpelt, M.; Myles, K. M., **1993**, U.S. Patent 5,248,566.
- (5) Ahmed, S.; Krumpelt, M. *Int. J. of Hydrogen Energy*, **2001**, *26(4)*, 291.
- (6) Krumpelt, M.; Ahmed, S.; Kumar, R.; Doshi, R. **2000**, U.S. Patent 6,110,861.
- (7) Rostrup-Nielsen, J. R., *J. Catal.*, **1973**, *31*, 173.
- (8) Kopasz, J.; Krause, T., "Fuel Requirements for Fuel Cell Systems," *Preprints Symposium of the Division of Fuel Chemistry of the American Chemical Society*, **2002**, *47(2)*, 489.
- (9) Wang, X.; Gorte, R. *J. Appl. Catal. A Gen.*, **2002**, *224*, 209.

# HYDROGEN PRODUCTION FROM METHANE USING A REDUCTION-FREE NICKEL CATALYST

Richard A. Couttenye\*, Marianela Hoz de Vila\*, Steven L. Suib<sup>†</sup>

U-60, <sup>†</sup>Department of Chemistry, and \*Department of Chemical Engineering, University of Connecticut, Storrs, Connecticut 06269

## Introduction

Hydrogen (H<sub>2</sub>) has been widely used in: a) petroleum industry, b) production of ammonia, c) hydrogenation of fats and oils, d) welding, e) production of hydrochloric acid, f) fuel for rockets, and recently for fuel cells. Worldwide, 48% of hydrogen is produced from natural gas, 30% from oil (mostly consumed in refineries), 18% from coal, and the remaining (4%) via water electrolysis. The conventional steam reforming for the production of H<sub>2</sub> from methane (CH<sub>4</sub>) is a high-temperature process (>800°C) and produce carbon monoxide also. The latest publications in catalytic decomposition of methane to produce hydrogen have been reviewed by Choudhary<sup>3</sup> et.al. It is noticed that nickel catalysts needed to be activated prior to use (i.e. reduction with H<sub>2</sub> at 600°C for 2h), hence, having a reduction-free catalyst is desirable.

The present investigation involved the synthesis and characterization of a novel nickel catalyst (no activation required) for H<sub>2</sub> production from CH<sub>4</sub>.

## Experimental

**Catalyst preparation.** The cordierite ((Mg<sub>2</sub>Al<sub>4</sub>Si<sub>5</sub>O<sub>18</sub>, Corning's Celcor substrate code 9475 with 400 squares/inch<sup>2</sup>) monolith substrate was initially dipped into a 0.5 M nickel (II) acetate tetrahydrate ((CH<sub>3</sub>CO<sub>2</sub>)<sub>2</sub>Ni.4H<sub>2</sub>O, CAS: 6018-89-9, Aldrich Chemical company Milwaukee, WI) solution for 24 hours at room temperature, and dried at 120°C for 5 hours. The monoliths were then calcined in air at 500°C during 2h. The final catalyst content on the monolith was 8 wt%.

**X-ray Photoelectron Spectroscopy (XPS).** Thermal decomposition (25-400°C) of Nickel(II) acetate, in vacuum, was followed by C 1s, O 1s, Ni 2p regions in the XPS spectra using a Leybold-Heraeus spectrometer model LHS-11.

**X-ray Diffraction (XRD).** X-ray diffraction (XRD) analysis was used to identify the nature of the powder material. X-ray diffraction (XRD) data were obtained with a Scintag 2000 XDS

diffractometer with CuK $\alpha$  X-ray radiation. Powder samples were placed on aluminum slides and scanned at 4° 2 $\theta$ /min. The beam voltage and beam current were 45 kV and 40 mA, respectively.

**Scanning electron microscopy (SEM).** The morphology of the materials, before and after reaction, was checked by scanning electron microscopy (SEM). SEM micrographs were taken in an Amray 1810 Scanning Electron Microscope. Samples were mounted on carbon tape onto aluminum sample holders for analysis.

**Catalyst activity.** The Nickel catalysts was tested in a quartz tube reactor operating at atmospheric pressure. A reactant mixture of 15% methane in helium was fed to the reactor at 30mL/min. Three catalytic monoliths (D= 10mm, L= 20mm) were staked in the reactor with a total catalyst load of 0.12 g. The product stream was analyzed using mass spectrometry (MS) with a MKS-UTI PPT quadrupole residual gas analyzer. The effect of flow rate (5-60mL/min) and reaction temperature (450-550°C) on hydrogen production was evaluated.

## Results and Discussion

Ni (2p) regions in the XPS spectra for nickel (II) acetate decomposition in vacuum showed formation of metallic nickel on the surface at 400°C. The decrease of O (1s) line intensity also confirmed the presence of small amounts of nickel oxide.

Likewise, decomposition of nickel (II) acetate in air at 500°C for 1 hour results in the formation of a mixture of nickel oxide and metallic nickel as shown in the XRD spectrum (Figure 1)

Mass spectroscopy data showed 100% selectivity toward hydrogen in the gas phase for methane decomposition on the nickel catalyst. No detrimental effect on activity or selectivity was observed after 25 hours of continuous operation.

Figure 2 shows the effect of temperature on methane conversion. Conversion increases linearly with temperature in the 450-550°C range. The flow rate effect on hydrogen production is shown in Figure 3. For this particular system, it is confirmed that further increase in flow rate (>30mL/min), will result in only a small increase in hydrogen production.

SEM micrograph of the sample taken after 3 hours of reaction (475°C) showed carbonaceous materials deposited on the catalyst surface. This result was expected since CO and CO<sub>2</sub> were not generated during the reaction due to the lack of oxygen.

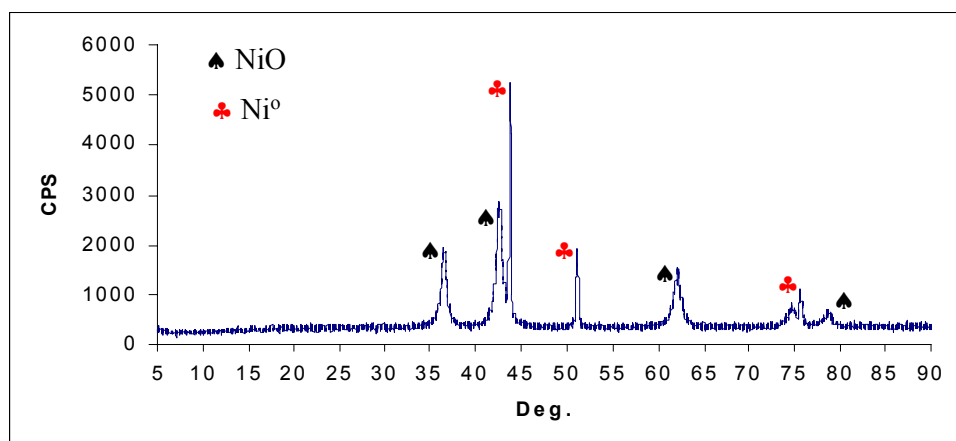
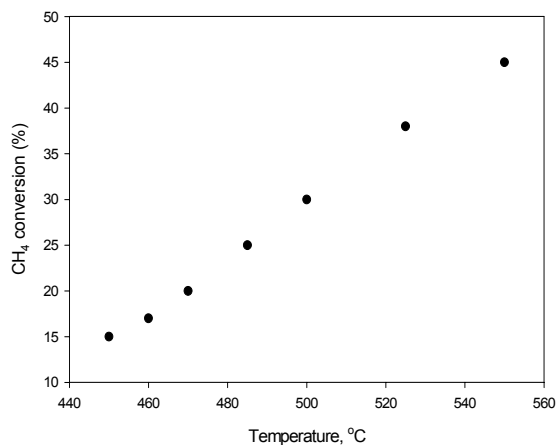
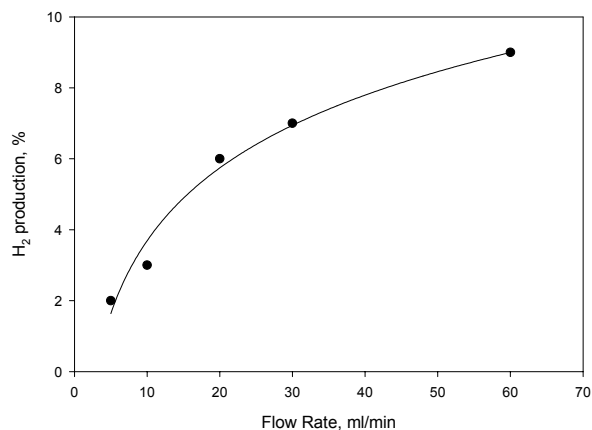


Figure 1. XRD of nickel acetate after decomposition in air at 500°C during 1hr.



**Figure 2.** Effect of Temperature on the methane production conversion. Feed, 15% CH<sub>4</sub> in He. Flow rate, 30 ml/min



**Figure 3.** Effect of Flow rate on H<sub>2</sub> Feed, 15% CH<sub>4</sub> in He. Temperature: 475°C.

## Conclusions

Thermal decomposition (500°C for 1h) of nickel acetate in air results in the formation of a mixture Ni<sup>0</sup> and NiO. This mixture is catalytically active for decomposition of methane at 450°C, and reduction of the catalyst prior to the reaction, is not needed.

The active specie during the methane decomposition at 475°C seems to be Ni<sup>0</sup> as suggested by the XRD and XPS results. Conversion of methane range from 15% (450°C) to 45% (550°C), with 100% selectivity to H<sub>2</sub> in the gas phase.

## References

- (1) Recupero, V.; Pino, L.; Di Leonardo, R.; Lagana, M.; Maggio, G. *Journal of Power Sources.*, **1998**, *71*, 208.
- (2) Lindström, B.; Agrell, J.; Pettersson, L.J. *Chemical Engineering Journal.*, **2003**, *93*, 91.
- (3) Choudhary, V.R.; Banerjee, S.; Rajput, A.M. *Applied Catalysis A: General.*, **2002**, *234*, 259.

# COMPARATIVE STUDY OF CARBON FORMATION ON SUPPORTED NI CATALYSTS DURING CH<sub>4</sub> REFORMING USING TEOM, TPO-IR, TPD-IR AND TGA TECHNIQUES

Jian Zheng<sup>a</sup>, Chunshan Song<sup>a\*</sup>, Wei Pan<sup>a</sup>, Lu Sun<sup>a</sup>, Shankar Nataraj<sup>b</sup>, Frederick Wilhelm<sup>b</sup>, and John N. Armor<sup>b</sup>

<sup>a</sup>Clean Fuels and Catalysis Program, The Energy Institute and Department of Energy & Geo-Environmental Engineering, Pennsylvania State University, University Park, PA 16802

\*Contact e-mail: csong@psu.edu

Email: csong@psu.edu; Tel: 814-863-4466; Fax: 814-865-3248

<sup>b</sup>Air Products & Chemicals Inc., Allentown, PA 18195.

## Introduction

Carbon formation is an important problem in steam reforming and CO<sub>2</sub> reforming of hydrocarbons on supported metal catalysts, which has been an active research subject for several decades<sup>1,2</sup>.

Different techniques have been used to obtain quantitative information regarding the carbon deposition. Thermogravimetric analyzer (TGA) has been frequently applied for analyzing the deposited carbon. However, some concerns have been raised on the TGA method, such as incomplete contact between the reaction mixture and the catalyst, buoyancy effect, as well as different values for the flow resistance<sup>3</sup>.

Recently, a new technique for measuring the weight changes of the sample during the process of coking or gasification has been employed, i.e. the so-called TEOM (tapered element oscillating microbalance), in which the changes in sample weight (ATM, average total weight signal) are determined from changes in the vibration frequency of the cell containing the catalyst<sup>4,5</sup>. It appears that this method is free from disadvantages inherent in the conventional TGA method, since TEOM determines changes in the weight of the catalyst sample that is in contact with the full reaction mixture stream<sup>6</sup>. The TEOM reactor can be operated up to a pressure of 6 MPa and 700°C.

More recently, another sensitive method for measuring of carbon formation on used catalysts has been studied, i.e. the so-called TPO-IR, which combines the temperature-programmed oxidation of carbon with the infrared detection of CO<sub>2</sub> (highly sensitive to existence of CO<sub>2</sub>)<sup>7-8</sup>. However, there has been less study on the comparison of these two new techniques (TPO-IR and TEOM) with the conventional TGA methods.

Commercial Ni/Al<sub>2</sub>O<sub>3</sub> reforming catalysts with or without CaO promoters were chosen in this study for the steam reforming and CO<sub>2</sub> reforming of methane at different temperatures. The above-mentioned three techniques were used for the detection of carbon deposition, with emphasis on the reliability and accuracy of each method.

## Experimental

Two commercial Ni/Al<sub>2</sub>O<sub>3</sub> catalysts were obtained from Süd Chemie: un-promoted C11-9-09 with 1-15% NiO, 85-99% Al<sub>2</sub>O<sub>3</sub> (as per the data provided by vendor), and promoted G-91 with 15-25% NiO, 45-60% Al<sub>2</sub>O<sub>3</sub>, 5-15% CaAlO<sub>2</sub>, 5-15% CaO and 1-10% K<sub>2</sub>O.

**TEOM.** CO<sub>2</sub> reforming of CH<sub>4</sub> was performed in the TEOM (1500PMA, Rupprecht & Patashnick Co.) reactor at temperature of 450°C-650°C at atmospheric pressure and a CO<sub>2</sub>/CH<sub>4</sub> ratio of 1.0. Before each reaction, the catalyst (50mg) was reduced in a mixture of H<sub>2</sub> and Ar (5/15 ml/min). The temperature was increased with a rate of 10°C/min from room temperature to 650°C and kept for 1.5 hours. After pre-reduction process and upon reaching stabilized baseline of

microbalance at reaction temperature, reactant gas containing CO<sub>2</sub> and CH<sub>4</sub> (1:1 mol ratio) was introduced into the TEOM reactor. The ATM weight change of the tapered element was monitored continuously by computerized data acquisition system.

**TPO-IR, TPD-IR, TPOr-IR.** LECO RC-412 multiphase carbon determinator was used for all the temperature-programmed oxidation (TPO-IR) studies, where gases evolved from the sample during the TPO (30°C/min from 100°C to 1000°C) were transferred from the furnace by a purge gas (300 ml/min) into the flow cell of the infrared spectrometer. The furnace was cleaned by running the same TPO on blank quartz sample boat. The IR intensity as related to amount of CO<sub>2</sub> (therefore carbon) was calibrated daily by running TPO-IR using standard carbon material (containing known amount of CaCO<sub>3</sub>).

For the temperature-programmed desorption, ultra-high-purity N<sub>2</sub>, was used as the inert purge gas, which was therefore named as TPD-IR since no oxidation (besides desorption) could occur. In some cases, a TPOr-IR (r- stands for second) was carried out on the samples following a TPD-IR run.

**TPO-TGA.** 20 mg of used catalysts after methane reforming was put on a ceramic sample boat for TPO analysis in Mettler TG-50 instrument. By heating the sample in high flow of air (100 ml/min) from room temperature to 900°C with 10°C/min, the weight change was recorded as related to possible carbon burning or metal oxidation.

## Results and Discussion

After steam methane reforming for 5 hours at 540-820°C and 200-400 psi with steam/carbon ratio ranging from 1 to 3.5 on two commercial SMR catalysts (C11-9-09 and G-91), we carried out TPO-TGA experiments trying to determine the amount of carbon deposited after each SMR experiments. To our surprise initially, there was no weight loss (attributing to burning of carbon) on all the used samples. Instead, a weight gain was observed at TPO temperature range of 300°C-600°C. For comparison, the TPO-TGA experiments of the two catalysts after pre-reduction at different temperature (450°C-650°C) but without SMR reaction have also been done. A similar weight gain of the catalysts is also found with changing amount. This weight gain can therefore be attributed to the oxidation of Ni metal reduced during SMR.

It is clear that TPO-TGA alone can not discriminate carbon burn off and Ni oxidation, especially when only a trace amount of carbon was formed that needs to be detected. Therefore, the set up and reliable use of other sensitive techniques is needed specifically for carbon formation study.

TEOM was used to analyze dynamic process of carbon formation on the same commercial catalysts in terms of change of catalyst weight. Since TEOM was run on-line during methane reforming, it is therefore capable to avoid any other effects (such as the post-run oxidation of Ni, as mentioned above) besides the reforming reactions.

In order to simplify the carbon analysis, we carried out CO<sub>2</sub> (instead of steam) reforming of methane at 650°C under atmospheric pressure, since carbon formation during CO<sub>2</sub> reforming of methane is known to occur readily and it is easier to analyze when compared with steam reforming of methane<sup>2,9-14</sup>.

**Figure 1** shows the TEOM profile of CO<sub>2</sub> methane reforming on G-91 (CaO-promoted) catalyst at 650°C and atmospheric pressure. It should be noted that the time on stream is in term of seconds. It can be seen that carbon forms quickly with the catalyst as soon as the reforming is started. By changing the reaction time, it is possible for us to finely control the amount of carbon deposited on the Ni catalyst, since the ATM signal stabilized quickly after stopping of CO<sub>2</sub> and CH<sub>4</sub> flow simultaneously.

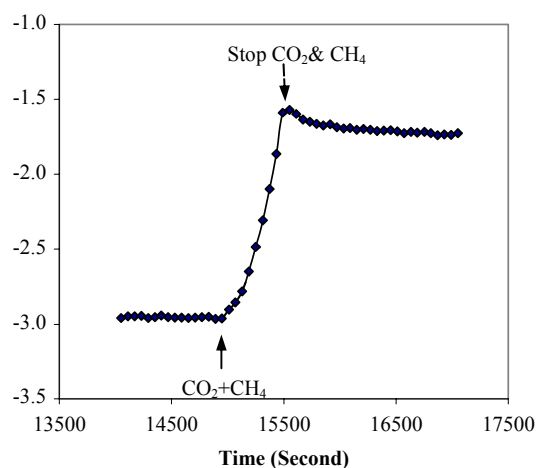


**Figure 1.** TEOM profile on G-91 catalysts during CO<sub>2</sub> reforming of CH<sub>4</sub> (CO<sub>2</sub>:CH<sub>4</sub>=1:1, 650°C, atm)

**Figure 2** shows the comparative TEOM results of CO<sub>2</sub> reforming of CH<sub>4</sub> on C11-9-09 (un-promoted) and G-91 (CaO-promoted) catalysts. Both catalysts show very quick carbon formation. However, contrary to the results by Wang and Lu<sup>9</sup>, we find that the CaO-promoted G-91 catalyst shows more resistance to carbon formation in the initial reaction as compared with C11-9-09 in terms of the slope of the curves in **Figure 2**.

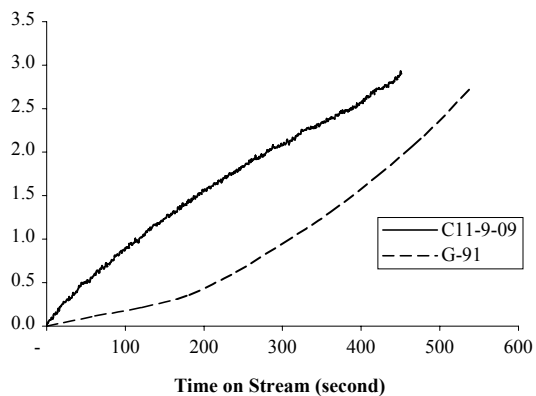


**Figure 2.** TEOM Results on C11-9-09 and G-91 catalysts during CO<sub>2</sub> reforming of CH<sub>4</sub> (CO<sub>2</sub>:CH<sub>4</sub>=1:1, 650°C, atm)

TPO-IR experiments have also been done on the used catalysts after CO<sub>2</sub> reforming of methane using TEOM reactor. Previously, we found that the amount of the TPO-IR peaks at lower temperature (<400°C) almost kept constant in all used SMR catalysts, these peaks are probably related to desorption of CO<sub>2</sub> chemisorbed on Ni supported catalysts during reforming reaction<sup>7</sup>.

**Figure 3** shows the TPO-IR (a), TPD-IR (b), and TPD-IR immediately followed by TPO-IR (c) on G-91 catalyst after CO<sub>2</sub> reforming of CH<sub>4</sub>. Comparing curve (a) and curve (b), the TPO-IR and TPD-IR were done with same temperature program using similar

amount of sample but with different carrier gases (O<sub>2</sub> and N<sub>2</sub>, respectively). It can be seen that the peaks at T<400°C are present in both cases, which verifies that these peaks may not be related to the carbonaceous carbon deposit, but the chemically adsorbed CO<sub>2</sub> on either Al<sub>2</sub>O<sub>3</sub> support or certain metal species. It is also worth mentioning that the TPD-IR signal tends to have higher intensity than that of TPO-IR, as also observed but not discussed by Li and Gonzalez<sup>8</sup>. This might be related to different interfering effects of O<sub>2</sub> and N<sub>2</sub> for IR detection. Therefore, care should be taken when trying to simply subtract the TPO-IR with TPD-IR spectra to derive the amount of carbon deposit.

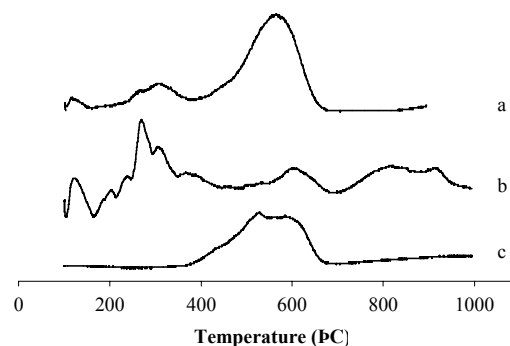


**Figure 3.** TPO-IR (a), TPD-IR (b), and TPD-IR immediately followed by TPO-IR (c) on G-91 catalyst after CO<sub>2</sub> reforming of CH<sub>4</sub> (CO<sub>2</sub>:CH<sub>4</sub>=1:1, 650°C, atm)

It is interesting to note that following TPD-IR of G-91, if the sample was allowed to expose to air for certain time before a subsequent TPO-IR (thus named as TPO-IR), the peaks in this temperature range (T<400°C) could re-appear. However, if the TPO-IR was carried out immediately after TPD-IR, as shown in curve (c) of **Figure 3**, no such peaks is present, which verifies again the above attribution.

TPO-IR of activated carbons or other non-graphitic carbon materials shows peaks generally in the range of 400-600°C, while that of graphite carbon shows peak in the range of 600-800°C. None of these peaks can be seen in TPD-IR profile.

As discussed for our previous observation<sup>7</sup>, we believe that the peak at 400°C-600°C in curve (a) and (c) is due to oxidation of filament carbon on G-91 catalyst. Using SEM, we actually observed the carbon filaments on the catalysts<sup>7</sup>.

The TPD-IR of C11-9-09 (figures not shown) has no peaks at 400°C-900°C, therefore the TPO-IR alone gives the information of carbon formation. On the contrary, care should be taken for the samples containing CaO and other promoters (such as in the case of G-91), since it is possible for the formation of CaCO<sub>3</sub> (noting the TPD-IR peak at around 800°C in curve b of **Figure 3**) or some other carbonate during the reforming of methane. As observed previously, the presence of CaO made the reduction of NiO much harder<sup>7</sup>, the formation of certain carbonate from un-reduced NiOx is therefore also possible, which complicates the TPD-IR as seen in curve b of **Figure 3**.

It is interesting to make a comparison of the quantitative analytical results of TEOM and TPO-IR in terms of amount of carbon formed. Such a comparison can also be a validation to each other.

In doing so, we have carried out CO<sub>2</sub> reforming of methane on G-91 and C11-9-09 catalysts in the TEOM system with the amount of carbon formation controlled by changing the time on stream and determined the amount of carbon from TEOM profiles. TPO-IR was conducted on the used catalysts collected from TEOM for independently analyzing the amount of carbon deposits.

The comparison of carbon formation detected by these two methods is shown in **Figure 4**. There is a fairly good correlation between these two techniques. Furthermore, the un-promoted C11-9-09 shows a better consistence between the two methods, noting that the slope of the linear trend line is very close to 1, while G-91 shows larger amount of carbon detected by TEOM than by TPO-IR. This is possibly again related to the complication due to the existence of CaO promoters as discussed above.

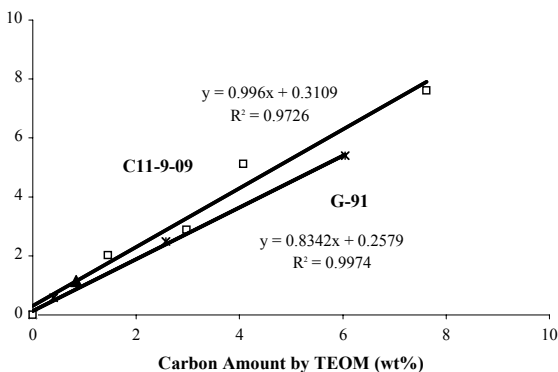


**Figure 4.** Comparison of carbon formation by TEOM & TPO-IR (CO<sub>2</sub>:CH<sub>4</sub>=1:1, 650°C, atm)

We should point out that it is more difficult to quantify the amount of carbon deposits after steam reforming, although the results in Figure 4 show very good correlations for carbon deposits on catalysts used for CO<sub>2</sub> reforming.

## Conclusions

Four different methods (TEOM, TPO-IR, TPD-IR, and TPO-TGA) have been used comparatively for more accurate and reliable measurements of carbon formation on used Ni/Al<sub>2</sub>O<sub>3</sub> reforming catalysts with and without Ca-promotion. By changing purge gas during TPO-IR from O<sub>2</sub> to N<sub>2</sub> (thus TPD-IR), the present study distinguished the origin of each TPO-IR peaks. The accuracy of the TPO-IR analysis has been further verified by means of CO<sub>2</sub> reforming of methane using TEOM for dynamic characterization of carbon formation.

**Acknowledgment.** We are grateful to Air Products and Chemicals Inc., and the Pennsylvania State University for partial financial supports, and to the members of HYCO group of APCI and the APCI-PSU SAMCOM for their support of this collaborative project. We also wish to thank United Catalyst Inc./Süd Chemie for providing the catalyst samples. JZ would like to thank Dr. Orhan Altin of PSU for assistance with the use of TPO-IR instrument and Dr. Yinzhi Zhang of PSU for providing activated carbon samples.

## References

- (1) Rostrup Nielsen, J. Steam Reforming Catalysts, **1975**, Danish Technical Press, Copenhagen.
- (2) Bartholomew, C. H. Catal. Rev. - Sci. Eng., **1982**, 24, 67-112.
- (3) Stasinska, B.; Golebiowski, A.; Stolecki, K.; Borowiecki, T. Ads. Sci. Tech., **2001**, 19, 441-453.
- (4) Fung, S.C.; Querini, C.A.; Lium, K.; Ho, T.C.; Rumschitzki, D.S. Stud. Surf. Sci. Catal., **1994**, 88, 305.
- (5) Pan, W.; Srimat, S.; Song, C.S.; Armor, J. North Am. Catal. Soc. Meet., Toronto, Canada, June **2001**.
- (6) Liu, K.; Fung, S.C.; Querini, C.A.; Rumschitzki, D.S.; Ho, T.C. Stud. Surf. Sci. Catal., **1997**, 111, 652.
- (7) Zheng, J.; Pan, W.; Song, C.S. Prepr.- Am. Chem. Soc. Fuel Div., **2002**, 47, 245-248.
- (8) Li, B.; Gonzalez, R.D. Catal. Lett., **1998**, 54, 5-8
- (9) Wang, S.; Lu, G. Q. J. Chem. Tech. Biotechnol., **2000**, 75, 589-595
- (10) Song C; Srimat S.T.; Murata, S.; Pan W.; Sun, L.; Scaroni, A.W.; Armor J.N. Am. Chem. Soc. Symp. Ser., **2002**, 809, 258-274.
- (11) Srimat S.T.; Pan W.; Song C; Armor J.N. Am. Chem. Soc. Div. Fuel Chem. Prepr., **2001**, 46 (1), 92-93.
- (12) Armor J.N.; Martenak, D.J. Appl. Catal. A: Gen, **2001**, 206 (2), 231-236.
- (13) Srimat S.T.; Song C. Am. Chem. Soc. Symp. Ser., **2002**, 809, 289-302.
- (14) Pan W.; Song C. Am. Chem. Soc. Symp. Ser., **2002**, 809, 316-329.

# HYDROGEN PRODUCTION FROM INTEGRATED METHANOL REFORMING OVER Cu-ZnO/Al<sub>2</sub>O<sub>3</sub> AND Pt/Al<sub>2</sub>O<sub>3</sub> CATALYSTS FOR PEM FUEL CELLS

Weidong Gu, Jian-Ping Shen and Chunshan Song\*

Clean Fuel and Catalysis Program, The Energy Institute and  
Department of Energy & Geo-Environmental Engineering  
The Pennsylvania State University, 209 Academic Projects Building,  
University Park, PA 16802  
\*E-mail: csong@psu.edu

## Abstract

The objective of this work is to design a fuel processor based on integrated oxidative steam reforming of methanol that can achieve efficient production of H<sub>2</sub> with minimum CO (<30ppm CO) in a single reactor for proton-exchange membrane fuel cell applications. This paper reports on hydrogen production from methanol using four different Cu-ZnO/Al<sub>2</sub>O<sub>3</sub> and two different Pt/Al<sub>2</sub>O<sub>3</sub> catalysts from commercial sources. For low-temperature steam reforming, Cu-ZnO/Al<sub>2</sub>O<sub>3</sub> catalysts show high activity for methanol conversion. Pt/Al<sub>2</sub>O<sub>3</sub> catalyst displays very low activity for methanol conversion but high activity for CO conversion. By using a combination of selected Cu-ZnO/Al<sub>2</sub>O<sub>3</sub> and Pt/Al<sub>2</sub>O<sub>3</sub> catalysts under tailored conditions, integrated oxidative steam reforming of methanol can achieve effective H<sub>2</sub> production at low temperatures (≤ 230 °C) with minimum CO (<30 ppm) which is suitable for PEM fuel cell applications.

## Introduction

Fuel cells are one of the most promising energy conversion devices due to their high intrinsic efficiency and ultra low emissions.<sup>1-3</sup> Fuel cell vehicle based on proton-exchange membrane fuel cells can use hydrogen in an electrochemical cell to convert chemical energy directly into electricity for use with an electric motor. Of the five types of fuel cells, the proton exchange membrane fuel cell is considered to be most promising for transportation application.<sup>1-4</sup> While the ideal fuel is pure hydrogen, it is not yet widely available due to the lack of infrastructure coupled with higher cost of pure H<sub>2</sub>. On-board reforming of methanol and hydrocarbon fuels to produce hydrogen is considered to be a practical solution for automotive fuel cell applications.<sup>2-4</sup>

Methanol is one of the promising candidate fuels<sup>5-16</sup> for producing hydrogen on-board due to the following advantages: mild reforming reaction conditions; no needs for desulfurization; no needs for pre-reforming; no serious carbon formation problem. Under ambient condition, liquid methanol has a high volumetric energy density. Many studies have been conducted on steam reforming of methanol.<sup>2-16</sup> Methanol can be produced from natural gas, coal, other fossil fuels as well as renewable resources. H<sub>2</sub> production from methanol may involve various reactions:

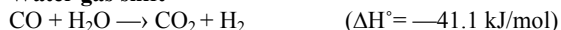
### Methanol decomposition:



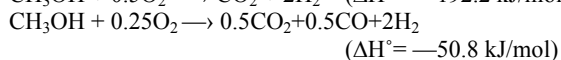
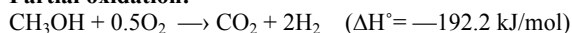
### Steam reforming:



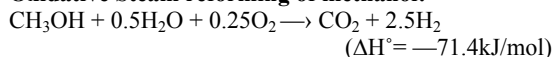
### Water gas shift



### Partial oxidation:



### Oxidative Steam reforming of methanol:



The objective of this work is to design a fuel processor based on integrated oxidative steam reforming of methanol that can achieve efficient production of H<sub>2</sub> with minimum CO (<30ppm CO) in a single reactor for proton-exchange membrane fuel cell applications. In this paper, we report our studies on the methanol reforming over four different Cu-ZnO/Al<sub>2</sub>O<sub>3</sub> and two different Pt/Al<sub>2</sub>O<sub>3</sub> catalysts obtained from commercial sources, with emphasis on the effects of reaction conditions and configuration of catalyst combinations to minimize CO formation and efficient CO cleanup (<30ppm), that will simplify reformer design for on-board application.

## Experimental

Three Cu-ZnO/Al<sub>2</sub>O<sub>3</sub> catalysts, C18HA, C18-7-01 and C18 HALM, were obtained from Sud Chemie Ltd. Another Cu-ZnO/Al<sub>2</sub>O<sub>3</sub> catalyst, KATALCO 83-3, was received from Syntex, ICI. We obtained 3 different Pt/Al<sub>2</sub>O<sub>3</sub> catalysts, 5%Pt/Al<sub>2</sub>O<sub>3</sub> from Pressure Chemical Co. and 1% Pt/Al<sub>2</sub>O<sub>3</sub> and 0.5% Pt/Al<sub>2</sub>O<sub>3</sub> from Engelhard Corp. We also prepared two hybrid catalysts with C18HA and 5% Pt/Al<sub>2</sub>O<sub>3</sub>, C18HA and 1% Pt/Al<sub>2</sub>O<sub>3</sub> (weight ratio is 3:1) as well as two layer catalysts.

The methanol reforming experiments were performed in a fixed-bed down-flow stainless steel reactor with 0.4 inch ID. The reactor temperature was maintained with a tubular electric furnace. The reactor was charged with 0.3 g of the catalyst with particle size 0.5-1 mm and borosilicate beads supported the catalyst bed. A premixed methanol and water with a H<sub>2</sub>O to methanol mole ratio of 1.4 was pumped through the reactor using a liquid pump (ISCO Syringe Pump 500). Helium was used as carrier gas with mass flow controller from Brooks Instrument. The outlet stream of reaction products was analyzed by on-line gas chromatography (SRI8610C) equipped with thermal conductivity detector and 6'SIL GEL/3' MOL SIEVE columns. In order to detect the outlet CO concentration in ppm level, an Agilent 3000 Micro GC equipped with TCD detector, and Molecular sieve 5A and Plot Q columns was used. Prior to the reforming reaction, the catalysts were reduced in H<sub>2</sub> atmosphere at 350°C for 30 min. using a temperature ramp of 2°C/min. and then cooled down to the reaction temperature (180°C-275°C).

## Results and Discussion

The methanol reforming reaction has been performed over four different commercial Cu/Zn/Al catalysts in the temperature range 180-275°C. The catalyst activity in terms of methanol conversion is shown in **Table 1** [Reaction condition: liquid feed (H<sub>2</sub>O/CH<sub>3</sub>OH=1.4 mol ratio) 3ml/h; WHSV= 8.69 h<sup>-1</sup>; Catalyst loading 0.3g; Carrier gas He 80ml/min].

**Table 1.** Effect of temperature on catalytic activity for methanol conversion over four different CuZn-based commercial catalysts

Temperature	Methanol conversion (mol%)			
	KATALCO 83-3	C18-7-01	C18 HA	C18 HALM
180°C	39.66	40.35	32.52	34.27
210°C	68.4	72.84	77.79	55.34
230°C	93.61	98.14	97.34	95.91
275°C	100	100	100	100

When the reaction temperature is at ≥ 230 °C, all catalysts showed similar activity. For a given catalyst, the activity increases with reaction temperature. When the reaction temperature reaches 230°C, methanol conversion over the Sud Chemie catalysts exceeds 95% and at 270°C methanol is totally converted over all the four

Cu/Zn/Al catalysts. The more interesting aspect is that CO formation also changes as a function of reaction temperature. With the temperature decrease from 275°C down to 180°C, CO content decreases from around 1.5% to about 0.05%. This is due to two reasons, the low reaction temperature can suppress the methanol decomposition, which leads to CO, and water gas shift reaction is favored at low temperature, which converts CO into CO<sub>2</sub> and H<sub>2</sub>.

Comparisons of methanol conversion and CO formation are shown in **Figures 1** and **2**, respectively, for tests over different Cu-ZnO/Al<sub>2</sub>O<sub>3</sub> and Pt/Al<sub>2</sub>O<sub>3</sub> catalysts as well as a hybrid catalyst at 230°C after 3 hours time on stream.

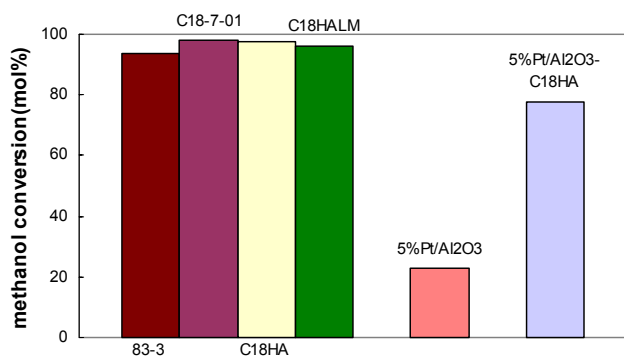


**Figure 1.** Conversion of methanol in steam reforming over CuZn-based and Pt-based commercial catalysts. Reaction conditions: temperature 230°C; liquid feed (H<sub>2</sub>O/CH<sub>3</sub>OH=1.4 mol ratio) 3ml/h; Catalyst loading 0.3g; WHSV= 8.69h<sup>-1</sup>; Carrier gas He 80ml/min; time on stream 3 hr.

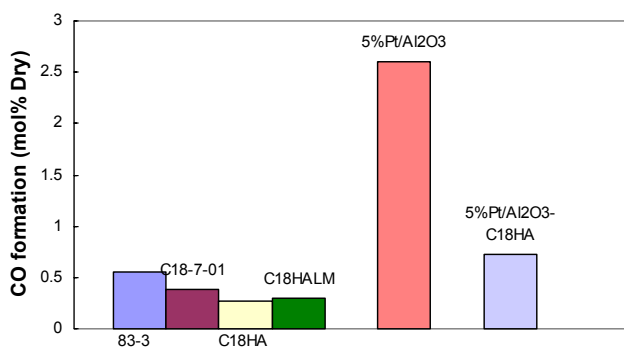


**Figure 2.** Yield of CO from methanol steam reforming over CuZn-based and Pt-based commercial catalysts. Reaction Conditions: temperature 230°C; liquid feed (H<sub>2</sub>O/CH<sub>3</sub>OH=1.4 mol ratio) 3ml/h; Catalyst loading 0.3g; WHSV= 8.69h<sup>-1</sup>; Carrier gas He 80ml/min; time on stream 3 hr.

It can be seen that all the CuZn-based commercial catalysts exhibit a high methanol conversion of over 90 % under the present experimental conditions. Although the methanol conversions over these catalysts are similar at ≥ 230 °C, a considerable difference in CO yield can be noted. For instance, the C18HA offers the lowest CO yield of about 0.3 %. This is lower at least by 1000 ppm compare to the CO yield obtained over other CuZn-based catalyst. Such a

difference in CO yield is significant because the CO content in the final product needs to be ≤ 30 ppm for on-board PEM fuel cell applications. On the other hand, the platinum-based catalyst has a very low activity for low-temperature methanol steam reforming. In addition, they produce relatively large amount of CO. It is likely that methanol undergoes decomposition rather reforming over these catalysts under the present operating conditions.

For oxidative steam reforming of methanol, air is a convenient oxidant for on-board application. Since the CuZn-based commercial catalyst, C18HA offered the lowest CO yield in the methanol steam reforming (see Fig. 2), this catalyst was used to evaluate the performance in the Oxidative steam reforming of methanol (OSRM) reaction. The experiments were conducted using O<sub>2</sub>/CH<sub>3</sub>OH mol ratio from 0 to 0.5. Carrier gas was not used in the OSRM reaction because the N<sub>2</sub> present in the air acted as a carrier gas. **Table 2** shows the effects of O<sub>2</sub>/CH<sub>3</sub>OH mol ratio on methanol conversion, H<sub>2</sub> yield and CO formation at 230°C [liquid feed 1.8ml/h (H<sub>2</sub>O/CH<sub>3</sub>OH=1.4 mol ratio); C18HA catalyst loading 0.3g; time on stream for the reaction 3hr].

**Table 2.** Oxidative steam reforming of methanol over C18HA catalyst at different O<sub>2</sub>/MeOH ratios at 230°C

O <sub>2</sub> /CH <sub>3</sub> OH ratio	CH <sub>3</sub> OH conversion	CO yield (ppm)	H <sub>2</sub> yield (mol%)
0	60.8	848	70.4
0.1	74.6	2602	66.6
0.2	86.9	3125	69.2
0.3	97.4	3371	54.4
0.5	98.4	3642	49.4

As the O<sub>2</sub>/CH<sub>3</sub>OH ratio increases, the methanol conversion also increases. This increase is apparently related to oxidative conversion. However, a related fact is that as O<sub>2</sub>/CH<sub>3</sub>OH ratio is decreased, the carrier (inert N<sub>2</sub> in air) is also reduced. During the reaction process, the carrier gas also affects heat transfer, and the heat transfer speed could decrease due to lower carrier gas flow rate. Heat transfer affects the reaction due to endothermic nature of steam reforming reaction and exothermic nature of partial oxidation. Another evidence for the inert gas effect comes from a comparison between 230°C steam reforming with 80ml/min carrier gas flow and with 15 ml/min carrier gas flow [230 °C “oxidative” steam reforming with O<sub>2</sub>/CH<sub>3</sub>OH =0 (carrier Ar at 15ml/min)]. The methanol conversion with 15 ml/min carrier gas flow is much lower than that with 80ml/min carrier gas flow. Therefore, the heat transfer seems to be a very important factor. CO formation increased and H<sub>2</sub> formation decreased with increasing O<sub>2</sub>/CH<sub>3</sub>OH ratio, indicating that partial oxidation is the reason.

We also examined methanol oxidative steam reforming using one hybrid catalyst (1% Pt/Al<sub>2</sub>O<sub>3</sub> mechanical mixture with C18HA, weight ratio is 1:3) and two-layer catalyst bed (upper layer is 1%PtAl<sub>2</sub>O<sub>3</sub> and lower layer C18HA, weight ratio is 1:3). Air was used as oxidant and O<sub>2</sub>/CH<sub>3</sub>OH ratio is 0.3. Other reaction condition is the same as above. **Figure 3** compares methanol conversion over C18HA, hybrid (1% Pt/Al<sub>2</sub>O<sub>3</sub> + C18HA mix) catalyst and two-layer (1% Pt/Al<sub>2</sub>O<sub>3</sub> // C18HA) catalyst. The observed catalytic activity order is C18HA > hybrid > two layers cat. This once again indicated that at 230°C Pt activity is low and heat transfer is important during reforming process.

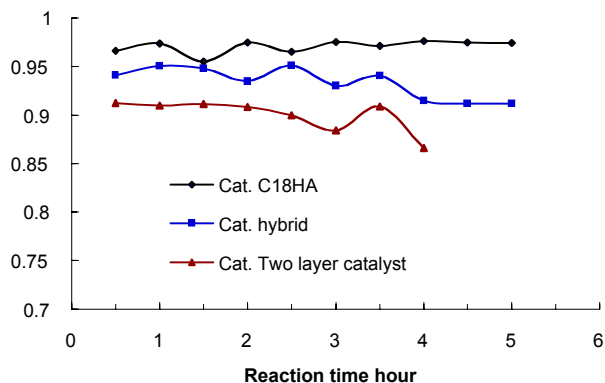


**Figure 3.** Comparison of catalytic activity of C18HA with hybrid and double layer commercial catalysts in the oxidative steam methanol reforming at 230 °C.

On the basis of the above results, we designed a two-zone reactor. Methanol steam reforming or oxidative steam reforming over CuZn-based commercial catalysts takes place in the first zone placed at the top while the CO conversion by preferential oxidation (PrOX) takes place over 1%Pt/Al<sub>2</sub>O<sub>3</sub> catalyst in the second zone with air feed before the second zone, as shown in **Figure 4**.

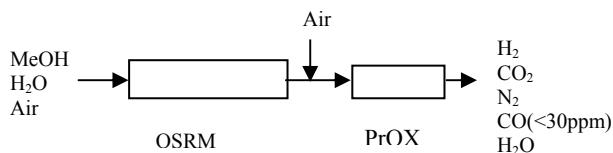


**Figure 4.** Scheme of integrated methanol reformer

The first zone for oxidative steam reforming (OSRM) was kept at 230 °C; liquid feed 1.8ml/h (H<sub>2</sub>O/CH<sub>3</sub>OH=1.4 mol ratio); OSRM-O<sub>2</sub>/MeOHmole ratio 0.3; catalyst loading (C18HA) 0.3g. The air ratio, defined as the amount of air used in the PrOX reaction in the second zone to the amount of air used in the OSRM reaction in the first zone, varied between 0.11 to 0.53. The second zone for CO oxidation was kept at 150 °C.

**Table 3.** Integrated MeOH OSRM and PrOX at different air ratio

Air ratio	MeOH conversion	CO yield (ppm Dry)	H <sub>2</sub> yield (mol % Dry)
0.11	92	1330	63.9
0.12	96.3	477	57.2
0.15	96.4	215	55.1
0.39	94.1	139	56.0
0.47	95.3	102	55.4
0.53	96.8	31.2	52.4

**Table 3** Summarizes the results of integrated OSRM reaction over C18HA and PrOX reaction over 1%Pt/Al<sub>2</sub>O<sub>3</sub> in a two-zone reactor after 3 h time on stream. With the increasing air ratio, the CO concentration in the outlet product gases (dry) decreases greatly, down to as low as 31 ppm. The H<sub>2</sub> yield changes only to a small extent as the air ratio is varied between 0.12-0.47. Thus Pt has a

good selectivity and activity for CO preferential oxidation under the conditions used.

We further examined the effect of the Pt loading under the same conditions: 230 °C MeOH oxidative reforming over C18HA (0.3g), 150 °C preferential oxidation over 0.5%Pt and 1%Pt Al<sub>2</sub>O<sub>3</sub>. **Table 4** shows the experimental results (after 3hr time on stream) corresponding to air ratio 0.39 and 0.53.

**Table 4.** Comparison Pt loading under air ratio 0.39 and 0.53

	Air ratio 0.39		Air ratio 0.53	
	0.5% Pt Al <sub>2</sub> O <sub>3</sub>	1% Pt Al <sub>2</sub> O <sub>3</sub>	0.5% Pt Al <sub>2</sub> O <sub>3</sub>	1% Pt Al <sub>2</sub> O <sub>3</sub>
MeOH conversion (mol %)	95.1	92.4	95.8	96.8
H <sub>2</sub> yield (mol %)	50.4	55.5	50.2	52.4
CO yield (ppm, Dry)	122	106	10.5	31.2

It is interesting to note that CO concentration over the 0.5%Pt/Al<sub>2</sub>O<sub>3</sub> with an air ratio of 0.53 is lower than that over 1%Pt/Al<sub>2</sub>O<sub>3</sub> indicating that Pt loading significantly affects the CO conversion in the PrOX reactor. The results clearly demonstrate that by using a two-zone reactor design with a combination of two types of commercial catalysts, high methanol conversion and very low CO concentration (10-30 ppm) could be achieved under mild reaction conditions.

### Conclusions

Our preliminary results on the steam reforming and oxidative steam reforming of methanol over different CuZn-based and Pt-based commercial catalysts indicated that the CuZn-based catalysts have high activity at low temperature of around 230 °C. Among the catalysts tested, the C18HA commercial CuZn-based catalyst offered the lowest CO yield in the steam reforming of methanol. The Pt-based catalysts are not effective for methanol reforming, but good for CO oxidation.

By designing the two-zone reactor with a combination of a selected Cu-ZnO/Al<sub>2</sub>O<sub>3</sub> catalyst and a selected Pt/Al<sub>2</sub>O<sub>3</sub> catalyst, a high methanol conversion (above 95 %) and very low CO concentration (10-30 ppm) could be achieved under mild reaction conditions (≤ 230 °C). An integrated oxidative steam reforming of methanol over C18HA Cu-ZnO/Al<sub>2</sub>O<sub>3</sub> at 230 °C coupled with CO preferential oxidation over 0.5%Pt/Al<sub>2</sub>O<sub>3</sub> at 150 °C produced H<sub>2</sub>-rich gas with a CO concentration well below 30ppm suitable for on-board PEM fuel cell applications.

### Acknowledgement.

This work was supported by Conoco Phillips and DOE under DOE Cooperative Agreement. Instrument No. DE-FC26-01NT41098. We wish to thank Dr. Etop Esen, Dr. Joe Allison, Dr. Steven McDonald, and Mr. Kirk Miller of Conoco Phillips, Mr. Daniel Cicero of DOE NETL, Dr. Andre' Boehman of PSU and Dr. Chao-Yang Wang of PSU for helpful discussions. We gratefully acknowledge Sud Chemie Ltd, Syntex, and Engelhard for providing various catalyst samples. We also thank Dr. S. Velu for his assistance in setting up the online micro-GC and for helpful discussions on methanol conversion, and Mr. Ronald Copenhaver for his help in setting up the flow reactor.

## References

- 1). Larminie, J.; Dicks, A. Fuel cell Systems Explained. John Wiley, New York, **2000**, 308 pp.
- 2). Chalk, S.G.; Miller, J.F., Wagner, F.W. J Power Sources, **2000**, 86 (1-2), 40-51.
- 3). Trimm, D.L.; Onsan, Z.I. Catalysis Reviews-Science and Engineering, 2001, 43 (1-2), 31-84.
- 4). Song, C. *Catal. Today*, **2002**, **77**, 17-49.
- 5). Edwards, N.; Ellis, S.R.; Frost, J.C.; Golunski, S.E.; van Keulen, A.N.J.; Lindewald, N.G.; Reinkingh, J.G. J. Power Sources, 1998, 71 (1-2), 123-128.
- 6). Breen, J.P.; Ross, J.R.H. Catal. Today, **1999**, 51 (3-4), 521-533.
- 7). Peppley, B.A.; Amphlett, J.C.; Kearns, L.M.; Mann, R.F. Appl. Catal. A: Gen., 1999, 179 (1-2), 21-29 APR 5
- 8). Peppley, B.A.; Amphlett, J.C.; Kearns, L.M.; Mann, R.F. Appl. Catal. A: Gen., **1999**, 179 (1-2), 31-49.
- 9). Wiese W, Emonts B, Peters R. J. Power Sources, **1999**, 84 (2), 187-193.
- 10). Peters R, Dusterwald HG, Hohlein B. J. Power Sources, **2000**, 86 (1-2), 507-514.
- 11). Reitz, T. L., Ahmed, S., Krumpelt, M., Kumar, R. and Kung, H. H. Stud. Surf. Sci. Catal., **2000**, 130, 3645-3650.
- 12). Fierro, J. L. G. Stud. Surf. Sci. Catal., **2000**, 130, 177-186.
- 13). Velu S, Suzuki K, Okazaki M, Kapoor M.P., Osaki T, Ohashi F. J. Catal., **2000**, 194 (2), 373-384.
- 14). de Wild PJ, Verhaak MJFM. Catal. Today, **2000**, 60 (1-2), 3-10.
- 15). Lindstrom, B. Agrell, J. Pettersson, L.J. *Chem. Eng. J.*, **2002**, **4053**, 1-11
- 16). Shen, J.; Song, C. *Catal. Today* , **2002**, **77**, 89-98

## Water-Gas Shift Catalysis on Pt Bimetallic Catalysts

Sara Yu Choung, Magali Ferrandon, and Theodore Krause

Chemical Engineering Division  
Argonne National Laboratory  
9700 South Cass Ave.  
Argonne, IL 60439

### Introduction

The water-gas shift (WGS) reaction ( $\text{CO} + \text{H}_2\text{O} = \text{CO}_2 + \text{H}_2$ ) is of interest due to its presence in the fuel processing process for fuel cell applications. For polymer electrolyte fuel cells, the CO levels in reformat must be reduced to <100 ppm because CO poisons the Pt anode catalyst of the fuel cell. Current commercial WGS catalysts, CuZn and FeCr, have some drawbacks for use in on-board fuel processing. These catalysts require an activation step consisting of a controlled *in situ* reduction. In the reduced state, large temperature excursions are observed when they are exposed to air, resulting in loss of activity because of sintering. In addition, exposure to condensation during shutdown can cause reoxidation and poor mechanical stability. For on-board reforming, the Department of Energy has established the following performance and cost targets for new WGS catalysts: gas hourly space velocity (GHSV)  $\geq 30,000 \text{ h}^{-1}$ , CO conversion  $\geq 90\%$ , CO selectivity  $\geq 99\%$ , lifetime  $> 5000 \text{ h}$ , and cost  $< \$1/\text{kW}_e$ .

Ceria based WGS catalysts were chosen for study because they possess redox properties under WGS reaction conditions. These catalysts are reported to undergo a bifunctional redox mechanism where CO is adsorbed on a transition metal, oxygen is transferred from ceria for the oxidation of CO, and ceria is reoxidized by the dissociation of  $\text{H}_2\text{O}$  [1]. In this study, ceria was doped with zirconia due to its smaller ionic radius, which causes strain in the ceria lattice and promotes the formation of oxygen vacancies and  $\text{Ce}^{3+}$  [2]. We have found that the addition of a dopant (Zr or Gd) increases WGS activity of Pt-supported samples at temperatures above  $300^\circ\text{C}$  [3]. In addition, we observed that the WGS activity (per gram catalyst) increased with Pt loading (0.87–2.86 wt%) [3]. When compared on a per mole of Pt basis, the rates were similar, indicating that the WGS rates (per mole of Pt) are independent of Pt loading (0.87–2.86 wt%) [3]. In order to reduce the amount of Pt necessary to achieve higher WGS rates and enhance the activity of the Pt, different Pt bimetallic formulations were investigated for their role as possible promoters to enhance the WGS activity and stability of Pt/doped ceria catalysts. The bimetallic formulations were selected on the basis of theoretical studies of the energetics of  $\text{H}_2\text{O}$  dissociation and reactions between  $\text{CO}_{\text{ads}} + \text{OH}_{\text{ads}}$  on Pt-mixed metal clusters [4].

### Experimental

Doped ceria supports were prepared by coprecipitation or purchased from Rhodia. The supports were all calcined in air at  $500^\circ\text{C}$  before introduction of the metal(s). Tetraammineplatinum(II) nitrate [ $\text{Pt}(\text{NH}_3)_4(\text{NO}_3)_2$ ] was used as the Pt precursor for Pt, Pt+B, and Pt+C and hydrogen hexachloroplatinate(IV) [ $\text{H}_2\text{PtCl}_6$ ] was used for Pt+A and Pt+D. Metals were introduced using incipient wetness impregnation techniques. The samples were dried in air at  $120^\circ\text{C}$  overnight and calcined in air at  $500^\circ\text{C}$  for 2 h. Pt contents ranged from 0.87–1.0 wt%. The effects of the Pt precursor and the different supports on WGS rates were found to be minimal ( $\leq 20\%$ ).

The WGS activity measurements were carried out in a flow microreactor using a synthetic reformat with the following composition: 6.9% CO, 10.35%  $\text{CO}_2$ , 31.05%  $\text{H}_2$ , 31.0%  $\text{H}_2\text{O}$ , and 20.7%  $\text{N}_2$ . In order to maintain a constant bed volume,  $\alpha$ -alumina

was used as a diluent. The WGS activity of the  $\alpha$ -alumina was found to be negligible. The total volume of catalyst and diluent loaded into the reactor was 0.5 ml. The amounts of catalyst (0.05–0.4 ml) and diluent (0.1–0.45 ml) and the gas flow rate were adjusted to maintain differential reactor conditions at the lower temperatures (conversion  $\leq 15\%$ ) by varying the GHSV (200,000–1,500,000  $\text{h}^{-1}$ ). The samples were pretreated in 4%  $\text{H}_2/\text{He}$  at  $400^\circ\text{C}$  for 1 h. The WGS rate measurements were performed at a catalyst bottom bed temperature of  $250$ – $400^\circ\text{C}$ . The temperatures at the top of the catalyst bed and the outside wall of the reactor were also monitored during the experiment. The CO and  $\text{CO}_2$  concentrations in the effluent were continuously monitored using an on-line infrared gas analyzer (California Analytical Instruments, Model ZRH Infrared Analyzer). Samples were also analyzed using a gas chromatograph (Hewlett Packard 5890 Series II) equipped with thermal conductivity detectors to determine and verify the concentration of the gases and to determine whether methane formation occurs during reaction.  $\text{CO}_2$  was separated on a J&W Scientific GS-CarbonPLOT column using He as the carrier gas. CO,  $\text{H}_2$ ,  $\text{N}_2$ , and  $\text{CH}_4$  were separated on a J&W Scientific GS-MolSieve column using Ar as the carrier gas.

### Results and Discussion

The WGS activities (CO converted to  $\text{CO}_2$ ) of different Pt bimetallic formulations (Pt+M) are compared to Pt on a per Pt basis in Figure 1. Pt+A and Pt+B have higher rates than when Pt is present alone, indicating that the addition of A and B is favorable for promoting the WGS reaction. Slight methane formation is observed on Pt+B with methane selectivities  $\leq 5\%$ . On the other hand, the addition of C and D seems to have inhibiting effects on WGS because lower rates are observed on Pt+C and Pt+D than with Pt.

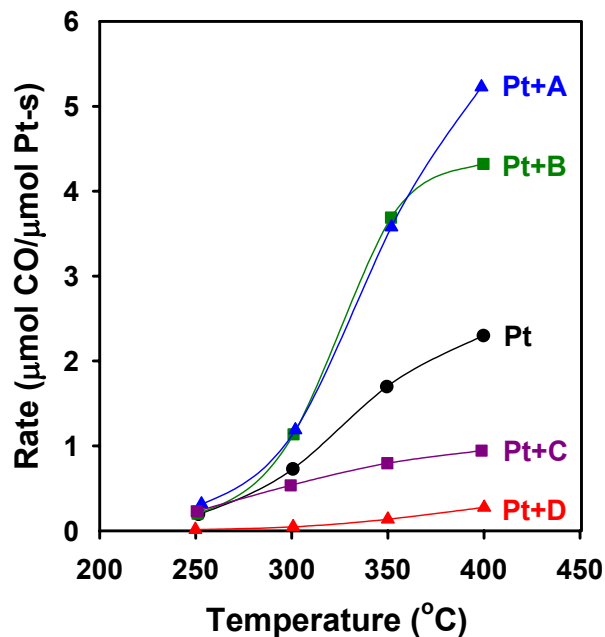


**Figure 1.** WGS activity of Pt and Pt+M supported on doped ceria [250–400°C, GHSV = 200,000–1,500,000  $\text{h}^{-1}$ ].

The activities of Pt+A and Pt+B are compared to Pt at  $300^\circ\text{C}$  with time on stream in Figure 2 in order to compare the stability of these samples during WGS. Both Pt and Pt+B deactivate rapidly initially and then deactivate more slowly after some time on stream. Pt loses half of its activity after about 40 h and Pt+B deactivates

more rapidly than Pt and loses half of its activity after about 2 h. Pt+A is more stable than Pt and maintains its initial activity over 60 h. Wang *et al.* report that the deactivation observed during WGS on Pt/ceria and Pd/ceria catalysts is caused by the loss of metal surface area [5]. The Pt+A bimetallic formulation may inhibit the sintering of Pt, resulting in the enhanced stability during WGS.

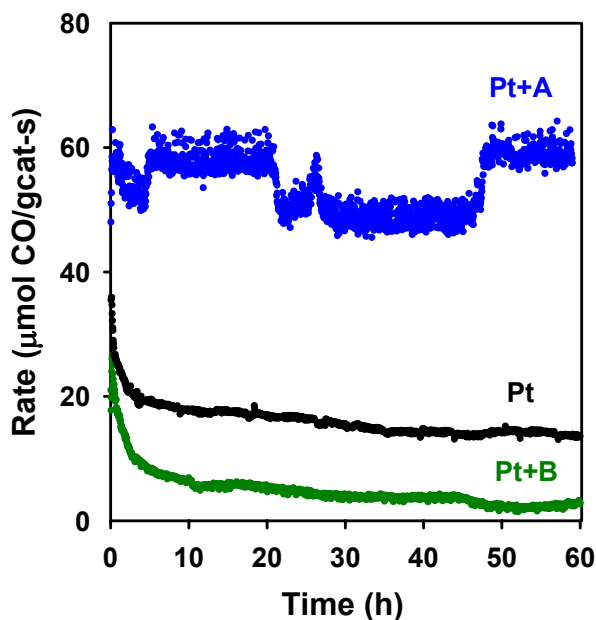


**Figure 2.** WGS activity of Pt, Pt+A, and Pt+B supported on doped ceria vs. time on stream [300°C, GHSV = 300,000–400,000 h<sup>-1</sup>].

### Conclusions

The bimetallic formulations, Pt+A and Pt+B supported on doped ceria, showed higher rates than Pt alone, demonstrating that the addition of A and B enhances WGS. Lower rates were observed on Pt+C and Pt+D, indicating that the presence of C and D inhibits WGS. The samples that showed enhanced WGS activity, Pt+A and Pt+B, were tested for their stability and compared to Pt. By itself, Pt loses half of its activity after about 40 h; Pt+B deactivates more rapidly than Pt, losing half of its activity after about 2 h. Pt+A is more stable than Pt and maintains its initial activity over at least 60 h. The WGS activity and stability of Pt were increased by the bimetallic formulation, Pt+A.

**Acknowledgement.** This work was supported by the Office of Hydrogen, Fuel Cells, and Infrastructure Technologies, U.S. Department of Energy, Office of Energy Efficiency and Renewable Energy. Argonne National Laboratory is operated by the University of Chicago for the Department of Energy under Contract No. W-31-109-ENG-38.

### References

- (1) Bunluesin, T.; Gorte, R. J.; and Graham, G.W. *Appl. Catal. B.* **1998**, *15*, 107.
- (2) Trovarelli, A.; de Leitenburg, C.; and Dolcetti, G. *Chemtech* **1997**, 32.
- (3) Choung, S. Y.; Krebs, J.; Ferrandon, M.; Souleimanova, R.; Myers, D.; and Krause, T. "Water-gas Shift Catalysis," presented at DOE Hydrogen, Fuel Cells, and Infrastructure Technologies 2003 Merit Review Meeting, May 19-22, 2003, Berkeley, CA.
- (4) Ishikawa, Y.; Liao, M.-S.; and Cabrera, C. R. *Surf. Sci.* **2002**, *513*, 98.
- (5) Wang, X.; Gorte, R. J.; and Wagner, J. P. *J. Catal.* **2002**, *212*, 225.

# CERIA-SUPPORTED Cu-Pd BIMETALLIC CATALYSTS FOR OXYGEN-ASSISTED WATER-GAS-SHIFT REACTION FOR PROTON-EXCHANGE MEMBRANE FUEL CELLS

Elise S. Bickford<sup>ab\*</sup>, S.Velu<sup>a</sup>, and Chunshan Song<sup>abc</sup>

<sup>a</sup>Clean Fuels and Catalysis Program, The Energy Institute

<sup>b</sup>Intercollege Graduate Program in Materials

<sup>c</sup>Department of Energy and Geo-Environmental Engineering

The Pennsylvania State University

209 Academic Projects, University Park, PA 16802

\*Presenting author

## Introduction

Proton exchange membrane (PEM) fuel cell, which operates at low temperature, is considered to be the potential candidate for on-board power generation in automobiles. The major impediment to commercialization of PEM fuel cells for automobiles is the need for a fuel processing system to convert liquid fuels such as methanol, gasoline, etc into a CO-free hydrogen-rich gas, because the presence of even traces of CO, over 10 ppm, is a poison to the platinum electro catalysts used in the PEM fuel cells. It has been shown<sup>1</sup> that as the CO concentration increases, the cell voltage drops and the performance of PEM fuel cell deteriorates dramatically.

Water-gas shift (WGS) reactor, which significantly reduces the CO concentration in the down stream of the reformer, is the critical component of the fuel processor. Cu/Al<sub>2</sub>O<sub>3</sub> commercial catalysts have long been used in the water-gas-shift reaction.<sup>2,3</sup> Although the results have been positive, it is very difficult to achieve CO levels below 10 ppm with these catalysts. In addition, the catalysts are pyrophoric and consequently they degrade during operation.

CeO<sub>2</sub> has been known to have many beneficial properties in catalysis, such as promoting the water-gas-shift reaction in steam reforming, improving the dispersion of surface metals, and store and release oxygen.<sup>4,5</sup> The later property is expected to help minimizing the pyrophoricity of the copper metal supported on CeO<sub>2</sub>.

The use of Pd as the sole active metal component in three-way catalyst (TWC) has received considerable attention on the basis of economical aspects and its remarkable activity in oxidation reactions. Many tests have been conducted on Pd/CeO<sub>2</sub> catalysts to understand the metal support interactions.<sup>6,7</sup> These tests and others have helped to fuel research on these catalysts for reforming<sup>8</sup>, oxidation<sup>9</sup> and WGS reactions.<sup>10-13</sup> The addition of base metals such as Cu, Cr and Mn to the Pd/CeO<sub>2</sub> catalyst improved the performance of NO reduction reactions due to the formation of Cu-Pd alloy.<sup>13</sup> These properties have lead to understanding the role of ceria and precious metals in the TWC for vehicle exhausts emission conversion and the desire to harness these properties into creating newer, cheaper and more efficient catalysts for low temperature WGS reaction.

The objective of the present investigation was to develop a new CeO<sub>2</sub>-based Cu-Pd bimetallic catalyst for low temperature WGS reaction for on-board fuel cell applications and to study in detail the role of each metal on the catalytic performance. In order to achieve a good metal dispersion, nano structured high surface area CeO<sub>2</sub> was prepared and used as a support. Commercial high surface area CeO<sub>2</sub> was used to optimize the Cu/Pd atomic ratio in the WGS reaction. The preliminary results are presented in this communication.

## Experimental

**Cu-Pd/CeO<sub>2</sub> optimization:** A series of catalysts with 0.5-1.5 wt % Pd and 1-40 wt% Cu were prepared by depositing them on to a

commercial high surface area CeO<sub>2</sub> support with a BET surface area of 148 m<sup>2</sup> g<sup>-1</sup>, obtained from Rhodia, using deposition precipitation (DP) method as described in the literature.<sup>14</sup> CeO<sub>2</sub> was placed in a beaker and submerged in H<sub>2</sub>O. Appropriate solutions of Cu(NO<sub>3</sub>)<sub>2</sub> in H<sub>2</sub>O and Pd(CH<sub>3</sub>COO)<sub>2</sub> in acetone were prepared. Meanwhile, the pH of the CeO<sub>2</sub>/H<sub>2</sub>O suspension was adjusted to ~9.2 using dilute KOH solution and then the salt solution was added drop-wise to the CeO<sub>2</sub>/H<sub>2</sub>O slurry. After complete addition, the pH of the solution was measured and adjusted to ~9.0. The solution was aged for one hour at room temperature and filtered and washed with distilled water until the pH of the filtrate was 7. The catalysts were dried overnight at 120°C before calcination at 2°C/min to 400°C and held for 3 1/3 hours.

**Water-Gas-Shift Reaction:** The WGS reaction was performed at 210°C in a down-flow fixed-bed stainless steel reactor using 0.5 mL of the catalyst (particle size 1000-500µm). This temperature was chosen because the commercial Cu-ZnO/Al<sub>2</sub>O<sub>3</sub> catalysts obtained from Sud Chemie exhibited better performance and was chosen as a base of comparison. The experimental conditions consisted of using an initial CO concentration of 2000 ppmv, and the space velocity of 12,000 h<sup>-1</sup> (dry basis). The gas compositions used in the WGS reaction over the catalysts were 0.2 % CO, 10% CO<sub>2</sub>, 40.0 % H<sub>2</sub>O, and the balance was Ar gas. In the O<sub>2</sub> assisted WGS reaction, 1.0 % O<sub>2</sub> in the form of air was also added to the feed. The effluent of the reactor was analyzed on-line using an Agilent 3000 A MicroGC equipped with thermal conductivity detectors. The CO detection limit was well below 10 ppm. Prior to the reaction, the catalyst was reduced in situ at 250°C for 2 h in H<sub>2</sub> gas (flow rate : 15mL/min).

## Results and Discussion

Preliminary experiments on the optimization of Cu/Pd ratio for the WGS were performed over Cu-Pd supported on a commercial high surface area CeO<sub>2</sub> obtained from Rhodia. Fig. 1 shows the effect of Pd loading on the catalytic performance in the WGS reaction at 210°C. It can be seen that, under the present experimental conditions, the 1 wt% Pd exhibits a maximum CO conversion of about 46 %. All subsequent catalysts were therefore synthesized with 1 wt% Pd by varying the Cu loading from 1 to 40 wt %.

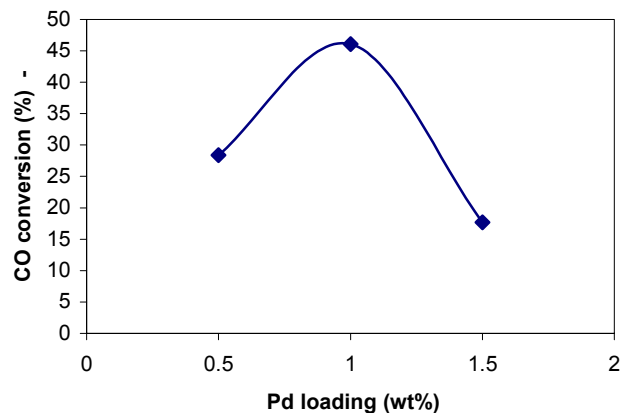


**Figure 1.** Effect of Pd loading on CO conversion in the WGS reaction over Cu-Pd/CeO<sub>2</sub> catalyst

The effect of Cu loading on the catalytic performance shown in Fig. 2 indicates that the CO conversion remains between 40 and 50 % until the Cu loading of 20 wt % and shows a maximum CO conversion close to 80 % when the Cu loading is increased to 30

wt %. The CO conversion decreases with further increase in Cu loading and this supports the previous findings<sup>13</sup> that in the Cu-Pd bimetallic catalysts, as the Cu concentration increases the turnover frequency of the catalyst decreases, and the CO light off temperature decreases. It also supports the findings of Kundajovic and Flytzani-Stephanopoulos<sup>16</sup> that Cu is present as larger CuO particles at the surface, that do not interact strongly with the support, thereby decreasing the overall activity of the catalyst at higher Cu loadings.

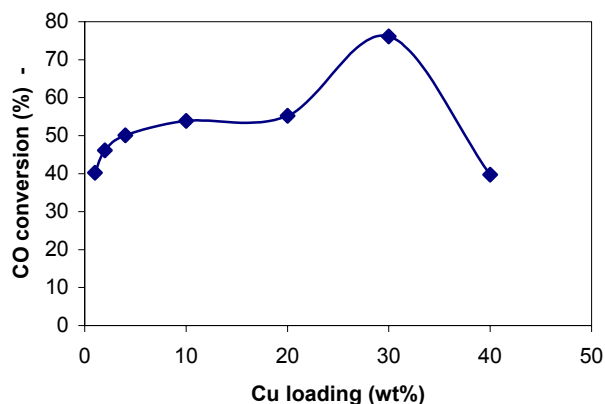


**Figure 2:** Effect of Cu loading on CO conversion in the WGS reaction over Cu-Pd/CeO<sub>2</sub> catalyst

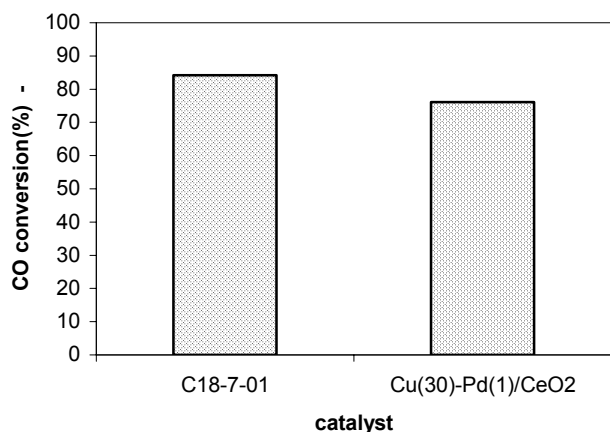


**Figure 3:** Comparison of commercial CuO/ZnO/Al<sub>2</sub>O<sub>3</sub> catalyst with the Cu(30)-Pd(1)/CeO<sub>2</sub> in the WGS reaction

Figure 3 shows a comparison of the conversion results over a commercial CuO/ZnO/Al<sub>2</sub>O<sub>3</sub> catalysts obtained from SudChemie (C18-7-01) and the laboratory made Cu-Pd bimetallic catalyst with 30 wt % of Cu and 1 wt % of Pd supported on commercial CeO<sub>2</sub>. It is interesting to note that the catalytic performance of the laboratory-made Cu-Pd/CeO<sub>2</sub> is very close to that of commercial catalyst under the present experimental conditions. Several parameters such as catalyst composition, pre-reduction temperature, etc. are needed to be optimized in order to achieve higher CO conversion at relatively low temperature. Thus, there is a lot of scope to improve the performance of Cu-Pd/CeO<sub>2</sub> catalyst in the low temperature WGS reaction.

Future tests will include optimizing the conditions for this catalyst, investigating the effect of different methods of support preparation, method of metal loading, etc. Later tests will also include investigating the oxygen-assisted WGS reaction to better utilize the oxidation properties of precious metal within the bimetallic catalyst.

### Conclusions

The effect of Cu and Pd loading on the catalytic performance in the WGS reaction over Cu-Pd/CeO<sub>2</sub> catalyst at 210°C indicated that the catalyst with 30 wt % of Ce and 1 wt % of Pd exhibit a higher CO conversion close to 80 %. This laboratory prepared catalyst is as active as commercial CuO/ZnO/Al<sub>2</sub>O<sub>3</sub> catalyst obtained from Sud Chemie. Since the composition of the Cu-Pd/CeO<sub>2</sub> catalyst and the pretreatment conditions are not yet optimized, it is anticipated that the catalytic performance in the low temperature WGS reaction can be further improved.

**Acknowledgements.** The authors wish to thank US Department of Energy for partial support of the project work.

### References

- (1) Springer, T. E.; Rockward, T.; Zawodzinski, T. A.; Gottesfeld, S. *Journal of The Electrochemical Society* **2001**, *148*, A11-A23.
- (2) Sengupta, G.; Gupta, D. K.; Sen, S. P. *Indian Journal of Chemistry* **1978**, *16A*, 1030-1032.
- (3) Utaka, T.; Sekizawa, K.; Eguchi, K. *Applied Catalysis A: General* **2000**, *194-195*, 21-26.
- (4) Trovarelli, A. *Catal. Rev.-Sci. Eng.* **1996**, *38*, 439-520.
- (5) Whittington, B. I.; C.J., J.; Trimm, D. L. *Catalysis Today* **1995**, *26*, 41-45.
- (6) Badri, A.; Binet, C.; Lavalley, J.-C. *J.Chem.Soc.Faraday Trans.* **1996**, *92*, 1603-1608.
- (7) Cordatos, H.; Gorte, R. J. *Journal of Catalysis* **1996**, *159*, 112-118.
- (8) Craciun, R.; Daniell, W.; Knozinger, H. *Appl. Catal. A-Gen.* **2002**, *230*, 153-168.
- (9) Sharma, S.; Hilaire, S.; Vohs, J. M.; Gorte, R. J.; Jen, H. W. *Journal of Catalysis* **2000**, *190*, 199-204.
- (10) Hilaire, S.; Wang, X.; Luo, T.; Gorte, R. J.; Wagner, J. *Appl. Catal. A-Gen.* **2001**, *215*, 271-278.
- (11) Wang, X.; Gorte, R. J.; Wagner, J. P. *Journal of Catalysis* **2002**, *212*, 225-230.
- (12) Kang, M.; Song, M. W.; Kim, K. L. *React.Kinet.Catal.Lett.* **2002**, *75*, 177-183.
- (13) Hungria, A.B.; Iglesias-Juez, A.; Martinez-Arias, A.; Anderson, J. A.; Conesca, J. C.; Soria, J. *Journal of Catalysis* **2002**, *206*, 281-294.
- (14) Fu, Q.; Weber, A.; Flytzani-Stephanopoulos, M. *Catalysis Letters* **2001**, *77*, 87-95.
- (15) Zhang, Y.; Andersson, S.; Muhammed, M. *Appl. Catal. B-Environ.* **1995**, *6*, 325-337.
- (16) Kundakovic, L.; Flytzani-Slephanopoulos, M. *Appl. Catal. A-Gen.* **1998**, *171*, 13-29.

## Synthesis of nanocrystalline catalysts for the water-gas shift reaction

Ranjan K. Pati<sup>a</sup>, Ivan Lee<sup>b</sup>, Deryn Chu<sup>b</sup> and Sheryl H. Ehrman<sup>a</sup>

<sup>a</sup>Department of Chemical Engineering, University of Maryland, College Park, MD 20742

<sup>b</sup>US Army Research Laboratory, 2800 Powder Mill Road, Adelphi, MD 20783

### Introduction:

In recent years fuel cell technology is a promising method for generating electricity for mobile and stationary applications. Interest in fuel cells is driven by their potentially high efficiency and lower emissions [1]. A factor that draws interest to the fuel cell is that it can operate at efficiencies two to three times that of the internal combustion engine, and it requires no moving parts. Many different types of fuel cells have been developed, with the proton exchange membrane (PEM) fuel cell attracting the most interest for mobility applications. This type of fuel cell operates by electrochemical oxidation of hydrogen generating electricity, while forming water. The partial oxidation and steam reformation reactions are the two key steps for the generation of hydrogen from hydrocarbons and alcohols. In both, the products are carbon monoxide, carbon dioxide and hydrogen. The fuel cell is highly sensitive to poisoning especially by carbon monoxide, which can significantly lower the performance of the fuel cell at concentrations above 50 ppm. The water-gas shift (WGS) reaction is used to convert carbon monoxide and water to hydrogen and CO<sub>2</sub> products. In most of the cases, the presence of suitable catalysts in the WGS reaction can reduce the concentration of CO down to 10 ppm. In this study, the focus will be on the development of improved catalysts for the WGS reaction as it plays a potential role for generating fuel cell hydrogen.

There are various kinds of catalysts used commercially for the WGS reaction including binary CuO-ZnO and ternary CuO-ZnO-Al<sub>2</sub>O<sub>3</sub> and CuO-ZnO-Cr<sub>2</sub>O<sub>3</sub> mixed oxides, Au supported on Fe<sub>2</sub>O<sub>3</sub>, Au supported on TiO<sub>2</sub> etc [2]. Recently, it has been reported that pure ceria and a combination of transition metal supported ceria increases the rate of the WGS reaction as compared to the binary CuO-ZnO and ternary CuO-ZnO-Al<sub>2</sub>O<sub>3</sub> and CuO-ZnO-Cr<sub>2</sub>O<sub>3</sub> commercial water gas shift catalysts [2]. Ceria-based WGS catalysts have attracted increasing attention because of the high oxygen storage capacity and mobility of oxygen. Additionally the ceria based catalysts are also expected to be more stable with respect to high temperature, water and air. Various chemical methods have been reported in the literature for the preparation of ceria and ceria based catalysts including co-precipitation [3, 4], hydrothermal [5, 6], microemulsion [7, 8], surfactant assisted precipitation [9] etc. All of the above methods involve multiple, time consuming step. The objective of this study is to prepare high surface area pure and transition metal supported ceria by the flame spray pyrolysis method (FSP).

### Experimental Procedure:

For this investigation, cerium acetate, cerium-triethanolamine, cerium-diethanolamine, and transition metal nitrate precursor solutions have been used as the feed. The principle of the process is the *in situ* evaporation and subsequent burning of the precursor droplets, which leads to gas-phase synthesis of the desired product. In the flame, the precursors are expected to vaporize and to react to form oxides. The liquid precursor feed was supplied by a nebulizer and atomized with compressed air resulting in a fine spray with a droplet mass. Premixed methane/oxygen/nitrogen gas was used in the

burner. The resulting powder has been collected onto a water cooled substrate via thermophoresis.

Cerium (III) acetate hydrate, Ce(CH<sub>3</sub>CO<sub>2</sub>)<sub>3</sub>.xH<sub>2</sub>O was dissolved in glacial acetic acid at 80°C to obtain a 0.3M Ce<sup>3+</sup> solution. The solution was diluted either with acetic acid or a mixture of 80 vol% isooctane and 20 vol% isobutanol to obtain a 0.15 M Ce<sup>3+</sup> solution. These precursor solutions were stable above 65°C. For making the cerium-TEA and cerium DEA solutions, a stoichiometric amount of cerium acetate was dissolved in DI water and mixed with ammonia solution to make the precipitation of cerium hydroxide and then this precipitate has been dissolved in TEA and DEA to make Ce-TEA and Ce-DEA. All these solutions were filtered before filling into the syringe.

### Characterization:

Bulk chemical composition was determined by using electron microprobe analysis. Thermogravimetric analysis (TGA) was used to determine if the precursors have completely reacted to the oxides. Transmission electron microscopy (TEM) was used to determine the morphology of the powder and to quantitatively investigate dispersion. Surface area of the powder has been measured using the Brunauer, Emmett and Teller (BET) gas absorption method. To understand the chemical composition and phase relationship, Fourier transform infrared spectroscopy (FTIR) was used to determine the bonding between the transition metal and cerium species and X-ray diffraction (XRD) was used to investigate the crystal structure of the synthesized powder.

The activity of the synthesized catalysts for the WGS reaction was investigated using a small plug flow reactor. Gas chromatography is used to quantify the concentrations of products. To determine the reaction rate, measurements has been made of CO conversion as a function of the partial pressures of the reactants and products, CO, CO<sub>2</sub>, H<sub>2</sub>O and H<sub>2</sub>. Catalysts performance has been determined by generating conversion profiles as a function of temperature under realistic WGS conditions. The objective here is to identify the compositions that result in the improved activity, as measured by conversion, at the expected operating temperatures (~200°C and ~400°C).

### Results and Discussion

Thermogravimetric analysis (TGA) of the synthesized powder has been carried out in a Perkin Elmer TGA 7 thermal analyzer at a heating rate of 10°C/min. Fig-1 illustrates the thermogram of CeO<sub>2</sub> powder prepared from the cerium acetate precursor as a typical example. The synthesized powder may be considered to be composed of some carbonaceous material and the metal oxides trapped in the pyrolysed mass produced by the oxidation process during flame synthesis. There is a total of ~2.14% wt loss with two steps of wt loss is shown in the thermogram. The first wt loss is in the temperature range of ~20 - 200°C, which is associated with the loss of water absorbed by the sample from atmosphere. The major wt loss was happened at a temperature range of 300 - 500°C. This wt loss is basically due to the loss of a small amount of carbonaceous material present in the sample, which is also clear from FTIR (fig-2). After 500°C, the sample is almost carbon free.

Fourier transformed infrared (FTIR) ( ) spectrum of the ceria powder obtained from cerium acetate precursor is shown in Fig-2. The IR absorption bands in the region of 2800-2900 cm<sup>-1</sup> are the C-H stretching mode of hydrocarbons. These bands may be due to the presence of acetic acid in the product. Residual water and a hydroxyl group are detected with a large band at around 3500 cm<sup>-1</sup>, corresponding to the O-H stretching frequency, and broad band at 1600 cm<sup>-1</sup> due to the bending vibration of associated water. An

additional band at around  $1400\text{ cm}^{-1}$  may be due to the presence of carboxylic acid in the sample.

The morphology of the ceria particles obtained from the cerium acetate precursor was investigated by transmission electron microscopy (TEM) (Hitachi 600AB, operated at 200kV). The bright field micrograph (Fig-3) of the synthesized powder reflected the basic powder morphology where the smallest visible particle can be identified with the crystalline and / or their aggregates. From the micrograph it is revealed that the particles are nearly spherical with the average particle size in the range of 50-60 nm.

The appearance of large particles (~150 nm) in the TEM may indicate that two particle formation mechanisms are present independently. Large particles may be formed directly from precursor droplets that do not completely evaporate. It may be presumed that the particles having size of 50nm could be formed by precursor evaporation and subsequent gas phase reaction, ceria nucleation, surface growth, coagulation and sintering.

#### Future work:

The addition of iso-octane, which has high combustion enthalpy and high evaporation/burning rate, increases the flame temperature enhancing precursor evaporation [10], which therefore reduces the formation of the byproduct. Similarly homogeneous ceria powders can be obtained by using large amounts of oxygen in the flame where the particles experience high temperatures and long residence times.

#### Conclusion:

The Flame Spray Pyrolysis method (FSP) is promising method for the synthesis of nanocrystalline ceria and metal supported ceria powder. The particle size of the synthesized ceria powder is in the range of 50-60 nm.

**Acknowledgement:** R. K. Pati and S. H. Ehrman acknowledge the support from the ARL under the ARL PEER program.

#### References:

1. Ahmed, S., Krumpelt, M., Intl. J. Hydrogen Energy, 2001. 26: p. 291
2. Li, Y., Fu, Q., Stephanopoulos, M F., Appl. Catal B: Environmental, 2000. 27: p. 179
3. Djuricic, B., Pickering, S., J. Europ. Ceram. Soc., 1999. 19: p.1925
4. Bruce, L A., Hoang, M., Hughes, A E., Turney, T W., Appl. Catal., A 1996. 134: p. 351
5. Hirano, M., Inagaki, M., J. Mater. Chem., 2000. 10: p. 473
6. Hakuta, Y., Onai, S., Terayama, H., Adschiri, T., Arai, K., J. Mater. Sci. Lett. 1998. 17: p. 1211
7. Martinez-Arias, A., Fernandez-Garcia, M., Ballesteros, V., Salamanca L N., Conesa, J C., Otero, C., Soria, J., Langmuir, 1999. 15: p. 4796
8. Masui, T., Fujiwara, K., Peng, Y M., Sakata, T., Machida, K., Mori, H., Adachi, G., J. Alloy. Compd. 1998. 269: p. 116
9. Terrible, D., Trovarelli, A., Llorca, J., deLeitenburg, C., Dolcetti, G., J. Catal., 1998. 178: p. 299
10. Mädler, L., Stark, W J., Pratsinis, S E., J. mater. Res., 2002. 17: 1356

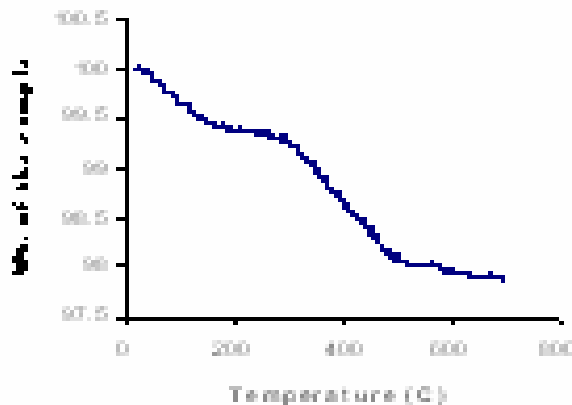


**Fig-1:** Thermogravimetric analysis of the ceria powder obtained from cerium acetate precursor

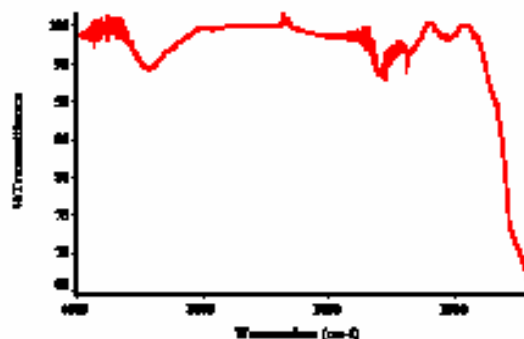


**Fig-2:** FTIR spectra of the ceria powder obtained from cerium acetate precursor.

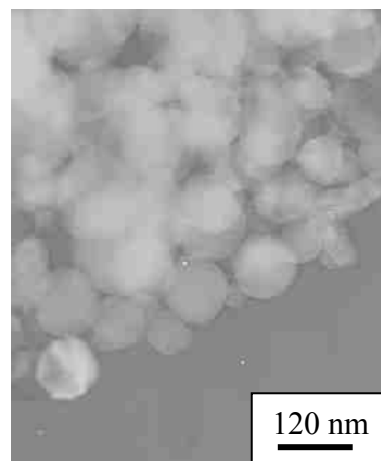


**Fig- 3:** Transmission electron micrograph of the ceria powder.

## PrOx Reactor Startup and Transient Control Options

Michael A. Inbody, Rodney L. Borup,  
and José I. Tafuya

Fuel Cell Team, MST-11  
Los Alamos National Laboratory  
MS J-579, P.O. Box 1663  
Los Alamos, NM 87545

### Introduction

Low-temperature polymer electrolyte membrane (PEM) fuel cells require a hydrogen-rich fuel stream that has a carbon monoxide (CO) concentration less than 10 to 100 ppm, depending on the CO tolerance of the fuel cell. Fuel processing systems for PEM fuel cells that do not use separation processes to purify the hydrogen-rich fuel stream typically use a final CO removal step to meet the CO tolerance requirements of the fuel cell stack. A common method of final CO removal is by Preferential Oxidation (PrOx) of CO by oxygen from injected air over a catalyst. The selection of the catalyst and operating conditions such as temperature are critical to oxidize CO preferentially or selectively instead of oxidizing hydrogen, a parasitic loss of the fuel cell system fuel.

The PrOx reactor component of the fuel processor is used to remove the remaining CO from the outlet of the water-gas shift (WGS) reactor stages, in the range of 2% CO to 5000 ppm CO. The PrOx design inlet CO concentration reflects a trade-off between size of the WGS reactor stages and the efficiency penalty of the PrOx removal of CO. The efficiency penalty can be offset by adding system complexity through the use of multiple stages of PrOx. Because the CO and H<sub>2</sub> oxidation reactions are exothermic and selectivity for CO decreases with increasing temperature, achieving high CO conversions can increase the parasitic loss of hydrogen. Multiple stages with lower CO conversion per stage can be used to achieve a higher overall conversion with reduced parasitic loss of hydrogen by maintaining the catalyst in each stage in a temperature range where it is more selective for CO oxidation.

Transportation applications and some stationary applications of fuel cell systems require that the fuel processor respond to transient power demands. Transportation fuel cell systems, in particular, may undergo frequent startup/shutdown cycles. The PrOx reactor component, as the final stage in the fuel processor, is critical for maintaining the outlet CO concentration within the fuel cell stack tolerance through the startup transient and the transition to normal operation and then during subsequent system power transients.

In the PrOx reactor research at Los Alamos National Laboratory, we conduct experiments on laboratory PrOx reactor components to identify the performance of catalysts and PrOx reactors under steady-state and transient operating conditions. We have examined the response of PrOx reactors and catalysts to three types of transients, power, composition, and startup.

A power transient is a change in the total flow through the fuel processor as it responds to changes in the hydrogen demand of the fuel cell. Power transient experiments are used to identify the air injection and temperature control requirements to maintain specified outlet CO levels.

A composition transient is a change in the gas composition such as variations in the CO concentration caused by instabilities or variations in the fuel processor inlet flows. Composition transient experiments were conducted to measure the sensitivity of the PrOx reactor to variations in the inlet CO composition and the requirements to control the outlet CO concentration. These experiments can be used to identify requirements for a CO sensor for a control system input.

The PrOx startup transient is difficult to define and simulate because the character of the transient will vary depending on the particular fuel processor and startup strategy. However, the desired end in all cases is to deliver a fuel cell quality gas as quickly as possible. To achieve this end in the PrOx reactor, the mass of the catalysts and components in the flow need to be minimized, the catalyst should have a low light-off temperature for CO oxidation so that CO oxidation can begin before the fuel processor has completely warmed up, and should have good CO selectivity over a wide temperature range from low temperature at startup to normal operating temperature at steady-state. An additional desired characteristic is the capability to oxidize higher than normal concentrations of CO. Then, with proper design and controls, the PrOx reactor may be able to compensate for off-design performance of the upstream WGS reactors to maintain the required system outlet CO concentration.

We report here on our experimental approach to measure single-stage PrOx reactor response to composition transients and startup transients. The results of the composition transients are presented showing an option to controlling varying CO concentrations. The startup transient results also are presented showing a rapid decrease to steady-state outlet CO levels.

### Experimental Approach

**PrOx Reactor Test Facility and Hardware.** PrOx reactor components were tested in a facility capable of simulating the outlet stream and conditions from a fuel processor. The major components of reformat, hydrogen, nitrogen, carbon dioxide, and water (as steam) along with carbon monoxide as a trace component, were metered with mass flow controllers. The reformat flow was heated with inline gas heaters to simulate the outlet temperatures from a fuel processor. Fuel processor operating pressures were obtained using a back pressure regulator. Computer control and measurement of these functions allowed for simulation of a variety of fuel processor configurations and transient operating conditions. CO, CO<sub>2</sub>, and CH<sub>4</sub> concentrations were measured with NDIR analyzers and O<sub>2</sub> concentrations were measured with a paramagnetic O<sub>2</sub> analyzer.

Experiments reported here were conducted with a single-stage PrOx reactor set up with a 3 inch diameter by 5 inch long 600 cpsi monolith coated with a precious-metal-based catalyst.

**Composition Transient Experiments.** The response of the single-stage PrOx reactor was measured with a modulated inlet CO concentration with an overall steady flow with composition, 38.1% H<sub>2</sub>, 27.3% N<sub>2</sub>, 15.7% CO<sub>2</sub>, and 17.1% H<sub>2</sub>O. The space velocity was set to 38,000 hr<sup>-1</sup> with an inlet gas temperature set to 97 °C. In one set of experiments simulating an inlet stage, the CO concentration was modulated between 8000 ppm and 12000 ppm with a 60 s period sine wave. The air stoichiometry was set for a steady-state value at 10000 ppm CO. In a second experiment simulating an outlet stage, the CO concentration was varied between 0 and 2000 ppm again with a 60 s period sine wave. The air injection was held constant with the stoichiometry set for 2000 ppm.

**Startup Transient Experiments.** The startup response of the PrOx reactor catalyst from room temperature was measured by establishing a room temperature gas flow through the reactor and then injecting air at time = 0.0 s. A dry gas flow with 46.0% H<sub>2</sub>, 32.9% N<sub>2</sub>, and 19.0% CO<sub>2</sub> was established with a GHSV = 31,000 hr<sup>-1</sup> at an inlet temperature of 20 °C. Experiments were conducted with inlet CO concentrations of 1.2% and 2350 ppm. Outlet CO concentration and the temperature profile of the catalyst monolith were recorded from before the start of air injection to approximately steady-state. Temperatures in the catalyst monolith were monitored by 0.020" K-type thermocouples inserted at 1.0" depth intervals.

## Results and Discussion

**Composition Transient Experiments.** Figure 1 shows the outlet CO concentration from the PrOx catalyst in response to a modulated inlet CO concentration from 8000 to 12000 ppm. The air stoichiometry ( $\lambda$ ) is set to 1.44 for the mean CO level of 10000 ppm and held constant through the modulation. The peak-to-peak outlet CO variation is 1350 ppm and the mean is 506 ppm. As the air stoichiometry is increased the magnitude of the peak-to-peak variation and the mean outlet CO concentration both decrease. At  $\lambda=1.24$ , the peak-to-peak CO was 2700 ppm and the mean CO = 1300 ppm. At  $\lambda=1.65$ , the peak-to-peak CO was 460 ppm and the mean CO=235 ppm.

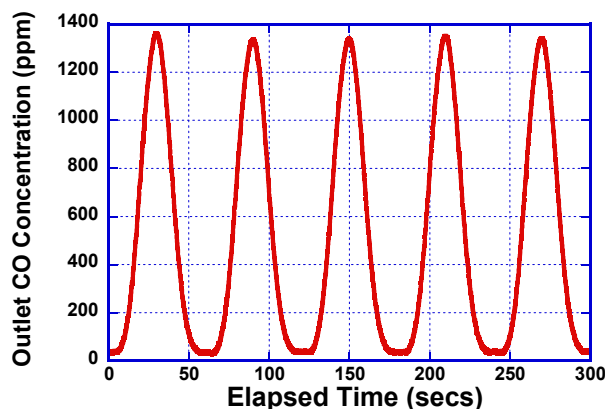


**Figure 1.** Outlet CO concentration as a function of time for a modulated CO input from 8000 to 12000 ppm.

The second set of composition transient experiments examined a hypothetical inlet to a second stage with a modulated inlet CO from 0 to 2000 ppm. With  $\lambda=2.4$ , the outlet CO was held in the range of 10 ppm. The combination of this second stage with the first stage performance at  $\lambda=1.44$  suggests that the overall stoichiometry of 1.84 could control an 8000 to 12000 ppm variation at these flow rates.

**Startup Transient Experiments.** Figure 2 shows the outlet CO concentration measured as a function of time from the start of air injection for an inlet CO concentration of 1.2% at  $\lambda=1.09$ . The outlet CO concentration drops rapidly within 15 s of the start of air injection and reaches 730 ppm at 30 s. A similar test with inlet CO concentration of 2350 ppm CO at  $\lambda=2.4$  shows a similar response of rapid CO decrease within 15 s and reaches 30 ppm at 30 s. Some of the delay in the outlet CO concentration response is due to sampling line delays in the gas analyzers.

Figure 3 shows the monolith temperature response for the 1.2% CO case. The temperature rise moves down the monolith in the 60 s shown as the temperature response takes longer to reach steady-state than the CO concentration. The catalyst used here has a low light-off temperature that facilitates its use in startup.

The rapid decline in outlet CO concentration at low inlet temperatures before the temperature profile has reached steady-state suggests that the thermal response of the PrOx catalyst substrate may not be a major factor in the startup of a PrOx reactor. In these experiments, low CO concentrations can be reached in 15 s after the start of air injection.

## Conclusions

The response of a PrOx reactor catalyst to composition transients and to startup transients has been measured. The composition transient experiments suggest that variations in the inlet CO concentration can be tolerated without additional controls if the

inlet stages of the PrOx reactor can bring the inlet CO to the final stage to within 2000-1000 ppm. At these low concentrations, the excess air does not generate a significant temperature rise to increase the reverse water-gas shift kinetics. Simple control of CO variations at constant flow can be achieved at the expense of additional H<sub>2</sub> consumption.

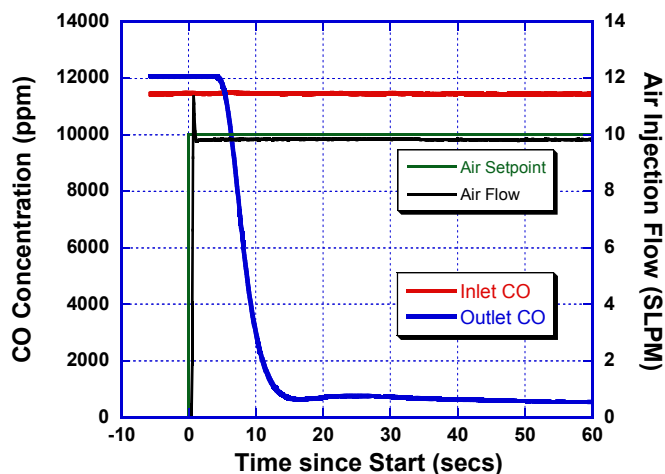


**Figure 2.** Outlet CO concentration measured as a function of time since the start of air injection.

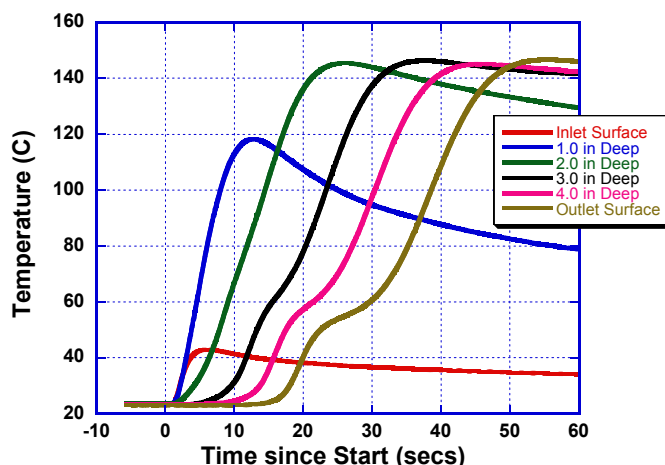


**Figure 3.** Temperature response at various depths in the monolith during startup.

The startup transient experiments demonstrate that the outlet CO concentration can be decreased rapidly. A low catalyst light-off temperature makes this feasible. Based on the rapid response within 15 s, a fast start less than 30 s appears feasible. Quantification of the sampling delays is needed and the startup performance needs to be confirmed in a multi-stage reactor.

Future experiments will examine the composition and startup transient response of multi-stage PrOx reactors to confirm the feasibility of CO control using these methods. Startup at higher inlet CO concentrations will be examined to determine the feasibility of high CO startup.

**Acknowledgement.** This work was funded through the DOE Office of Hydrogen, Fuel Cells and Infrastructure Technologies Program, Program Manager Nancy Garland.

# STRUCTURE SENSITIVITY OF SELECTIVE CO OXIDATION IN H<sub>2</sub> OVER WATER-PRETREATED Pt/ $\gamma$ -Al<sub>2</sub>O<sub>3</sub>

In Hyuk Son, Soon Cheon Byeon\*, and Alan M. Lane

Department of Chemical Engineering, University of Alabama, Tuscaloosa, AL, 35487, USA \*Center for Materials for Information Technology (MINT), University of Alabama, Tuscaloosa, AL 35487

## Introduction

Carbon monoxide must be removed from the hydrogen feed to Polymer Electrolyte Fuel Cells (PEFCs) because it poisons the anode. A new pretreatment method, involving saturation of the catalyst with liquid water during reduction (water-pretreatment), improved activity and selectivity of Pt/ $\gamma$ -Al<sub>2</sub>O<sub>3</sub> in the low-temperature preferential oxidation (PROX) of CO in H<sub>2</sub>. TEM, XRD, and CO/H<sub>2</sub>-TPD experiments confirmed that the improvements were due to smaller (~2 nm) Pt particles with an alloy-like interaction between the Pt and Al atoms, making them particularly stable against sintering. The stabilization of Pt particles is related to increased H<sub>2</sub> spillover during water-pretreatment<sup>2</sup>. This catalyst has a strong SMSI that increases the reducibility of alumina. Structure sensitivity is quite controversial concerning supported Pt catalysts and depends on the oxide support and the Pt dispersion. Evidences by XPS will show that the water-pretreated Pt/ $\gamma$ -Al<sub>2</sub>O<sub>3</sub> is structure sensitive in the selective CO oxidation in H<sub>2</sub> rich condition.

## Experimental

**Activity tests:** The following notation identifies the catalysts: (W)XPt/Al where W is Water-pretreatment, X is wt%, and Al is  $\gamma$ -Al<sub>2</sub>O<sub>3</sub>. Four kinds of pretreatments were applied to 5Pt/Al: calcination at 400°C in air (After Cal. 5Pt/Al), reduction at 400°C in H<sub>2</sub> after at 120°C in He (LR5Pt/Al), conventional reduction in H<sub>2</sub> at 500°C (5Pt/Al), and water-pretreatment (W5Pt/Al)<sup>1</sup>. For various pretreated catalysts, CO conversion and selectivity were measured in the simulated reforming gases (1% CO, 1% O<sub>2</sub>, H<sub>2</sub> balance, and total flow rate: 100 ml/min).

**Characterization methods:** Pt dispersions and their particle size were measured by CO chemisorption, TEM, and XRD. To investigate the oxidation state of Pt and alumina after different treatments, X-ray photoelectron spectroscopy (XPS) was used. A Kratos Axis 165 was used with an Al anode as the X-ray source.

## Results and Discussion

After preferential oxidation (PROX) of CO in H<sub>2</sub>, the average particle sizes of 5Pt/Al and W5Pt/Al are 16 and 2 nm, respectively<sup>1,2</sup>. The dispersion of 5Pt/Al is 0.16 (CO/Pt mol ratio). Due to large amounts of H<sub>2</sub> spillover, the dispersion of W5Pt/Al cannot be measured accurately<sup>1</sup>. For After Cal. 5Pt/Al, its average particles size and dispersion were not measured. For LR5Pt/Al, the dispersion and average particle size are around 0.41 (CO/Pt) and 3 nm, respectively<sup>3</sup>. Thus, W5Pt/Al and LR5Pt/Al have better dispersions and smaller Pt particles. While, 5Pt/Al has less dispersed bigger Pt particles. Activity and selectivity of CO oxidation in H<sub>2</sub> were tested over the various pretreated catalysts as a function of temperature and the data were obtained after 1 hour for the steady-state reaction (Figure 1). The CO oxidation activity of After Cal. 5Pt/Al was low due to the oxide type Pt particles. W5Pt/Al showed higher CO oxidation activity and selectivity over the entire temperature range, particularly at low temperatures (below 100°C).

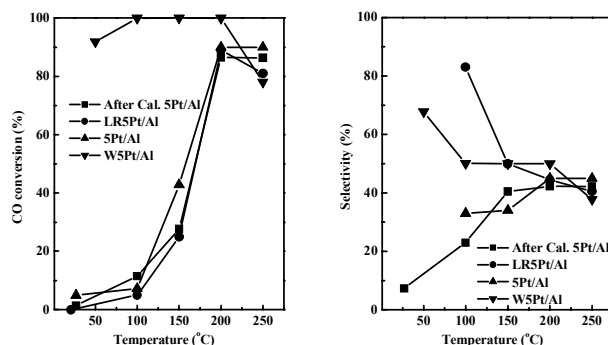


**Figure 1.** CO conversion, O<sub>2</sub> conversion, and selectivity for the catalysts after calcination at 400°C (After Cal. 5Pt/Al), lower temperature reduction at 400°C (LR5Pt/Al), reduction at 500°C (5Pt/Al), and water-pretreatment (W5Pt/Al) (1% CO, 1% O<sub>2</sub>, H<sub>2</sub> balance, and total flow rate: 100 ml/min).

LR5Pt/Al, although it has more highly dispersed, small Pt particles (similar to W5Pt/Al), it showed the lowest activity over the entire temperature range. Over 100°C, the less dispersed bigger Pt particles on 5Pt/Al have a higher CO oxidation activity compared to the better dispersed smaller Pt particles on LR5Pt/Al, agreeing with previous studies<sup>3</sup>. In flowing He (as opposed to H<sub>2</sub>), larger Pt particles on alumina have a higher CO oxidation rate because bridged CO adsorption, a weaker interaction caused by a weaker “strong metal-support interaction” (SMSI), facilitates oxygen adsorption on Pt. Highly dispersed small Pt particles have a lower CO oxidation rate because linearly adsorbed CO, a stronger interaction caused by stronger SMSI, blocks oxygen adsorption on Pt.

Thus, on W5Pt/Al, the highly dispersed, small Pt particles are different. Due to the H<sub>2</sub> spillover, the CO oxidation activity was higher under hydrogen-rich reaction conditions [2]. The controversy of structure-sensitivity/insensitivity of the CO oxidation reaction in H<sub>2</sub> over Pt on alumina catalysts cannot be determined simply based on particle size and dispersion. We hypothesize that much larger SMSI caused the greater H<sub>2</sub> spillover. The following XPS and H<sub>2</sub>-TPR studies will illustrate the different interactions between Pt and alumina according to their oxidation states.

XPS tests were performed for understanding the differences in the interaction between Pt particles and alumina after the reaction. The states of Pt (metal Pt, Pt<sup>0</sup>, PtO, PtO<sub>2</sub>, or Pt-Al alloy) over catalysts were analyzed using the BE line positions of Pt 4d and Al 2s spectra (Figures 2 and 3). For After Cal. 5Pt/Al, the highest Pt 4d<sup>5/2</sup> line position (317 eV) assigns to PtO<sub>2</sub> which is lower CO oxidation activity sites. The Pt 4d<sup>5/2</sup> line positions of LR5Pt/Al, 5Pt/Al, and W5Pt/Al are 0.4, 1.1, and 1 eV higher than Pt metal. Thus, for LR5Pt/Al, the state of Pt is much closer to metallic Pt. The Pt 4d<sup>5/2</sup> BEs of 5Pt/Al and W5Pt/Al are centered at similar positions (315.2 and 315.1 eV, respectively), while that of W5Pt/Al is skewed toward higher BEs. For W5Pt/Al, the positive shift is caused by the electron-deficiency of Pt from the Pt-Al alloy. Under reducible reaction conditions, the positive shift effect is less because of the oxidized Pt state (PtO<sub>2</sub>)<sup>4</sup>. Thus, W5Pt/Al has the characteristics of Pt-Al alloy states.

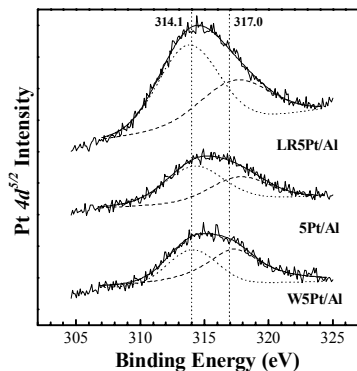


**Figure 2.** Deconvolution of Pt  $4d^{5/2}$  XPS spectra.

The following analysis of Al 2s states supports the hypothesis of Pt-Al alloy formation on W5Pt/Al. Mecoville et al.<sup>5</sup> reported that Al 2p BEs chemically shift up 2.5-2.7 eV from metallic Al (72.5 eV) in an O<sub>2</sub> atmosphere due to surface oxides on Al (111). In the same way, the higher BEs of After Cal. 5Pt/Al (119.4 eV) and 5Pt/Al (118.7 eV) were caused by the oxide state from chemically adsorbed O<sub>2</sub> (highest dash line area in Figure 3). For W5Pt/Al, the shape of Al 2s is similar to LR5Pt/Al. But, its higher Al 2s BEs (119.1) indicates a higher Pt-Al alloy states. Thus, Pt particles on W5Pt/Al have a Pt-Al alloy type of interaction with stronger SMSI, while those on LR5Pt/Al are metallic Pt with a weaker SMSI.

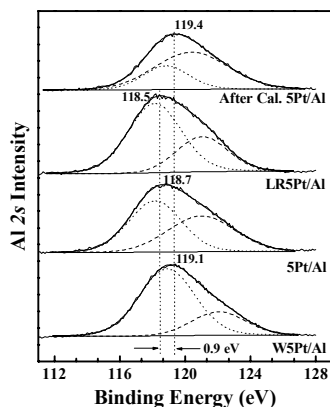


**Figure 3.** Deconvolution of Al 2s XPS spectra.

### Conclusion

The low temperature reduction method and the water-pretreatment method generated highly dispersed small Pt particles over  $\gamma$ -Al<sub>2</sub>O<sub>3</sub>. The water-pretreated catalyst showed particularly high activity for low-temperature selective CO oxidation under H<sub>2</sub> rich conditions. XPS analysis showed that highly dispersed small Pt particles with a Pt-Al alloy character existed on the W5Pt/Al with stronger SMSI that increased the reducibility of alumina. Thus, the water-pretreated Pt/ $\gamma$ -Al<sub>2</sub>O<sub>3</sub> is structure sensitive in selective CO oxidation under H<sub>2</sub> rich conditions.

### Acknowledgement.

The work presented in this paper is supported by the Center for Advanced Vehicle Technologies at the University of Alabama, which is funded by the U.S. Department of Transportation Federal Highway Administration under Grant DTFH61-99-X-00007 and by the DOE EPSCoR Implementation Grant DE-FG02-ER45867.

### References

- (1) Son, I. H.; Shamsuzzoha, M.; and Lane, A. M. *J. Catal.* **2002**, *210* (2), 460.
- (2) Son, I. H.; and Lane, A. M. 2nd Topical Conference on Fuel Cell Technology, AIChE 2003 annual meeting, April, **2003**, New Orleans, Louisiana, U.S.A.,.
- (3) Sarkany, J.; and Gonzalez, R. D. *Appl. Catal.* **1982**, *4*, 53.
- (4) Bouwman, R.; and Biloen, P. *J. Catal.* **1997**, *48*, 209.
- (5) Mcconville, C. F.; Seymour, D. L.; Woodruff, D. P.; and Bao, S. *Surf. Sci.* **1987**, *188*, 1.

# PREFERENTIAL CATALYTIC OXIDATION (PROX) OF CO FROM MODEL REFORMATES FOR PEM FUEL CELLS

Bong-Kyu Chang and Bruce J. Tatarchuk\*

Center for Microfibrous Materials Manufacturing (CM<sup>3</sup>)  
Department of Chemical Engineering,  
Auburn University, Auburn, AL 36849

## Introduction

During the last several decades, there has been a significant increase in the research on fuel cells since it can offer a cleaner alternative for conventional internal combustion engines. Due to both kinetic and thermodynamic constraints of hydrocarbons (e.g.: methanol) reforming, however, significant concentration of CO are produced from the hydrogen producing catalytic reformers. And there is a limit, unfortunately, regarding the thermodynamic conversion of the water-gas shift reaction (WGS), so that a CO concentration which is sufficiently low to be acceptable by the PEMFC system cannot be achieved using WGS only. The reformat coming from the fuel processing section contains 50~65 vol% H<sub>2</sub>, 25~40 vol% CO<sub>2</sub>, 2~5 vol% H<sub>2</sub>O, and 1 vol% CO. The fuel cell performance significantly deteriorates if the feed stream contains even trace amount of CO (more than 20 ppm) since the Pt or Pt-Ru anodes are poisoned by CO, which strongly chemisorbs on the active sites, thus blocking the sites where the dissociation/oxidation of H<sub>2</sub> takes place. Among the many approaches to reduce CO concentration in the reformed gas mixture, selective catalytic oxidation of CO to CO<sub>2</sub> has been found to be the most effective way to remove the trace amount of CO from hydrogen.

In our previous study<sup>1</sup>, over 150 catalysts were evaluated for selective oxidation of CO in model reformat in the temperature range of from room temperature to 250°C. Based on the amount of catalyst used, Pt/ $\gamma$ -Al<sub>2</sub>O<sub>3</sub>, promoted Pt-M/ $\gamma$ -Al<sub>2</sub>O<sub>3</sub>, Au/ $\alpha$ -Fe<sub>2</sub>O<sub>3</sub>, and CuO-CeO<sub>2</sub>, showed complete CO conversion activity in model reformat in integral reactor conditions. In the present study, catalytic activities of the four catalysts are investigated in differential reactor conditions and reveal that the promoted Pt-M/ $\gamma$ -Al<sub>2</sub>O<sub>3</sub> catalyst is a superior candidate compared to other catalysts. The promoted Pt-M/ $\gamma$ -Al<sub>2</sub>O<sub>3</sub> catalyst is, then, examined in the presence of excess water for practical PEM fuel cell applications and the result indicates that the promoted Pt-M/ $\gamma$ -Al<sub>2</sub>O<sub>3</sub> catalyst retains its highest activity even in the presence of 30vol% water in the feed gas.

## Experimental

Catalysts are prepared by conventional co-precipitation or incipient-wetness method followed by drying and calcination processes.

Differential reactor experiments are carried out using a 4mm I.D. quartz tube reactor. 0.01g (10mg) of catalysts are diluted with 0.1g of inert support material ( $\alpha$ -Al<sub>2</sub>O<sub>3</sub>) to make the reactor isothermal. The particle size is 150-250  $\mu$ m (60-100 mesh). Dry feed gas consists of 1% CO, 1% O<sub>2</sub>, 20.6% CO<sub>2</sub>, 40% H<sub>2</sub>, and balance N<sub>2</sub> and feed flow rate is controlled by gas mass flow controller. The total feed flow rate is changed from 50 to 200 (ml/min) to produce the differential reactor conditions. The temperature range investigated in the differential reactor study is 100 to 180°C.

The reaction products were analyzed with gas chromatograph (TCD-GC);

$$\text{Conversion of CO to CO}_2 (\%) = \frac{(C_{\text{CO}}^{\text{in}} - C_{\text{CO}}^{\text{out}})}{C_{\text{CO}}^{\text{in}}} \times 100\%$$

Selectivity for CO oxidation over H<sub>2</sub> oxidation (%)

$$= \frac{\text{O}_2 \text{ consumption by CO oxidation} / \text{Total O}_2 \text{ consumption} \times 100\%}{= \frac{1}{2}(C_{\text{CO}}^{\text{in}} - C_{\text{CO}}^{\text{out}}) / (C_{\text{O}_2}^{\text{in}} - C_{\text{O}_2}^{\text{out}}) \times 100\%}$$

## Results and Discussion

### (1) Integral reactor

In our previous study<sup>1</sup>, over 150 catalysts were evaluated for selective oxidation of CO in H<sub>2</sub>-rich gas in the temperature range of from room temperature to 250 °C.

Among the catalysts investigated Pt/ $\gamma$ -Al<sub>2</sub>O<sub>3</sub>, promoted Pt-M/ $\gamma$ -Al<sub>2</sub>O<sub>3</sub>, Au/ $\alpha$ -Fe<sub>2</sub>O<sub>3</sub>, and CuO-CeO<sub>2</sub>, showed extremely high CO conversion activity in model reformat in integral reactor conditions based on the amount of catalyst loaded. Figure 1 shows the results of the integral reactor study.

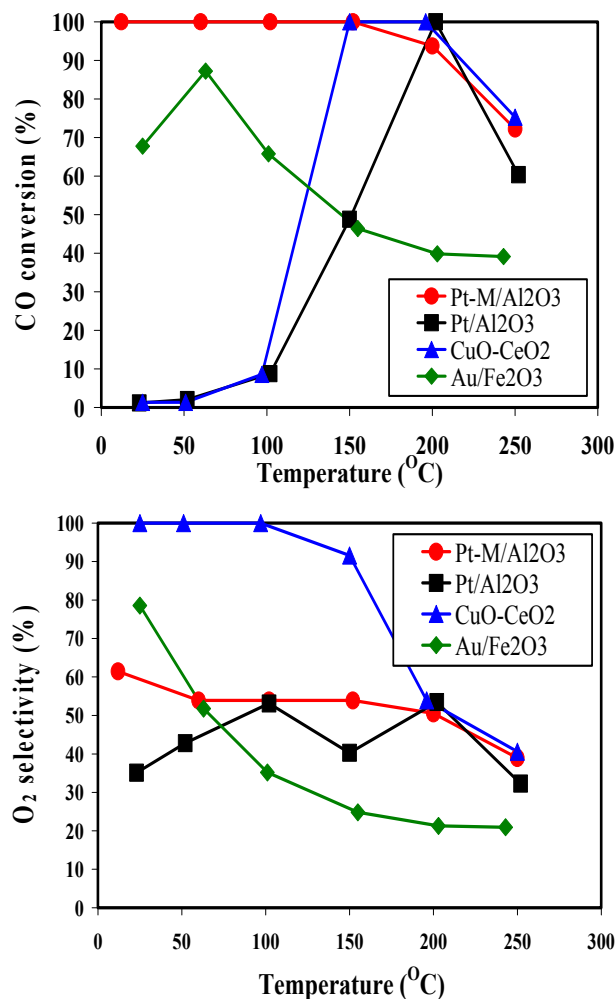


**Figure 1.** Comparison of the performance of Pt-M/Al<sub>2</sub>O<sub>3</sub> (1.1wt%Pt), Pt/Al<sub>2</sub>O<sub>3</sub> (1.1wt%Pt), Au/ $\alpha$ -Fe<sub>2</sub>O<sub>3</sub> (5at%Au), and CuO-CeO<sub>2</sub> (5.7% Cu, Cu:Ce = 0.143:1) in the presence of CO<sub>2</sub> and H<sub>2</sub>O. (1.1% CO, 1.1% O<sub>2</sub>, 20.6% CO<sub>2</sub>, 40% H<sub>2</sub>, 2.9% H<sub>2</sub>O, and balance N<sub>2</sub> in the reactant feed, 0.1g catalyst, total flow rate 100 ml/min)

And table 1 summarizes the comparison of the four catalysts in integral reactor in terms of active reaction temperature range, CO conversion, and O<sub>2</sub> selectivity.

**Table 1. Comparison of the performance of Pt-M/Al<sub>2</sub>O<sub>3</sub> (1.1wt%Pt), Pt/Al<sub>2</sub>O<sub>3</sub> (1.1wt%Pt), Au/α-Fe<sub>2</sub>O<sub>3</sub> (5at%Au), and CuO-CeO<sub>2</sub> (5.7% Cu, Cu:Ce = 0.143:1) in the presence of CO<sub>2</sub> and H<sub>2</sub>O. (1.1% CO, 1.1% O<sub>2</sub>, 20.6 % CO<sub>2</sub>, 40% H<sub>2</sub>, 2.9% H<sub>2</sub>O, and balance N<sub>2</sub> in the reactant feed, 0.1g catalyst, total flow rate 100 ml/min)**

Catalyst	Temp. (°C)	CO conversion (%)	O <sub>2</sub> selectivity (%)
Pt-M/Al <sub>2</sub> O <sub>3</sub>	RT – 200	90 – 100	50 – 60
Pt/Al <sub>2</sub> O <sub>3</sub>	200	80 – 100	20 – 50
Au/α-Fe <sub>2</sub> O <sub>3</sub>	RT – 50	65 – 95	50 – 80
CuO-CeO <sub>2</sub>	120 – 200	80 – 100	50 – 95

## (2) Differential reactor

A differential reactor is defined in which the reaction rate is almost constant throughout the reactor due to the minimal changes in the reactant concentration. The reaction rate (r) thus can be calculated according to

$$\frac{W}{F} = \frac{X}{r} \quad \text{or} \quad X = r \left( \frac{W}{F} \right)$$

Since reaction rate is a constant, a plot of reaction conversion (X) versus inverse space velocity (W/F) should be linear with the slope equal to the reaction rate (r).

Figure 2 demonstrates differential reactor conditions at conversions below 15% for Pt-M/γ-Al<sub>2</sub>O<sub>3</sub>, Pt/γ-Al<sub>2</sub>O<sub>3</sub>, Au/α-Fe<sub>2</sub>O<sub>3</sub>, CuO-CeO<sub>2</sub>, respectively. The purpose of this study is to compare the catalytic activity of the four catalysts in differential reactor conditions since all the four catalysts show complete CO conversion activity in integral reactor conditions in which the true catalytic activity of the four catalysts cannot be readily compared. As it can be clearly seen, the reaction rate (slope) increases as temperature increases from 100 to 180°C for all four catalysts. Figure 3 compares Pt-M/γ-Al<sub>2</sub>O<sub>3</sub>, Pt/γ-Al<sub>2</sub>O<sub>3</sub>, Au/α-Fe<sub>2</sub>O<sub>3</sub>, CuO-CeO<sub>2</sub> catalysts in differential reactor conditions at 150°C. The catalytic activity for the selective catalytic oxidation of CO in H<sub>2</sub> decreases in differential reactor conditions in the following order; Pt-M/γ-Al<sub>2</sub>O<sub>3</sub> > CuO-CeO<sub>2</sub> > Au/α-Fe<sub>2</sub>O<sub>3</sub> > Pt/γ-Al<sub>2</sub>O<sub>3</sub>.

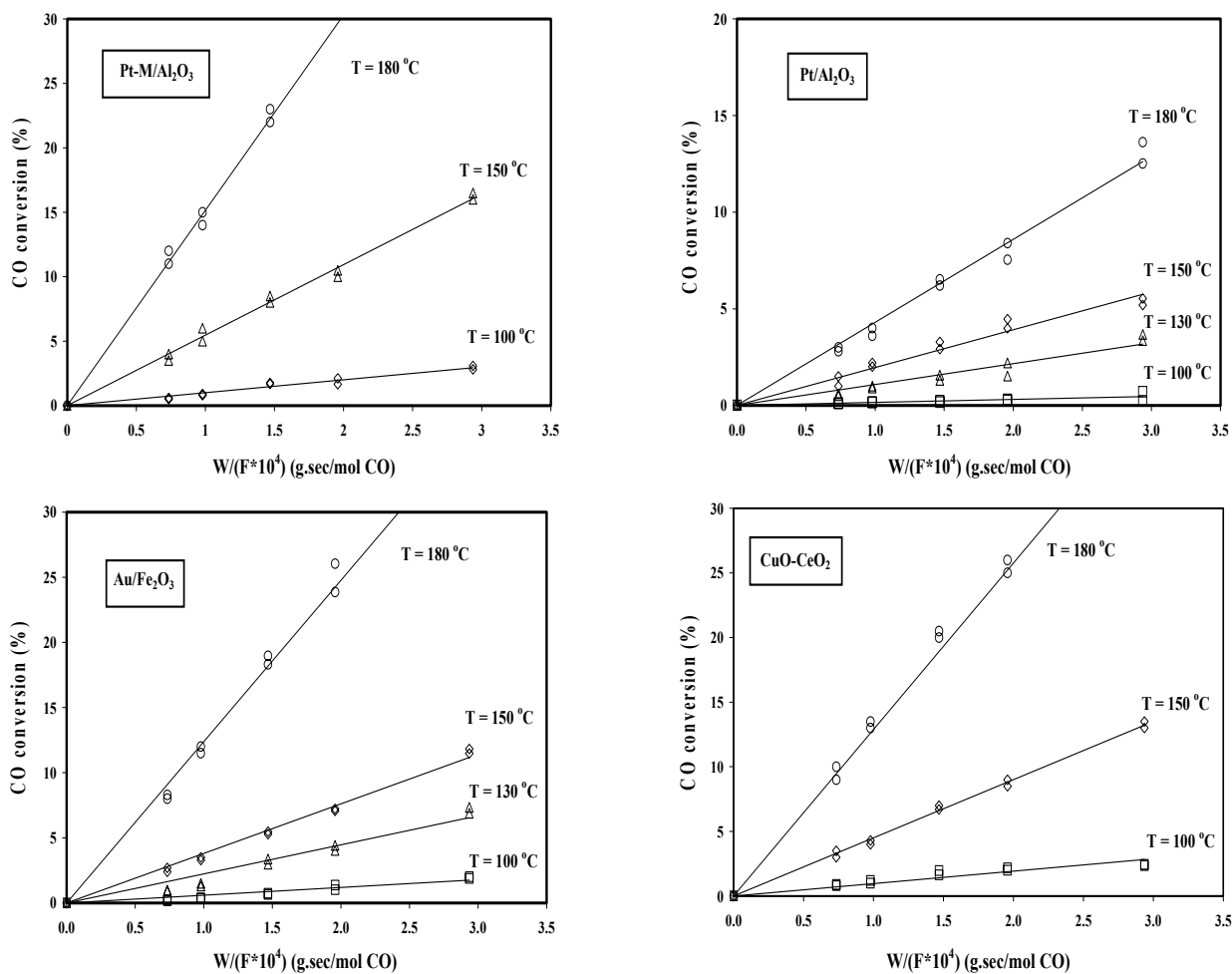


**Figure 2.** Demonstration of differential reactor conditions for Pt-M/Al<sub>2</sub>O<sub>3</sub> (1.1wt%Pt), Pt/Al<sub>2</sub>O<sub>3</sub> (1.1wt%Pt), Au/α-Fe<sub>2</sub>O<sub>3</sub> (5at%Au), and CuO-CeO<sub>2</sub> (5.7% Cu, Cu:Ce = 0.143:1). (1.1% CO, 1.1% O<sub>2</sub>, 20.6 % CO<sub>2</sub>, 40% H<sub>2</sub>, and balance N<sub>2</sub> in the reactant feed)

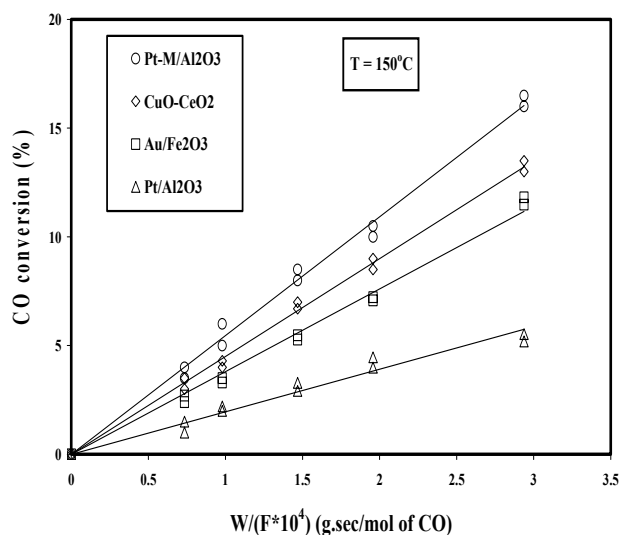


**Figure 3.** Comparison of the four catalysts in the differential reactor conditions ( $T = 150^{\circ}\text{C}$ )

### Conclusions

Pt/ $\gamma$ -Al<sub>2</sub>O<sub>3</sub>, promoted Pt-M/ $\gamma$ -Al<sub>2</sub>O<sub>3</sub>, Au/ $\alpha$ -Fe<sub>2</sub>O<sub>3</sub>, and CuO-CeO<sub>2</sub> have demonstrated promising catalytic activities for selective CO oxidation in integral reactor conditions in the temperature range from 298 to 523K with up to 30% H<sub>2</sub>O. Catalytic activities of these four systems have been further evaluated in differential reactor studies in the absence of heat and mass transfer limitations. Specific activities occur in the order: promoted Pt-M/ $\gamma$ -Al<sub>2</sub>O<sub>3</sub> > CuO-CeO<sub>2</sub> > Au/ $\alpha$ -Fe<sub>2</sub>O<sub>3</sub> > Pt/ $\gamma$ -Al<sub>2</sub>O<sub>3</sub>. Comparison of specific activities and selectivities over the temperature range from 298 to 473K indicate that promoted Pt-M/ $\gamma$ -Al<sub>2</sub>O<sub>3</sub> is the best candidate for operation with up to 30% H<sub>2</sub>O from 298 to 373K.

### References

1. Chen. L.; Chang. B-K.; Lu. Y.; Yang. W.; and Tatarchuk. B. J. Prepr. Pap. - *Am. Chem. Soc., Div. Fuel Chem.*, **2002**, 47 (2), 609.

---

\* Corresponding Author. Tel: 1-334-844-2023; Fax: 1-334-844-2065  
E-mail address: brucet@eng.auburn.edu

## Preferential oxidation of CO in a microreactor with a single channel

L. Bednarova, X. Ouyang, H. Chen, W. Y. Lee, R. S. Besser

Department of Chemical, Biochemical and Materials Engineering,  
Stevens Institute of Technology, Hoboken, NJ 07030, USA

### Introduction

Fuel cells have been extensively studied in the last two decades for different stationary and mobile applications. Hydrogen-rich reformat is the preferred feed for fuel cells and can be produced in a reformer by partial oxidation or steam reforming followed by water-gas shift reaction to reduce CO to about 1%. The remaining CO in the H<sub>2</sub>-rich reformat is further decreased to less than 10 ppm CO by selective catalytic oxidation/preferential oxidation of CO ("PrOx") using O<sub>2</sub> or air to avoid poisoning of the Pt anode in the fuel cell.

Therefore, the conversion of CO during PrOx must be at least 99.9% in order to achieve a concentration of 10 ppm or less. Furthermore, the PrOx unit should be operated between 80°C and 200°C to minimize additional heating or cooling steps. Operation at low temperature is also very important for start-up in transportation application fuel cells. Therefore, the PrOx system must operate over a wide temperature range to be practical (1).

Research in the microreactor technologies has been extensive and intensive in the past several years. We have been deeply involved in this research and have now designed a simple, robust microreactor with a single channel for rapid catalyst characterization. The advantage over a multichannel reactor is that possible maldistribution of flow is eliminated. The channel length was estimated by preliminary modeling to be sufficient for treating approximately 5 Ncm<sup>3</sup>/min of reformat. This microreactor is also suitable for acquisition of appropriate kinetic data which can be used for design of future PrOx microreactors and for scale up for higher throughputs. The fabrication is inexpensive and straight forward which makes the technology attractive because the microreactors can be disposed after single use.

Catalysts for PrOx usually consist of Pt (2), Au (3) or promoted Pt, Ru, Rh, Pd, alloys of Pt-Sn or Pt-Ru, or Rh (4) supported on alumina (2, 3, 4), silica (4), or zeolites (2). Copper catalysts on alternative supports such as ceria, ceria-samarium, or other ceria-promoted supports are also being developed in an attempt to provide selective surface oxygen for CO oxidation at low temperatures (3).

We fabricated silicon microreactors and deposited a thin-film of Pt/Al<sub>2</sub>O<sub>3</sub> catalyst that was prepared by sol-gel technique. Different sequences were used to deposit the catalyst on the microreactor walls. The microreactor was tested for preferential oxidation of CO to reduce CO in reformat. The goal was to reduce CO content in the stream from 1.7% to below 10 ppm using the microchannel reactor.

### Experimental

The micro-scale chemical reactors were successfully fabricated on p-type <100> 4 and 8 inch silicon wafers without any oxide layer by using state-of-the-art silicon bulk micromachining techniques. The reactor is comprised of dual gas inlets, a mixing region, and a single reaction channel with outlet. Two different microreactors with different dimensions were tested: the first one had a channel 4.5 cm long, 500 μm wide and 610 μm deep channel (Figure 1a) and the channel in the second one was 21.9 cm long and 500 μm wide and 75 μm deep. Each individual silicon chip was anodically bonded with a Pyrex<sup>TM</sup> glass piece for hermeticity. The catalyst was deposited in the microchannel either before the silicon chip was sealed with a Pyrex<sup>TM</sup> glass or after anodic bonding (AB) of chip with the glass.

Platinum supported on alumina was synthesized using a sol-gel technique (5, 6, 7). Alumina support was prepared from aluminum isopropoxide (Aldrich, 99.99+%) by adding it to deionized water at 85 °C to start the hydrolysis reaction resulting in a sol. After 45 min under continuous stirring, HNO<sub>3</sub> was added. Platinum metal was introduced by using a solution of H<sub>2</sub>PtCl<sub>6</sub>.xH<sub>2</sub>O (Aldrich, 99.9+%) in 1,3-butanediol (Aldrich, 99%, anhydrous) at room temperature. The platinum content in the catalyst was 2 wt%.

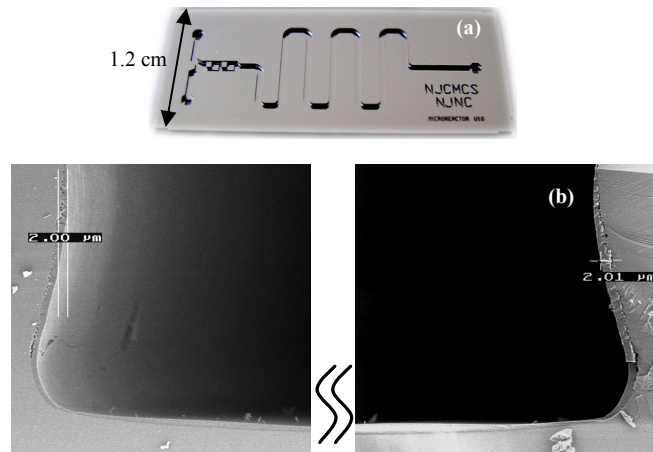


**Figure 1.** (a) Silicon microreactor for reaction characterization (BL\_A3, BL\_D7 and BL\_C3 in Table 1); (b) Cross-section of left and right side of microchannel with 2μm layer of catalyst (BL\_A3)

The gel (liquid catalyst precursor) deposited in the microchannel was dried in air at 120 °C for 12 hours or at 40 °C for 24 hours, respectively (Table 1), and then calcined at 500 °C for 2 hours. The samples were investigated by XRD (Siemens D5000).

**Table 1. Summary of microreactors**

Reactor ID	Microchannel length [cm]	Catalyst deposition	Catalyst [mg]	Drying temperature [°C]
BL_A3	4.5	Before AB	0.54	120
BL_D7	4.5	Before AB	0.97	120
BL_C3	4.5	After AB	0.45	120
IT_A2	21.9	After AB	N/A (0.2) <sup>1</sup>	40

The microreactor was tested in a microkinetic array test rig wherein more than one reactor could be characterized simultaneously. In order to begin testing, the reactor was evacuated at room temperature for 30 minutes followed by heating (10°C/min) in pure H<sub>2</sub> (5 Ncm<sup>3</sup>/min) to 450 °C and kept at this temperature for 4 hours, then allowed to cool to room temperature. Feed was introduced and temperature was stepwise increased at 10 °C/min from 20 °C to 100 °C, 120 °C, 140 °C, 160 °C, 180 °C, 200 °C, 240 °C, 260 °C, 280 °C and 300 °C. The temperature was kept at each set point for 40-60 min. The feed consisted of simulated reformat (1.7% <sup>13</sup>CO, 49.3% H<sub>2</sub> and N<sub>2</sub> as balance) and dry air (78.1% N<sub>2</sub> and 21.9% O<sub>2</sub>). The flow of the reformat was kept at 5 Ncm<sup>3</sup>/min and dry air at 0.5 Ncm<sup>3</sup>/min (λ = 2.57). The reformat passes through the reaction zone in the microreactor designated "BL" in about 0.1 second and through microreactor "IT" in about 0.9 second. The products were analyzed by gas chromatograph (Varian CP-4900) and mass spectrometer (Stanford Research Systems QMS-200).

<sup>1</sup> estimated to 0.2 mg

## Results and Discussion

The surface area of the catalyst is 480 cm<sup>2</sup>/g. No peaks were observed on the XRD pattern, which indicates that the alumina structure was amorphous. The adhesion of the catalyst to the microchannel walls is excellent and fairly uniform (Figure 1b).

The feed was introduced at room temperature and no CO conversion was observed. The conversion of CO increased with increasing temperature; however, the activity of the catalyst in all microreactors was low (1<sup>st</sup> cycles in Figure 2). There did not appear to be a significant difference between performance of the microreactors. Each microreactor after being tested to up to 300 °C was reduced again in pure hydrogen. A new testing cycle was performed (2<sup>nd</sup> cycles in Figure 2) and CO conversion was monitored. The conversion increased with temperature and catalyst activity improved dramatically for some of them (BL\_A3, BL\_D7). The differences will be discussed further.

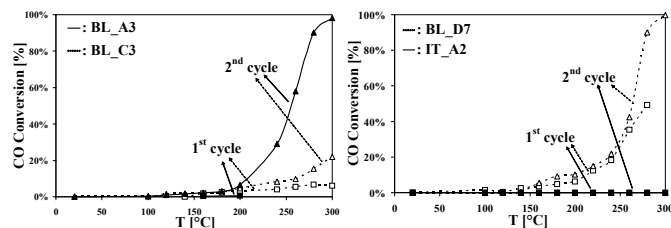


**Figure 2.** The effect of temperature on CO conversion in microreactors: a/ BL\_A3, BL\_C3; b/ BL\_D7, IT\_A2. Feed: 5 Ncm<sup>3</sup>/min reformat (1.7% <sup>13</sup>CO, 49.3% H<sub>2</sub> and N<sub>2</sub> as balance), 0.5 Ncm<sup>3</sup>/min air

Microreactor BL\_A3 contains about the same amount of the catalyst as BL\_C3 (Table 1) and the geometry of both reactors is identical. The difference between them is that microreactor BL\_A3 had the catalyst deposited before being sealed while the other was first sealed and then the catalyst was infiltrated into the closed channel. That means that the microreactor BL\_A3 has catalyst deposited on the silicon microreactor as well as on the glass on the top while BL\_C3 contains catalyst only on three walls (the silicon part of microreactor). Because the catalyst amount is the same in the reactors, the catalyst layer is thicker in BL\_A3 than in BL\_C3. However, it is believed that this difference cannot be attributed to the difference in catalytic activity. It is proposed that the catalytic activity is rather enhanced due to performed pretreatment. The microreactor BL\_A3 with catalyst was exposed during anodic bonding to 450 °C in furnace without controlled environment followed by *in-situ* reduction at 450 °C in the test rig (oxidation-reduction pretreatment). The latter microreactor (BL\_C3) was pretreated only by reduction.

The microreactors were tested across a wide temperature range, starting at room temperature and increasing in steps to up to 300 °C. As mentioned before, the catalyst activity was low in the investigated temperature range. The microreactors with the thin-film catalyst were studied further. The microreactors were reinstalled in the microkinetic array and reduced again as they were exposed to air while stored. Reformat was introduced again at room temperature and stepwise increased to 300 °C as during previous testing (Figure 3a). The activity of catalysts in all microreactors was higher than during the first cycle of testing. There can be at least two explanations: (a) platinum was not fully reduced during the first testing cycle; (b) the catalyst behavior changed, possibly due to catalyst structural changes. We believe that the second possibility is more likely because the platinum was reduced before each cycle following the same procedure and the microreactors were exposed to

air before each reduction. It appears that repeated catalyst exposure to higher temperature is likely an important factor in enhancing the catalyst activity.

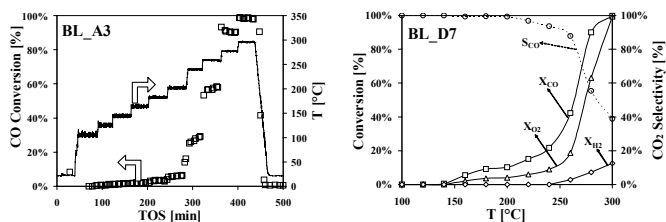


**Figure 3.** a/ CO conversion as a function of temperature and time on stream (reactor BL\_A3); b/ Effect of temperature on conversion of CO, O<sub>2</sub> and H<sub>2</sub> (microreactor BL\_D7). Feed: 5 Ncm<sup>3</sup>/min reformat (1.7% <sup>13</sup>CO, 49.3% H<sub>2</sub> and N<sub>2</sub> as balance), 0.5 Ncm<sup>3</sup>/min air

It should be noted that the microreactors with a highly active catalyst show a characteristic behavior. The conversion of CO increases with increasing temperature fairly linearly and there is a characteristic temperature at which we observe a steep increase in conversion reaching almost 100%. This is in agreement with previous studies (8). When the conversion of CO reached almost 100% we observed that hydrogen starts to oxidize, thus, the selectivity towards CO<sub>2</sub> decreases dramatically (Figure 3b). Therefore, there is a narrow temperature window at which high CO conversion can be obtained and consumption of hydrogen is not yet significant.

## Conclusions

Thin-film Pt/Al<sub>2</sub>O<sub>3</sub> catalyst was deposited on walls of microreactors with two methods and its activity was evaluated after different pretreatments. It was found that a more active catalyst is obtained after oxidation-reduction pretreatment than after only reduction. Moreover, the catalysts became more active after repeated catalytic testing.

**Acknowledgement.** The authors gratefully acknowledge the support of DARPA (Contract No. N66001-01-X-6039) and Stevens Institute of Technology. They also thank Dr. Stanley Pau of the New Jersey Nanotechnology Consortium (NJNC) at Bell Labs for fabricating some of the reactors.

## References

- (1) Thomas, C. E.; James, B. D.; Lomax Jr., F. D.; Kuhn Jr., I. F. *Int. J. Hydrogen Energy* **2000**, *25*, 551.
- (2) Igatashi, H.; Uchida, H.; Suzuki, M.; Sasaki, Y.; Watanabe, M. *Appl. Cat. A:General* **1997**, *159*, 159.
- (3) Avgouropoulos, G.; Ioannides, T.; Papadopoulou, Ch.; Batista, J.; Hocevar, S.; Matralis, H. K. *Catalysis Today* **2002**, *75*, 157.
- (4) Dudfield, C. D.; Chen, R.; Adcock, P. L. *Int. J. Hydrogen Energy* **2001**, *26*, 763.
- (5) Yoldas, B. E. *Am. Ceramic Soc. Bul.*, **1975**, *54*(3), 289.
- (6) Manasilp, A.; Gulari, E. *Appl. Cat. B: Environmental* **2002**, *37*, 17
- (7) Besser, R.S.; Zhao, S. *Proc. 6th Int. Conf. Microreac. Techn. - IMRET VI*, **2002**, 289.
- (8) Kahlich, M. J.; Gasteiger, H. A.; Behm, R. J. *J. Catal.* **1997**, *171*, 93.

# PREFERENTIAL OXIDATION OF CO ON A NOBLE-METAL CATALYST COATED CERAMIC MONOLITH

Rajesh K. Ahluwalia, Qizhi Zhang, and Michael A. Inbody\*

Argonne National Laboratory, Argonne, IL  
\*Los Alamos National Laboratory, Los Alamos, NM

## Introduction

Whereas the anode catalyst, typically Pt-Ru, in the polymer electrolyte fuel cells has low tolerance for carbon monoxide, 10-100 ppm, reforming of gasoline and other hydrocarbon fuels generally produces 1-2% of CO. Of the many methods of removing CO from the reformer gas, such as membrane separation of H<sub>2</sub> and methanation, preferential oxidation (PrOx) of CO over noble-metal catalysts is practiced most frequently.<sup>1, 2</sup> One index for characterizing the performance of a PrOx catalyst is CO selectivity (*S*) defined as the ratio of oxygen consumed by the desired CO reaction to the total oxygen consumed by the parallel CO and H<sub>2</sub> oxidation reactions. Another related index is the process stoichiometry  $\lambda$  which is the ratio of oxygen used in relation to the theoretical amount needed for complete conversion of CO.

From the standpoint of process efficiency, it is desirable to select the PrOx catalyst and operating conditions that lead to *S* and  $\lambda$  being as close to unity as possible. Additional considerations arise if reforming is to be carried out onboard a vehicle. For fast start, the PrOx reactor must be compact and, in particular, the thermal mass of the catalyst and the components in contact with the flow should be minimized. The catalyst should maintain the fuel processor outlet CO concentration within the fuel cell stack tolerances through the startup transient and transition to normal operation. For cold start, it helps if the catalyst has low light-off temperature for CO oxidation. The catalyst should retain CO selectivity over the range of temperatures representative of cold start and normal operation. It should be capable of oxidizing high concentrations of CO if the upstream water gas shift reactor is not operating at its optimal temperature as at start-up and during up-load transients.

The purpose of this paper is to present recent results on a low temperature, supported PrOx catalyst that has shown light-off for CO oxidation at room temperature. The focus is on taking data from single-stage PrOx experiments under steady-state conditions and applying them to multi-stage reactors.

## Experimental

Engelhard Spectra-PROX I catalyst was coated on a 600-cpsi (cells per square inch) Corning monolith, 7.62 cm in diameter by 12.7 cm long, and evaluated in a single-stage test reactor shown in Fig. 1. The coated monolith, 297 g in mass, was instrumented with 0.02" K-type thermocouples inserted to various depths from the top of the monolith. The tests were conducted with a reformed gas of nominal composition 1.3% CO, 48.0% H<sub>2</sub>, 19.8% CO<sub>2</sub>, and 30.9% N<sub>2</sub> at inlet temperature of 85-100°C, the variation in temperature being caused by the injection of steam. The major gas flows were set and the air injection was varied to obtain measurements over a wide range of oxygen stoichiometry usually to identify the minimum CO concentration and limited to an outlet temperature below 300°C. The experiments were conducted at the same pressure, ~1.5 bar.

In all nine series of tests were conducted by varying CO concentration, H<sub>2</sub>O concentration, and space velocity. The test matrix included three levels of CO concentration (0.2%, 1% and 2.6%), two levels of H<sub>2</sub>O concentration (0 and 20%), and two levels of space velocity (15,000 and 30,000/h). Addition of steam and air resulted in the inlet CO concentration varying between 0.17 and 0.2% in the low range and between 1% and 1.3% in the medium range and in the space

velocity varying between 31,300/h and 38,000/h at high flow rates and between 14,800/h and 19,000/h at low flow rates.

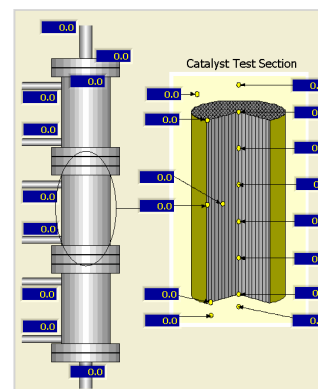


Figure 1. PrOx single-stage configuration for measurement of catalyst temperature response.

Within each series of tests oxygen stoichiometry was the variable. In all tests, the outlet oxygen concentration was below the detection limit. Tests with and without steam showed little change in the outlet CO concentration suggesting that the kinetics of water-gas shift reaction over the Pt catalyst formulation in the temperature range 100-300°C is quite slow in comparison to the oxidation reactions. Figure 2 presents typical axial temperature profiles from a test series with dry reformate, 1.3% inlet CO concentration and 30,000/h space velocity. These suggest that the oxidation reactions are essentially complete half way across the reactor for  $\lambda = 2$  but continue down the length for  $\lambda < 1$ .

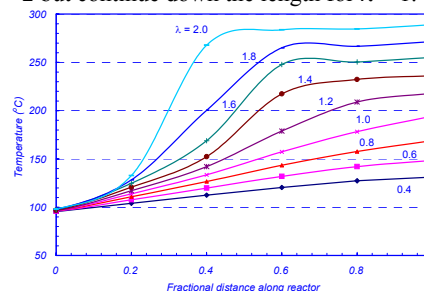
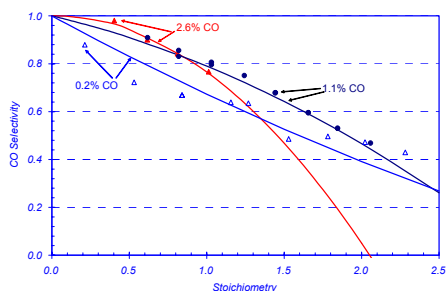


Figure 2. Measured temperature profiles for different oxygen stoichiometry at 1% inlet CO concentration and 30,000/h nominal space velocity.

We attempted to develop a correlation for CO selectivity at 30,000/h space velocity by analyzing the data at high flow rates. A plot of selectivity as a function of stoichiometry for different inlet CO concentrations revealed that *S* can be represented as a function of the reduced parameter  $\lambda X^{1/4}$ , where *X* is %CO concentration at inlet. A second-order polynomial in  $\lambda X^{1/4}$  gave an adequate correlation of selectivity with the coefficients themselves second-order polynomials in *X*. In developing the correlation given below it was assumed that the selectivity approaches one as  $\lambda X^{1/4}$  goes to zero and  $\lambda S$  was constrained to be always less than one.

$$S = 1 - (0.6394 - 0.6004X + 0.1352X^2)(\lambda X^{1/4}) + (0.0825 - 0.1554X + 0.0251X^2)(\lambda X^{1/4})^2$$

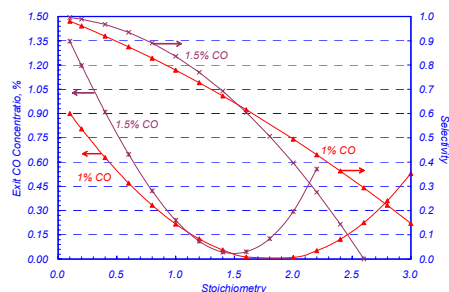
Figure 3 compares the correlation with the data and shows that CO selectivity decreases with  $\lambda$  and increases with CO concentration for  $\lambda < 0.8$ , but the behavior with respect to CO concentration is more complex for  $\lambda > 0.8$ .



**Figure 3.** Correlation of selectivity data for 30,000/h nominal space velocity.

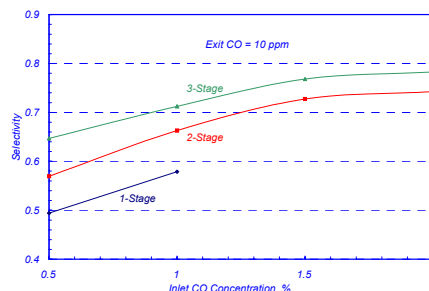
## Results and Discussion

Figure 4 shows CO conversion and selectivity in a single-stage PrOx reactor calculated using the above correlation for 100°C inlet gas temperature. For 1% inlet CO concentration, the exit CO concentration decreases monotonically with oxygen stoichiometry, becoming vanishingly small at  $\lambda = 1.8$ , and increases thereafter. We conclude that for inlet CO concentration less than 1%, a single-stage reactor is capable of reducing CO to any level and should always be operated at  $\lambda < 1.8$ . A different behavior is seen at 1.5% inlet CO concentration. Here, the exit CO concentration decreases with  $\lambda$  until it reaches a minimum of 300 ppm at  $\lambda = 1.5$  and begins to rise as  $\lambda$  is raised further. The CO selectivity actually goes to zero at  $\lambda = 2.6$  and all added O<sub>2</sub> is consumed by the oxidation of H<sub>2</sub>. Thus, more than one stage is required to reduce CO concentration to less than 300 ppm if the inlet CO concentration is 1.5% or higher.



**Figure 4.** CO conversion and selectivity in a single-stage monolith reactor.

We have used an optimization algorithm to determine the operating conditions of an intercooled multi-stage PrOx reactor that can reduce CO concentration to 10–100 ppm at highest selectivity. It is assumed that the reformed gas is cooled to 100°C between stages. Typical results for 10-ppm exit CO concentration, shown in Fig. 5, confirm that the highest CO concentration that can be handled in a one-stage monolith reactor is about 1%. The CO selectivity in a one-stage reactor is 48% at  $X = 0.5\%$  and 58% at  $X = 1\%$ . A two-stage reactor can achieve optimum selectivities of 57% at  $X = 0.5\%$ , 66% at  $X = 1\%$ , and 75% at  $X = 2\%$ . With a three-stage reactor, it is possible to obtain selectivities of 65%, 71% and 78% at inlet CO concentrations of 0.5%, 1% and 2%, respectively. At 1% inlet CO concentration, the optimum stoichiometries are 1.0 for stage 1, 1.1 for stage 2 and 2.3 for stage 3. The first stage has a selectivity of 77% and reduces the CO concentration to 0.2% from 1%. The second stage has a selectivity of 64% and reduces the CO concentration to 0.07% from 0.2%. The third stage has a selectivity of 42% and reduces CO concentration to 10 ppm from 0.07%. Together, the three stages have a combined overall stoichiometry of 1.4 and selectivity of 71%.



**Figure 5.** Optimum CO selectivities in one-, two-, and three-stage reactors with gas cooled to 100°C between the stages.

For more general application, the experimental data was used to derive a kinetic model of CO conversion. It was found that the intrinsic kinetics for CO and H<sub>2</sub> oxidation on the catalyst could be represented by the following power-law expressions.

$$r_{CO} = A_{cat} k_{CO} e^{-E_{CO}/RT} P_{CO}^{\alpha_1} P_{O_2}^{\beta_1}$$

$$r_{H_2} = A_{cat} k_{H_2} e^{-E_{H_2}/RT} P_{H_2}^{\alpha_2} P_{CO}^{\beta_2} P_{O_2}^{\beta_2}$$

where  $r$  is the reaction rate (mol/m<sup>3</sup>.s) and  $A_{cat}$  is the specific internal and external area of the catalyst (m<sup>2</sup>/m<sup>3</sup>). From data fitting and experience of others with noble metal catalysts,

$$E_{CO} = 83 \text{ kJ/mol}, E_{H_2} = 107.6 \text{ kJ/mol}, k_{CO} = 2.95 \times 10^6 \text{ mol/m}^2 \cdot \text{s},$$

$$k_{H_2} = 1.4 \times 10^8 \text{ mol/m}^2 \cdot \text{s}, \alpha_1 = -0.5, \beta_1 = 0.85, \alpha_2 = -1.0, \text{ and}$$

$\beta_2 = 0.75$ . We found that CO and H<sub>2</sub> oxidation on the coated ceramic monolith are affected by both the intrinsic kinetics and mass transfer. At low CO concentration, CO conversion and selectivity are determined by the mass transfer limitation. The model also indicates that CO selectivity decreases with gas temperature.

## Conclusions

It is feasible to conduct preferential oxidation of CO on a noble-metal catalyst coated ceramic monolith at 100°C to produce a PEFC quality gas at space velocities in excess of 38,000/h. A single-stage reactor can reduce CO concentration from 1% to 10 ppm or lower at a selectivity of 58%; more than one stage is needed for inlet CO concentration higher than 1.5%. Under the same conditions a two-stage reactor yields a selectivity of 66%. The selectivity can be further improved to 71% by incorporating a third stage. The CO selectivity decreases as CO concentration is lowered. With a three-stage reactor, it is preferable to operate stages one and two under near-stoichiometric conditions and use excess oxygen in the last stage where the CO concentration is the lowest. Numerical simulations show that at low CO concentration, conversion is limited by diffusion of CO from the bulk phase to the surface of the catalyst. Under this condition, parallel oxidation of H<sub>2</sub> can only be controlled by also limiting the diffusion of O<sub>2</sub> to the catalyst. Finally, the activation energy is higher for H<sub>2</sub> oxidation than for CO oxidation so that CO selectivity always decreases with temperature.

**Acknowledgement.** This work is supported by the Office of Hydrogen, Fuel Cell and Infrastructure Technologies (HFCIT), U.S. Department of Energy. Dr. Nancy Garland is the program manager.

## References

- (1) Kahlich, M. J.; Gasteiger, H. A.; Brehm, R. J.; *J. Catalysis*, **1997**, 171, p. 93-105.
- (2) Dudfield, C.D.; Chen, R.; Adcock, P.L.; *J. Power Sources*, **2000**, 86, p. 214-222.

# PROCESSING OF GOLD NANOPARTICLES AS FUEL CELL CATALYSTS

Jin Luo, Mathew M. Maye, Vivian W. Jones<sup>†</sup>, Chuan-Jian Zhong\*

Department of Chemistry, State University of New York at Binghamton, Binghamton, NY 13902. <sup>†</sup>3M Corporate Analytical Technology Center, 3M Center, St. Paul, Minnesota 55144.

\*cjzhong@binghamton.edu

## Introduction

The study of nanosized gold catalysis has attracted increasing interest because of the discovery of unprecedented catalytic activity and specificity of gold at nanometer sizes [1,2]. The catalytic activity of such materials requires the ability to manipulate the interparticle spatial and surface access properties [3]. This ability is inherently linked to the controllable activation of the core-shell nanostructure, or removal or reconstitution of the shell components. We report here recent findings of an investigation of core-shell assembled gold and alloy nanoparticles as catalysts for electrooxidation of carbon monoxide and methanol. This investigation is aimed at understanding the structural and morphological evolution upon catalytic activation.

## Experimental

We synthesized gold nanoparticles of 2-nm core size ( $1.9 \pm 0.7$  nm, Au<sub>2-nm</sub>) capped with decanethiolate (DT) monolayer shell using two-phase method [4]. The particles were assembled as a thin film on freshly-cleaved mica or polished glassy carbon (GC) substrates ( $0.5 \text{ cm}^2$ ) by exchange-crosslinking-precipitation route using 1,9-nonanedithiolate (NDT) as a linking or wiring agent [5]. Such a film consists of both wiring NDT and capping DT molecules. The thickness was controlled by assembling time and monitored by surface plasmon resonance absorbance and mass loading [5], which was equivalent to a few monolayers or sub-monolayer coverages.

## Results and Discussion

Figure 1 shows a typical set of AFM phase images for a thin film on mica surface to compare the morphology before and after the thermal treatment at 225 °C for 30 min. The particles are clustered into wire or chain-like morphologies. From cross-section data of corresponding topographic images, we found that there was an overlapping of  $\sim 3$  nanoparticles in average [6]. The outline of individual nanoparticles is slightly blurred or not well resolved. After the treatment, not only the outline of individual particles is better resolved, but also the chain-like feature remains intact. The removal of thioliates at this temperature was clearly supported by the tapping-mode phase imaging data. This set of data reveals that the phase contrast, which is associated with the thioliolate monolayer on the gold nanoparticle, is change upon thermal activation. Before thermal treatment, it was dark contrast (Figure 1 a); After thermal treatment, the dark contrast disappeared (Figure 1 b). In addition, our height analysis of the cross-section data reveal  $11.1 \pm 3.9$  nm and

$13.1 \pm 3.4$  nm (not shown), respectively, suggesting little change in height. The small increase in particle size is believed to be due to localized aggregation largely from the overlapped particles. The unchanged interparticle spatial feature in the xy-plane demonstrates that the interparticle spatial property can be controlled even if there is a local aggregation from the overlapped nanoparticles. The combination of the initial molecular wiring and the subsequent adhesive interaction of the particle to the substrate must have played an important role in the spatial fixation. The results of infrared reflection spectroscopic analysis (Figure 2) provide the further evidence for the removal of hydrocarbons. Our XPS data (not shown) also supported the removal of sulfur species after the thermal treatment.

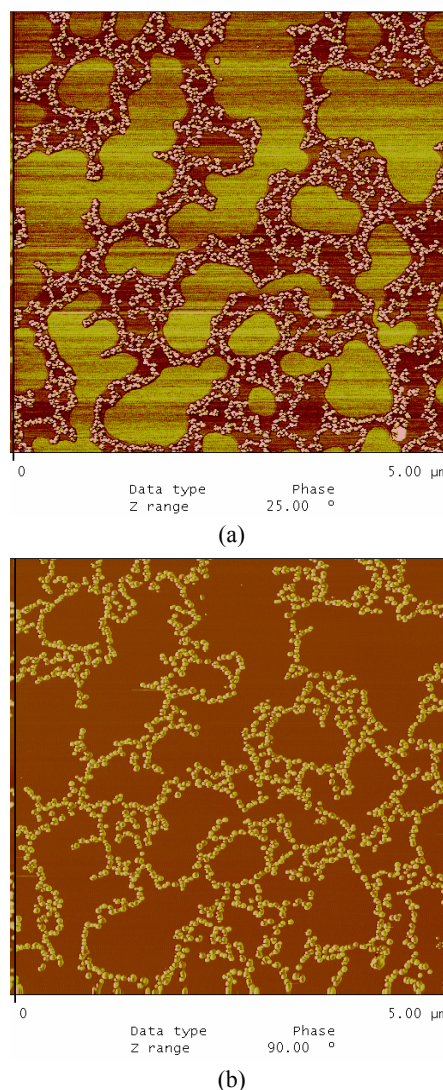


**Figure 1.** In-situ AFM phase images of a NDT-Au<sub>2-nm</sub>/mica film (a) before and (b) after heating to 225 °C for 30 min.

The catalytic activity of the activated nanoparticles was examined for the electrooxidation of CO and methanol. We note that AFM feature of the film on the conductive GC substrate is largely

similar to that on mica except for a much rougher morphology due to the substrate effect. We compare the electrocatalytic activity between the thermally activated gold catalysts with the electrochemically activated catalysts based on voltammetric data. The anodic current density for the thermally-activated film is twice as large as the electrochemically-activated catalyst (same film thickness), with the oxidation potential being slightly less positive than the electrochemically-activated film. The results demonstrate that the nanostructured catalytic activity can be thermally activated by the controlled temperature.

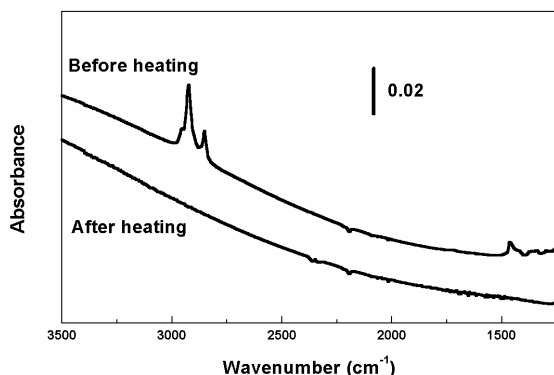


**Figure 2.** IR spectra for an NDT-Au<sub>2-nm</sub>/Au/glass film before and after heating at 250 °C for 30 min. The spectral background for the entire spectral region is not corrected.

In conclusion, we have shown that the activation of the catalytic activity of the catalysts can be controlled by manipulation of the core-shell structure, interfacial reactivity, and adhesions to the supporting substrate. These findings have important implications to the design and processing of nanostructured catalysts. We are currently investigating different molecular structures of the wiring agents, and developing an in-depth understanding of the size evolution as a function of temperature and substrate properties.

## References

- (1) Haruta, M. *Catal. Today*, **1997**, *36*, 153.
- (2) Valden, M.; Lai, X.; Goodman, D. W. *Science*, **1998**, *281*, 1647.
- (3) Zhong, C. J.; Maye, M. M. *Adv. Mater.*, **2001**, *13*, 1507.
- (4) Brust, M.; Walker, M.; Bethell, D.; Schiffrin, D. J.; Whyman, R. *J. Chem. Soc., Chem. Comm.* **1994**, 801.
- (5) (a) Leibowitz, F. L.; Zheng, W. X.; Maye, M. M.; Zhong, C. J. *Anal. Chem.*, **1999**, *71*, 5076. (b) Zheng, W. X.; Maye, M. M.; Leibowitz, F. L.; Zhong, C. J. *Anal. Chem.*, **2000**, *72*, 2190.
- (6) Luo, J.; Jones, V. W.; Maye, M. M.; Han, L.; Kariuki, N. N.; Zhong, C. J. *J. Am. Chem. Soc.*, **2002**, *124*, 13988.

# LANTHANIDE-PROMOTED SOL-GEL Ni-BASED CATALYSTS FOR STEAM REFORMING OF PROPANE

Sittichai Natesakhawat, Okan Oktar, and Umit S. Ozkan

Department of Chemical Engineering  
The Ohio State University  
140 W. 19<sup>th</sup> Ave.  
Columbus, OH 43210

## Introduction

Steam reforming of hydrocarbons to produce hydrogen is a well-established industrial process.<sup>1,2</sup> It is usually performed at high temperatures (500-950 °C) over Ni-based catalysts. However, these catalysts suffer from coke formation more severely when higher hydrocarbons are reformed at low steam/carbon ratios. Recently, on-board steam reforming of hydrocarbons for proton exchange membrane (PEM) fuel cell-powered vehicles has attracted much attention. Widespread applications of fuel cells in transportation will depend on the development of an effective and efficient fuel processing technology from existing liquid fuels. Therefore, development of novel catalysts with improved catalytic activity and stability for the steam reforming process is essential.

There is evidence in the literature pointing to an increase in the coking resistance of Ni-based catalysts with an addition of lanthanide elements.<sup>3,4</sup> Zhuang et al.<sup>3</sup> investigated the effect of cerium oxide as the promoter in supported nickel catalysts for methane steam reforming at 550 °C. It showed a beneficial effect by not only decreasing the rate of carbon deposition but also increasing the catalytic activity. Su and Guo<sup>4</sup> reported an improvement in the stability and high-temperature steam resistance of Ni/ $\alpha$ -Al<sub>2</sub>O<sub>3</sub> catalysts doped with rare earth oxides in methane steam reforming. The growth of Ni particles and the formation of inactive NiO and NiAl<sub>2</sub>O<sub>4</sub> phases were suppressed by the addition of rare earth oxides (4 wt%). In addition, oxides of heavy rare earth elements (Gd, Er, and Dy) exhibited a more pronounced effect than that of the light ones (La, Pr, Nd).

This paper presents results of propane steam reforming over sol-gel Ni-based catalysts promoted with La, Ce, and Yb. The effect of adding these lanthanide elements on reaction performance and properties of the catalysts will be discussed.

## Experimental

**Catalyst preparation.** Sol-gel Ni/Al<sub>2</sub>O<sub>3</sub> catalysts promoted with La, Ce, and Yb were prepared by a sol-gel technique. Metal nitrates (99.999 wt%, Aldrich) and aluminum tri-*sec*-butoxide (ATB) (Aldrich) were used as metal precursors. Ethanol (Alfa Aesar) of 130 cm<sup>3</sup> was used as a solvent. The H<sub>2</sub>O/ATB molar ratio was kept constant at 3.6. Initially, ATB was added into ethanol and the mixture was subsequently mixed vigorously. The aqueous solutions of metal nitrates were then added dropwise to the ATB-ethanol mixture using a syringe pump at the flow rate of 0.49 cm<sup>3</sup>/min. The pH of the resulting gel was measured and adjusted to pH = 4.8 by adding HNO<sub>3</sub> or NH<sub>4</sub>OH. The samples were stirred for an additional 15 min and were kept at the room temperature for 30 min. The samples were subsequently dried in the oven at 110 °C overnight. The dry samples were ground into a fine powder and were calcined in flowing O<sub>2</sub> at 450 °C for 4 hr. It is noted that Ni and lanthanide contents were 20 wt% and 2 wt%, respectively for all catalysts prepared. For simplicity, all the catalysts prepared were denoted to indicate compositions: for example, 20Ni2YbAl represents 20%Ni-2%Yb/Al<sub>2</sub>O<sub>3</sub> catalyst.

**Reaction studies.** Steam reforming of C<sub>3</sub>H<sub>8</sub> was carried out in a 1/4 in. O.D. stainless steel flow reactor at 400-550 °C at atmospheric pressure. The total flow rates were 300-400 cm<sup>3</sup>(STP)/min. The feed stream consisted of C<sub>3</sub>H<sub>8</sub>, H<sub>2</sub>O, and N<sub>2</sub> as a diluent. The catalyst weight was varied between 30 and 50 mg in order to keep the total surface area in the reactor constant at 9 m<sup>2</sup>. Prior to the reaction, catalysts were reduced *in situ* in flowing 20% H<sub>2</sub>/N<sub>2</sub> of 50 cm<sup>3</sup>/min at 600 °C for 2 hr. The catalysts were flushed with N<sub>2</sub> and then cooled to the desired reaction temperature. The effluent from the reactor was analyzed using an automated Shimadzu GC-14A equipped with FID and TCD detectors. A GOW- MAC 069-50 ruthenium methanizer operated at 350 °C was used with the FID for accurate determination of CO and CO<sub>2</sub>. Reaction experiments were conducted for 20 hr until it reached a steady state. The product distributions maintained a carbon balance of 100% (±5%).

**Catalyst Characterization.** BET surface areas, pore volumes, and pore size distributions of sol-gel Ni-based catalysts were determined by N<sub>2</sub> adsorption-desorption at 77 K using a Micromeritics ASAP 2010 instrument. Temperature-programmed reduction (TPR) experiments were performed using a laboratory-made gas flow system. 10% H<sub>2</sub>/Ar was used as a reducing gas at the total flow rate of 40 cm<sup>3</sup>/min. The temperature of the catalyst samples was raised using the temperature program as follows: 10 min at room temperature, ramp rate of 10 °C/min to 900 °C, and 10 min at 900 °C. H<sub>2</sub> consumption was measured using a thermal conductivity detector (TCD) connected to a data-acquisition computer. The XRD analysis was carried out using a Scintag PAD-V diffractometer using Cu K<sub>α</sub> radiation operated at 45 kV and 20 mA.

## Results and Discussion

C<sub>3</sub>H<sub>8</sub> conversion at 500 °C as a function of time on stream for different sol-gel Ni-based catalysts is plotted in Figure 1. It is clearly seen that the 20Ni2YbAl and 20Ni2CeAl catalysts showed significant improvement in both catalytic activity and stability compared to the monometallic 20NiAl catalyst.

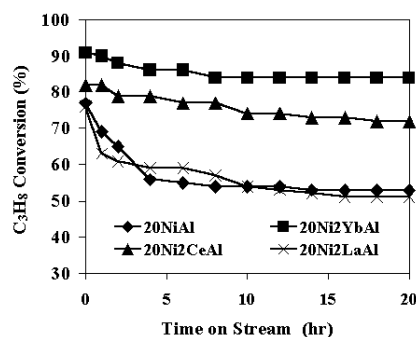


**Figure 1.** C<sub>3</sub>H<sub>8</sub> conversion as a function of time on stream for different sol-gel Ni-based catalysts [Reaction conditions: 500 °C, 1 atm, total flow rate = 300 cm<sup>3</sup>(STP)/min, C<sub>3</sub>H<sub>8</sub>/H<sub>2</sub>O/N<sub>2</sub> = 1:4:95, equal surface area reactions (9 m<sup>2</sup>), GHSV > 250,000 hr<sup>-1</sup>].

On the other hand, the activity of the 20Ni2LaAl catalyst was comparable to that of the 20NiAl catalyst. The catalytic activity of C<sub>3</sub>H<sub>8</sub> steam reforming at 500 °C decreased in the following order:



It is noted that all bimetallic catalysts have higher BET surface areas (230-300 m<sup>2</sup>/g) than the monometallic catalyst (209 m<sup>2</sup>/g). The TPR profiles of sol-gel Ni-based catalysts are shown in Figure 2. The position of the peak maximum shifted towards lower temperatures (570-600 °C) for all bimetallic catalysts. This high-temperature (HT) broad reduction peak may be due to bulk reduction of Ni in crystalline NiO or NiAl<sub>2</sub>O<sub>4</sub> phase. On the other hand, a small low-temperature (LT) reduction peak around 400 °C could be attributed to the reduction of a well-dispersed and possibly amorphous NiO phase on the alumina support surface. However, the LT reduction peak could not be observed for the Ce-promoted catalyst. It is concluded that the reduction of Ni species is facilitated by the presence of lanthanide elements in the Al<sub>2</sub>O<sub>3</sub>-supported Ni catalysts.

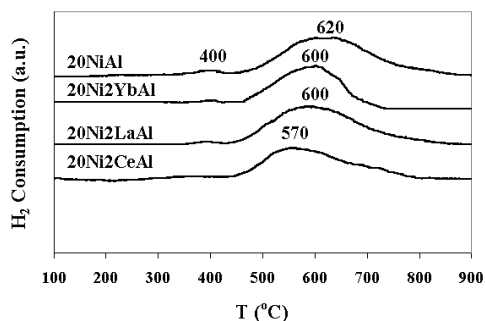


**Figure 2.** The TPR profiles of sol-gel Ni-based catalysts.

The XRD patterns of sol-gel Ni-based catalysts were obtained after calcination under O<sub>2</sub> at 450 °C. The major crystalline phases correspond to NiO, NiAl<sub>2</sub>O<sub>4</sub>, and  $\gamma$ -Al<sub>2</sub>O<sub>3</sub>. However, it is difficult to distinguish between NiAl<sub>2</sub>O<sub>4</sub> and  $\gamma$ -Al<sub>2</sub>O<sub>3</sub> because the diffraction lines of these two phases overlap, as evidenced by broad peaks.<sup>5</sup> No lanthanide-related crystalline phases could be detected. It is suggested that the lanthanide species could be well-dispersed or could exist in the form of a two-dimensional overlayer on the alumina support undetectable by XRD.<sup>6</sup>

It is known that metallic nickel is the active site for steam reforming reaction. As shown in Figure 3, after reduction under 20% H<sub>2</sub>/N<sub>2</sub> at 600 °C, the metallic Ni crystalline phases [(111), (200), (220)] were observed at  $2\theta = 44.5, 51.8,$  and  $76.4^\circ$ , respectively. Moreover, the NiO phase seemed to disappear while the diffraction lines of NiAl<sub>2</sub>O<sub>4</sub> spinel were retained.

TPR results suggested that the activity of sol-gel Ni-based catalysts depended on the catalyst reducibility. More detailed reaction experiments and catalyst characterization are underway to investigate the promotion effect of lanthanide elements on sol-gel Ni-based catalysts.

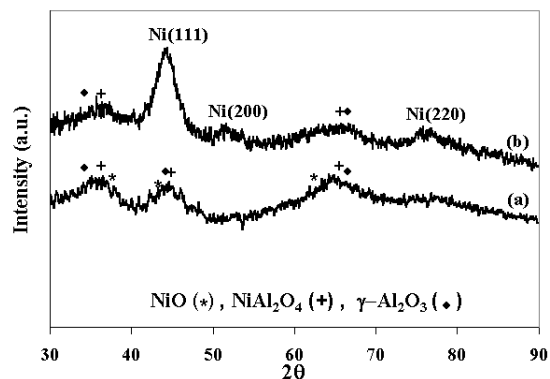


**Figure 3.** The XRD patterns of the sol-gel bimetallic 20Ni2YbAl catalysts after: (a) calcination at 450 °C (b) reduction at 600 °C.

### Conclusions

Sol-gel Ni-based catalysts promoted with lanthanide elements such as La, Ce, and Yb have been synthesized and tested in steam reforming of propane at 500 °C and H<sub>2</sub>O/C<sub>3</sub>H<sub>8</sub> = 4. It was found that the addition of Yb or Ce (2 wt%) into the Ni/Al<sub>2</sub>O<sub>3</sub> catalyst improved both catalytic activity and stability significantly. TPR results further revealed that the catalytic activity was influenced by catalyst reducibility.

**Acknowledgement.** The financial support provided by Honda Research Institute, USA Inc. is gratefully acknowledged.

### References

- (1) Rostrup-Nielsen, J.R. In *Catalysis: Science and Technology*; Anderson, J.R. and Boudart, M., Eds.; Springer: New York, 1984, pp. 3-117.
- (2) Ridler, D.E. and Twigg M.V., in: M.V. Twigg (Eds.), *Catalyst Handbook*, Wolfe, London, 1989, pp. 225-282.
- (3) Zhuang, Q.; Qin Y.; and Chang L. *Appl. Catal.* **1991**, *70*, 1.
- (4) Su, B.-L. and Guo, S.-D. In *Catalyst Deactivation*; Delmon, B. and Froment, G.F., Eds.; Elsevier: Amsterdam, 1999; pp. 325-\*
- (5) Vos, B.; Poels, E.; and Blik, A. *J. Catal.* **2001**, *198*, 77.
- (6) Bettman, M.; Chase, R.E.; Otto, K.; and Weber, W.H. *J. Catal.* **1989**, *117*, 447.

## OPERATION OF DIRECT CARBONATE FUEL CELL WITH PROPANE

*Sai P. Katikaneni\*, C.Y. Yuh, T.W. Lee and M. Farooque*

FuelCell Energy, Inc.  
3 Great Pasture Road  
Danbury, CT 06813, USA

[skatikaneni@fce.com](mailto:skatikaneni@fce.com)  
Phone: (203) 825-6067  
Fax: (203) 825-6273

FCE has designed propane clean-up processor and propane prereformer to meet DFC fuel cell grade fuel. This presentation will discuss FCE's experience with operation of DFC on propane and focusing on clean-up considerations, LPG compositions and its effect on fuel processing operations, prereforming results, steam to carbon effects on prereforming and 30 kW stack operation with propane.

Carbonate fuel cells are new generation of power plants that provide electricity at very high efficiency and low environmental emissions. FCE's "direct carbonate fuel cell" operates on a variety of hydrocarbon fuels such as natural gas, biogas, coal gas, diesel and LPG. Conventionally, an external reformer is used to supply hydrogen rich gas to fuel cell. FuelCell Energy's DFC<sup>TM</sup> technology has adopted an internal reforming approach that eliminates the need for an external reformer, resulting in increased efficiency, compactness, better thermal management and lower cost.

DFC operation on natural gas, peak shaving gas, LPG, digester gas, syngas, coal bed methane, and liquid fuels such as diesel, methanol and ethanol has been already demonstrated. Fuel clean-up and fuel processing operation varies based on the nature of fuel. However, the fuel thus supplied to the fuel cell has a two-step refinement approach. Step 1 involves fuel clean up system to remove impurities such as sulfur, halides, solid particulates, aromatic hydrocarbons, and oxygen. The second step is pre-reforming desulfurized fuel to knock out higher hydrocarbons in order to eliminate coke formation during reforming inside the fuel cell. Methane-rich gas obtained from prereformer is thus fed into fuel cell for internal reforming to produce hydrogen in DFC stacks which in turn is electrochemically converted to water, thereby producing DC power. At each stage of this operation, catalysts are used to facilitate production of desirable fuel cell fuel.

Fuel clean-up considerations vary with type of fuel and its constituents. The nature of impurities and their concentration will be considered to design suitable clean-up processor for each type of fuel for DFC applications. Table 1 indicates various fuels specification including type of impurities and their levels for designing clean-up processor. The impurities present in fuels will impact the performance of reforming catalysts, cell performance and overall life of fuel cell. Ni-based catalysts are used for internal reforming and prereforming of higher hydrocarbons. Nickel catalysts are sensitive for sulfur, chloride and particulate poisoning, thus, require impurity-free fuel for fuel cell applications. The tolerance level of these impurities on both catalyst and fuel cell components are significantly lower than conventional fuel processing operations. Also, the tolerance level is based on the type of impurity. Although worldwide standards favor a gradually lowering sulfur and other impurity levels in transportation fuels, it is necessary to further reduce the sulfur levels in fuel cells to sub-ppm levels prior to use in fuel cell power plants. Depending on the nature of fuel and impurity levels, an appropriate fuel clean-up process with suitable adsorbents/catalysts is required in DFC balance of power plant operation.

## Fuel Cells Operating in the “Gap” Temperature Regime

Eugene S. Smotkin

Department of Chemistry  
University of Puerto Rico @ Rio Piedras  
San Juan, Puerto Rico 00931  
Department of Chemical Engineering  
Illinois Institute of Technology  
Chicago, IL 60616

### Introduction

Low temperature fuel cells are based on solid polymer electrolyte membranes (PEMs), e.g. Nafion™. The thickness of Nafion™ membranes (25–175 μm) permits compact series stacking of cells enabling high power and energy density systems. PEM electrolytes require sufficient hydration of the anchored sulfonate groups to support the Grotthus hopping proton conduction mechanism (1). The maintenance of adequate hydration (e.g. about 3 water molecules per proton exchange site) requires precise water management, which sets the upper limit of practical PEM operation at about 90°C. Pt based electrocatalysts are poisoned by CO, which is an intermediate in the formation of hydrogen prepared by steam reforming of commodity fuels such as gasoline or methane. Although CO can be removed by the addition of a water-gas-shift (WGS) reactor and a preferential oxidation (PROX) unit to the reformer, the overall power density of the fuel cell system is substantially reduced and, more significantly, the interfacing of a 1000°C reformer to a 90°C fuel cell is daunting process control task. Finally, the kinetics of the four-electron oxygen reduction reaction (ORR) at the cathode of PEM fuel cells demands about 400 mV of polarization to obtain 1 mA/cm<sup>2</sup> of Pt. The surface area of Pt catalysts is typically about 25 cm<sup>2</sup> per mg. Thus low temperature fuel cell membrane electrode assemblies (MEAs) require substantial Pt loadings. A 50 kW traction power fuel cell requires over 125 g of Pt.

An intermediate temperature electrolyte system enabling fuel cell operation between 250°C and 400°C—i.e. in the gap between the PEM fuel cell and the molten carbonate fuel cell (MCFC)—has the benefits of enhanced ORR kinetics, CO tolerance, and a simplified fuel processor without the materials thermal instability problems of the high temperature systems. Additionally the gap temperature region enables downward scalability for portable power, a power regime not accessible by MCFCs. A “gap” electrolyte would radically change the paradigm of fuel cell engineering. Inorganic electronically insulating proton conductors (EIPCs) are the most likely candidates for gap electrolytes and are widely studied.(2, 3, 4, 5, 6, 7) The best inorganic EIPCs in the gap regime have conductivities ranging from 10<sup>-3</sup> to 10<sup>-2</sup> S/cm. For comparison the conductivity of hydrated Nafion 117 (175 μm) at 100°C is approximately 10<sup>-1</sup> S/cm.

Thus a membrane based on an inorganic proton conductor must be about 5–20 μm thick in order to achieve the same conductivity as Nafion™. Until now, there have been no reports of fuel cell performance using inorganic EIPCs in the gap range. Researchers have failed to prepare freestanding films of inorganic EIPCs that can withstand the mechanical stresses associated with fuel cell assembly. The EIPC must simultaneously serve as an electrolyte and as a separator of the fuel and oxidant streams.

We report the first demonstration of a fuel cell operating in the gap regime. The innovation is a support structure that enables the use of very thin inorganic EIPCs. Figure 1 shows a schematic of a fuel cell assembly using a supported EIPC. The composite electrolyte system is based on an EIPC supported on a thin metal hydride membrane—e.g. Pd (8), a Pd alloy (9), or a group Vb alloy coated

with a thin layer of Pd (10, 11, 12, 13)—that is strong, flexible, and has excellent hydrogen transport properties. The metal hydride is coated on one or both sides with a thin film of the inorganic EIPC. By themselves, neither the metal hydride foil nor the EIPC can make an acceptable fuel cell membrane. The metal alone, being an electronic conductor, would short circuit the cathode and anode; the EIPC alone has poor mechanical properties and may also be fuel-permeable. Together, the two components form an electronically insulating, mechanically strong, fuel impermeable thin membrane that is ideally suited to the intermediate temperature regime.

We exemplify the support structure using ammonium polyphosphate/silica as the EIPC and Pd as the metal hydride support structure. Ammonium polyphosphate, which has the maximum conductivity of  $5 \times 10^{-3}$  S/cm at 300°C, is made proton-conductive by the thermal decomposition to polyphosphoric acid (2). Silica is added to the framework material to keep the composite material in the solid state up to 400°C. While this EIPC has been studied in pellet form, until now, freestanding films have never been studied because the EIPC is brittle and difficult to work with.

### Experimental

The composite membrane electrolyte was prepared as follows: ammonium polyphosphate and silica spheres were stirred in methanol for two days. The slurry was sprayed onto one side of a 25 μm palladium foil. The coated foil was sintered in an ammonium atmosphere to melt and mix the ammonium polyphosphate with the silica spheres. The thickness of the EIPC layer can be varied by repetitive spraying and sintering. In this study, the EIPC thickness is 20 μm. The hybrid membrane, with the EIPC facing the cathode oxygen flow fields, was assembled into a fuel cell with Pt electrodes (4 mg/cm<sup>2</sup> Pt black with 10 wt% ammonium polyphosphate) contacting both faces of the ITEC system. The fuel cell assembly was placed in a press equipped with electrically insulated heating platens.

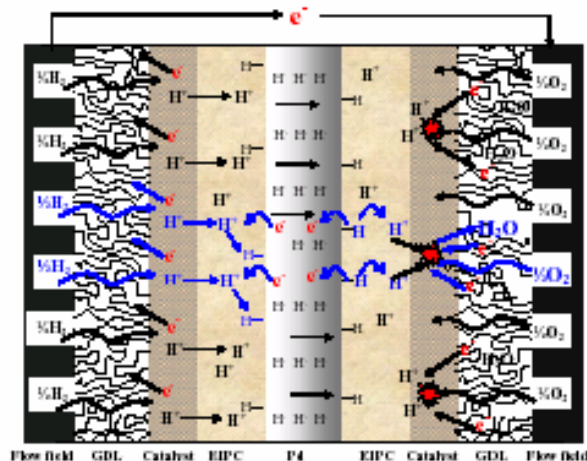


**Figure 1.** Schematic of an intermediate temperature hybrid electrolyte composite incorporated into a fuel cell. The metal hydride foil could be Pd, a Pd alloy, or a group Vb alloy coated with Pd. An EIPC layer covers the foil on one or both sides. The catalytic area is prepared in a “solid state ink” incorporated into the EIPC.

### Results and Discussion

Figure 2 shows the fuel cell performance at 250°C using humidified fuel. The fuel was either hydrogen or a reformat containing 5% CO balanced with hydrogen. Both fuel compositions were studied with oxygen at the cathode. In both cases, the CO had no effect on the performance curve: The ITEC shows

complete tolerance to CO. The use of air instead of pure O<sub>2</sub> results in a decrease of OCV and cell performance due to the lower partial pressure. Increasing the air flow-rate from 100 sccm to 200 sccm causes an increase in the OCV from 0.66 V to 0.71 V.

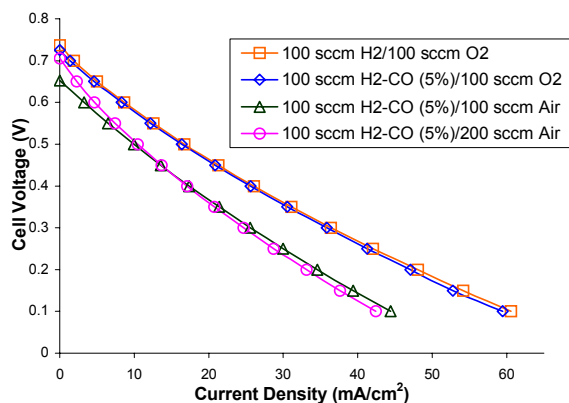


**Figure 2.** I-V curves obtained at 250°C for a hydrogen/oxygen fuel cell containing a poly-phosphate-silica (4:1) 20 μm thick EIPC on the cathode side of a 25 μm thick Pd foil. Pt catalysts were used on both the anode and cathode sides of the cell.

## Conclusions

We have demonstrated the first example of a fuel cell operating in the “gap” regime. Within the gap regime, the water-gas-shift reactor and the PROX reactor will not be needed. Further, the intermediate temperature operation will permit downward scalability for portable power, not available to higher temperature fuel cell systems such as the MCFC or solid oxide fuel cell (SOFC).

**Acknowledgement.** Funding for this work was provided by NuVant Systems Inc. and the Army Research Office through the STTR program.

## References

1. P. Atkins, *Physical Chemistry*, 6th ed., Freeman, New York, 1999, p. 741.
2. T. Kenjo, Y. Ogawa, *Solid State Ionics*, **76**, 29 (1995).
3. Y. Du, A. S. Nowick, *Solid State Ionics*, **91**, 85 (1996).
4. K. D. Kreuer, *Solid State Ionics*, **97**, 1 (1997).
5. A. S. Nowick, Y. Du, *Solid State Ionics*, **77**, 137 (1995).
6. B. Gross, *et al*, *Solid State Ionics*, **125**, 107 (1999).
7. S. M. Haile, D. A. Boysen, C. R. I. Chisholm, R. B. Merle, *Nature*, **410**, 910 (2001).
8. T. Graham, *Phil. Trans. Roy. Soc.*, **156**, 399 (1866).
9. J. B. Hunter, *U. S. Patent*, 2,773,561 (1956).
10. A. C. Makrides, M. A. Wright, D. N. Jewett, *U. S. Patent* 3,350,846 (1967).
11. C. Nishimura, M. Komaki, S. Hwang, M. Amano, *Journal of Alloys and Compounds*, **330-332**, 902 (2002).
12. R. E. Bexbaum, A. B. Kinney, *Ind. Eng. Chem. Res.*, **35**, 530 (1996).
13. N. M. Peachey, R. C. Snow, R. C. Dye, *J. Membrane Sci.*, **111**, 123 (1996).

## Application of Sulfonated Diels-Alder Polyphenylenes in Hydrogen Based PEM Fuel Cells.

Cy H. Fujimoto and Christopher J. Cornelius

Chem and Bio Technologies, Sandia National Laboratories,  
Albuquerque, New Mexico 87185-0888.

### Introduction:

The limitations of perfluorinated PEMs (i.e. Nafion) such as, low performance at temperatures above 80 °C, high fuel permeation in DMFCs, cost and environmental processing issues have spurred the search for a cheaper and efficient alternative.<sup>1,2,3</sup>

Polyphenylenes represent a promising class of thermoplastics that show potential as a PEM fuel cell material. Moreover, polyphenylene synthesized through Diels Alder (DA) polymerization has advantages of thermal stability, organic solubility and mechanically robust films.<sup>4,5,6</sup>

Until now DA polyphenylenes have not been applied towards polyelectrolyte usage, even though this class of polymer exhibits promising physical properties such as, easily tunable backbone/lateral groups and the potential of incorporating three acidic functional groups per repeat unit compared to one in most poly(arylene) systems. We report here the physical properties and preliminary hydrogen fuel cell performance data of this class of polymer.

### Experimental:

**Membrane Preparation.** 0.5 g of sulfonated DA polymer was casted on a clean glass plate as the sodium salt form in 10 mL of NMP. The cast was left to evaporate at 80 °C under a constant flow of N<sub>2</sub> for 12 hrs. The film was then dried at 100 °C under vacuum for 24 hrs and acidified (soak in 2M H<sub>2</sub>SO<sub>4</sub> for 24 hrs)

**Ion-Exchange Capacity.** 0.2 g of acidified polymer was dried and weighed. The sample was then treated with 10 mL of 0.1 M NaOH and stirred for 24 hrs. The sample was then filtered and titrated against 0.01 M HCl.

**Water Uptake.** The acidified films were immersed in DI water for 24 hrs. at 25 °C. They were then blotted dry and weighed (W<sub>s</sub>). The films were then dried and weighted until a constant weight was achieved (W<sub>d</sub>). Water uptake was calculated by:

$$\text{Water uptake} = [(W_s - W_d) / W_d] \times 100\%$$

**Proton Conductivity.** The conductivities were determined in fully hydrated films by AC impedance spectroscopy over a frequency range of 1x10<sup>3</sup> Hz to 1x10<sup>6</sup> Hz using a Solartron 1260 gain phase analyzer.

**Fuel Cell Testing.** Polarization curves of the membranes were taken on a Fuel Cell Technologies instrument using UP H<sub>2</sub> and O<sub>2</sub> as reactant gases.

### Results and Discussion.

Sulfonated DA polymers were readily cast into films from NMP. These films were robust and showed no forms of brittleness even when dried.

The films displayed proton conductivities ranging from 10-80 mS/cm while still maintaining mechanical stability (swelling under 50%).

IEC	Swelling	Conductivity (mS/cm)
0.92	10%	10
1.03	15%	19
1.51	27%	29
1.70	35%	49
2.25	50%	62

Fuel cell performance data indicated that the sulfonated DA polymers could obtain high power levels and current densities of 342 mW/cm<sup>2</sup> at 800 mA/cm<sup>2</sup>.

### References:

1. Savadogo, O. J. *New Mater. Electrochem. Syst.* **1998**, 1, 47.
2. Rikukawa, M.; Sanui, K. *Prog. Polym. Sci.* **2000**, 25, 1463.
3. Steck, A.; Stone, C. Proceedings of the Second International Symposium on New Materials for Fuel Cell and Modern Battery Systems.
4. Stille, J. K. *J. Macromol. Sci. Chem.* **1969**, 3, 1043.
5. Neenan, T. X.; Kumar, U. *Macromolecules.* **1995**, 28, 124.
6. Fujimoto, C. H.; Loy, D. A.; Wheeler, D. R.; Jamison, G. M.; Cornelius, C. J. *Polymer Preprints.* **2002**, 43, 2, 1376.

**SCREENING AND PERFORMANCE EVALUATION  
TESTING OF MATERIALS FOR PROTON  
EXCHANGE MEMBRANE FUEL CELL STACK  
SEALING**

*Lawrence E. Frisch*

Engineered Elastomers Science & Technology,  
Dow Corning Corporation,  
3901 S Saginaw Rd, Building 2202 E-3 Mail 131, Midland, MI  
48686, larry.frisch@dowcorning.com

The economic viability of PEM Fuel Cells requires significant reduction in the cost of assembling and sealing the PEM stack. Resistance to the range of fuels, reactants, coolants and other system components is critical to the seal material performance. Additionally the stack sealing system or method must last the life of the stack, is often used to enhance the structural strength of the stack and provide performance-enhancing functionality. This paper discusses Dow Corning's Proton Exchange Membrane Fuel Cell (PEMFC) stack sealing material development. Specifically the selection and development of appropriate test methods for screening and long-term performance assessments are presented. Standard and accelerated testing of sealing materials is discussed as well as specifications for key life testing of the sealing materials and stack assembly for sealing integrity. Key parameters for materials to be used in various sealing methods are discussed.

# TUNGSTEN CARBIDES AS POTENTIAL ELECTROCATALYSTS

Jingguang G. Chen\*, Henry H. Hwu, Michael B. Zellner

Center for Catalytic Science and Technology (CCST)  
Department of Chemical Engineering  
Department of Materials Science and Engineering  
University of Delaware  
Newark, Delaware 19716

## Introduction

As the global supply of fossil fuels predictably diminishes, there have been overwhelming interests in developing the fuel cell technology. While there exist many types of fuel cells each requiring different electrocatalysts and fuels, systems involving the oxidation of methanol to obtain hydrogen fuel or electrons appear to exhibit potential advantages over others [1, 2]. In the case of the direct methanol fuel cell (DMFC), the ideal chemistry at the anode involves the oxidation of methanol in the presence of water to produce CO<sub>2</sub>, electrons, and protons

Currently, the electrocatalyst of choice for the DMFC system is the bimetallic system of Pt/Ru; this material is favored because it demonstrates significant activity for methanol oxidation *as well as* the dehydrogenation of water, which is critical for the removal of adsorbed CO species [1, 4-6]. Aside from its activity, however, the Pt/Ru system is disadvantageous in terms of its prohibitively high costs and its susceptibility to be poisoned by CO [7]. As a result, the discovery of less expensive and more CO-tolerant alternatives to the Pt/Ru electrocatalysts would greatly facilitate the commercialization of the methanol-based fuel cell systems.

The carbides of Groups IV-VI early transition metals often show catalytic properties similar to that of the Pt-Group metals, especially in hydrogenation and dehydrogenation reactions involving unsaturated hydrocarbons [8, 9]. In particular, there have been numerous studies on tungsten carbides (WC and W<sub>2</sub>C) since Levy and Boudart suggested that WC displayed Pt-like behavior in a variety of catalytic reactions in 1973 [10]. There have also been several attempts to utilize tungsten carbides as an electrocatalyst [11-16], as it is resistant to acid solutions at anodic potentials [13, 14].

In this presentation we will provide a comparison of the general trend in the activity and product selectivity of methanol and water on C/W(111), Pt/C/W(111), O/C/W(111), and C/W(110). We will also compare the desorption temperature of CO from these surfaces. Finally, we will briefly compare our results on tungsten carbides to those on the surfaces of Pt(111) and Ru(0001) under identical UHV conditions.

## Experimental

The UHV chamber used in the current study has been described in detail previously [21]. Briefly, it is a three-level stainless steel chamber equipped with Auger electron spectroscopy (AES), low-energy electron diffraction (LEED), and temperature-programmed desorption (TPD) in the top two levels, and high-resolution electron energy loss spectroscopy (HREELS) in the bottom level. For TPD experiments the W(111) and W(110) samples were heated with a linear heating rate of 3 K/s.

Clean W(110) and W(111) crystal surfaces were prepared by cycles of Ne<sup>+</sup> bombardment at 500K (sample current ~6  $\mu$ A) and flashing to 1200K, as described previously [17, 20]. The procedures for preparing the carbide-modified W surfaces using ethylene or other unsaturated hydrocarbon molecules as a carbon source are described elsewhere [21, 22]. The carbide surfaces will be referred to

as C/W(110) or C/W(111). The preparation of oxygen-modified C/W(111) involved first making the carbide layer and then dosing 1L of oxygen at 900K; this surface will be referred to as O/C/W(111). For the Pt-modified C/W(111) surface, submonolayer coverages of Pt was achieved by heating Pt wire (0.127 mm in diameter, 99.9% from Alfa Aesar) that was wrapped tightly on W heating wires, as described elsewhere [23].

## Results and Discussion

Recently our group has published several papers to demonstrate that tungsten carbide surfaces possess characteristics that are desirable for fuel cell electrocatalysts. In particular, we show that carbide-modified W(111), or C/W(111), is significantly more active toward the decomposition of methanol and water than Pt-group metals [17, 18]. We further modified the C/W(111) surface with submonolayer coverages of Pt and oxygen to examine possible synergistic or deactivating effects [17-19]. Lastly, we explored the effect of substrate structure by performing identical experiments on carbide-modified W(110) [20].

This preprint compares and summarizes a series of studies on the reactions of CH<sub>3</sub>OH, H<sub>2</sub>O, and CO over several model tungsten carbide surfaces. Our results demonstrate that methanol and water readily dissociate on C/W(111), Pt/C/W(111), O/C/W(111), and C/W(110). Although the presence of submonolayer Pt on C/W(111) reduces the activity toward the dissociation of methanol, the added Pt leads to a complete suppression of the undesirable methane product. When the C/W(111) surface is modified by oxygen, significant activities toward the decomposition of methanol and water are maintained while the CO desorption temperature is reduced to below room temperature (242K). Finally, comparative studies of the C/W(111) and C/W(110) surfaces show only minor differences regarding the reactions with CH<sub>3</sub>OH, H<sub>2</sub>O, and CO.

**Table 1. Reactivity of methanol on different C/W Surfaces**

Surfaces	Total Number Of CH <sub>3</sub> OH Reacting per W Atom
W(111) [17]	0.411
C/W(111) [17]	0.280
0.6ML Pt/C/W(111) [19]	0.177
O/C/W(111) [17]	0.236
C/W(110) [20]	0.304
Pt(111) [33, 34]	~0
Ru(0001) <sup>†</sup> [35]	N/A

**Table 2. Reactivity of water on different C/W Surfaces**

Surfaces	Activity (H <sub>2</sub> O Molecules per W atom)
W(111) [18]	0.320
C/W(111) [18]	0.180
0.6ML Pt/C/W(111) [19]	0.056
O/C/W(111) [18]	0.095
C/W(110) [20]	0.153
Pt(111) [36, 37]	~0
Ru(0001) [38, 39]	~0

Overall, as shown in Tables 1, 2, and 3, the tungsten carbide surfaces exhibit characteristics more favorable toward DMFC applications than Pt or Ru surfaces in two important aspects: (1) The tungsten carbide surfaces are more active toward the dissociation of methanol and water. (2) The CO desorption temperature is at least 100 degrees lower, suggesting that tungsten carbides might be more resistant to CO-poisoning. As a result, the current study demonstrates the feasibility for potential application of tungsten carbides as electrocatalysts. We are currently using physical vapor deposition (PVD) films of tungsten carbides and Pt-modified to correlate surface science studies with electrochemical performance.

**Table 3. Desorption temperature of CO from different C/W Surfaces**

Surfaces	CO Desorption Temperature <sup>a</sup> (K)
W(111) [18]	292, 874
C/W(111) [18]	330, 355
0.3ML Pt/C/W(111) [19]	357
O/C/W(111) [18]	242, 284
C/W(110) [20]	284, 335
Pt(111) [27, 28]	~460
Ru(0001) [25, 26]	~475

#### Acknowledgment

We acknowledge financial support from the Basic Energy Sciences, Department of Energy (DOE/BES Grant No. DE-FG02-00ER15014). HHH also acknowledges financial support from the Presidential Fellowship at the University of Delaware and the American Vacuum Society Graduate Student Fellowship. MBZ acknowledges partial financial support from a National Aeronautics and Space Administration (NASA) Graduate Fellowship.

#### References

- [1] R. Parsons and T. VanderNoot, *J. Electroanal. Chem.* **257**, 9 (1988).
- [2] A. Hamnett, *Catal. Today* **38**, 445 (1997).
- [3] G. J. K. Acres, et. al. *Catal. Today* **38**, 393 (1997).
- [4] A. Hamnett and B. J. Kennedy, *Electrochim. Acta.* **33**, 1613 (1988).
- [5] M. M. P. Janssen and J. Moolhuysen, *Electrochim. Acta.* **21**, 869 (1976).
- [6] S. A. Campbell and R. J. Parsons, *Chem. Soc. Faraday Trans.* **88**, 833, (1992).
- [7] P. Stonehart in *Electrochemistry and Clean Energy*, edited by J. Drake (Royal Society of Chemistry, Cambridge, 1994).
- [8] S. T. Oyama, *The Chemistry of Transition Metal Carbides and Nitrides* (Blackie Academic and Professional, Glasgow, 1996).
- [9] J. G. Chen, *Chem. Rev.* **96**, 1477 (1996).
- [10] R. Levy and M. Boudart, *Science* **181**, 547 (1973).
- [11] H. Okamoto, G. Kawamura, A. Ishikawa, and T. Kudo, *J. Electrochem. Soc.* **134**, 1645 (1987).
- [12] G. Kawamura, H. Okamoto, A. Ishikawa, and T. Kudo, *J. Electrochem. Soc.* **134**, 1653 (1987).
- [13] H. Boehm and F. A. Pohl, *Wiss. Ber. AEG-Telefunken* **41**, 46 (1968).
- [14] H. Binder, A. Koehling, and G. Sandstede, *Am. Chem. Soc. Div. Fuel Chem. Prepr.* **13**, 99 (1969).
- [15] R. Fleischmann and H. Boehm, *Ber. Bunsenges, Phys. Chem.* **84**, 1023 (1980).
- [16] P. N. Ross, Jr. and P. Stonehart, *J. Catal.* **48**, 42 (1977).
- [17] H. H. Hwu, J. G. Chen, K. Kourtakis, and G. Lavin, *J. Phys. Chem. B* **105**, 10037 (2001).
- [18] H. H. Hwu, B. D. Polizzotti, and J. G. Chen, *J. Phys. Chem. B* **105**, 10045 (2001).
- [19] N. Liu and J. G. Chen, *J. Catal.* accepted (2003).
- [20] H. H. Hwu and J. G. Chen, *J. Phys. Chem. B* **107**, 2029 (2002).
- [21] B. Fruhberger and J. G. Chen, *J. Am. Chem. Soc.* **118**, 11599 (1996).
- [22] N. Liu, S. A. Rykov, H. H. Hwu, M. T. Buelow, and J. G. Chen, *J. Phys. Chem. B* **105**, 3894 (2001).
- [23] N. Liu and J. G. Chen, *Catal. Lett.* **77**, 35, (2001).
- [24] K. D. Childs, et. al., *Handbook of Auger Electron Spectroscopy; Physical Electronics, Third Edition* (1995).
- [25] F. Bautier de Mongeot, M. Scherer, B. Gleich, E. Kopatzki, and R. J. Behm, *Surf. Sci.* **411**, 249 (1998).
- [26] K. L. Kostov, H. Rauscher, and D. Menzel, *Surf. Sci.* **278**, 62 (1992).
- [27] A. Crossley and D. A. King, *Surf. Sci.* **68**, 528 (1977).
- [28] G. Ertl, M. Neuman, and K. M. Streit, *Surf. Sci.* **64**, 393 (1977).
- [29] E. Iglesia, F.H. Ribeiro, M. Boudart and J.E. Baumgartner, *Catal. Today* **15**, 307 (1992); E. Iglesia, J.E. Baumgartner, F.H. Ribeiro and M. Boudart, *J. Catal.* **131** 523 (1991).
- [30] E.A. Blekkan, C.C. Pham-Huu, M.J. Ledoux, and J. Guille, *Ind. Eng. Chem. Res.* **33**, 1657 (1994).
- [31] N. Liu, S. A. Rykov, and J. G. Chen, *Surf. Sci.* **487**, 107 (2001).

# MEMBRANE-ELECTRODE ASSEMBLY FOR HIGH-TEMPERATURE PEMFC

Chao-Yi Yuh, Ludwig Lipp, Pinakin Patel and Ray Kopp

FuelCell Energy, Inc.  
3 Great Pasture Road  
Danbury, CT 06813

## Introduction

Fuel cells offer the best alternative to conventional fossil fuel combustion power generation technologies. However, for fuel cells to be commercially viable, issues such as cost, size, and functionality need to be addressed. A natural-gas fueled PEMFC system for stationary application desires near atmospheric pressure operation, >35% HHV efficiency, >100°C operation for cogeneration, simple construction, reliable >40,000h life, and low system cost (<\$1500/kW). A PEMFC system for transportation application requires <3 atm pressure operation, >5,000h life and <\$10/kW MEA cost. Although research efforts so far have advanced PEMFC technology significantly, substantial performance and endurance improvements beyond the current state-of-the-art are required before the above goals can be achieved.

At present, the state-of-the-art PEMFC is operated at ~60 to 80°C. CO poisoning of its anode precious metal catalyst is a major barrier for its commercialization utilizing hydrocarbon feedstock<sup>1</sup>. Various approaches to mitigate CO poisoning such as alternative anode catalysts, PROX, or air bleeding have not completely alleviate the issue. Since the chemisorption of CO weakens considerably with temperature, one approach to mitigate the CO poisoning is to operate at higher temperatures. Additional advantages such as faster electrode kinetics and higher quality waste heat for cogeneration can also be realized. Operating at >100°C also mitigates cathode flooding by the liquid water reaction product and allows a greater ability to remove waste heat. Therefore, MEA operating above 100°C (preferably >120°C) is highly desired. The ultimate MEA goals for commercial use include: 1) higher membrane proton conductivity with negligible electronic conductivity, area specific resistance less than 100 mΩcm<sup>2</sup>; 2) improved humidification properties (minimal water transport and low hydration) and dimensional stability (low swelling); 3) high mechanical strength; 4) low gas permeability (less than 0.1 percent gas crossover); 5) long life of 40,000h for stationary and 5,000h for transportation applications; 6) cell performance >0.7 V (0.8V preferred) at 400-500 mA/cm<sup>2</sup>; 7) low cost.

## Challenges with high-temperature operation

Most developers presently use perfluorosulfonic acid (PFSA) polymer membrane such as Nafion<sup>®</sup> made by DuPont. It is deficient in terms of ionic conductivity at temperatures above 100°C and at low relative humidity (R.H.). High-temperature operation dries out the membrane, drastically reducing proton conduction. To operate Nafion<sup>®</sup> beyond 100°C, pressurization is needed to maintain high R.H., requiring complicated compressor system. Dried Nafion<sup>®</sup> is also more permeable to gases, resulting in increased cross-leakage. Furthermore, the loss of liquid water embrittles the membrane and could cause membrane cracking and poor electrode-membrane contact. Another important challenge for >100°C operation of the baseline Nafion<sup>®</sup>-base MEA is the significantly reduced cell voltage, mainly due to a large cathode polarization increase. This increase is mainly caused by a loss of proton conductivity and catalyst utilization

in the cathode catalyst layer. Membrane improvement alone is not sufficient to achieve the PEMFC commercialization goal.

## Advanced Proton-Conducting Membranes

Proton-conducting mechanisms have been extensively discussed by Kreuer<sup>2,3</sup>. Literature survey has showed that a useable proton conducting membrane material with desired proton conductivity comparable to fully hydrated Nafion<sup>®</sup> (>0.1 S/cm) between 100-150°C is not yet available<sup>4-6</sup>. Because useable 100-150°C proton-conducting materials are not yet available, many new high-temperature proton-conducting materials are being actively developed. The reported approaches include:

Mechanical Support to enhance high-temperature mechanical strength for ultra-thin membranes

Solid Proton Conductor to enhance proton conductivity at low R.H.

New High-Temperature Proton-Conducting Ionomer

Substitutes for Water in Nafion to reduce humidity effect

Ultra-thin membrane or Pt Doping for Self Humidification

The solid proton conductors (superacid) under evaluation include PTA (phosphotungstic acid), ZHP (zirconium hydrogen phosphate), zeolite, silica, etc. These materials are brittle inorganics and therefore are generally incorporated into a composite structure containing flexible polymeric ionomer phases. However, although to a lesser extent than Nafion<sup>®</sup>, they also lose water at high temperatures, with reduced proton conductivity. Considerable modifications of their morphologies (such as fine nano-size) may be needed to effectively enhance proton conductivity. New high-temperature ionomers are in general sulfonated or phosphonated polymers, usually containing aromatic backbone<sup>7-9</sup>, including sulfonated polyphosphazene, polysulfone, or PEEK. So far, long-term high-temperature proton conductivity and durability under low R.H. have yet to be demonstrated. These liquid acid (less volatile than water) impregnated membranes may adsorb at the Pt surface, resulting in high cathode polarization. The liquid acids may also evaporate away slowly during long-term use, limiting their high-temperature durability. Because water dry-out is the main cause of proton-conductivity loss in many materials at high temperatures, substitutes for water in the ionomers with high boiling-point proton-conducting liquid such as pyrazole or imidazole have been evaluated. However, these liquid proton conductors may adsorb on the Pt catalyst surface, interfering ORR and resulting in high cathode polarization. The liquid proton conductor may also slowly evaporate away. The composite approaches are adopted by many researchers because few single-component monolithic materials have all the desired properties. So far, few composite materials have sufficient proton conductivity comparable to a fully hydrated Nafion<sup>®</sup>.

Many of the membrane materials reported above were studied for their proton-conducting and mechanical properties. However, very little performance data of MEA incorporating the advanced membranes at high temperatures were reported. The reported performance data were usually obtained with non-system conditions (e.g., very high R.H. or stoichs). The electrode Pt catalyst loading level was also usually too high (such as using Pt black, >1mg/cm<sup>2</sup> per electrode), not practical for commercial use.

In order for the Pt catalyst in the cathode to be utilized, its surface needs to be accessed by the proton-conducting phases and reactant oxygen. Therefore, an ionomer of high proton conductivity is not sufficient to guarantee a high cathode performance. The acid groups (ionic clusters) of the ionomers have to be situated right at the Pt for it to be active for the ORR. The water in the acidic ionic

clusters is also needed to facilitate ORR<sup>1</sup>. Furthermore, high oxygen permeability is needed to reduce mass-transfer loss. The baseline Nafion<sup>®</sup> ionomer if well humidified has a very high oxygen permeability<sup>1</sup>. Any new proton-conducting phase in the cathode catalyst layer also needs to have similarly high oxygen permeability.

This paper detailed the MEA work performed at FCE focusing on improving high-temperature membrane durability and cathode catalyst layer activity.

## MEA EVALUATION

A number of composite membrane and MEA have been developed to improve water retention and proton conduction at 120°C. The experimental MEA are all less than 75 μm thick. The composite membranes consist of ionomer and solid superacid. Fine additives/modifiers with high-proton conductivity have been incorporated into the MEA (membrane and/or cathode). The proton-conducting additives include: PTA, sulfated nano-oxide, ZHP and several types of zeolites. The ionomer phase under study in the composite MEAs include Nafion<sup>®</sup> of various EW as well as low EW experimental ionomers. Cross-linking approach is also adopted to strengthen membrane mechanical strength. The fabricated MEAs were tested in laboratory-scale 25cm<sup>2</sup> cells at 80-140°C to evaluate promising MEA formulations.

FCE has achieved significant performance and endurance improvements<sup>10</sup> under atmospheric pressure operation, hydrogen/air atmosphere, at 400mA/cm<sup>2</sup>. The cross-linking approach has enhanced membrane durability significantly, by reducing MEA OCV decay rate. The CO tolerance was significantly improved (at least to 100ppm CO) as illustrated in Figure 1, demonstrating the benefit of >100°C operation. Detailed MEA test results will be presented at the meeting.

## Acknowledgement

This study was supported by the Office of Energy Efficiency and Renewable Energy, U.S. Department of Energy, under Contract DE-FC02-99EE27567. And by U.S. National Science Foundation, under Contract DMI-0232574.

## References

1. Gottesfeld, G. and Zawodzinski, Z. in *Electrochemical Science and Engineering*, R. Alkire, H. Gerischer, D. Kolb and C. Tobias, Editors, Wiley-VCH, New York, 1994, **5**, p.195-301,
2. Kreuzer, K., *Solid State Ionics*, 2000, **136-137**, 149.
3. Kreuzer, K., *Solid State Ionics*, 1997, **94**, 55.
4. Roziere, J. and Jones, D., in 1<sup>st</sup> European PEFC Forum, F. Buchi, G. Scherer and A. Wokaun, Editors, 2001, p. 145.
5. Zawodzinski, T., et al., in 2002 US DOE Hydrogen and Fuel Cell Joint Program Review, May 6-10, 2002.
6. Norby, N., *Solid-State Ionics*, 1999, **125**, 1.
7. Kerres, J., *J. Membrane Science*, 2001, **185**, 3.
8. Jones, D. and Roziere, J., *J. Membrane Science*, 2001, **185**, 41.
9. Kreuzer, K., *J. Membrane Science*, 2001, **185**, 29.
10. Yuh, C, FY2002 Progress Report, Hydrogen, Fuel Cell and Infrastructure Technologies, Energy Efficiency and Renewable Energy, IV.B.5, 297-299.

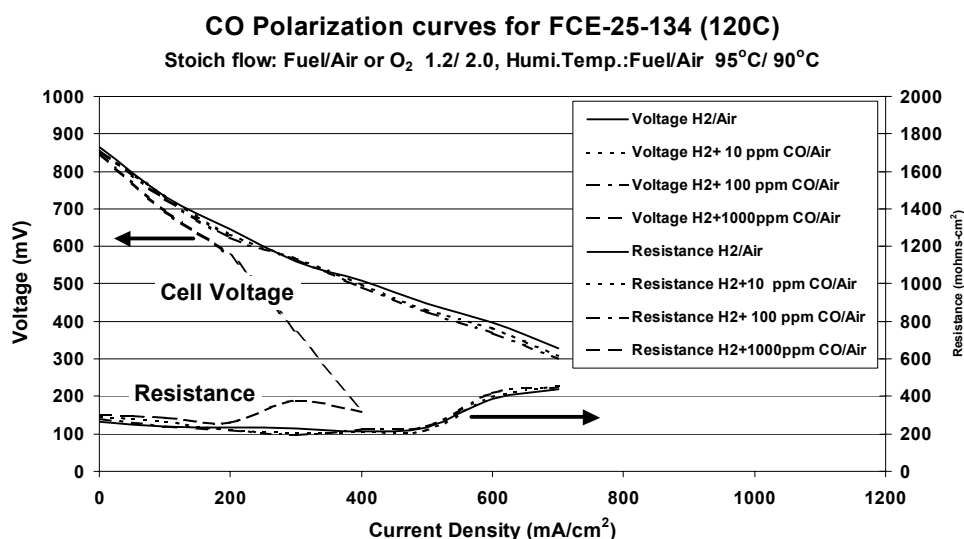


Figure 1. Significant tolerance to 100ppm CO was achieved at 120°C.

# TOWARDS THE DEVELOPMENT OF A MEMBRANE ELECTRODE ASSEMBLY (MEA) STYLE BIOFUEL CELL

Nick L. Akers and Shelley D. Minteer

Department of Chemistry  
Saint Louis University  
3501 Laclede Ave.  
St. Louis, MO 63103

## Introduction

A biofuel cell is an electrochemical device in which electrical energy is produced from chemical reactions by means of the catalytic activity of living cells and/or their enzymes. Enzyme-based biofuel cells were introduced in the 1960's [1], but the technology has not developed at the rate of traditional fuel cells for a number of reasons. The main problems that have plagued the technology have been the inability to immobilize the enzyme at the electrode surface, the lack of stability of the enzyme, and the lack of stability of the redox mediator (if a redox mediator is necessary).

Recent research in our group has focused on developing biofuel cells where the enzyme is immobilized in a membrane that buffers the pH and confines the enzyme to an area that helps maintain its structural integrity [2]. A secondary aspect of our biofuel cell has been to immobilize and stabilize the redox mediator at the electrode surface using electropolymerization. Alcohol/O<sub>2</sub> biofuel cells were fabricated using dehydrogenase enzyme-immobilized membranes that were cast on the surface of poly(methylene green)-modified anodes. The alcohol fuels are oxidized to aldehydes in the presence of alcohol dehydrogenase and NAD<sup>+</sup>. The NADH product is the redox mediator for the fuel cell. NADH oxidation on platinum and carbon electrodes has poor reaction kinetics and occurs at large overpotentials [3]. Therefore, a polymer-based electrocatalyst was used to regenerate NAD<sup>+</sup> and to shuttle electrons from the NADH to the electrode. The electrocatalyst employed in this study is methylene green. Cyclic voltammetric studies of poly(methylene green)-coated glassy carbon electrodes have shown that poly(methylene green) is an electrocatalyst for NADH [4].

The enzyme-immobilization membrane is a quaternary ammonium salt modified Nafion<sup>®</sup> membrane that maintains the advantageous electrochemical properties of Nafion<sup>®</sup>. The immobilization membrane protects the enzyme from elevated temperatures experienced during heat pressing and allows for the biofuel cell to be tested under the same conditions that a traditional fuel cell is tested. Therefore, these new biofuel cell electrodes are optimal for the formation a membrane electrode assembly (MEA) style biofuel cell.

## Experimental

**Reagents.** Methylene green (Sigma), sodium nitrate (Fisher), sodium borate (Fisher), Nafion<sup>®</sup> 1100 suspension (Aldrich) and Nafion<sup>®</sup> 117 (Aldrich) were purchased and used as received. Enzymes employed include alcohol dehydrogenase (E.C. 1.1.1.1, initial activity of 300-500 Units/mg), aldehyde dehydrogenase (E.C. 1.2.1.5, initial activity of 2-10 Units/mg), formaldehyde dehydrogenase (E.C. 1.2.1.2, initial activity of 1-6 Units/mg), and formate dehydrogenase (E.C. 1.2.1.46, initial activity of 5-15 Units/mg). Enzymes were purchased from Sigma (St. Louis, MO) and Rosche Applied Science (Indianapolis, IN), stored at 0° C, and used as received. Additionally, NAD<sup>+</sup> was purchased from Sigma and used as received.

**Preparation of the Bioanode.** The bioanode consists of 1cm x 1cm square GAT expanded graphite worms (Superior Graphite CO.)

that are compressed at pressures varying from 1500 psi to 10000 psi depending on conditions and requirements. Before hydraulic pressing, the expanded graphite is pretreated with methylene green by allowing the material to soak in the methylene green buffer solution. After pressing, methylene green is electropolymerized onto the pressed GAT material. Polymerizing a thin film of poly(methylene green) was accomplished by performing cyclic voltammetry using a CH Instruments 810 or 620 potentiostat (Austin, TX) from -0.3 Volts to 1.3 Volts for 12 sweep segments at a scan rate of 0.05 V/s in a solution containing 0.4 mM methylene green and 0.1 M sodium nitrate in 10 mM sodium tetraborate. The electrode was rinsed and then allowed to dry overnight before further modification.

Nafion<sup>®</sup> membranes incorporated with quaternary ammonium salts were formed in a two-step process. The first step was to co-cast the quaternary ammonium salt with 5% by wt. Nafion<sup>®</sup> suspension into a weighing boat. All mixture-casting solutions were prepared so the concentration of quaternary ammonium salt is in a three-fold excess of the concentration of sulfonic acid sites in the Nafion<sup>®</sup> suspension. Previous studies had shown that all of the salt ions that were introduced into a membrane were ejected from the membrane upon soaking in water [5]. Therefore, 18 MΩ water was added to the weighing boats and allowed to soak overnight. The water was removed and the films were rinsed thoroughly with 18 MΩ water. The films were resuspended in lower aliphatic alcohols, which were then employed in forming the enzyme casting solutions.

Enzyme/ Nafion<sup>®</sup> casting solutions with an enzyme to quaternary ammonium salt/ Nafion<sup>®</sup> casting solution ratio of 2:1 (usually 1200 μL of 1.0 μM enzyme: 600 μL Nafion<sup>®</sup> suspension) and 0.03g NAD<sup>+</sup> were vortexed in preparation for coating on electrode. The solution was pipetted onto the surface of the methylene green coated graphite support, and the solution was allowed to thoroughly dry before the MEA was fabricated.

**MEA Fabrication.** The cathode material is an ELAT electrode with 20% Pt on Vulcan XC-72 (E-Tek). The anode construction is previously described. Assembly of the MEA occurs at custom heating elements connected to the platens of a hydraulic laboratory press (Carver). First, a piece of Kapton (American Durafilm) is laid down, followed by the cathode, Nafion<sup>®</sup> 117 membrane, bioanode, and finally another piece of Kapton. This MEA assembly is placed between the heating elements. Pressure is typically applied to 3000 psi but can differ depending on conditions. Concurrently to pressing, the heating elements are elevated to a temperature of 125°C as measured by external thermistors. The MEA remains at temperature for three minutes, after which the pressure is released and the MEA is allowed to cool. A schematic of the completed MEA cell can be seen in Figure 1.

**Electrochemical Measurements.** All data were collected and analyzed for the test cell with a CH Instruments 810 potentiostat interfaced to a PC computer. The potentiostat functions to measure open circuit potentials and can apply varying loads to the test cell. The MEA is contained in a custom fabricated test apparatus with compartments for fuel delivery for the anode and ventilation for the cathode. Electrical connection to the anode and cathode is achieved with stainless steel wire mesh.

## Results and Discussion

Previous research has shown that it is possible to immobilize oxidase enzymes (such as: glucose oxidase) in Nafion<sup>®</sup> while maintaining enzyme activity by diluting Nafion<sup>®</sup>. However, diluting Nafion<sup>®</sup> makes unstable and non-uniform films [6-7]. The most recent approach by Karyakina and coworkers has been to neutralize Nafion<sup>®</sup> and dilute it to a lesser degree in ethanol [8]. However, both

of these approaches are problematic as the pH environment in the solution around the Nafion<sup>®</sup> decreases, Nafion<sup>®</sup> will exchange protons back into the membrane and re-acidify the membrane.

Previous research in our group has shown that we can immobilize dehydrogenase enzymes (a group of enzymes that have been more difficult to immobilize) in a quaternary ammonium salt doped Nafion<sup>®</sup> membrane while prolonging the active lifetime of the enzyme to 60-90 days [2]. The quaternary ammonium salt doped Nafion<sup>®</sup> suspension buffers the pH of the membrane to neutral levels, while the micellar structure of the polymer acts to protect the enzymes. Initial enzyme activity studies of dehydrogenase enzymes immobilized in quaternary ammonium salt doped Nafion<sup>®</sup> membranes have shown that the dehydrogenase enzymes remain active after heat treatment in an oven at 130 °C for 10 minutes. These preliminary results have shown the feasibility of forming a MEA style biofuel cell. MEA style fuel cells have the advantage of a zero gap format that increases power outputs.

Currently, we are optimizing the system for hydraulic pressures and heating element temperatures. Ideally, the amount of time the MEA spends at elevated temperatures should be no longer than is necessary to bind the anode and cathode to the Nafion<sup>®</sup>.

Preliminary results from a completed biofuel cell MEA have shown open circuit potentials ranging from 0.34 - 0.21 V with currents from 3.6 - 1.4 mA. Optimization of the heat pressing conditions should result in open circuit potentials and current densities at least equaling non-MEA biofuel cells, and most likely surpassing them due to the advantages of zero gap between the electrodes.

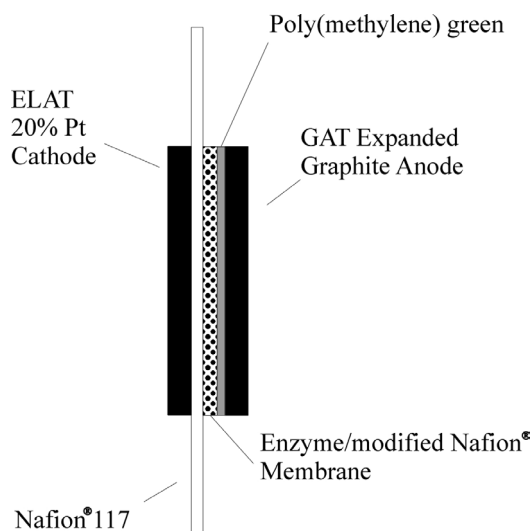


**Figure 1.** A schematic of how the MEA is assembled. Schematic is not to scale.

## Conclusions

Biofuel cells with high current densities have previously been characterized in a non-MEA format by the authors [2]. The desire is to further increase the power densities of these biofuel cells by creating an MEA biofuel cell. MEA's offer advantages of zero gap between the anode and cathode, improving the power densities. Previously, it has not been possible to create a biofuel cell MEA due to denaturing of the enzymes that would occur at high temperatures. The protective environment created by the quaternary ammonium salt modified Nafion<sup>®</sup> is sufficient for the enzymes to retain activity after exposure to high temperatures. This allows for the creation of the first known MEA based on biofuel cell technology. Future work will focus on optimizing experimental conditions to fully capitalize on the advantages of the MEA format.

**Acknowledgement.** The authors wish to thank the Office of Naval Research and the Saint Louis University Beaumont Faculty Development Fund for funding this research. The authors would also like to thank Christine M. Moore for her help with heat treatment studies.

## References

- (1) Yahiro, A.T.; Lee, S.M.; Kimble, D.O. *Biochim. Biophys. Acta* **1964**, 88, 375.
- (2) Akers, N.L.; Moore, C.M.; Minter, S.D. *Electrochim. Acta* **2003**, in press.
- (3) Blaedel, W.J.; Jenkins, R.A. *Analytical Chemistry* **1975**, 47, 1337-1338.
- (4) Zhou, D.; Fang, H.Q.; Chen, H.; Ju, H.; Wang, Y. *Analytica Chimica Acta* **1996**, 329, 41-48.
- (5) Schrenk, M.; Villigram, R.; Torrence, N.; Brancato, S.; Minter, S.D. *J. Membrane Sci.* **2002**, 205, 3-10.
- (6) Fortie, G; Vaillancourt, M.; Belanger, D. *Electroanalysis*, **1992**, 4, 275.
- (7) Rishpon, J.; Gottesfeld, S.; Campbell, C.; Davey, J.; Zawodzinski, T.A.J. *Electroanalysis*, **1994**, 6, 17.
- (8) Karyakin, A.A.; Kotel'nikova, E.A.; Lukachova, L.V.; Karyakina, E.E. *Anal. Chem.*, **2002**, 74, 1597.

# ALTERNATE METHANOL TOLERANT CATHODES FOR PEMFC APPLICATIONS

Vadari Raghuvveer and Balasubramaniam Viswanathan

Department of Chemistry  
Indian Institute of Technology, Madras  
Chennai 600 036, India

## Introduction

The application of fuel cells to electric vehicles requires a PEMFC offering a high power density and low noble metal catalyst loading or cheap electrocatalyst, to reduce weight, volume and cost. However, at high potentials the formation of adsorbed species on the platinum surface inhibit the oxygen reduction reaction and hence result in loss of fuel cell performance<sup>1</sup>. The most commonly employed solid polymer electrolyte, Nafion 117, has the drawback of methanol permeation across the membrane<sup>2-4</sup>, which poisons the platinum catalyst at the cathode. Attempts are therefore being made to find methanol tolerant oxygen reduction electrocatalyst for SPE-DMFCs. Many mixed oxide systems such as spinels, perovskites<sup>5</sup> have been investigated for the possible application as cathode materials. These are restricted to alkaline medium as they are not stable in acids. The Pb-Ru pyrochlore is known to be stable in acid, but at high cathodic potentials, the topotactic extrusion of lead takes places. They exhibit better stability if bonded to any solid polymer proton-exchange membrane<sup>7</sup> that is exposed to an aqueous electrolyte reservoir on the opposite side of the membrane. The Pb-Ru pyrochlore prepared by convention ceramic method shows quite low activity for oxygen reduction. Upon dispersing on the carbon matrix, significant enhancement in the activity was observed<sup>7</sup>.

The activity of the electrochemical charge transfer reaction across the electrode/electrolyte interface depends on the density of states of the electrode. Hence the Pb-Ru pyrochlore oxide, when prepared in the nanocrystalline form, can be expected to exhibit altered electrochemical behaviour by virtue of an enhanced surface to volume factor as well as due to alterations in the density of states, because of the broken bonds, in the diffuse space charge region inside the solid<sup>8-10</sup>.

In the present study, the electrochemical reduction of oxygen was carried out using the nanocrystalline Pb-Ru pyrochlore sample of composition  $Pb_2Ru_{1.95}Pb_{0.05}O_7$  which was prepared by polymer modified sol-gel method (PMSGpyro) as cathode electrocatalyst, by gas diffusion mode using proton exchange membrane (Nafion 117) as electrolyte. The nanomaterial thus obtained was characterized by XRD and transmission electron microscopy. The activity and stability comparison of the nanocrystalline oxide and commercial platinum were made using cyclic voltammetry and chronoamperometry respectively, at RT and 70°C.

## Experimental

### Preparation of Nanocrystalline Pb-Ru pyrochlore

The chemicals used for the synthesis of nanocrystalline Pb-Ru pyrochlore of composition  $Pb_2Ru_{1.95}Pb_{0.05}O_7$  are Lead nitrate (CDH, 99.1%), Ruthenium chloride (s.d.fine chemicals Ltd.). Polyacrylamide gel was used as protecting agent to prevent crystal growth. High molecular weight polyacrylamide was prepared by radical polymerization of the monomer using  $H_2O_2$  as radical generator.

The polyacrylamide gel solution was prepared by taking 2 g of gel in 500 ml distilled water and the resulting solution was kept

aside for two days to obtain sufficient viscosity. The optimized concentration of the polymer gel solution taken is 0.4%. The stoichiometric amounts of metal nitrates and chlorides were taken in one burette and in another burette 5% KOH solution was taken. The solutions from the two burettes were released into the gel solution maintained at 75-80°C with vigorous stirring, by maintaining the pH 7.5-8.5. After the completion of precipitation, the precipitate was aged for 30 min. at 75-80°C, followed by filtration and dried in an air oven maintained at 373 K for 2 h. The precursor was calcined at 500°C for 2 h in air.

**Characterization methods.** The thermograms of the samples were obtained using Perkin Elmer TGA (Delta Series, TGA 7) instrument with a steady heating rate and flow of 20 ml min<sup>-1</sup> of nitrogen. The XRD measurements were obtained using a Philips PW 1130 at room temperature. The radiation used is Ni filtered Cu  $k_{\alpha}$  ( $\lambda = 1.5405 \text{ \AA}$ ). The C, H and N analysis were obtained using Heraeus CHN analyzer. The microscopic analyses was carried out using Philips EM430ST operated at 300 kV. The sample was dispersed in ethanol by sonication and dropped on to a carbon grid and imaged. All the electrochemical measurements were performed using Wenking potentiostat (POS 73) with a Philips digital X-Y recorder (PM 8033). A Pt (1.5 cm<sup>2</sup>) and saturated Ag/AgCl was used as counter and reference electrode respectively. Chronoamperometric responses were obtained by fixing the potential and recording the current response with time using Philips X-t recorder. The flow rate of the oxygen gas in the gas diffusion electrodes was controlled using mass flow controller.

**Gas diffusion electrode and Membrane electrode assembly.** The gas diffusion electrode was prepared by mixing the Pb-Ru pyrochlore oxide catalyst with carbon (Vulcan XC 72R) in 1:3 ratio and suspended in water with 5% Nafion. For, the commercial catalyst, the platinum supported carbon (20% Pt/C, Arora Mathey) was taken as such and suspended in water and 5% Nafion solution. The mixture was thoroughly homogenized with a ultrasonicator before and a dilute PTFE dispersion was added, for 30 minutes. The active layer contains 20 wt% of PTFE. The resulting semi-solid paste was then spread onto the previously treated Teflon containing uncatalysed carbon coated carbon cloth and leveled by roller.

The membrane electrode assembly was constructed based on the literature<sup>7</sup>. The carbon cloth containing the catalyst layer side was bonded to a previously treated Nafion 117 membrane by placing the Nafion membrane on top of the coated surface, the assembly was then hot pressed for 3 min. The other side of the carbon cloth which contains Teflon containing uncatalysed carbon was used as gas diffusion layer. The geometric area of the carbon cloth with the catalyst layer used in the present study is 2.5 cm<sup>2</sup>.

## Results and Discussion

The TGA/DTG (figure not shown) obtained for the the assynthesized sample before calcination, show peaks corresponding to 110°C and 475°C attributed to the removal of physisorbed water, condensation process for the formation of oxide framework and polymer decomposition. The decomposition of polyacrylamide takes place at 450°C. The water removal during the condensation process as well as decomposition of the polymer takes place at almost the same temperature. Thus the calcinations temperature chosen is 500°C in air. The XRD pattern observed for pyrochlore in **Figure 1** confirms the formation of single phase material with well defined superstructure reflections

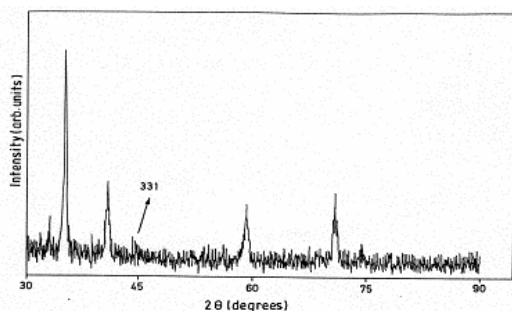


**Figure 1** X-ray diffraction pattern obtained for nanocrystalline Pb-Ru pyrochlore sample

corresponding to the pyrochlore order (331 reflection). The pattern is matching well with JCPDS standard file No. 34-472. The XRD peaks observed are characteristically broader which is normally expected for the nanosized crystallites. The percentage of C (<0.5%), H (<0.08%) and N (<0.5%) are considerably low confirming the removal of the polyacrylamide during calcination at 500<sup>o</sup>C for 2h. The TEM micrograph of the nanocrystalline Pb-Ru pyrochlore sample is shown in **Figure 2**. The sample was imaged at different regions. It is seen from the micrograph that the overall particle size ranges from 1-15 nm and the particles are spherical in nature, confirming the particles are in nanosize region.

The nanocrystalline Pb-Ru pyrochlore sample was found to be stable in the test cell where the catalyst was bonded to one side of the Nafion 117 membrane and 2.5 M sulphuric acid solution contacted to the other side. The cyclic voltammograms taken in the presence of nitrogen and oxygen gas on the back side of the Pb-Ru pyrochlore sample (PMSGpyro) and commercial platinum (20%Pt/C), electrode in the potential range of +0.8 to -0.5 V vs Ag/AgCl, at room temperature, at a scan rate of 25 mV/s, are shown in **Figure 3** and **Figure 4** respectively. The higher current response in the presence of oxygen compared to that of the nitrogen, suggests that the oxygen reduction reaction is taking place on the nanocrystalline oxide and platinum surface. The magnitude of the current during the forward and reverse scan are almost equal. The current density at +0.2 V vs Ag/AgCl, during the forward cathodic scan, provides a measure of electrocatalytic activity and is tabulated in Table 1. The oxygen reduction onset potential is almost same for the nanocrystalline pyrochlores (**Figure 4a**) and commercial platinum (**Figure 4b**). The nanocrystalline pyrochlore exhibited better activity compared to that of the same material prepared by conventional ceramic method (Sspyro). This may be due to the increase in the density of states upon decrease in the particle size<sup>10</sup>. No change in the cyclic voltammetric response was observed upon the addition of methanol in the sulphuric acid with respect to time, suggesting that the pyrochlore is methanol tolerant. The chronoamperometric response of the sample PMSGpyro and commercial platinum electrodes for the oxygen reduction at +0.2V vs Ag/AgCl for 1.5h, at room temperature and 70<sup>o</sup>C (**Figure 5**) shows comparable stability during the oxygen reduction reaction.

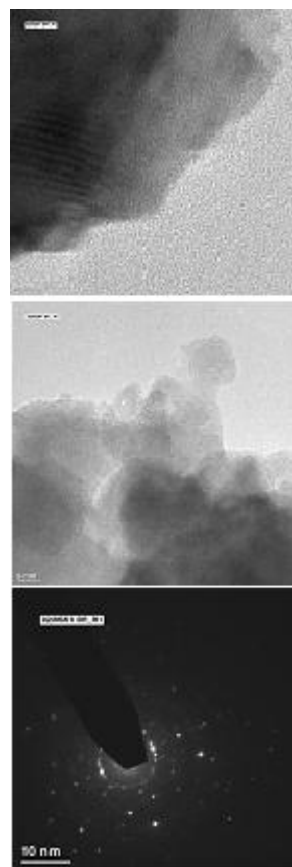


**Figure 2** TEM micrograph of nanocrystalline Pb-Ru pyrochlore prepared by polymer modified sol-gel method taken in different t regions

**Table 1. Comparison of electrocatalytic activity for the oxygen reduction using pyrochlore and commercial platinum as cathode**

Electocatalyst	OCV (V vs Ag/AgCl)	Activity at +0.2 V vs Ag/AgCl I (A/2.5 cm <sup>2</sup> )
SSpyro	-	1.6
PMSGpyro	0.500	16.4
Commercial Pt (20%Pt/C)	0.520	14.0

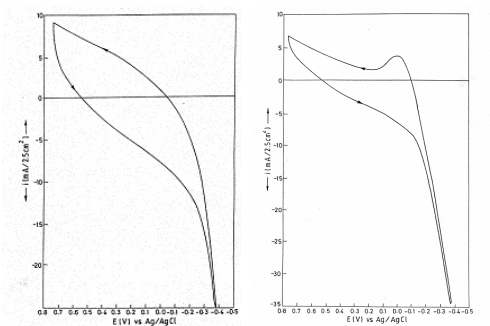


**Figure 3** Cyclic voltammogram obtained for (a) Nanocrystalline Pb-Ru pyrochlore and (b) commercial platinum (20%Pt/C) bonded to Nafion 117 membrane in the presence of nitrogen gas

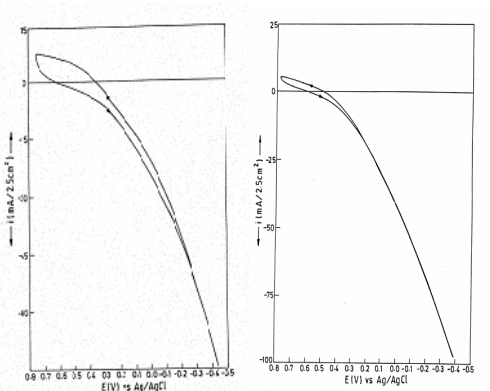


**Figure 4** Cyclic voltammogram obtained for (a) Nanocrystalline Pb-Ru pyrochlore and (b) commercial platinum (20%Pt/C) bonded to Nafion 117 membrane in 12 ml/min flow rate of oxygen gas on the back side of the electrode at a scan rate of 25 mV/s at RT

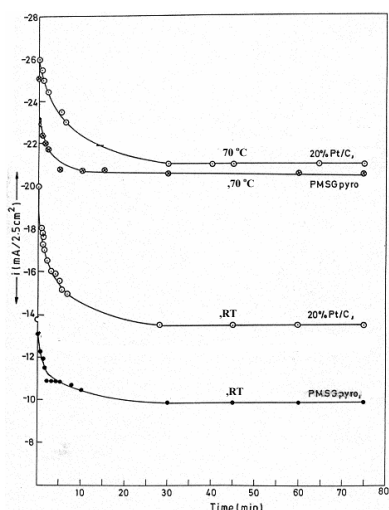


**Figure 5** Chronoamperometric response of nanocrystalline Pb-Ru pyrochlore sample and commercial platinum (20%Pt/C) for the oxygen reduction polarization potential at +0.2V vs Ag/AgCl in the presence of oxygen gas.

## Conclusions

The nanocrystalline Pb-Ru pyrochlore prepared by polymer modified sol-gel method has been evaluated as the electrode for the oxygen reduction reaction in proton exchange membrane (PEM) medium. The oxide particle obtained are nanocrystalline in nature, which is evident from the XRD and TEM measurements. The nanocrystalline Pb-Ru pyrochlore (2.05 mg/2.5 cm<sup>2</sup>) exhibits comparable activity with that of the commercial platinum catalyst (0.6 mg/2.5 cm<sup>2</sup>), for oxygen reduction reaction in the proton exchange membrane medium. The chrono amperometric measurements reveal that the nanocrystalline pyrochlore exhibits comparable stability to that of commercial platinum electro catalyst for oxygen reduction reaction. The enhancement in the activity exhibited by the nanocrystalline Pb-Ru pyrochlore may be due to the enhanced surface to volume ratio.

## References

- (1) Burke, L. D.; Casey, J. J.; Morrissey, J. A.; Sullivan, J. F. O'. *J. Appl. Electrochem.* **1994**, *24*, 30.
- (2) Kauranen, P. S.; Skou, D. *J. Electroanal. Chem.* **1996**, *408*, 189.
- (3) Scott, K.; Taama, W. M.; Argyropoulos, P.; Sundmacher, K. *J. Power Sources.* **1999**, *83*, 204.
- (4) Longo, J. W.; Stround, R. M.; Swikur-Lyons, K. E.; Rolison, D. R. *J. Phys. Chem. B.* **2000**, *104*, 9772.
- (5) Hayashi, M.; Hyodo, T.; Miura, N.; Yamazoe, N. *Electrochemistry*, **2000**, *68*, 112.
- (6) Goodenough, J. B.; Manoharan, R.; Paranthaman, M. *J. Am. Chem. Soc.*, **1990**, *112*, 2076.
- (7) Zen, J.-M.; Manoharan, R.; Goodenough, J. B. *J. Appl. Electrochem.* **1992**, *22*, 140.
- (8) Memming, R. *Solid State Ionics*, **1997**, *94*, 131.
- (9) Kuznetsov, A. M.; Ulstrup, J. *Electrochim. Acta.* **2000**, *45*, 2339.
- (10) Raghuvveer, V.; Viswanathan, B. *Fuel*, **2002**, *81*, 2191

# Production of Pure Hydrogen and Novel Carbon Nanotube Structures by Catalytic Decomposition of Propane and Cyclohexane

Yuguo Wang, Naresh Shah, and Gerald P. Huffman

University of Kentucky, 107 Whalen Building, 533 South Limestone Street, Lexington, KY 40506-0043

## Introduction

The U.S. Department of Energy has recently announced its intention to develop "FreedomCar", a hydrogen-powered vehicle. Such vehicles would likely use polymer electrolyte membrane (PEM) fuel cells, which require very pure hydrogen. Currently, the most common method of producing high purity hydrogen is a multi-step process, involving steam reforming or partial oxidation of natural gas or gasification of hydrocarbons (including coal and biomass) to produce synthesis gas ( $\text{CO} + \text{H}_2$ ), water-gas shift reactions to convert  $\text{CO}$  to  $\text{CO}_2$  and  $\text{H}_2$ , and various purification steps to reduce the  $\text{CO}$  to ppm levels. Direct non-oxidative catalytic decomposition of hydrocarbons into hydrogen and carbon is an alternative, one-step process to produce hydrogen of the required purity.

In previous work<sup>1-4</sup>, we have investigated the decomposition of methane and ethane into hydrogen and carbon nanotubes using nano-scale, binary Fe-based catalysts supported on high surface area alumina ( $\text{M-Fe}/\text{Al}_2\text{O}_3$ ,  $\text{M}=\text{Mo}$ ,  $\text{Pd}$  or  $\text{Ni}$ ). These binary catalysts exhibited high activity for the catalytic decomposition of undiluted methane into pure hydrogen and carbon nanotubes, while ethane was decomposed into hydrogen, methane, and carbon nanotubes. In certain temperature ranges, the catalytic decomposition of ethane produced carbon nanotubes with a novel structure that resembled stacked traffic cones<sup>3</sup>. This is a very open structure that appears to have potential as a hydrogen storage material. In this work, we present the results for the production of hydrogen by catalytic decomposition of propane and cyclohexane.

## Experimental

Supported catalysts were prepared by co-precipitation or incipient wetness methods by adding aqueous solutions of appropriate catalyst metal ( $\text{Fe}$ ,  $\text{Mo}$ ,  $\text{Ni}$  and  $\text{Pd}$ ) salts in the desired proportions to  $\gamma$ -alumina ( $150 \text{ m}^2/\text{g}$ ). The composition of the binary metal catalysts,  $\text{M-Fe}$  ( $\text{M}=\text{Mo}$ ,  $\text{Pd}$  or  $\text{Ni}$ ) was 0.5 wt%  $\text{M}$  and 4.5 wt%  $\text{Fe}$  with respect to the alumina support.

The propane experiments were carried out as described previously<sup>1</sup>, in a fixed bed, plug-flow quartz reactor. The cyclohexane experiments were carried out in a fixed bed, plug-flow stainless steel reactor. Prior to reaction, the catalysts were reduced in flowing hydrogen ( $50 \text{ mL}/\text{min}$ ) for 2 h at  $700^\circ\text{C}$ . After reduction, the reactor was flushed with an inert gas until the GC showed no residual hydrogen peak ( $\sim 15 \text{ min}$ ). The gaseous decomposition products of propane were analyzed by an online GC with a TCD detector, while the products from decomposition of cyclohexane were analyzed in the gas state online by two GC's, the first for hydrocarbon analysis and the second downstream for hydrogen analysis.

## Results and Discussions

The product distributions of thermal and catalytic cracking of propane using a  $(0.5\% \text{Pd}-4.5\% \text{Fe})/\gamma\text{-Al}_2\text{O}_3$  catalyst are shown in Figures 1 and 2, respectively. It is seen that the thermal cracking starts at about  $525^\circ\text{C}$  and catalytic decomposition starts at about  $375^\circ\text{C}$ . At approximately  $475^\circ\text{C}$ , propane is catalytically completely decomposed into a mixture of methane and hydrogen. Propane is not completely decomposed by thermal cracking until a temperature of  $725^\circ\text{C}$  is reached. Moreover, thermal cracking of propane produces

a mixture of ethane, ethylene, methane, and hydrogen, while only hydrogen and methane are produced by catalytic cracking.

Not surprisingly, hydrogen production at higher temperatures is similar to that of pure methane. The most active of the current suite of catalysts was the  $0.5\% \text{Ni}-4.5\% \text{Fe}/\text{Al}_2\text{O}_3$  catalyst, which yielded approximately 85 volume% of hydrogen at a fairly modest temperature of  $625^\circ\text{C}$ . Time on stream studies (TOS) were carried out at  $625^\circ\text{C}$  to determine the rate of deactivation of the various pre-reduced (at  $700^\circ\text{C}$ ) catalysts (Figure 3). The activities of the  $\text{Mo-Fe}$  and  $\text{Ni-Fe}$  catalysts decrease relatively slowly at rates of  $\sim 1\text{-}2\%$  per hour. This rate of deactivation is considerably slower than that of a  $5\% \text{Fe}/\text{Al}_2\text{O}_3$  catalyst (shown in Fig. 3). However, a considerable loss in activity for the  $\text{Pd-Fe}$  catalyst is seen at  $625^\circ\text{C}$  after only about 1.5 hours. The reason for this is not known at this time, but may be clarified by investigation of the structure of the catalyst by XAFS and Mössbauer spectroscopy, which is currently in progress. Our previous investigations have indicated that the most active form of the  $\text{M-Fe}$  catalysts is a mixture of an active austenitic  $\text{Fe-M-C}$  alloy phase and support binding iron aluminate<sup>4</sup>. It may be that these structures were not achieved in the current  $\text{Pd-Fe}$  catalysts for some reason.

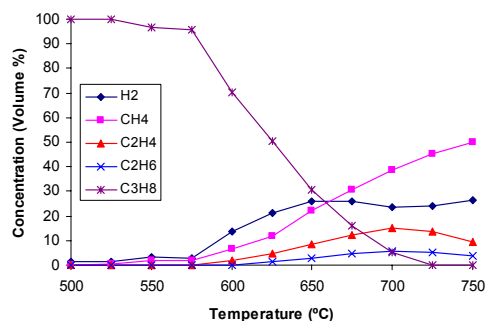


Figure 1. Product distribution of thermal cracking of propane at different temperatures.

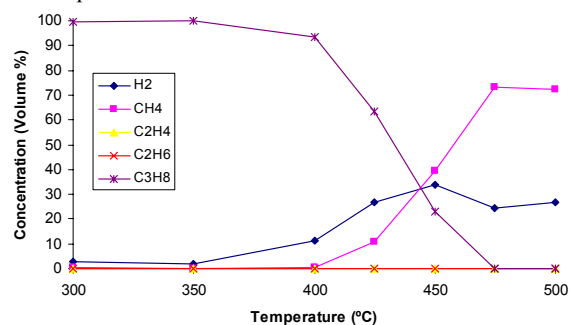


Figure 2. Product distribution of catalytic cracking of propane.

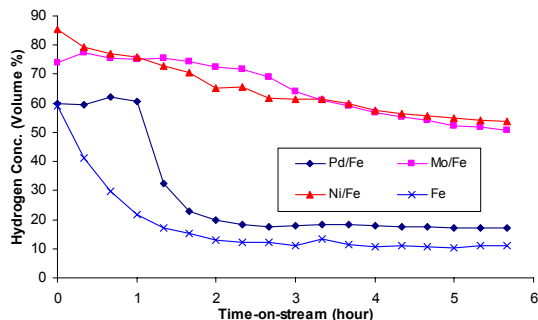
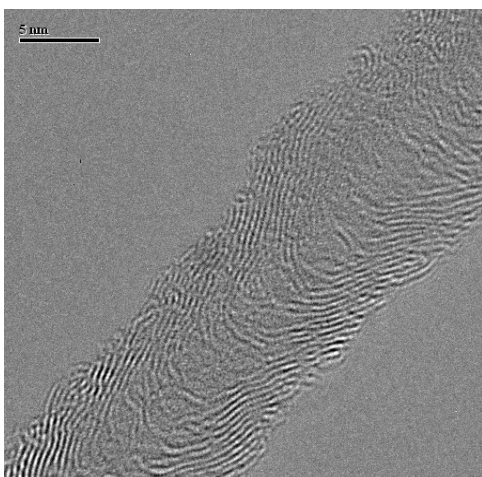
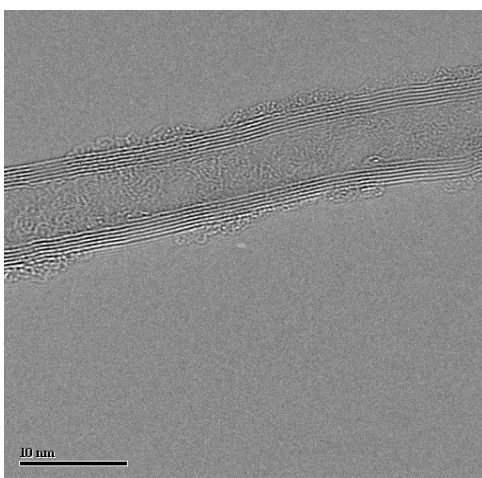


Figure 3. Time-on-stream catalytic decomposition of propane at a reactor temperature of  $625^\circ\text{C}$ .



**Figure 4.** HRTEM image of MWNT grown by decomposing undiluted propane at 475 °C over Pd-Fe/Al<sub>2</sub>O<sub>3</sub> pre-reduced at 700 °C.



**Figure 5.** HRTEM image of MWNT grown by propane decomposition at 625 °C over Mo-Fe/Al<sub>2</sub>O<sub>3</sub> (pre-reduced at 700 °C).

An HRTEM image of carbon multiwalled nanotubes (MWNT) grown by decomposing undiluted propane over the Pd-Fe catalyst at 475 °C is shown in Figure 4. Decomposition of ethane with Pd-Fe also produced the same type of MWNT<sup>2,3</sup>, with an interesting structure resembling nested cones stacked over one another. Because there are many more side openings in these novel MWNTs, they have more potential for hydrogen storage than conventional MWNTs, whose walls are parallel and cylindrical. The hydrogen storage capability of these nanotubes is currently under investigation. The MWNTs produced by decomposition of propane over the Ni-Fe and Mo-Fe catalysts at 625 °C were predominantly the more conventional type, consisting of parallel concentric hollow cylinders (Figure 5).

Preliminary experiments have also been conducted using the Ni-Fe/Al<sub>2</sub>O<sub>3</sub> for hydrogen production from cyclohexane. Figure 6 shows the distribution of different products in the outgoing gas flow from the reactor as a function of temperature. No reaction products were observed below 400 °C and the only products produced above that temperature were methane, benzene, and hydrogen. It appears that the Ni-Fe/Al<sub>2</sub>O<sub>3</sub> catalyst mainly cleaves carbon-carbon bonds to produce hydrogen, methane and carbon nanotubes. At 475 °C, benzene production reaches its highest point, but is still insignificant (~3 vol.%) compared to the production of methane. Consequently, it

appears that the catalyst is not effective in dehydrogenating cyclohexane to benzene. At 500 °C, no benzene is observed in the outgoing gas flow from the reactor, which is consistent with results obtained by Otsuka et al.<sup>5</sup> using a Ni/SiO<sub>2</sub> catalyst to produce hydrogen from C6 hydrocarbons.

The results for a TOS run of cyclohexane with Ni-Fe/Al<sub>2</sub>O<sub>3</sub> are shown in Figure 7. The reaction was stopped after about one hour because the carbon produced in the stainless steel reactor prevented accurate flow control of cyclohexane through the catalyst bed. Within this one hour period, hydrogen is about 60% of the outgoing gas flow. Methane production increases after about 50 minutes, and at the same time, the remaining cyclohexane in the outgoing gas flow decreases. This may be because carbon deposits on the catalyst bed decreases the flow of cyclohexane through the bed. Preliminary HRTEM observations of carbon build up on the catalyst bed showed similar “nested cone” structure MWNTs.

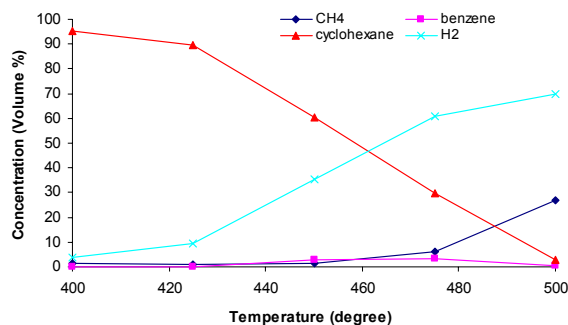


**Figure 6.** Product distribution of Ni-Fe/Al<sub>2</sub>O<sub>3</sub> catalytic conversion of cyclohexane at different temperatures.

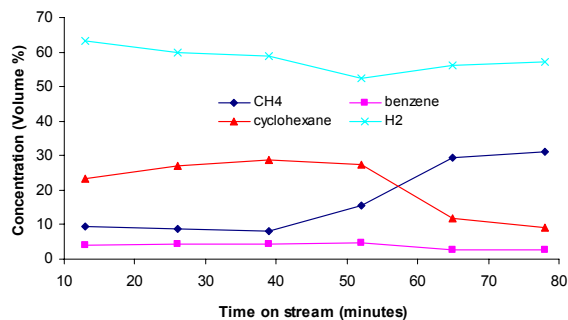


**Figure 7.** Product distribution of cyclohexane conversion on Ni-Fe/Al<sub>2</sub>O<sub>3</sub> at 475 °C.

**Acknowledgement.** This research was supported by the U.S. Department of Energy through the Office of Fossil Energy (FE) under the National Energy Technology Laboratory (NETL) under DOE contract No. DE-FC26-02NT4159.

## References

- (1) Shah, N.; Panjala, D.; Huffman G. P. *Energy & Fuels*, **2001**, *15*(6), 1528.
- (2) Makkuni, A.; Panjala D.; Shah N.; Huffman G. P. Prepr. Pap. - Am. Chem. Soc., *Fuel Chem. Div. Preprints*, **2002**, *47*(2), 782-783.
- (3) Shah, N.; Wang, Y.; Panjala, D.; Huffman, G.P. “Production of High Purity Hydrogen and Novel Carbon Nanostructures by Non-Oxidative Catalytic Dehydrogenation of Ethane”, submitted to *J. Phys. Chem. B*.
- (4) Shah, N.; Pattanaik, S.; Huggins, F.E.; Panjala, D.; Huffman, G.P. “XAFS and Mössbauer spectroscopy characterization of supported binary catalysts for non-oxidative dehydrogenation of methane”, *Fuel Proc. Tech.*, in press.
- (5) Otsuka K.; Shigeta Y.; Takenaka S. *Int J Hydrogen Energy*, **2002**, *27*, 11.

## Analysis of the Distributed Feed IRSOFC

Ayman M. Al-Qattan and Donald J. Chmielewski

Department of Chemical & Environmental Engineering  
Illinois Institute of Technology  
10 West 33<sup>rd</sup> Street, Chicago, IL 60616

### Background

The electrochemical reactions occurring within a SOFC are:  $H_2 + O^- \rightarrow H_2O + 2e^-$  at the anode and  $\frac{1}{2}O_2 + 2e^- \rightarrow O^-$  at the cathode. As these reactions proceed, a certain amount of energy is released. Unfortunately, only a portion of this released energy can be converted to electrical power, the balance showing up as heat. In steam reforming, the endothermic reforming reaction ( $CH_4 + H_2O \rightarrow 3H_2 + CO$ ) is followed by the equilibrium dominated exothermic shift reaction ( $CO + H_2O \leftrightarrow H_2 + CO_2$ ).

It was concluded by Yakabe *et al.*<sup>1</sup> that thermal stresses are a significant issue in IRSOFCs. Peters *et al.*<sup>2</sup> also state that "Large temperature gradients ... can cause damage to one or more of the components ..." These thermal stresses are due to a mismatch in reaction kinetics (i.e., reforming is fast and the electrochemistry is slow). Thus, a severe "cold spot" is created at the stack inlet. Another important issue is the need to feed excess pre-heated steam with the hydrocarbon fuel (a typical rule of thumb is an inlet steam-to-carbon ratio (SCR) of 2:1). This steam is required to guard against the occurrence of carbon depositing side reactions (a typical example being  $CO + H_2 \leftrightarrow C + H_2O$ ). If we can safely reduce the amount of steam fed to the IRSOFC, then a significant reduction in operating cost can be achieved due a reduction in pre-heating duty and cooling costs.

### Model Development

The local electrochemical reaction rate can be derived from the local current density  $j$ , given by  $j = \frac{E-V}{R}$ , where  $E$  is the local Nernst potential obtained from the expression  $E = E^o + \frac{RT_s}{nF} \ln\left(\frac{p_{H_2} p_{O_2}^{0.5}}{p_{H_2O}}\right)$ . The ratio  $\frac{p_{H_2}}{p_{H_2O}}$  can be simply exchanged for a ratio of concentrations, as we will assume the ideal gas law to hold throughout. The local rate of hydrogen generation can be expressed in terms of current density:  $r_{H_2} = -\frac{j}{hnF}$ , where  $h$  is the fuel cell channel height. Combining the above concepts yields the following expression for the electrochemical reaction rate:

$-r_{H_2} = \alpha(T_s) + \beta(T_s) \ln(\rho)$ , where  $\rho = \left(\frac{C_{H_2}}{C_{H_2O}}\right)$ . In the literature we

find a number of expressions aimed at describing the kinetics of steam reforming<sup>1,2,3</sup>. Using the results of Achenbach<sup>4</sup> we define the

$CH_4$  generation rate as:  $r_{CH_4} = -k_r C_{CH_4}$  where  $k_r = k_{ro} \exp\left(\frac{-\Delta E}{RT}\right)$ .

It should be noted that this expression was determined under excess steam conditions (i.e., a SCR above two). The rate expression for the generation of  $CO_2$  due to the shift reaction is assumed to be<sup>1</sup>:

$$r_{CO_2} = k_{s,f} \left( C_{CO} C_{H_2O} - \frac{C_{CO_2} C_{H_2}}{K_{eq}} \right).$$

In the development of mass balance equations we allow for the introduction of distributed feeds<sup>5</sup> along the length of the channel.

To highlight these terms a hat (^) notation will be used for all distributed feed terms. An overall molar balance leads to  $\frac{dF}{dz} = \hat{F} - \left(\frac{2}{C}\right) Ar_{CH_4}$  where  $\hat{F}$  is the distributed feed volumetric flow rate per reactor length. Species balance equations are given as:

$$\frac{d}{dz}(FC_i) = \hat{F}\hat{C}_i + A \sum_j \gamma_{ij} r_j$$
 where  $\hat{C}_i$  is the molar concentration in

the distributed feed for species  $i$ ,  $r_j$  is the reaction rate and  $\gamma_{ij}$  is the appropriate stoichiometric coefficient. Although the carbon deposition reactions will have a great impact on the activity of the anode, it is assumed that they will have negligible impact on the material balance of the gas stream. In the simulation section, we will describe how the above model will be used to indicate the potential of accelerated carbon deposition.

### Distributed Feed Design

The goal of the design scheme is to select the distributed feed flow rate profile such that the HSR will be spatially uniform. Define

$$\text{the desired (or set-point) HSR as: } \rho_{sp} = \exp\left[\frac{1}{\beta(T_s)} \left( \frac{j_{sp}}{hnF} - \alpha(T_s) \right)\right]$$

where  $j_{sp}$  is the desired current density. Next we make the following

assumptions: 1) the reaction surface temperature is spatially constant, 2) the shift reaction proceeds infinitely fast to the equilibrium condition. In the simulations, both of these assumptions will be

removed. Now we enforce the condition  $\frac{d\rho}{dz} = 0$ . After a number of

algebraic manipulations a spatially constant value of  $\hat{F}$  is determined, which will depend on  $\rho_{sp}, K_{eq}, k_r, \alpha, \beta, \hat{C}_i$  and  $A$ . Clearly, the assumptions used to derive this expression will not be valid in the

actual operation of the stack, however as we will see in the next section it does provide sufficient guidance such that the performance of the stack will be greatly improved.

### Simulation Analysis

In **figure 1**, the reaction surface temperatures of the two configurations are compared. The first two curves represent the conventional SOFC design under inlet SCR's of 2:1 and 1:1. The third curve is for the distributed feed configuration with a minimal amount steam in the feed (i.e., inlet SCR=1:10). Clearly, this profile is a significant improvement over the conventional design. Unfortunately, the concept of a spatially continuous distributed feed is possible only as a mathematical construct. To face this issue we propose a discrete injection design aimed at approximating the continuous distributed feed case. The fourth profile of **figure 1** shows the discrete injection results, again with a SCR=1:10. As discussed earlier, we do not consider carbon deposition kinetics explicitly. Instead, we define the carbon monoxide plus methane to steam ratio (CMMSR), which is proposed as a measure of carbon deposition rates. **Figure 2** compares the CMMSR for the two designs under various inlet SCR conditions. **Figure 3** compares the stack designs under various air stream flow rates. It is clearly seen that the distributed feed configuration requires much less heat from the air flow stream.

**Acknowledgements.** Support provided by IIT and the Kuwait Institute for Scientific Research.

### References

- (1) Yakabe, H.; Ogiwara, T.; Hishinuma, M.; and Yasuda, I. *Journal of Power Sources*, "3-D Model Calculation for Planar SOFC", **2001**, vol. 102, pp 144-154.
- (2) Peters, R.; Dahl, R.; Kluttgen, U.; Palm, C.; and Stolten, D. *Journal of Power Sources*, "Internal Reforming of Methane in Solid Oxide Fuel Cell Systems", **2002**, vol. 106, pp 238-244.
- (3) Selimovic, A. *Licentiate Thesis, Lund Institute of Technology*, "Solid Oxide Fuel Cell Modelling for SOFC/Gas Turbine Combined Cycle Simulations", **2000**.
- (4) Achenbach, E. *Journal of Power Sources*, "Three-Dimensional and Time-Dependent Simulation of a Planar Solid Oxide Fuel Cell Stack", **1994**, vol. 49, pp 333-348.
- (5) Al-Qattan, A.; Chmielewski, D.J.; Al-Hallaj, S.; and Selman, J.R. *Chemical Engineering Science*, "A Novel Design for Solid Oxide Fuel Cell Stacks" submitted September, **2002**.

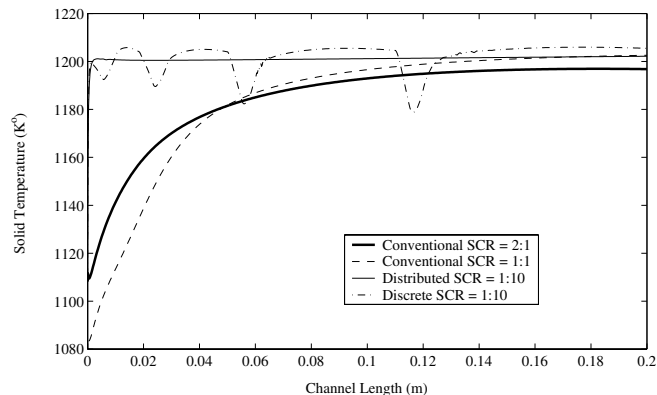


**Figure 1.** Temperature profiles under various stack designs and inlet conditions.

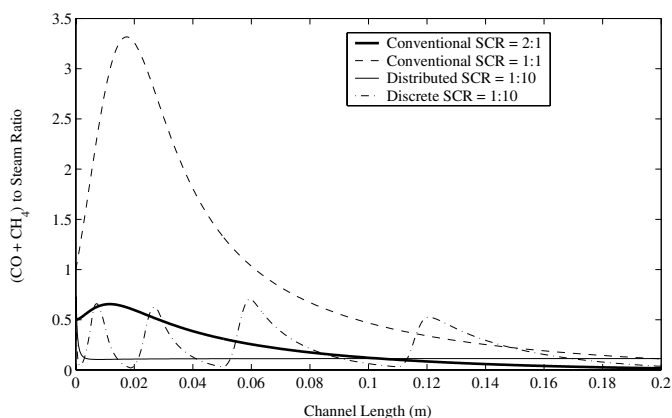


**Figure 2.** CMMSR profiles under various stack designs and inlet conditions.

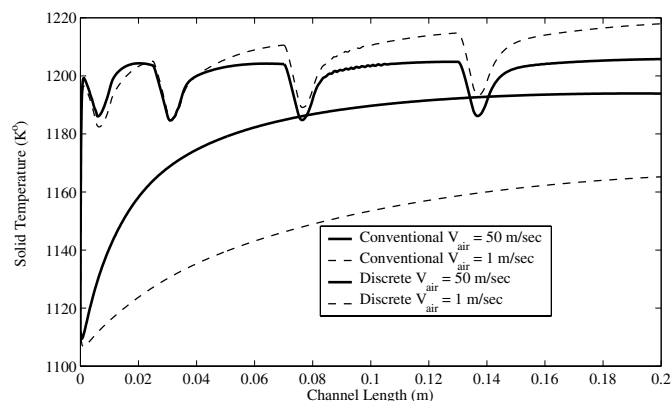


**Figure 3.** Temperature profiles under various stack designs and air flow conditions.

# TEMPERATURE EFFECTS ON THE FORMATION OF CARBON DURING PRE-REFORMING OF LOGISTIC FUELS OVER NOBEL METAL CATALYSTS FOR SOFC APPLICATIONS

James J. Strohm, Jian Zheng and Chunshan Song\*

Clean Fuels and Catalysis Program, The Energy Institute, and  
Department of Energy and Geo-Environmental Engineering  
The Pennsylvania State University  
209 Academic Project Building, University Park, PA 16802  
\*E-mail: [csong@psu.edu](mailto:csong@psu.edu)

## Introduction

The demand for on-site/on-board hydrogen production is increasing with growing interest in fuel cell applications. Reforming of logistic fuels provide a viable means for hydrogen production due to the existing infrastructure and higher energy density. However, the use of such hydrocarbon based fuels in the kerosene and diesel boiling ranges dramatically increase the risk of carbon formation during reforming operations both prior to the catalyst bed (during pre-heating and mixing) and on the catalyst leading to catalyst deactivation<sup>1,2</sup>.

Currently the most widely used reforming catalysts are based on supported nickel. Nickel catalysts are infamous for high levels of carbon formation leading to deactivation even with use of light hydrocarbons (C<sub>1</sub>-C<sub>4</sub>). Numerous studies have dealt with carbon formation on nickel catalyst and various ways to prevent carbon growth during steam reforming of light hydrocarbons.<sup>3-5</sup> Nobel metal catalysts have shown reduced carbon filament formation due carbon not being able to dissolve into the metal.<sup>6</sup> Pre-reforming allows for the production of a methane and hydrogen rich gas at lower temperatures (~500°C) helping alleviate the risk of carbon formation<sup>6</sup>.

Much of the current focus on pre-reforming (or reforming) of higher hydrocarbons is based on the use of oxidative steam reforming.<sup>7,8</sup> Although this method allow for high conversion with minimal risk of carbon formation, the product gases are usually more dilute resulting in decreased efficiency of the fuel cell system.<sup>9</sup> Recently, work has shown rhodium supported catalysts can be effective in pre-reforming using only steam for model logistic fuels.<sup>10,11</sup>

The focus of the present work is to expand on the previous work on the use of noble metal supported catalyst in the pre-reforming of logistic fuels. The effect of temperature on the formation and type of carbon during pre-reforming of a model jet fuel is examined.

## Experimental

**Catalyst preparation.** A support of CeO<sub>2</sub>-Al<sub>2</sub>O<sub>3</sub> was prepared by calcination at 650°C in air for 6 hours of a physical mixture of Ce<sub>2</sub>(CO<sub>3</sub>)<sub>3</sub>•8H<sub>2</sub>O, Al(OH)<sub>3</sub> and polyvinylalcohol (Aldrich) as described by Suzuki and coworkers<sup>12</sup>. Wet impregnation of RhCl<sub>3</sub> (Aldrich) was used to give a nominal metal content of 2wt%. After thoroughly washing the sample, the catalyst was treated with 7M NH<sub>3</sub>-H<sub>2</sub>O at room temperature for 2 hours. The final catalyst pellets have a measured BET surface area of 64 m<sup>2</sup> per gram of catalyst.

**Reaction system.** One gram of catalyst with particle size of 18-35 mesh was placed into the middle of an Inconel 800H stainless steel reactor tube (0.375" I.D. and length of 24"). On either side of the catalyst bed, one inch of  $\alpha$ -alumina beads (4-5 mm diameter) were isolated to examine the carbon deposition before and after the catalyst bed. The remaining volume of the reactor tube was filled with  $\alpha$ -alumina beads with between 3.5-7 mm in diameter.

Catalyst reduction was conducted *in situ* with 20 ml/min hydrogen flow at 500°C for 12 hours. The carrier gas was then switched to nitrogen. Once the desired furnace temperature was reached, steam was introduced for 30 minutes followed by the introduction of the fuel stream as outlined elsewhere<sup>13</sup>. A thermocouple was placed on the outer-wall of the reactor tube and results are reported in terms of the measured wall temperature. The steam to carbon ratio was held constant at 3:1 with volumetric flow rates of 1.38 and 4.02 ml/hr for the fuel and water, respectively. The reaction was conducted at various furnace temperatures while the pressure and time on stream was held constant at 1 atm and 10 hours.

A model jet fuel was used comprising of approximately 20 wt% (10% trimethyl benzene, 5% ethyl benzene and 5% butyl benzene) aromatics in dodecane.

**Carbon analysis.** Temperature programmed oxidation (TPO) was conducted using a LECO RC-412 multiphase carbon analyzer equipped with an IR detector for CO<sub>2</sub> and H<sub>2</sub>O. The temperature programmed used was a 30°C/min heating rate from 100 to 900°C with a 5 minute hold under UHP oxygen flow. TPD experiments were also conducted using the LECO RC-412 carbon analyzer. For TPD experiments two separate temperature programs were used (i.) heating rate of 30°C/min from 100 to 350°C with a 5 minute hold and (ii.) heating rate of 30°C/min from 100 to 900°C with a 5 minute hold. After the furnace cooled, the gas stream was switched from UHP nitrogen to oxygen. TPO analysis was then conducted in the same manner described above.

Since the TPD equipment used can only detect CO<sub>2</sub> to measure the carbon coming off of the system, it was desired to look at the carbon species being removed. In this case, a pyrolysis GCMS (Py-GCMS) was used to determine carbon being desorbed or being removed during TPD analysis. Once again, two separate temperature programs were used for the Py-GCMS; the pyro-probe was either held at 350°C or 900°C for 90 seconds. During the heating of the sample in the pyro-probe, liquid nitrogen was used to cold-trap any elutants in the column. The GCMS was equipped with a Restek RXT15 column and the oven was then heated from 40 to 340°C at 6°C/min with an initial hold of 5 minutes and final hold time of 10 minutes.

## Results and Discussion

**Carbon formation prior to the catalyst bed.** To avoid carbon formation during mixing of the fuel, a pre-heater was designed using a wick and heated steam to vaporize the fuel. By carefully controlling the temperatures at each zone of the pre-heater, experiments in excess of 10 days have been achieved with minimal carbon formation due to fuel pre-heating and mixing. Further explanation of the pre-heater design can be found in one of our previous publications.<sup>14</sup>

As the fuel and steam mixture enters the higher temperature reaction furnace, coking on the alumina beads was observed prior to the mixture reaching the catalyst bed. To quantify the amount of carbon that is being coked prior to the catalyst bed, the alumina beds within one inch on either side of the catalyst bed were analyzed for any carbon formation. Figure 1 shows the effect of reaction temperature on the gas-phase carbon deposition prior to the catalyst bed. As shown in Figure 1, there is significant carbon formation from the model jet fuel prior to reaching the catalyst bed. With just an increase in less than 50°C, the amount of carbon formed on the alumina beads increases by over 100%. The carbon formed is due to gas-phase pyrolysis of the fuel and steam mixture and this is further supported by an increase in ethylene in the gaseous product stream as the temperature of pre-reforming is increased.

Previous work on thermal decomposition of pure jet fuels at similar temperatures have shown the formation of carbon is due to condensation and dehydration reactions of aromatics and once ring sizes greater than 4 is reached solid deposits are observed. From modeling of these results, Andresen and co-workers were able to determine that the coke formed consists mainly of 6-7 aromatic rings which can be linked by aliphatic side chains.<sup>14</sup> It is postulated here that a similar structure of carbon is most likely formed during the gas-phase pyrolysis of the steam and jet fuel mixture. It is apparent from the above figure that lower temperatures provide some relief from extensive carbon formation prior to the catalyst bed.

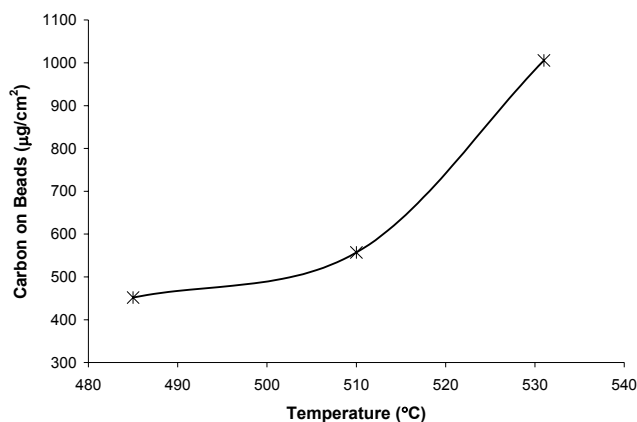


**Figure 1.** The impact of reaction temperature on the formation of carbon (in amount of carbon per unit surface area) on alumina beads directly before the catalyst bed.

In addition to examining the formation of carbon prior to the catalyst bed, the beads directly after the catalyst bed was also examined. At slightly lower temperatures of 485°C, there was some carbon detected (<100 µg/cm<sup>2</sup>) whereas at elevated temperatures of 510 and 531°C no carbon was detected. This implies that as pre-reforming nears completeness, the risk of carbon formation after the catalyst bed is minimized due to little to no slippage of higher hydrocarbons.

**Temperature effect on conversion.** As can be seen in Figure 2, as the temperature is increased slightly the conversion can be significantly enhanced. It should be noted that the conversion plotted in Figure 2 is the final conversion observed after 10 hours on stream. Initially for all temperatures the conversion was very close to 100%. After only one hour, at an outer-wall temperature of 485°C the conversion dropped to 90% and continued to decline to a final conversion of 74%. Similarly at an outer-wall temperature of 510°C the conversion dropped after 5 hours to 97% and continued to slightly fall to 96% after 10 hours on stream. At the last temperature studied, 531°C outer-wall temperature, the conversion remained constant at nearly 100% for the duration of the run with no measurable deactivation.

**Carbon formation on the catalyst.** Figure 2 also illustrates the total amount of carbon measured on the catalyst after being on stream for 10 hours at each temperature. A maximum amount of carbon (in wt% of catalyst) is observed at 510°C. By going to temperatures either higher or lower a reduction in the total amount of carbon is achieved. At higher temperatures, this can be related to the catalyst activity. If the reaction on the catalyst surface occurs at

sufficient rates, the adsorbed carbon species will not have the time to polymerize on the surface or spill-over to the support and polymerize. However at these elevated temperatures, gas-phase pyrolysis if more of a concern and can lead to enhanced formation of carbon on the support (and prior to the catalyst bed). Further evidence is from looking at the product distribution of the reformed gas, the increase in temperature shows enhanced ethylene formation which can be attributed to  $\beta$ -scission reactions during gas-phase pyrolysis of the hydrocarbon chains.

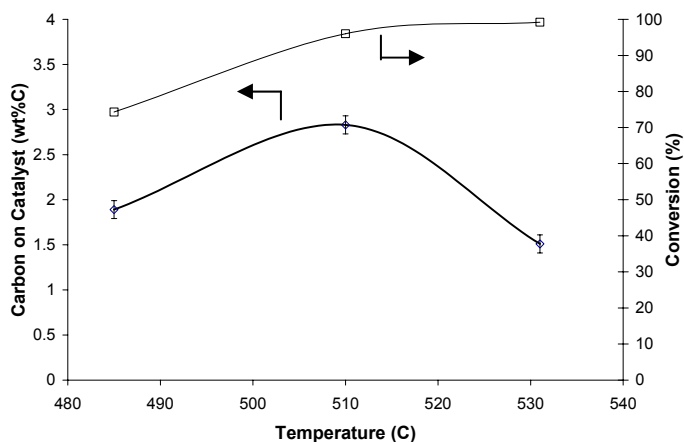


**Figure 2.** Temperature dependence on conversion of the model jet fuel and the total carbon formed on the catalyst.

Figure 3 shows the TPO profiles obtained from oxidation of the total carbon on the spent catalysts at the various temperatures examined. Peak I is attributed to CO<sub>2</sub> desorption from the catalyst which is supported by TPD at 350°C where the peak disappears. Upon exposing the catalyst sample that underwent TPD at 350°C to the air, peak I reappears. During TPD at 350°C, peaks II, III and part of IV are reduced indicating adsorbed hydrocarbon species. To further understand and identify peaks II-IV, py-GCMS was used to identify the species being desorbed. The first set of py-GCMS analysis was conducted with the pyro-probe being held at 350°C. The major products found desorbing at these temperatures were unreacted hydrocarbons (dodecane and aromatics) as well as some partially reacted hydrocarbons such as toluene and naphthalene. After py-GCMS analysis, the catalyst samples were then analyzed using TPO. TPO results showed a large reduction in peaks II and III with minor reduction in peak IV.

At the pre-reforming temperature of 531°C, Figure 3 does not exhibit peak II. From the py-GCMS analysis of the same catalyst, the only major product observed was some dodecane, with a large reduction when compared to the other temperatures. Thus indicating that peak II is adsorbed alkyl-benzenes either initially in the fuel or formed from partial reaction in the gas phase or the catalyst surface. This also corresponds to the boiling range of the alkyl-benzenes such as butyl benzene. This also implies that peak III is dodecane being desorbed from the catalyst, whose boiling point is 212°C.

To further support this, the fresh catalyst was exposed to JP-8 (military aviation fuel) and then dried in a vacuum oven at 150°C overnight. TPO analysis of this sample then showed an increase in peaks II, III and IV; further supporting that peaks II through IV are adsorbed hydrocarbon species rather than coke. At the pre-reforming temperature of 485°C, peak IV is more defined and py-GCMS

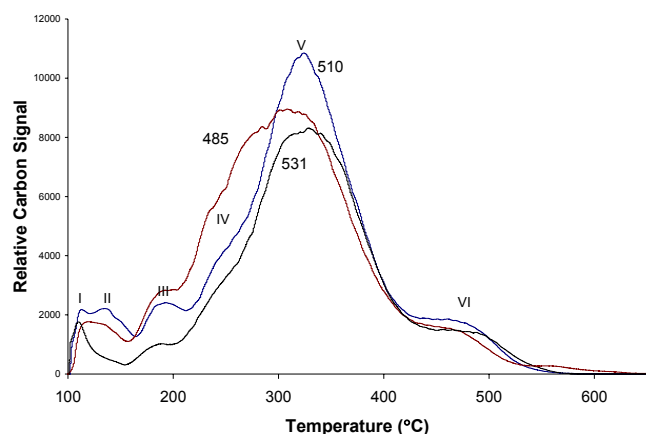


**Figure 3.** TPO profiles of the catalyst after 10 hours of pre-reforming of a model jet fuel at measured outer-wall temperatures of 485, 510 and 531°C.

showed high amounts of naphthalene and alkylated naphthalenes being desorbed indicating that peak IV is adsorbed naphthalenes that are formed from gas-phase pyrolysis or on the catalyst.

Peak V is being tentatively identified as highly amorphous carbon. Py-GCMS analysis with the pyro-probe being held at 900°C for 90 sec yielded a significant reduction in peak V. The major compounds being formed after flash pyrolysis of the sample were 3 to 7 ringed aromatic structures along with some light gaseous products. This indicates that the major building blocks of the carbon detected in peak V is large aromatic units that maybe connected with short aliphatic linkages. Due to the short time the pyro-probe is able to be held at 900°C, not all of the carbon was removed from peak V indicating insufficient heat transfer through the catalyst sample. To get an accurate estimation of the amount of amorphous (or easily removed) carbon on the surface, TPD analysis was conducted at 900°C. Figure 4 shows the resulting carbon remaining on the surface of the catalyst after TPD analysis at 900°C.

From Figure 4 it is shown that some of the initial peak V is still present. This could be due to there being an additional peak embedded in peak V or that some of the aromatic units contributing to the amorphous carbon are of extremely large ring sizes that are not volatile even at 900°C. Another important note is that the peak located between 400 and 550°C (peak VI) is enhanced after TPD at 900°C for the catalyst samples after pre-reforming at 510 and 531°C. This is most likely due to some of the amorphous carbon of peak V being transformed, during the TPD analysis, to peak VI.

For pre-reforming temperature of 485°C there is very little increase in peak VI after TPD analysis. This implies that the aromatic structure of the amorphous coke is of smaller ring size than at the higher temperatures. Py-GCMS verified that the majority of the decomposition of peak V for the pre-reforming temperature of 485 was 2-3 member aromatic rings as apposed to the higher member rings observed for the higher temperatures. This is further shown by Figure 3 where the maximum for peak V (and IV) is slightly shifted towards lower temperatures. Further py-GCMS analysis of all of the samples after TPD at 900°C shows no compounds coming off when the pyro-probe is taken to 1200°C, indicating that the carbon remaining on the sample is highly aromatic and is approaching a more graphitic carbon.

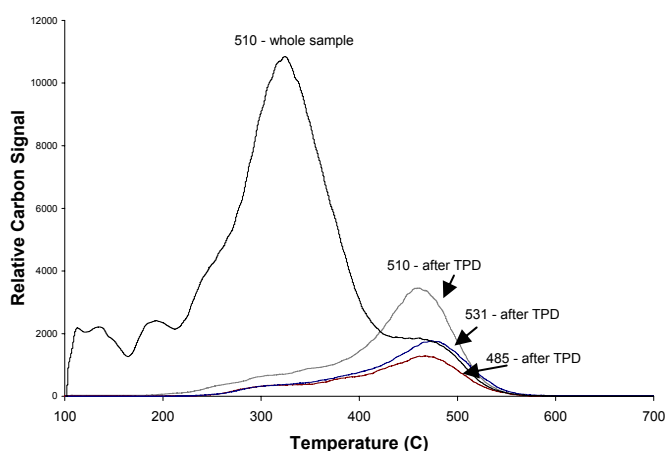


**Figure 4.** TPO profiles of the catalyst sample after pre-reforming at 485, 510 and 531°C after TPD at 900°C compared with the TPO profile of the whole spent catalyst (510°C pre-reforming temperature).

### Conclusions

The effect of temperature was studied on the formation of carbon on rhodium supported catalyst during pre-reforming of a model jet fuel. At pre-reforming temperatures of 510°C, maximum carbon formation was observed. By increasing the pre-reforming temperature to 531°C the amount of carbon formed on the catalyst is significantly reduced due to higher activity of the catalyst. However by increasing the reaction temperature the amount of carbon formed during gas-phase pyrolysis prior to the catalyst bed increased dramatically. To avoid carbon formation prior to the catalyst bed, without fuel modification, the pre-reforming temperature should be kept below 510°C thus requiring catalysts with higher activity at these temperatures.

**Acknowledgement.** We are grateful to the DoD/DARPA Palm Power Program and management team for supporting this work. We also wish to thank Dr. Mehdi Namazian of Altex Technologies Inc. for helpful discussions on the pre-mixing. Thanks also go to Ms. Lu Sun for BET surface measurements and Mr. Ronald Copenhagen for setting up the reactor system.

### References

- (1) Rostrup-Nielsen, J.R. *Cat. Today*, **1997**, 37, 225.
- (2) Song, C. *Cat. Today*, **2002**, 77, 17.
- (3) Rostrup-Nielsen, J.R. In *Catalysis Science and Technology*; Andersen, J.R.; Boudart, M., Ed.; Springer-Verlag, New York, **1984**, Vol. 4, pp.34.
- (4) Trimm, D.L. *Catal. Rev. – Sci. Eng.*, **1977**, 16(2), 155.
- (5) Rostrup-Nielsen, J.R. *J. Cat.*, **1974**, 33, 184.
- (6) Rostrup-Nielsen, J.R. Christensen, T.S. Dybkjaer, I. *Stud. Surf. Sci. Catal.*, **1998**, 113, 81.
- (7) Borup, R.; Perry, L.; Inbody, M.; Tafoya, J. Prepr. Pap. – *Am. Chem. Soc., Div. Fuel Chem.*, **2002**, 47(2), 548.
- (8) Trimm, D.L.; Onsan, Z.I. *Catal. Rev. – Sci. Eng.*, **2001**, 43, 31.
- (9) Larminie, J.; Dicks, A. *Fuel Cell Systems Explained*; John Wiley: New York, **2000**.
- (10) Zheng, J.; Strohm, J.J.; Song, C. Prepr. Pap. – *Am. Chem. Soc., Div. Fuel Chem.*, **2003**, 48(2), to be accepted.
- (11) Zheng, J.; Strohm, J.J.; Song, C. Prepr. Pap. – *Am. Chem. Soc., Div. Fuel Chem.*, **2003**, 48(2), to be accepted.
- (12) Suzuki, H.; Iwanami, H.; Iwanami, O.; Kitahara, T. *Int. J. Hydrogen Energy*, **2001**, 26, 935.
- (13) Zheng, J.; Shen, J.-P.; Song, C.; Pan, W.; Strohm, J.J. Prepr. Pap. – *Am. Chem. Soc., Div. Fuel Chem.*, **2003**, 48(1), 374.
- (14) Andresen, J.M.; Strohm, J.J.; Sun, L.; Song, C. *Energy & Fuels*, **2001**, 15(3), 714.

# CATALYTIC ELECTRODES FOR HIGH PERFORMANCE SOLID OXIDE FUEL CELLS OPERATED AT INTERMEDIATE AND LOW TEMPERATURES

Xiangrong Liu<sup>a, b</sup>, Zhigang Zhu<sup>b</sup>, Bin Zhu<sup>a, b\*</sup>, Ingvar Albinsson<sup>c</sup> and Bengt-Erik Mellande<sup>c</sup>

<sup>a</sup>Department of Chemical Engineering & Technology, Royal Institute of Technology (KTH), S-100 44 Stockholm, Sweden; <sup>b</sup>Goeta Technology Developer International, S-17160, Solna, Sweden; <sup>c</sup>Physics and Engineering Physics, Chalmers University of Technology, S-412 96 Göteborg, Sweden

## Introduction

During recent years many efforts have been contributed to the reduced temperature (800 to 1000°C) and intermediate temperature (IT, 400–700°C) solid oxide fuel cells (SOFCs). Challenges to develop high performance ITSOFCs rest on both electrolyte and electrodes. Recent research showed that the development in functional anode materials is one of the keys to enhance the fuel cell performance at lower temperatures. It has been reported in a number of publications that the ceria-composite electrodes (especially for the anode) could greatly enhance the YSZ SOFC performances for intermediate temperature operation.<sup>1-3</sup> Our approach to use the ceria-composite ceramic materials for both electrolyte and electrodes (anode and cathode) has shown promising performances.

Fuel cells that can be operated for hydrocarbon fuels, e.g., coal gas, natural gas and biomass fuels for the stationary power generation; alcohol (methanol, ethanol etc.) and gasoline/diesel oil for the tractionary power applications, have significant importance for the social sustainable development and further for an urgent marketing demand. The SOFC may in some respects be seen as an ideal source to generate electricity due to its high efficiency and flexibility regarding choice of the fuels, especially for the hydrocarbon fuels. However, when the hydrocarbon type fuels are adopted, the electrode catalytic function is strictly requested to be suitable for various gas or liquid fuels. There is thus an imperative need to develop efficient catalytic electrodes for ITSOFCs in both stationary and tractionary applications.

## Experimental

**Materials and preparation.** Commercial Gd<sub>0.1</sub>Ce<sub>0.9</sub>O<sub>1.95</sub> (GDC) powder was purchased from Seattle Specialty Ceramics, USA. Alkaline hydroxides, e.g., MOH and M<sub>2</sub>CO<sub>3</sub> (M = Li, Na) (A. R., Aldrich Chemical Company, Inc., USA), were used to prepare the composites with GDC for the electrolytes; NiO (Merck, A. R.) and La<sub>0.6</sub>Sr<sub>0.4</sub>Co<sub>0.8</sub>Fe<sub>0.2</sub>O<sub>3</sub> (LSCF) (Seattle Specialty Ceramics, Seattle, WA, USA) were used in the ceria-composite electrodes. Platinum (Leitplatin 308A, Hanau, Germany) and silver (Leitsilber 200, Hanau, Germany) pastes were also investigated for the electrodes for comparison. Stainless steel was adopted for the fuel cell device holder.

The ceria-composite electrolyte samples were prepared by mixing GDC with MOH or M<sub>2</sub>CO<sub>3</sub> in a 10 to 20 wt.% of the total weight and grinding well. The mixtures were heat-treated at 600–680°C for one hour depending on the salts. The resulting materials were grounded again thoroughly for use. The ceria-composite electrodes, e.g., the ceria-composite anode were prepared through a mixture of the ceria with 20–30 wt.% LiOH (or Li<sub>2</sub>CO<sub>3</sub>) composite (50 vol.%) and anode, NiO (50 vol.%). This mixture was grounded and then heat-treated at 700°C for 1 hour. After heat-treatment a 20 vol.% active carbon was added, then ground thoroughly for use. The ceria-composite cathode

was prepared in the same procedure in replacement of the NiO by LSCF.

**Fuel cell construction.** The composite anode-supported ITSOFCs were constructed by directly pressing the composite anode, electrolyte and cathode in one step. The cathode was much thinner compared to the anode thickness. To avoid cracking and separation of the ITSOFC components (anode, electrolyte and cathode) during heating, complete ITSOFC assemblies were heat-treated using a program-controlled furnace to carefully adjust the temperature rise and holding time, e.g., for minimum 30 minutes at 600°C. The finally completed fuel cell assembly for tests has a dimension of 1–2 mm in thickness and 13 mm in diameter. In some cases, the electrolyte support fuel cell assembly was also investigated for comparison. In this case, about 1 mm thick electrolyte disc was pasted by Pt paste.

**Characterisation.** Material characterisation of the electrical properties was carried with the help of a.c. impedance analysis. The impedance analysis was performed with a computerised Hewlett-Packard HP4274A LCR-meter. The measured frequency range covers from 0.1 Hz to 100 kHz with an applied signal of 20 mV. The temperature of the sample (holder) was controlled by an Eurotherm temperature controller and the sample temperature was measured with a Platinum thermocouple attached at the position of the sample. In most cases, the measurements were carried out between 400 and 650°C. At the same time the fuel cell was employed as an in-situ characterisation method for the materials as suggested before.<sup>4</sup>

## Results and Discussion

Performance for hydrogen fuelled ITSOFCs using the ceria-composite electrode have been reported elsewhere.<sup>5,6</sup> The maximum power densities 0.8 Wcm<sup>-2</sup> could be reached at 600°C. In some cases the ITSOFCs can even function at temperature as low as 200°C depending on the catalyst function of the ceria-composite electrodes. These advanced ITSOFC performances are contributed by excellent electrode function.

This electrode function, both catalyst and electrical/electrochemical property. This electrode function is marked by the non-polarization effects in I-V characteristics. Due to the interface between two fuel cell components, electrode and electrolyte, there is always a significant electrode polarization, can be normally observed. This is due to the fact of a discontinuous transport process between the electrons (external circuit) and ions (in the electrolyte and electrodes, internal circuit). However, if there is a continuous transporting process, i.e., the electrolyte is the ionic and electrodes are the electronic and ionic concentration gradient materials, the interfacial polarization would fade away. This effect was studied by the electrochemical characterization on the ITSOFC electrode activation and polarization with the help of the ceria-composite electrodes. **Figure 1** shows I-V characterizations during the in-situ OCV set up accompanying with the cell discharging processes. The freshly constructed ITSOFC at the immediate I-V measurement shows a rather high resistance, 4.2 Ω, deduced from its I-V characteristic. Accompanying with the reduction of NiO in the ceria-composite anode during the fuel cell (OCV) set-up process, the polarisation caused by the electrode activation and reaction kinetics in the I-V characteristics is removed significantly, thus decreasing the cell resistance from 4.2 to around 1 Ω during the first half an hour. The discharge reduces the polarisation more effectively and in turn improves the cell interfaces. After discharging under 200 mAcm<sup>-2</sup> for 5 and 10 minutes, the cell resistance drops rapidly from about 1 Ω to 0.5 Ω. Correspondingly the polarisation effect in the I-V characteristic partially and completely disappears for 5 and for 10

minutes discharge, respectively. It can be seen from Fig. 3 that there is a noteworthy polarisation loss in the electrode process reflected by the non-linearity in the I-V characteristics for the fresh fuel cell before discharge. This polarisation effect depends largely on the cell construction technique, mainly the interfacial structures between the electrolyte and electrodes, and also on the electrode materials. For example, the platinum electrode ITSOFCs always exhibit much stronger polarisation effects than that of the composite electrodes, to be further discussed below. The all-ceria-composite ITSOFCs with both ceria-composite electrolyte and electrodes may provide a continuous electronic and ionic transporting route in the electrolyte/electrode interfaces, and continuous ionic transport from the interface to the electrolyte, the interface being totally connected by electron and ion conducting bridge, making no observable electrode polarisation eventually for all-ceria-component ITSOFCs. This concept is further supported by studying the ITSOFCs constructed by different electrodes.

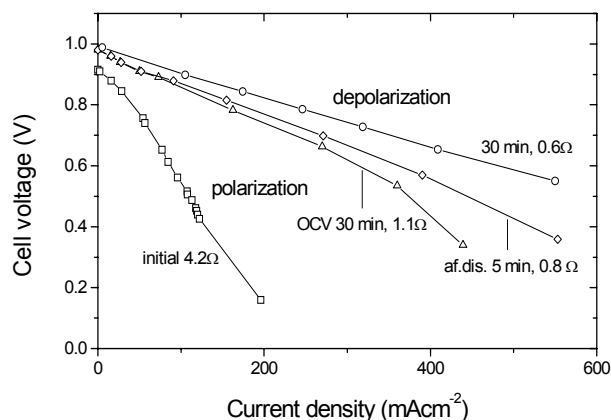


Figure 1. In-situ I-V characteristics

#### High catalyst function to methanol and ethanol liquid fuels.

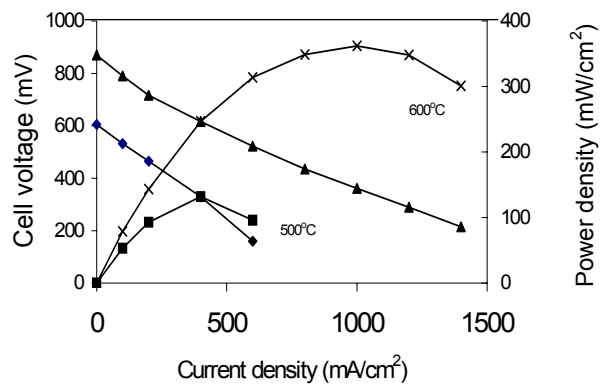
ITSOFCs devices based on the ceria-composite materials showed the OCV around 0.95 V for 2 M methanol, 0.91 V for 1 M ethanol and 0.78 V for 1 M acetone at 600°C. When these liquid fuels were adopted directly, the ITSOFCs operated under 300 to 450 mAcm<sup>-2</sup> (180 to 280 mWcm<sup>-2</sup>) at 600°C demonstrate a peak power density around 330 mWcm<sup>-2</sup> and 300 mWcm<sup>-2</sup> methanol and ethanol fuel cells, respectively, as shown in Figure 6. The performance of the liquid fuelled ITSOFCs can be certainly improved greatly by developing suitable catalysts as demonstrated for DMPEFCs. For example, very recently the CuO was found to be especially active for the direct liquid ceramic fuel cells. The CuO additives in the electrodes can significantly promote the electrode reaction for methanol and ethanol, and improve the DMSOFCs (direct methanol SOFCs) and DESOFCs (direct ethanol SOFCs) performances.

#### Electrode catalytic function to other hydrocarbon fuels.

Figure 2 exhibits some typical I-V characteristics of the ITSOFCs for using the biomass syngas composition. The ITSOFC performances obtained in Figure 2 are rather comparable with that obtained for the hydrogen fuel excluding some voltage/power loss caused by the lower cell voltage due to the hydrocarbon fuel very much related to the catalyst function of the anode when facing the hydrocarbon fuels.

Our ITSOFCs based on ceria-based composite electrolyte and electrodes have the advantages to directly operate various existing fuels, e.g. various hydrocarbon fuels: synthesized coal gas, biomass, nature gas, alcohol as well as ammonia. Hydrocarbon fuels can be

easily thermally decomposed, e.g. methanol: CH<sub>3</sub>OH (g) → 2 H<sub>2</sub> + CO. This process can theoretically deliver a product stream containing up to 67 vol% H<sub>2</sub>.<sup>7</sup> This type fuels can be directly operated in LTSOFCs. Ceria is known to perform functions, including the promotion of water-gas shift and steam-reforming reactions, stabilization of the surface area of the catalyst and maintenance of the dispersion of the catalytic metals. All these functions have provided the ceria-composite electrodes the efficient



ways to improve the cell performances.

Figure 2. FC performance using the biomass syngas composition fuel

#### Advantages of the ITSOFCs using the ceria-composite electrodes and electrolytes.

The major advantages of the ceria-composite materials may be summarised as follows: i) The ceria-composite electrodes are highly catalytic and conductive for both ion and electrons; ii) The ceria-composite electrolytes are highly electrolytic, which means that oxygen atoms can be oxidized as the ions as efficient as possible and transport as fast as possible, based on the high ionic conductivity and ionic entire transport ability of the ceria-composite electrolyte; iii) excellent compatibility between the electrodes and the electrolyte based on the use of one kind ceria composite material with different components. In addition, using the same ceria-based composite materials, there are excellently compatible without problems for the mechanical and thermal expansion compatibility. Compared to the case when ceria was used only as the anode to improve/enhance performance of the YSZ thin film electrolyte SOFCs, the all-ceria-composite ITSOFC systems are more promising. All these mentioned unique advantages, e.g., super ionic conductivity, highly catalyst and compatibility among all cell components make the ceria-composite ITSOFCs more efficient and more promising than the YSZ SOFCs.

**Acknowledgement.** This work is supported by Carl Tryggers Stiftelse for Vetenskap Forskning (CTS) and the Swedish Research Council (VR). Some experiments were completed by Goeta R&D base in China.

#### References

- (1). Murray, E. P.; Tsai, T.; Barnett, S. A., *Nature*, **1999**, *400*, 649.
- (2). Hibino, T.; Tsunekawa, H.; Tanimoto, S.; Sano, M., *J. Electrochem. Soc.* **2000**, *147*, 1338.
- (3). Seungdo, P.; John, M. V.; Raymond, J. G., *Nature*, **2000**, *404*, 265.
- (4). Zhu, B., *Electrochemistry Communication*, **1999**, *1*, 242-249.
- (5). Zhu, B., *J. Power Sources*, **2001**, *93*, 82-88.
- (6). Zhu, B., *J. Power Sources*, **2003**, *114*, 1-9.
- (7). Pettersson, L.; Sjöström, K.; *Combust. Sci. Technol.*, **1991**, *80*, 265.

# Microkinetic Modeling of Ammonia Synthesis and Decomposition on Ruthenium and Microreactor Design for Hydrogen Production

Soumitra R. Deshmukh, Ashish B. Mhadeshwar  
and Dionisios G. Vlachos

Department of Chemical Engineering and Center for Catalytic  
Science and Technology (CCST)  
University of Delaware, Newark, DE 19716-3110

## Introduction

The overall objective of this work is to develop design rules for production of hydrogen from ammonia at the small scale. While ammonia synthesis is one of the most extensively studied processes in catalysis, due to its use in the manufacturing of fertilizers, ammonia decomposition has only recently become of interest due to its potential use in CO-free hydrogen production for fuel cells. Ruthenium is one the better catalysts for the latter but the kinetics of decomposition is not as well understood. Noting the shortcomings of the literature models, we develop a complete microkinetic model to describe the ammonia synthesis as well as decomposition on Ru. An easy to implement reduced model is developed using a novel *computer-aided reduction methodology*. Computational fluid dynamics (CFD) simulations are then performed in a microreactor. Optimization of a microreactor for hydrogen production for fuel cell applications is also discussed.

## Chemistry Modeling

Although ammonia synthesis ( $2NH_3 \leftrightarrow N_2 + 3H_2$ ) is one of the better-studied reactions in the literature, decomposition kinetics on Ru is not as well established. Partial mechanisms and reduced rate expressions have been proposed<sup>1,2</sup> to qualitatively describe experimental trends. These reduced rate expressions have been derived based on the traditional Langmuir-Hinshelwood approximations where a posteriori validation has occasionally been done. As seen in Fig. 1, these models fail to capture the experimental data in a microreactor.

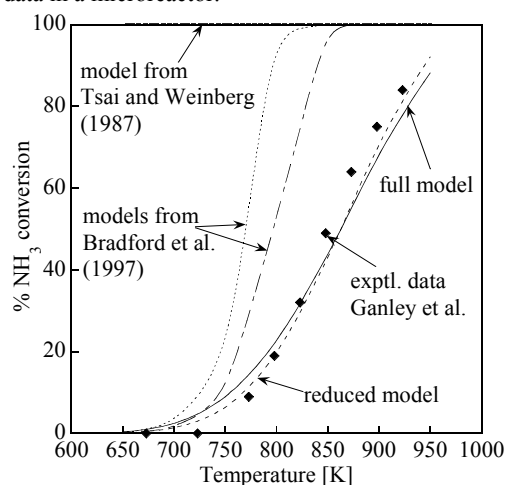


**Figure 1.** PFR simulations with full and reduced reaction models compared to the experimental data of Ganley et al.<sup>3</sup> The reaction model can describe faithfully the experimental data without any adjustment in rate parameters. The reduced reaction model is in very good agreement with the full model and the experimental data. Literature, reduced reaction models are not as accurate.

A detailed reaction mechanism for ammonia decomposition on Ru has been developed. Specifically, the multistep methodology described in Aghalayam et al.<sup>4</sup> is employed to construct a surface reaction mechanism for ammonia decomposition on Ru. In particular, 6 reversible elementary steps for ammonia decomposition are laid down, which include adsorption/desorption of  $NH_3$ ,  $N_2$ , and  $H_2$ , and hydrogen abstraction steps from  $NH_x$  intermediates and their reverse. Order of magnitude estimates of pre-exponential factors are determined using Transition State Theory (TST)<sup>5</sup>, whereas activation energies are calculated using the semi-empirical Bond Order Conservation (BOC) technique<sup>6,7</sup> with input from quantum mechanical density functional theory (DFT) as well as surface science experiments. Adsorbate-adsorbate interactions, shown in Table 1, are also taken into account through the BOC framework in desorption and surface reactions. The mechanism, shown in Table 2, is enthalpically consistent at 300 K. The entire semi-empirical framework has been integrated with surface CHEMKIN to enable transparent, easy use in computing the reaction rates. Simulations have then been carried out and compared to targeted experiments in order to slightly optimize the reaction mechanism against uncertainties. The reaction mechanism is able to predict well atmospheric ammonia decomposition and high-pressure ammonia synthesis data, along with various ultra-high vacuum temperature programmed desorption (TPD) and reaction (TPR) data.

**Table 1. Heat of Chemisorption Data.**  
 $\theta$  indicates coverage of surface species.

Species	Heat of chemisorption (kcal/mole)	References
$N^*$	135-35 $\theta_N$	8,9
$H^*$	63	10,11
$NH_3^*$	18.23	10,11
$NH^*$	86.79	Our BOC calcs.
$NH_2^*$	59.95	Our BOC calcs.

**Table 2: Screening surface reaction mechanism of ammonia decomposition on Ru at 300 K.**  
The activation energies are in kcal/mol, calculated in the zero coverage limit ( $\theta_i=1$ ). All activation energies are coverage dependent as determined from the BOC framework (see Table 1).

No.	Reaction	Sticking coefficient or pre-exponential [ $s^{-1}$ ]	Activation energy at $\theta_i=1$
1	$H_2 + 2^* \rightarrow 2H^*$	1	1.9
2	$2H^* \rightarrow H_2 + 2^*$	$1.0 \times 10^{13}$	23.7
3	$N_2 + 2^* \rightarrow 2N^*$	1	6.2
4	$2N^* \rightarrow N_2 + 2^*$	$1.0 \times 10^{13}$	50.3
5	$NH^* + ^* \rightarrow H^* + N^*$	$1.0 \times 10^{11}$	5.8
6	$H^* + N^* \rightarrow NH^* + ^*$	$1.0 \times 10^{11}$	37.2
7	$NH_2^* + ^* \rightarrow H^* + NH^*$	$1.0 \times 10^{11}$	19.1
8	$H^* + NH^* \rightarrow NH_2^* + ^*$	$1.0 \times 10^{11}$	17.4
9	$NH_3^* + ^* \rightarrow H^* + NH_2^*$	$1.0 \times 10^{11}$	17.5
10	$H^* + NH_2^* \rightarrow NH_3^* + ^*$	$1.0 \times 10^{11}$	13.2
11	$NH_3^* + ^* \rightarrow NH_3^*$	1	0
12	$NH_3^* \rightarrow NH_3 + ^*$	$1.0 \times 10^{13}$	18.2

Armed with a predictive reaction mechanism, we employ a systematic *computer-aided reduction methodology* based on reaction path analysis and small parameter asymptotics, the results of which are also depicted in Fig. 1.

### Computational Fluid Dynamics Modeling

The microreactor, fabricated for hydrogen production for portable applications, consists of an 11x25 array of diamond shaped posts (coated with Ru/Al<sub>2</sub>O<sub>3</sub> catalyst) each of size 300 μm x 300 μm x 3000 μm. Two-dimensional CFD simulations of the microreactor is carried out using the reduced kinetic model for ammonia decomposition. The elliptic Navier-Stokes equations are solved for the flow, along with the continuity, and species and enthalpy conservation equations. The computational mesh involves ~100,000 nodes (typical discretization of 220x575) and results in 800,000 unknowns, requiring about 1 hr of CPU time. The velocity and concentration contours for one such calculation are shown in Fig. 2.

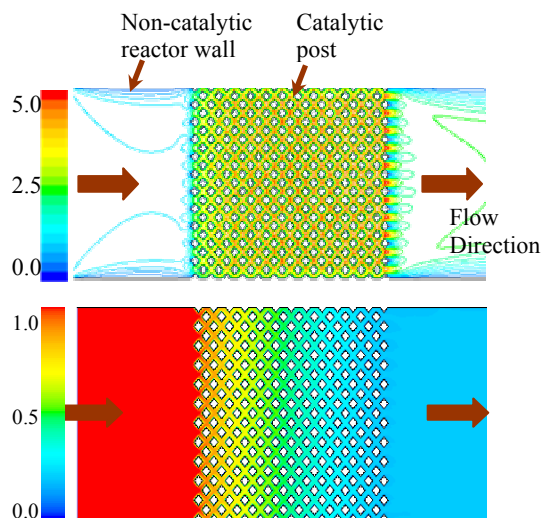


**Figure 2.** Flow (top) and mass fraction (bottom) contours for a full microreactor CFD simulation.

### Results and Discussion

Computational results are in excellent agreement with recent experiments on the effect of temperature on conversion. Comparing the results with those obtained for a tubular reactor we see that the posts play a significant role in reducing the mass transfer effects and thereby increasing the conversion considerably. Microreactor performance was also evaluated for various post geometries such as diamonds, triangles and circles keeping the active area per unit volume constant. The shapes of posts show no significant effect on the conversion in the microreactor but show significant influence on the flow patterns and therefore the pressure drop in these devices. It is found that the circular posts have a lower pressure drop by about a factor of 30%, which is of significant importance given the large pressure drop in these devices for high flow rates. It was found that the conversion in the microreactor decreased with increase in the flow velocity. Boundary layer separation is observed in the microreactor under certain flow conditions. Dimensionality effects will also be discussed.

### Conclusions

A complete microkinetic model for ammonia decomposition and synthesis on Ru is proposed and validated with experimental TPR and TPD data. Reduced models are developed for both cases. CFD

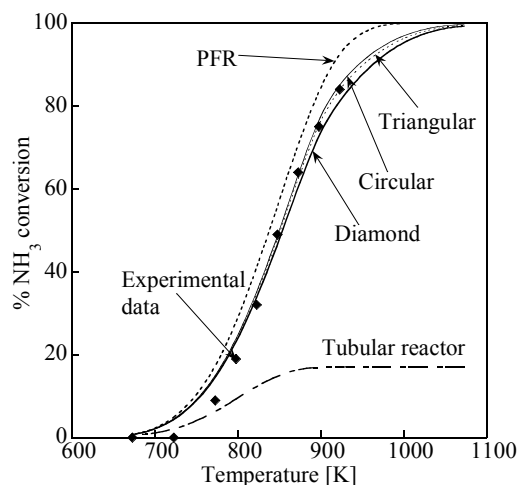


**Figure 3.** Comparison of conversion of PFR, tubular reactor, and microreactor with various post shapes to experimental data.

modeling is carried out for the microreactor to determine the influence of various geometric factors on ammonia conversion and pressure drop. Insights into the optimization of these microreactors are developed.

**Acknowledgement.** This work was supported by the Army Research Office under contract DAAD 19-01-1-0582. Any opinions, findings, and conclusions or recommendations expressed are those of the authors and do not necessarily reflect the views of the Army Research Office.

### References

- (1) Bradford, M. C. J.; Fanning, P. E.; Vannice, M. A., Kinetics of NH<sub>3</sub> decomposition over well dispersed Ru. *Journal of Catalysis* **1997**, 172, 479-484.
- (2) Tsai, W.; Weinberg, W. H., Steady-state decomposition of ammonia on the Ru(001) surface. *Journal of Physical Chemistry* **1987**, 91, (20), 5302-5307.
- (3) Ganley, J. C.; Seebauer, E. G.; Masel, R. I., Porous anodic alumina posts as catalyst support in microreactors for production of hydrogen from ammonia. *AIChE Journal* submitted.
- (4) Aghalayam, P.; Park, Y. K.; Vlachos, D. G., Construction and optimization of detailed surface reaction mechanisms. *AIChE J.* **2000**, 46, (10), 2017-2029, *This paper was selected in the highlights of Chem. Eng. Progress (paper of the month), p., Oct. issue, 2000.*
- (5) Dumesic, J. A.; Rudd, D. F.; Aparicio, L. M.; Rekoske, J. E.; Trevino, A. A., *The Microkinetics of Heterogeneous Catalysis*. ed.; American Chemical Society: Washington, D.C., 1993.
- (6) Shustorovich, E., Bond-order conservation approach to chemisorption and heterogeneous catalysis: Applications and implications. *Advances in Catalysis* **1990**, 37, 101-164.
- (7) Shustorovich, E.; Sellers, H., The UBI-QEP method: A practical theoretical approach to understanding chemistry on transition metal surfaces. *Surface Science Reports* **1998**, 31, 1-119.
- (8) Jacobi, K., Nitrogen on Ruthenium single-crystal surfaces. *Physica Status Solidi (a)* **2000**, 177, 37-51.
- (9) Zhang, C. J.; Luynch, M.; Hu, P., A density functional theory study of stepwise addition reactions in ammonia synthesis on Ru(0001). *Surface Science* **2002**, 496, (3), 221-230.
- (10) Shustorovich, E.; Bell, A. T., Synthesis and decomposition of ammonia on transition metal surfaces: Bond-order-conservation-Morse-potential analysis. *Surface Science Letters* **1991**, 259, L791-L796.
- (11) Savargaonkar, N.; Narayan, R. L.; Pruski, M.; Uner, D. O.; King, T. S., Structure sensitive hydrogen adsorption: Effect of Ag on Ru/SiO<sub>2</sub> catalysts. *Journal of Catalysis* **1998**, 178, 26-33.

# SYNTHESIS OF SODIUM BOROHYDRIDE FOR ENERGY APPLICATIONS

Ying Wu, Jason C. Brady, Michael T. Kelly,  
Jeffrey V. Ortega, Jonathan L. Snover

Millennium Cell Inc.  
1 Industrial Way West, Eatontown, NJ 07724, USA

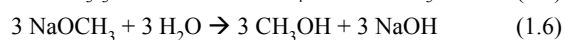
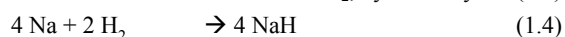
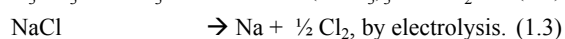
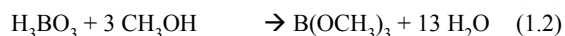
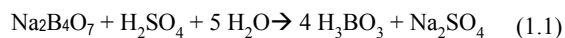
## Introduction

Sodium borohydride ( $\text{NaBH}_4$ ) has been demonstrated as an effective hydrogen storage material. Its hydrolysis generates high purity humidified hydrogen suitable for use in PEM fuel cells. Although the technology can be scaled and tailored for many different applications from very small portable power to fuel cell vehicles, the current high cost of  $\text{NaBH}_4$  is limiting early adoption of the technology to premium power applications. The utilization of  $\text{NaBH}_4$  in high demand, continuous power generation and fuel cell vehicles will not be economically feasible until the production cost of  $\text{NaBH}_4$  can be significantly reduced.

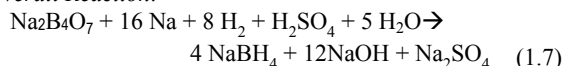
## Discussion

Sodium borohydride is a structurally simple, yet complex chemical. It does not occur in nature; therefore it has to be synthesized from sodium and boron containing raw materials. The production of  $\text{NaBH}_4$  requires the combination of three elements, Na, B, H, and a large amount of energy input. Intrinsically, the level of complexity is derived from significant enthalpic and entropic barriers associated with the strength of the boron-oxygen bond. Low cost  $\text{NaBH}_4$  will depend on the availability of a production process that combines the necessary raw materials (borates, hydrogen, and sodium) in a pathway of optimum overall energy efficiency.

The current state-of-the-art  $\text{NaBH}_4$  production process is based on the reduction of the trialkylborate,  $\text{B}(\text{OCH}_3)_3$ , with NaH, known as the Schlesinger Process [1]. The following chemical equations describe the synthetic pathway to  $\text{NaBH}_4$ .



### Overall Reaction:



The various steps of the Schlesinger Process are fragmented among various chemical producers, lacking integration and producing undesirable by-products. Although the process provides high purity  $\text{NaBH}_4$ , the individual reaction steps are not optimized for energy efficiency. An examination of the primary energy input for the process versus the eventual chemical energy stored in  $\text{NaBH}_4$  will be provided to identify areas for energy efficiency improvements. For example, the process uses large amounts of Na metal. This subjects the overall energy efficiency to the limitations in energy efficiency of the Na process. The current NaCl electrolysis process for Na metal is less than 50% energy efficient. Additionally, reactions (1.4) and

(1.5) are both exothermic, losing a significant portion of the original energy input to reaction heat. Compounded together, the overall reaction of (1.7) is less than 20% energy efficient. Clearly, for  $\text{NaBH}_4$  to become an effective energy carrier, the energy efficiency of its production process has to be significantly improved.

In light of the multi-step nature of the synthetic process, it is important to improve the energy efficiency of each step. The single most costly raw material is Na metal. It follows that major improvements in Na production will have a significant impact on the  $\text{NaBH}_4$  production efficiency. Alternatively, an intermediate other than NaH may be considered to avoid the large enthalpic losses associated with reactions 1.4 and 1.5.

In the first approach, we propose an electrochemical reaction utilizing an anodic reducing agent to lower the operating voltage of the electrochemical cell, thereby achieving overall energy savings in the production of Na. In the second approach, we propose an alternative synthetic pathway that proceeds through diborane ( $\text{B}_2\text{H}_6$ ), an energy-rich hydride intermediate that is closer in energy to  $\text{NaBH}_4$ . The interconversion of  $\text{B}_2\text{H}_6$  and  $\text{NaBH}_4$  can be manipulated by the appropriate selection of reagent. For example, the reaction of  $\text{NaBH}_4$  with certain oxidizing agents generates  $\text{B}_2\text{H}_6$ [2], and  $\text{B}_2\text{H}_6$  can be converted to  $\text{NaBH}_4$  with a variety of Na containing salts [3]. In this approach, the overall process will include the following proposed reaction steps:



### Overall Reaction:



## Experimental

In the first step, Reaction 2.1, relatively inexpensive sodium borates was used as the starting material. Building upon existing knowledge of alkylborate synthesis, we have developed an improved reaction for the preparation of  $\text{B}(\text{OR})_3$ , including trimethyl and tributyl borates, from the discharged product of the Hydrogen on Demand™ system. Other precursors investigated include borax and anhydrous sodium metaborate, and could be extended to any inexpensive borate salts. The reactions were carried out under reflux conditions in alcohol under a  $\text{CO}_2$  atmosphere. The use of  $\text{CO}_2$  produces  $\text{Na}_2\text{CO}_3$  as a byproduct, which is used in Reaction 2.3 to form  $\text{NaBH}_4$  from  $\text{B}_2\text{H}_6$ .

We also report here some preliminary results on Reaction 2.3, which was developed based on the knowledge that Na-containing Lewis bases can react with  $\text{B}_2\text{H}_6$  to form  $\text{NaBH}_4$ . Initial experiments were modeled after those described by Davis and Gottbrath [4], who conducted the reaction of  $\text{B}_2\text{H}_6$  with aqueous NaOH. In our experiments,  $\text{Na}_2\text{CO}_3$  was used instead of NaOH. Yields ranged from 6% to 25%, with higher concentration  $\text{Na}_2\text{CO}_3$  and greater ratio of  $\text{Na}_2\text{CO}_3$  to  $\text{B}_2\text{H}_6$  giving rise to higher yields. Product characterization carried out by infrared spectroscopy (IR), proton and boron nuclear magnetic resonance ( $^1\text{H}$  NMR and  $^{11}\text{B}$  NMR), and by powder X-ray diffraction (XRD) confirmed that  $\text{NaBH}_4$  was indeed synthesized.

The technique of ball-milling was then employed to study the direct interaction of the gaseous diborane and the solid Lewis bases. At the same time, the competing borane decomposition pathway with water was removed by avoiding the aqueous medium. Using this method, higher yields of  $\text{NaBH}_4$  were achieved, from 15% to 65%. The yield was further increased by increasing  $\text{B}_2\text{H}_6$  pressure within

the reaction vessel. Additionally, diglyme was added to the ball mill to facilitate the dissolution of product  $\text{NaBH}_4$ , thereby exposing more  $\text{Na}_2\text{CO}_3$  surfaces for further reaction. Pressures up to 40 psig were employed, and yields up to 72.8% were obtained at these increased pressures along with the utilization of diglyme.

Reaction 2.2 involves the hydrogenolysis of trialkyl borate,  $\text{B}(\text{OR})_3$ , to give the intermediate  $\text{HB}(\text{OR})_2$ , which subsequently disproportionates to generate  $\text{B}_2\text{H}_6$ . The details of this reaction is beyond the scope of this paper, and will be addressed in future publications.

### Conclusions

We have successfully demonstrated the feasibility of converting diborane to borohydride, which represents an important step towards developing a new  $\text{NaBH}_4$  synthesis process. Various reducing agents are being studied for the conversion of B-O bonds to B-H bonds.

### Reference

- (1) Schlesinger, H. I.; Brown, H. C.; Finholt, A. E. *J. Am. Chem. Soc.* **1953**, *75*, 205.
- (2) Kanth, J. V. B.; Brown, H. C. *Inorg. Chem.* **2000**, *39*, 1795-1802.
- (3) Narayana, C.; Periasamy, M. *J. Organomet. Chem.* **1987**, *323*, 145-147.
- (4) Davis, R. E.; Gottbrath, J. A. *Chem. Ind.* **1961**, 1961.

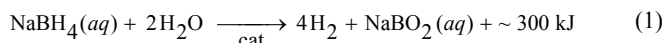
## SODIUM BOROHYDRIDE FOR HYDROGEN STORAGE

Ying Wu, Richard M. Mohring

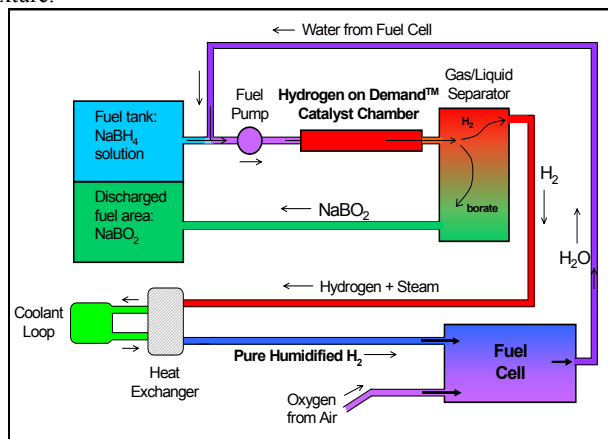
Millennium Cell Inc.  
1 Industrial Way West, Eatontown, NJ 07724, USA

### Introduction

The hydrolysis of sodium borohydride ( $\text{NaBH}_4$ ) is an exothermic reaction that releases hydrogen gas [1] as in Equation 1:



$\text{NaBH}_4$  can be dissolved in water and stabilized via the addition of base ( $\text{NaOH}$ ). In order to have any appreciable reaction, a catalyst is necessary for activation and control of the release of hydrogen gas. Based on this concept, Millennium Cell has developed a technology known commercially as Hydrogen on Demand™ fuel systems (HOD system) [2]. Hydrogen generated in this manner is of high purity and free of carbon, sulfur, or nitrogen containing impurities that poison the fuel cell catalyst. Scheme 1 illustrates the HOD system integrated with a PEM fuel cell, whose water is recycled back to the fuel mixture.



**SCHEME 1. Integrated HOD and Fuel Cell System.**

The reaction of Equation 1 allows for storage of hydrogen in aqueous solutions at high gravimetric density. In a stoichiometric mixture of  $\text{NaBH}_4$  and  $\text{H}_2\text{O}$ , the amount of  $\text{H}_2$  stored represents 10.8% of the mixture weight. The higher the  $\text{NaBH}_4$  concentration, the more hydrogen is stored in a given volume. Table 1 compares the volumetric storage efficiency of a 30wt%  $\text{NaBH}_4$  solution to compressed and cryogenic hydrogen storage. The advantage of  $\text{NaBH}_4$  is obvious.

**Table 1. Volumetric Storage Efficiency Comparisons.**

Storage Method	Storage Specifications	Volumetric Storage Efficiency
$\text{NaBH}_4$	30 wt% solution	~ 63 g $\text{H}_2/\text{L}$
Liquid $\text{H}_2$	cryogenic	~ 71 g $\text{H}_2/\text{L}$
Compressed $\text{H}_2$	5,000 psi	~ 23 g $\text{H}_2/\text{L}$
	10,000 psi	~ 39 g $\text{H}_2/\text{L}$

### Results and Discussion

A number of functioning prototype systems have been constructed and operated by Millennium Cell. One example is an 18 SLM system designed to be coupled to a Ballard Nexa® 1.2 kW

fuel cell. The rate at which  $\text{H}_2$  is generated is directly proportional to the rate at which  $\text{NaBH}_4$  solution is pumped into the catalyst chamber. This operational simplicity translates into relatively straightforward control strategies [3]. When the fuel cell demand for hydrogen gas increases, the system pressure begins to drop. The control system detects the load signal and the drop in pressure and responds by increasing the rate at which fuel is pumped into the catalyst chamber. As fuel reaches the catalyst,  $\text{H}_2$  gas is generated causing the pressure to increase, and the fuel pump is regulated accordingly. Examples of load following data will be presented.

Another important HOD application is in fuel cell vehicles. DaimlerChrysler's Natrium® and Peugeot-Citroën's  $\text{H}_2\text{O}$ ® are two examples. For automotive applications, system pressure can vary from 0-13 bar (0-190 psi) and the rated power output reaches 75 kW. These specifications demand much higher hydrogen flow rates, up to ~1000 SLM of  $\text{H}_2$ .

Figure 1 shows the results of a testing on an automotive-scale HOD system, designed to operate a  $\text{H}_2$  powered internal combustion engine vehicle (>50 kW) at Millennium Cell [3].

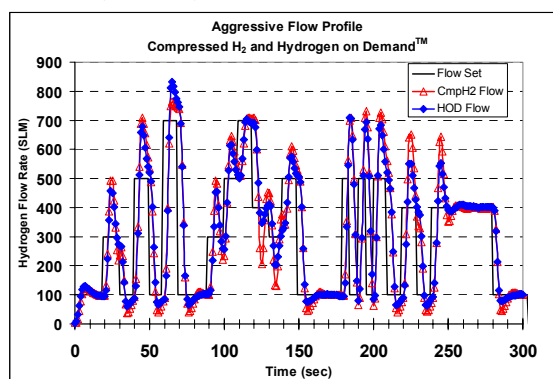


**Figure 1.** Data taken on an automotive scale Hydrogen on Demand™ system, compared to a baseline of compressed hydrogen.

The figure shows an “aggressive flow profile” where the hydrogen flow (directly related to the engine output power) was varied over a wide range of flows and steps to simulate a driving cycle. The HOD system response is shown by the solid diamond symbols. For comparison, a bank of manifolded 2200 psig compressed hydrogen cylinders was also run through the same profile, shown in open triangle symbols. The compressed hydrogen and HOD system response curves are essentially identical; both are clearly capable of supplying the required hydrogen for the application.

### Conclusion

In summary,  $\text{NaBH}_4$  has a high intrinsic gravimetric and volumetric hydrogen storage density for practical hydrogen generation. The Hydrogen on Demand™ technology has been successfully demonstrated over a wide range of hydrogen delivery flow rates and delivery pressures. Research progress is being made on improving current  $\text{NaBH}_4$  synthesis technology so that markets such as transportation can be accessed.

### Reference

- Schlesinger, H. I.; Brown, H. C.; Finholt, A. E. *et. al.*, *J. Am. Chem. Soc.* **1953**, *75*, 215.
- Amendola, S., *et al.*, “System for Hydrogen Generation”, WO Publication WO 01/51410 A1. US patent pending.
- Mohring, R. M.; Eason, I. A.; Fennimore, K. A. SAE World Congress, SAE Technical Paper Number 2002-01-0098, 2002.

# Improvement of Hydrogen Storage and Hydrogen Release Properties of Magnesium by in-situ Catalyst Deposition

Xiaochun Xu, and Chunshan Song\*

Clean Fuels and Catalysis Program, The Energy Institute, and Department of Energy & Geo-Environmental Engineering, The Pennsylvania State University, 209 Academic Projects Building, University Park, PA 16802, USA

\* Corresponding author. E-mail: csong@psu.edu; Tel: 814-863-4466; Fax: 814-865-3248

## Introduction

Because of its high theoretical hydrogen storage capacity (7.6 wt%), magnesium is amongst the most attractive materials for hydrogen storage. From thermodynamical view, the magnesium hydride should form readily at ambient temperature. However, this never occurs in practice.<sup>1</sup> The major problem of magnesium as a rechargeable hydrogen carrier has been its very slow hydriding/dehydriding kinetics. In order to improve the hydriding/dehydriding kinetic, attempts have been made in changing the microstructure of the magnesium and adding a promoter into the magnesium.<sup>2-5</sup> For the catalytic hydriding/dehydriding of magnesium, the catalyst should preferably deposited on the outer surface of the metal particles. However, the conventional techniques, such as ball milling, mechanic alloying and melt-spinning, etc., can not finely control the deposition of the catalyst. Some more complicated process, such as sputtering, etc., has been used.<sup>5</sup> In this paper, a novel in-situ catalyst deposition method was developed for depositing various catalysts on the outer surface of the magnesium particles through a simple wet chemical process. The hydrogen storage and release properties of the catalyst-modified magnesium are reported.

## Experimental

The catalyst-modified magnesium was prepared by auto-reduction of a metal salt in ethylene glycol<sup>6</sup> and in-situ deposited the metal on the magnesium powder (Aldrich, 99.8%, 325 mesh). The precursors for the preparation of the metal particles (catalysts) were palladium chloride, ruthenium chloride and hexachloroplatinic acid. The desired amount of catalyst deposited on the magnesium was 0.5 mol%. After preparation, the mixture dispersion was washed several times with anhydrous butanone and ether, centrifuged, and the collected precipitate was dried at room temperature. All the above processes were carried out under Ar atmosphere in a glove box.

The phase and microstructure of the as-prepared materials were characterized by X-ray diffraction (XRD) and Scanning electron microscopy (SEM). The XRD patterns were obtained on a Scintag Pad V using Cu K $\alpha$  radiation. The SEM images were photographed on a Hitachi S-3500N. The hydriding/dehydriding properties of the materials were measured in an apparatus similar to that in reference 7.<sup>7</sup> The hydriding properties of the materials were measured by monitoring the pressure change in an autoclave at desired temperatures and pressures. The dehydriding properties of the materials were measured by counting the volume of the blow-off hydrogen through a gas burette at ambient pressure and desired temperatures.

## Results and Discussion

### 1. Preparation and characterization of Pd-modified magnesium

Figure 1 shows the XRD patterns of magnesium and Pd-modified magnesium. From the XRD patterns, it can be learned that (1) magnesium was stable in the preparation procedures and did not transform into other phases, e.g., magnesium oxide or magnesium

hydroxide; (2) palladium was deposited on the magnesium particle. Since the desired amount of palladium was only 0.5 mol% in palladium-modified magnesium, the diffraction intensity for palladium was weak. In addition, the width of the diffraction patterns of palladium is broad, which indicate that the particle size of the palladium is small. Under a similar preparation condition, Bonet et al<sup>6</sup> reported that the particle size of palladium was about 19 nm.

Figure 2 shows the SEM images of magnesium and Pd-modified magnesium. By comparing the two SEM images, it can be found that palladium particles were uniformly dispersed on the outer surface of the magnesium particles. The particle size of palladium was around 50-100 nm.

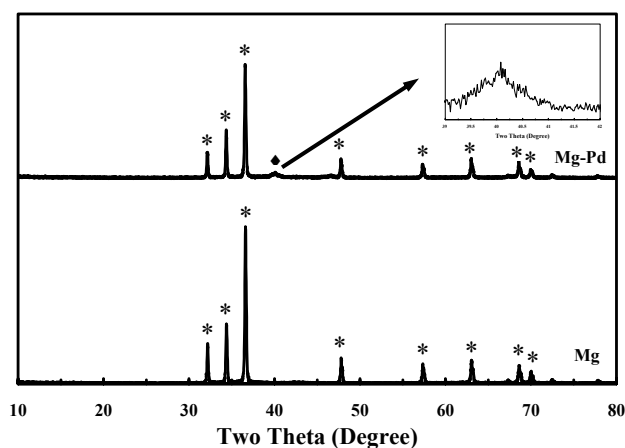


Figure 1. XRD patterns of magnesium and palladium-modified magnesium. (\*) Magnesium; (♦) Palladium.

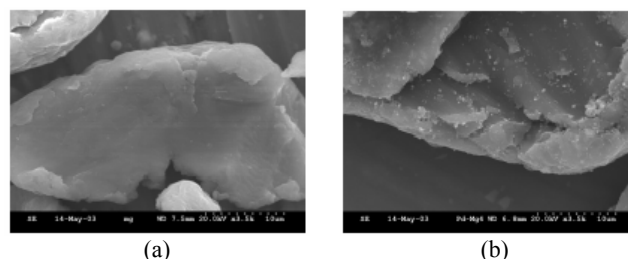
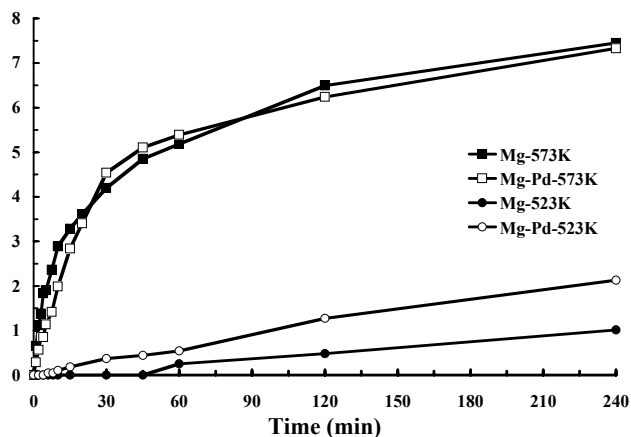


Figure 2. SEM image of magnesium (a) and palladium-modified Magnesium (b).

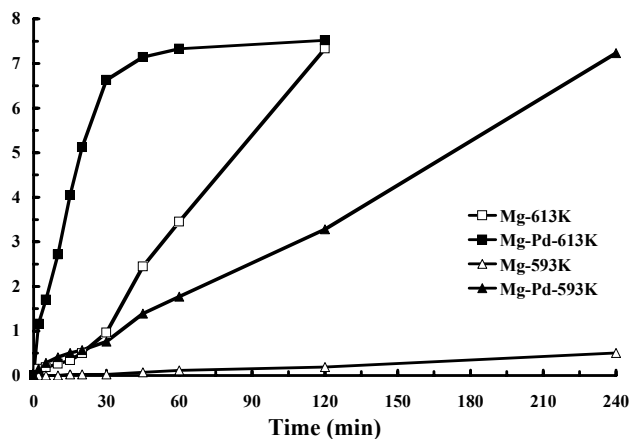
### 2. Hydriding/dehydriding kinetics of Pd-modified Mg

Figure 3 and Figure 4 compare the absorption and desorption kinetics of magnesium and Pd-modified magnesium, respectively. At high temperature, e.g., 573 K, depositing the palladium on the magnesium does not show any obvious catalytic effect on hydride kinetic. However, at a lower temperature, e.g., 523 K, the catalytic effect of palladium becomes significant. The palladium-modified magnesium readily absorbs hydrogen, while the un-modified magnesium absorbs hydrogen after 45 minutes. The amount of hydrogen absorbed is 2.13 wt.% for palladium-modified magnesium and 1.02 wt.% for un-modified magnesium after 4 hours absorption. The effect of palladium on desorption is more pronounced than that on absorption. At 613 K, the rate of dehydride of palladium-modified magnesium is much faster than that of the un-modified magnesium. For example, the palladium-modified magnesium hydride desorbs 5.12 wt.% hydrogen after 20 minutes desorption, which is 10 times faster than that of the un-modified magnesium hydride. Even at 593 K, the palladium-modified magnesium hydride

can still fully dehydride in 4 hours, while the un-modified magnesium hydride only desorbs 0.50 wt% hydrogen at the same desorption condition.



**Figure 3.** Comparative H<sub>2</sub> absorption kinetics of magnesium and Pd-modified magnesium under 400 Psi at 523 K and 573K.



**Figure 4.** Comparative H<sub>2</sub> desorption kinetics of magnesium and Pd-modified magnesium at 593 K and 613K under ambient pressure.

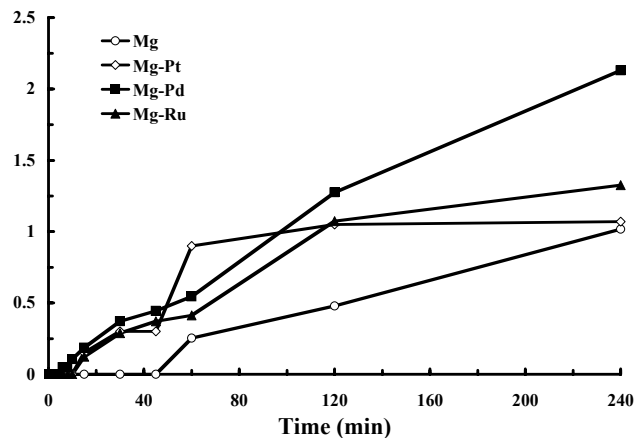
### 3. The types of catalysts

Figure 5 and Figure 6 compare the absorption and desorption kinetics of magnesium and Pd, Pt and Ru-modified magnesium, respectively. After the magnesium is modified with Pd, Pt and Ru, the hydriding and dehydriding kinetics of the magnesium are all improved. At 523 K and 400 Psi, the Pd, Pt and Ru-modified magnesium all readily absorb the hydrogen. The rate of absorption decreases in the following order: Pd > Pt ≈ Ru > Un-modified. The rate of desorption at 593 K shows different trend at different desorption time. At the beginning, the rate of desorption decreases in the following order: Pd ≈ Pt > Ru > Un-modified. The desorption rate of Pt-modified magnesium hydride becomes slowly after 120 minutes desorption.

### Conclusions

A novel in-situ catalyst deposition method that improves hydrogen uptake and release kinetics, was developed for depositing various catalysts (Pd, Pt and Ru) on the magnesium particles through a simple wet chemistry process. XRD and SEM characterizations indicated that nano-sized metal particles were deposited on the outer

surface of the magnesium particles. Both the hydriding and dehydriding kinetics of magnesium were improved significantly after depositing the catalysts on the outer surface of the magnesium particles. Among Pd, Pt and Ru, Pd showed the best catalytic effect.



**Figure 5.** Comparative H<sub>2</sub> absorption kinetics of magnesium and Pd, Pt, Ru-modified magnesium under 400 Psi at 523 K.

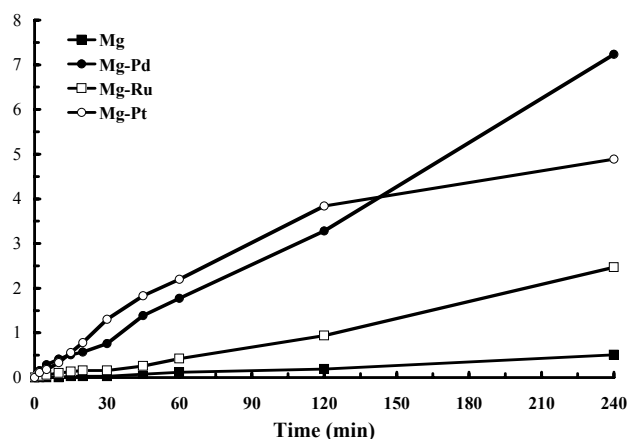


**Figure 6.** Comparative H<sub>2</sub> desorption kinetics of magnesium and Pd, Pt, Ru-modified magnesium at 593 K under ambient pressure.

**Acknowledgement.** We gratefully acknowledge the financial support by a Seed Grant from the Hydrogen Energy Center of the Pennsylvania State University.

### References

- (1) Zaluska, A.; Zaluski, L.; Strom-Olsen, J.O. *J. Alloy. Comp.* **1999**, *289*, 197-206.
- (2) Hout, J.; Tremblay, M.-L.; Schulz, R. *J. Alloy. Comp.* **2003**, *in press*.
- (3) Gross, K.J.; Chartouni, D.; Leroy, E.; Züttel, A.; Schlapbach, L. *J. Alloy. Comp.* **1998**, *269*, 259-270.
- (4) Yin, J.T.; Yamada, T.; Yoshinari, O.; Tanaka, K. *Materials Transactions* **2001**, *42*, 712-716.
- (5) Higuchi, K.; Yamamoto, K.; Kajioka, H.; Toiyama, K.; Honda, M.; Orimo, S.; Fujii, H. *J. Alloy. Comp.* **2002**, *330-332*, 526-530.
- (6) Bonet, F.; Delmas, V.; Grugeon, S.; Herrera Urbina, H.; Silvert, P.Y.; Tekcia-Elhissien, K. *Nano. Mater.* **1999**, *8*, 1277-1284.
- (7) Bogdanovic, B.; Schwickardi, M. *J. Alloy. Comp.* **1997**, *253-254*, 1-9.

# Can Heteroatoms be the activators for hydrogen storage in carbon nanotubes?

B. Viswanathan, M. Sankaran and R. Ganesan

Department of chemistry, Indian Institute of Technology, Madras 600036.

## Introduction

The studies on the storage of hydrogen took a dramatic turn in 1998-99, when Rodriguez et al [1,2] reported exotic values of hydrogen absorption by carbon nano structures up to 10-12 hydrogen molecules per carbon atom, though in a sequent communication they have reduced this up to 4 molecules per atom of carbon. This is nearly twice (0.4 g H<sub>2</sub>/g C) of the most hydrogenated carbon compound namely CH<sub>4</sub> where the hydrogen to carbon weight ratio is 0.25 g H<sub>2</sub>/g C. Subsequently there have been various reports in literature to substantiate these observations [3-7] and none of them in any way could realize the expected (DOE standards) 6.5 weight percent leave alone repeating the original adsorption capacity claimed.

The present investigation has therefore been undertaken with the following objectives and postulates (i) Hydrogen adsorption on carbon materials especially nanotubes, is possible only when it contains some sites wherein hydrogen molecule can be activated. Taking the clue from nature, it is postulated that the presence of heteroatoms in the carbon nanotubes may be the appropriate sites for activation of hydrogen and (ii) If heteroatom containing carbon nanotubes were to be one of the materials appropriate for hydrogen storage, then the questions to be addressed are: (a) what is the gradation of materials containing various heteroatoms? (b) What are the geometrical positions in the nanotubes that are active? In order to understand the interaction of hydrogen molecule in pure carbon nanotubes and heteroatoms (N, P, S and B) substituted carbon nanotubes, cluster model calculations have been carried out using Density Functional Theory (DFT). From the analysis of the reports in literature, it is clear that the hydrogen molecule is interacting at the interstitial positions of the carbon nanotubes than inside the nanotubes. The cluster model, which describes the interface of the three tubes, is considered in these studies (Fig.1).

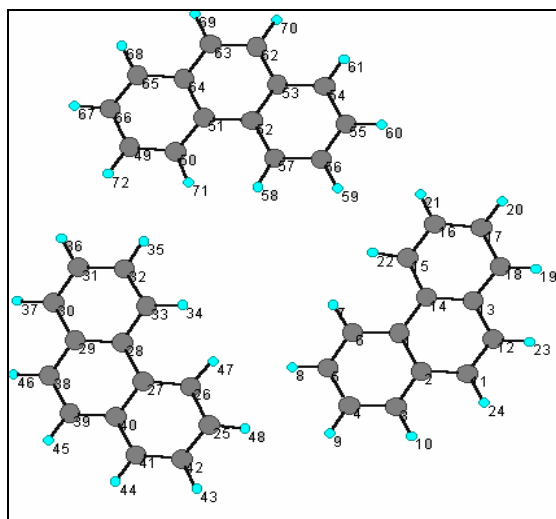


Figure 1. The Cluster model (the heteroatoms are substituted in positions (26,33,50,57,15 and 6)

## Theoretical methods

The terminal sites of the cluster are saturated with hydrogen in order to avoid the edge effect [8]. The geometry of the cluster is optimized using Universal Force Field (UFF 1.02) approach. The hydrogen molecule is allowed to interact with optimized cluster and the geometry of the system is optimized. Cerius2 software was used for force field calculations. Using force field optimized parameters, DFT single point energy and bond population calculations were done by Becke's three parameter hybrid functional with LYP correlation functional (B3LYP) and 6-31G(d) basis set using Gaussian98W. Similar procedure was adopted for heteroatom substituted cluster models.

## Results and discussions

The hydrogen molecule is allowed to interact with the carbon atoms of the unsubstituted nanotube and the dissociation energy of hydrogen was calculated (Table 1). The dissociation energy of hydrogen in its free state is 4.74 eV, and remains unaltered when it is placed in between the pure carbon nanotubes (4.76 eV). In order to study the influence of heteroatoms toward the activation of hydrogen, various heteroatoms (N, P and S) are substituted at different positions of the cluster as shown in Fig 1. The substitutional positions for heteroatoms as given in brackets (26,33,50,57,15,6) are chosen based on the fact that these interstitial positions offer minimum potential energy for the cluster. In the presence of heteroatoms, the dissociation energy of hydrogen molecule is considerably decreased compared to that of pure carbon nanotubes as can be seen from the values presented in Table 1. This indicates that heteroatom can activate the hydrogen molecule and its presence favors the dissociation of hydrogen. This conclusion can also be arrived from the redox potential values of the couples involved. For instance, redox potentials of heteroatoms are higher than that of carbon (S/S<sup>2-</sup>, N/N<sup>3-</sup>, P/P<sup>3-</sup>, C/C<sup>4-</sup> are respectively, 0.171, 0.057, -0.111 and -0.132 V). The same fact can be further independently supported by the Ellingham diagram which indicates that free energy of formation for N-H bond is more favourable than that of C-H bond. The bond length of the hydrogen molecule is elongated in heteroatom substituted carbon nanotube compared to that of pure carbon nanotubes, indicating that there is considerable activation of hydrogen molecule in heteroatom containing carbon nanotubes.

In order to understand the role of hetero atoms in hydrogen activation in carbon nanotubes the calculations have been carried out to estimate the value of activation energy value of each of the steps of hydrogen activation and migration (Fig 2) within the framework of Transition state theory and the essential results are given in Table 2. These results also support our contention that heteroatoms may be appropriate for activation of hydrogen on carbon nanotubes.

## Conclusions

Heteroatom containing carbon nanotubes are able to activate the hydrogen compared to pure carbon nanotubes. This activated hydrogen can migrate to other sites and opens up another avenue in the search of material for the hydrogen storage.

**Table 1. The Bond length and dissociation energy of hydrogen on the clusters.**

Heteroatom	Mode of substitution	Bond length (H-H) (Å)	H <sub>2</sub> dissociation energy (eV)
Hydrogen	-	0.708	4.74
Un substituted CNT	-	0.708	4.76
Nitrogen substituted CNT			
	1 N + 1 H <sub>2</sub>	0.84	0.31
	3 N + 1 H <sub>2</sub>	0.84	0.32
(Each ring 2N)			
	3 N + 3 H <sub>2</sub>	0.84	0.33
	6 N + 1 H <sub>2</sub>	1.08	0.56
Phosphorus substituted CNT			
	1 P + 1 H <sub>2</sub>	0.81	2.06
	3 P + 1 H <sub>2</sub>	0.82	1.36
Sulphur substituted CNT			
	3 P + 3 H <sub>2</sub>	0.82	1.51
	1 S + 1 H <sub>2</sub>	0.81	0.27
(Each ring 1S)			
	3 S + 1 H <sub>2</sub>	0.81	1.03
	3 S + 3 H <sub>2</sub>	0.81	0.25

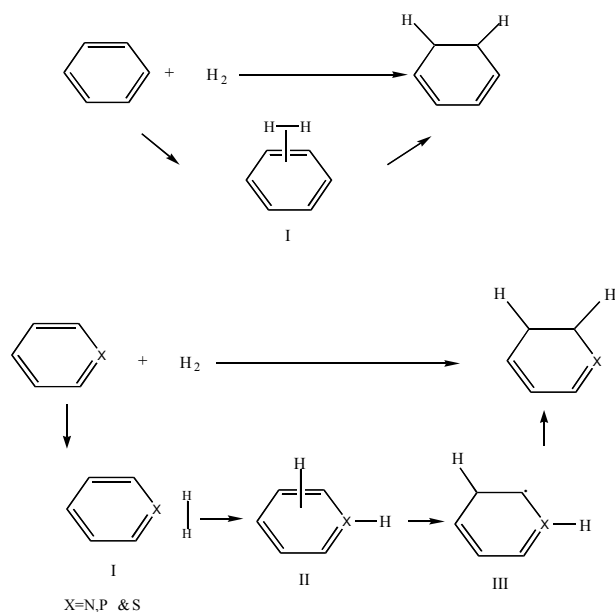


**Figure 2.** Proposed transition state pathways for hydrogen storage in carbon nanotubes and heteroatom (N,P and S) containing carbon nanotubes.

#### References

1. A. Chambers, C. Parks, R.T.K. Baker and N.M. Rodriguez *J.Phys. Chem.B* **1998**,102, 4253.
2. C. Park, P. E. Anderson, C. D. Tan, R. Hidalgo, A. Chambers and N. M. Rodriguez, *J.Phys. Chem.B* **1999**, 103, 10572.
3. C.C. Ahn, Y. Ye, B.V. Ratnakumar, C. Witham, R.C. Bowman, Jr. and B. Fultz *Appl. Phys. Lett.* **1998**, 73, 3378.
4. R. Ströbel, L. Jörissen, T. Schliermann, V. Trapp, W. Schütz, K. Bohmhammel, G. Wolf and J. Garcke *J. Power Sources* **1999**, 84, 221.
5. Y. Ye, C.C. Ahn, C. Witham, B. Fultz, J. Liu, A.G. Rinzler, D. Colbert, K.A. Smith and R.E. Smalley *Appl. Phys. Lett.* **1999**, 74, 2307.
6. C. Liu, Y.Y. Fan, M. Liu, H.T. Cong, H.M. Cheng and M.S. Dresselhaus *Science* **1999**, 286, 1127.
7. M. Hirscher, M. Becher, M. Haluska, A. Quintel, V. Skakalova, Y. -M. Choi, U. Dettlaff-Weglikowska, S. Roth, I. Stepanek, P. Bernier. *J. Alloys. Comp.* **2002**, 330, 654.
8. F.H. Yang and R.T. Yang, *Carbon* **2002**, 40, 437.

**Table 2. The transition state optimized parameters for various clusters and energy of activation for each pathway.**

Substitution	Ea <sup>c</sup> I (eV)	Ea II (eV)	Ea III (eV)	H-H (Å)	X-H (Å)	C <sub>2</sub> -H <sup>b</sup> (Å)	C <sub>2</sub> -H <sup>a</sup> (Å)	C <sub>3</sub> -H (Å)
Carbon	15.08	-	-	0.65	-	-	-	-
Nitrogen	3.91	8.50	1.30	1.69	1.19	1.39	1.16	1.13
Phosphorus	3.15	8.84	2.24	2.11	1.62	1.74	1.12	1.26
Sulphur	4.27	9.30	3.58	2.18	1.51	2.32	1.58	1.67

a - after migration, b - before migration, c - Ea=TE (each transition state) – TE (reactant)